Instituto Alberto Luiz Coimbra de
Pós-Graduação e Pesquisa de Engenharia

ON THE STRENGTH AND DSM DESIGN OF END-BOLTED COLD-FORMED STEEL COLUMNS BUCKLING IN DISTORTIONAL MODES

Warlley Soares Santos

Tese de Doutorado apresentada ao Programa de Pós-graduação em Engenharia Civil, COPPE, da Universidade Federal do Rio de Janeiro, como parte dos requisitos necessários à obtenção do título de Doutor em Engenharia Civil.

Orientadores: Alexandre Landesmann
Dinar Reis Zamith Camotim

Rio de Janeiro
Dezembro de 2017

ON THE STRENGTH AND DSM DESIGN OF END-BOLTED COLD-FORMED STEEL COLUMNS BUCKLING IN DISTORTIONAL MODES

Warlley Soares Santos

TESE SUBMETIDA AO CORPO DOCENTE DO INSTITUTO ALBERTO LUIZ COIMBRA DE PÓS-GRADUAÇÃO E PESQUISA DE ENGENHARIA (COPPE) DA UNIVERSIDADE FEDERAL DO RIO DE JANEIRO COMO PARTE DOS REQUISITOS NECESSÁRIOS PARA A OBTENÇÃO DO GRAU DE DOUTOR EM CIÊNCIAS EM ENGENHARIA CIVIL.

Examinada por:

Prof. Alexandre Landesmann, D.Sc.

Prof. Eduardo de Miranda Batista, D.Sc.

Prof. Pedro Colmar Gonçalves da Silva Vellasco, Ph.D.

Prof. Cilmar Donizeti Basaglia, D.Sc.

Prof. Eliane Maria Lopes Carvalho, D.Sc.

RIO DE JANEIRO, RJ - BRASIL
DEZEMBRO DE 2017

Santos, Warlley Soares

On the Strength and DSM Design of End-Bolted Cold-Formed Steel Columns Buckling in Distortional Modes / Warlley Soares Santos. – Rio de Janeiro: UFRJ/COPPE, 2017.

XIII, 140 p.: il.; 29,7 cm.

Orientadores: Alexandre Landesmann
Dinar Reis Zamith Camotim

Tese (doutorado) – UFRJ/ COPPE/ Programa de Engenharia Civil, 2017.

Referências Bibliográficas: p. 83-87.

1. End-bolted cold-formed steel columns. 2. Distortional failures. 3. Experimental and numerical investigation. 4 Direct Strength Method (DSM) design. I. Landesmann, Alexandre *et al.* II. Universidade Federal do Rio de Janeiro, COPPE, Programa de Engenharia Civil. III. Título.

À minha esposa Marla e aos meus filhos Anderson e Camila pelo infinito amor e compreensão.

Acknowledgements

To God for everything, to Him all the honor and all the glory.

To my parents, José Soares dos Santos and Maria de Fátima Araújo dos Santos for everything and to my brothers Welington and Welcius and my sister Manoela by the union of our family, because without that stability none of this would be possible.

To my advisor, professor Alexandre Landesmann, not only for his dedication and support during the preparation of each step of this thesis, but mostly the friendship.

To my advisor, professor Dinar Camotim, for the thesis organization, review and especially for his dedication not only in this work but for the benefit of technological development of engineering.

To the engineers Renato Evangelista and Gabriela Ribeiro Fernandes for the help in the development of the experimental tests of this study and especially the friendship.

To the professor Romildo Toledo and colleagues of Laboratory of Structures and Materials (LABEST – COPPE/UFRJ), in particular: Anderson Neves Viana, Anísio Ribeiro da Silva, Márcio de Souza and Osvaldo Oliveira Santiago.

To my friend Leonardo Souza Bueno for always helping with computer issues.

To Célio Noia Miranda for the friendship and Orlando José Moura Caldas for the tips and assistance in technology and for the help I will never forget for registration of the selection process for doctorate course.

To VALE SA, in the persons of the executive manager Luiz Fernando Landeiro, the manager José Fernando Varejão Fassarella and supervisor Marcelo Athanasio Strieder by the incentives and financial support.

To my coworker and friend Juliano Frigini for the development of welding procedure of the specimens. To my coworkers Humberto Carlos and his team, Rodrigo Lemos de Almeida and Tiago Correa Rangel for manufacturing the hinge devices.

To Zoráide Dantas Ribeiro Freitas for the help seeking scientific articles.

To MARKO for manufacturing and donation of the firsts three specimens.

To CEDISA, specially Silvino Canzian and Igor Ferreira for the donation of steel sheets.

To RID and PLAMONT, in the persons of Diego Volponi, Ivan de Lima, Reinaldo Okazaki, Oskar Wruck, Francisco Kulnig, Walace Laures and Fabiano Tosta for manufacturing 20 specimens.

To all those involved directly or indirectly that helped in this work.

“Geralmente a imperfeição vive satisfeita consigo mesma.”

- Carlos Drummond de Andrade

Resumo da Tese apresentada à COPPE/UFRJ como parte dos requisitos necessários para a obtenção do grau de Doutor em Ciências (D.Sc.)

SOBRE A RESISTÊNCIA E DIMENSIONAMENTO PELO MRD DE COLUNAS APARAFUSADAS DE PERFIS FORMADOS A FRIO FLAMBANDO SOB MODO DISTORCIONAL

Warlley Soares Santos

Dezembro/2017

Orientadores: Alexandre Landesmann
Dinar Reis Zamith Camotim

Programa: Engenharia Civil

A tese reporta uma investigação experimental sobre o comportamento e resistência última de colunas de perfil formado a frio de seção transversal tipo U enrijecido com extremidades parafusadas selecionadas para falharem sob modo distorcional. Além de descrever o procedimento dos ensaios, os resultados são apresentados e discutidos, estes consistem em três testes: (i) medições de imperfeições inicias, (ii) trajetórias de equilíbrio e (iii) configuração da deformada (modo de falha) e as resistências últimas. Os resultados experimentais são usados para validar modelos numéricos pelo método dos elementos finitos com a finalidade de analisar o comportamento não linear geometricamente e do material das colunas. Esses modelos são então usados em análise paramétrica envolvendo colunas de seção tipo U enrijecido com extremidades parafusadas e parafusada-fixa com diversas combinações de geometria (comprimento e dimensões de seção transversal) e material com comportamento elástico-plástico perfeito (tensão de escoamento), objetivando adquirir conhecimento sobre o mecanismo de pós-flambagem e gerar dados de resistência última das colunas. Finalmente, os dados experimentais e numéricos de resistência última obtidos são usados para avaliar a qualidade das previsões pelo MRD da atual curva de dimensionamento distorcional e, se necessário, propor preliminarmente diretrizes sobre como melhora-la.

Abstract of Thesis presented to COPPE/UFRJ as a partial fulfillment of the requirements for the degree of Doctor of Science (D.Sc.)

ON THE STRENGTH AND DSM DESIGN OF END-BOLTED COLD-FORMED STEEL COLUMNS BUCKLING IN DISTORTIONAL MODES

Warlley Soares Santos

December/2017

Advisors: Alexandre Landesmann
Dinar Reis Zamith Camotim

Department: Civil Engineering

The thesis reports an experimental investigation on the behavior and ultimate strength of end-bolted cold-formed steel lipped channel columns selected to fail in distortional modes. Besides describing the test set-up and procedure, the available results are presented and discussed: they concern three tests and consist of (i) initial imperfection measurements, (ii) equilibrium paths relating the applied load to key column displacements and (iii) deformed configurations (including the collapse mode) and failure loads. The experimental results are used to validate ANSYS shell finite models intended to analyze the column geometrically and materially non-linear behavior. These models are then employed to perform a parametric study involving end-bolted lipped channel columns with various combinations of geometry (length and cross-section dimensions) and elastic-perfectly plastic material behavior (yield stress), aimed at (i) acquiring knowledge on the column post-buckling mechanics and strength reserve, and (ii) gathering ultimate strength data. Finally, the experimental and numerical failure load data obtained are used to assess the quality of their predictions by the current DSM distortional design curve and, if needed, provide preliminary guidelines on how to improve them.

Summary

1 Introduction 1
  1.1 Historic 1
  1.2 Motivation 4
  1.3 Objectives 5
  1.4 Outline 6
2 Bibliography Review 7
  2.1 Cold-Formed Steel Member 7
  2.2 Connections in Cold-Formed Steel Members 9
    2.2.1 Welded Connection 9
    2.2.2 Bolted Connection 9
  2.3 Instability Modes 12
    2.3.1 Global Buckling 13
    2.3.2 Local Buckling 14
    2.3.3 Distortional Buckling 16
  2.4 Direct Strength Method 18
    2.4.1 Origin and Development 18
    2.4.2 Column Compressive Strength 18
    2.4.3 Determination of Critical Buckling Loads 19
    2.4.4 Remarkable Advance 21
3 Column Geometry Selection – Buckling Behavior 24
4 Experimental Investigation 29
  4.1 Column Specimens 29
  4.2 Material Properties 32
  4.3 Initial Geometric Imperfections 35
  4.4 Test Set-up 41
  4.5 Test Results 44
    4.5.1 Equilibrium paths 44
    4.5.2 Failure Loads 46
    4.5.3 Deformed configurations and failure modes 47
5 Numerical Investigation 52
  5.1 SFE Model 52
    5.1.1 Loading and End Conditions 52
    5.1.2 Analysis 54
    5.1.3 Mesh 58
  5.2 Validation Study 60

5.3 Numerical Results ... 63
5.3.1 Elastic Post-Buckling Analysis ... 64
5.3.2 Elastic-plastic Post-Buckling Analysis and Ultimate Strength ... 65
5.3.3 Ultimate Strength Data ... 70
6 DSM Design Considerations ... 75
6.1 Load and Resistance Factor Design (LRFD) ... 79
7 Concluding Remarks ... 81
7.1 Suggestions for future works ... 82
8 Bibliography ... 83
Appendix A ... 88
Appendix B ... 112
Appendix C ... 120

Symbols

Capital roman letters

A – Cross section area.

A_c – Contact area in bolted bearing-type load.

C_ϕ – Calibration coefficient.

C_h – Factor for fillers.

C_P – Correction factor.

C_w – Torsional warping constant.

E – Modulus of elasticity of steel.

F_m – Mean value of the fabrication factor.

$F_{t,i}$ – Clamping force in the screw connections by friction.

F_{Rd} – Bearing strength.

F_{Tb} – Minimum fastener tension.

$F_{t,Rd}$ – Available tension strength on bolt.

$F_{t,Sd}$ – Required tension force.

$F_{v,Rd}$ – Available shear strength on bolt.

$F_{v,Rd}$ – Available tension strength on the bolt.

G – Shear modulus of steel.

I_o –Polar moment of inertia of a plane area with respect to shear center.

I_T – Torsional constant (*Saint Venant*).

I_x and I_y – Moments of inertia of a plane area with respect to the X and Y axes.

K – Stress concentrator coefficient.

L – Span length.

L_D – Member length associated to distortional buckling.

L_x – Unbraced length of compression members for bending about X–axis.

L_y – Unbraced length of compression members for bending about Y–axis.

L_z – Unbraced length of compression members for bending about Z–axis.

M_m – Mean value of the material factor.

P – Compressive force.

$P_{b1.e}$ – Lower global buckling force.

$P_{b1.L}$ – Lower local buckling force.

P_{cr} – Critical elastic buckling force.

$P_{cr.e}$ – Elastic global buckling force.

$P_{cr.e\_x}$ – Elastic global buckling force with respect to main axis X of the section.

$P_{cr.e\_y}$ – Elastic global buckling force with respect to main axis Y of the section.

$P_{cr.e\_z}$ – Torsional elastic buckling force of column due to compression.

$P_{cr.D}$ – Distortional buckling force.

$P_{n.D}$ – Nominal axial strength for distorcional buckling.

$P_{n.e}$ – Nominal axial strength for overall buckling.

$P_{n.l}$ – Nominal axial strength for local buckling.

$P_{n.Le}$ – Nominal axial strength for interactive local/global buckling.

P_m – Mean value of professional factor, for tested component.

P_u – Ultimate strength.

P_y – Yield load.

Q – Greater intensity of gradient distributed load in bolted bearing load-type.

V_F – Coefficient of variation of the fabrication factor.

V_M – Coefficient of variation of the material factor.

V_p – Coefficient of variation of test results.

V_Q – Coefficient of variation of the load effect.

Lowercase roman letters

a and b – Length and width of a plate respectively.

b_a – Shorter distance from the hole edge to the web.

b_f – Nominal flange width in lipped channel section.

$b_{f.12}$ and $b_{f.76}$ – Measured flange widths in lipped channel specimens.

b_l – Nominal edge stiffener width in lipped channel section.

$b_{l.12}$ and $b_{l.76}$ – Measured edge stiffener widths in lipped channel specimens.

b_w – Nominal and measured web in lipped channel section.

d – Width of the coupon specimen in the test characterization of the material.

d_f – Standard hole diameter.

d_p – Bolt nominal diameter.

f_u – Ultimate stress.

f_{ub} – Ultimate stress of bolt.

f_y – Yield stress.

k – Plate buckling coefficient.

k_x, k_y and k_z – Effective length factors with respect to X, Y and Z axes respectively.

m – Degrees of freedom.

n – Numbers of tests.

r_i – Inner bending radius in lipped channel section.

t – Plate thickness.

t_{12} and t_{76} – Measured wall thickness in lipped channel specimens.

w – Plate normal translations in its average plan.

x_o – Distance from centroid to shear center section in principal *X*-axis direction.

y_o – Distance from centroid to shear center section in principal *Y*-axis direction.

Greek letters

α – Contact angle in bolted bearing load-type.

α_{12} and α_{76} – Angles formed by the undeformed and deformed flanges 12 and 76 respectively.

β – Cross-section torsional rotation.

β_0 – Target reliability index.

δ – Lateral displacement.

δ_0 – Initial geometric amplitude imperfection.

δ_{12}^{D} and δ_{76}^{D} – Distortional displacements.

δ_{W}^{L} – Mid-web wall bending displacement.

δ_{m}^{G} and δ_{M}^{G} – Translations due to minor and major-axis flexure respectively.

Δ – Axial shortening.

ε – Unit strain.

ϕ – Resistance factor.

γ_e – Resistance factor in slip-critical connections.

η_s – Number of slip planes in slip-critical connections.

$\bar{\lambda}_e$ – Global buckling slenderness ratio.

$\bar{\lambda}_D$ – Distortional buckling slenderness ratio.

$\bar{\lambda}_{Le}$ – Local-global interaction slenderness ratio.

μ – Mean slip coefficient in slip-critical connections.

ν – *Poisson* coefficient.

θ_1, θ_2, θ_3 and θ_4 – Angles formed by adjacent components in lipped channel section.

σ – Stress.

σ_{cr} – Compressive critical stress.

1 Introduction

Cold-formed steel structures are steel structural products that are made by bending flat sheets of steel at ambient temperature into shapes that will support more than the flat sheets themselves. They have been produced for more than a century since the first flat sheets of steel were produced by the steel mills [1].

Cold-formed steel profiles are widely used in the construction industry due to the fact that they provide high structural efficiency (large strength-to-weight ratio), low production and erection costs and notable fabrication versatility.

1.1 Historic

Relative to cold-formed steels, the use of high strength steels and thinner sections leads inevitably to complex design problems, particularly in the fields of structural stability and joints. In compression, cold-formed members can exhibit three modes of instability: local, distortional and flexural or flexural–torsional buckling [2].

Among the instabilities modes in prismatic structural elements under compression load, the global buckling mode was the first to be studied. Euler, in 1744, demonstrated an analytical solution to the instability problem of flexural buckling. Wagner, 1929, developed an analytical solution for the torsional buckling phenomenon. Finally, Kappus, in 1937, analytically solved the instability problem of flexural and torsional buckling [3].

The local buckling mode was investigated by Bryan who solved analytically the problem of local instability in supported plates in 1891 [3]. SCHUMAN and BACK [4] have shown experimentally that additional load could be supported by rectangular metal plates after local buckling occur, thus revealing, the local buckling strength post-reserve. In the period between 1930 and 1935, experimental research in thin-walled structures showed no full agreement between theory (analytical equations) and the buckling experiments. Thus, the demand for empirical equations of allowable stress increased and accelerated out experiments in companies, research laboratories and universities [5]. Following this line, von KARMAN *et al.* [6] introduced the concept of effective width, later corrected by WINTER [7]. Basically, this concept is essentially the reduction in the effectiveness of the plates that comprise a cross-section after local buckling occurs [8].

The newest buckling mode to be unveiled was the distortional, this type of instability was first observed by LUNDQUIST and STOWELL [9] and then by GALLAHER and BOUGHAN [10] in the investigation of stability of panels stiffened with Z profiles.

In 1950s, van der Maas studied the buckling behavior in hat type columns and reported the occurrence of “other local buckling” involving rotation stiffened elements [11]. Chilver (1951 and 1953) and Harvey (1953) considered the interaction between the elements that make up the profile section in determining the local buckling stress. In addition, for lipped channels, Chilver stated that the reinforcing “lip” should be sufficiently stiff to insure local buckling (and thus avoid distortional buckling), but gave no criteria for achieving this [12].

SHARP [13] presented an early theoretical treatment of distortional buckling, or as he termed it “overall” buckling. This approach was based on the torsion buckling analysis in which it was considered a stiff component restricted to rotation at the junction with another component of the section.

In 1978, Thomasson performed experiments on lipped channels with slender webs. In order to elevate local buckling stress of the plates small groove stiffeners were folded in. This eliminated the local buckling problem, but created what Thomasson called a “local-torsional” problem – *i.e.*, distortional buckling. This is a recurring theme for distortional buckling – optimization to remove a local mode creates a distortional problem. Thomasson considered this “local-torsional” mode undesirable and thus put closely spaced braces from lip to lip insuring that distortional buckling did not occur and therefore making the local mode again dominant [12].

TAKAHASHI and MIZUNO [14] analytically demonstrated the main deformation characteristics of the distortional mode considering two shear centers, distortional rigidity and analogy of beam on an elastic foundation.

In the 1980s, the need to investigate the profiles behavior made of cold-formed rack sections used as pallet columns for storage, led some researchers to focus more attention on distortional buckling phenomenon, since the racks profiles often fail by distortion [12]. SRIDHARAN [15] developed the finite strip method to study the post-buckling in the distortional mode (called local-torsional) and demonstrated the rapid increase in membrane stress at the tips of edge-stiffening lips after distortional buckling.

This indicated that the post-buckling reserve in the distortional mode might not be as great as local mode since yielding would occur earlier in the post-buckling range [12]. Among the researchers, Hancock excelled due to extensive investigation on the behavior of distortional buckling of cold-formed sections, on his extensive research provided experimental evidence of the occurrence of distortional instability and improved numerical tools [16] to assist the understanding of distortional buckling behavior and post-buckling of cold-formed profiles with various cross-sections. LAU and HANCOCK [17] also proposed an analytical method for predicting the elastic distortional buckling stress applying a technique similar to the approach used by SHARP [13], however, including the instability of the web.

KWON and HANCOCK [18] conducted experiments on lipped channels with and without groove stiffeners in the web. The distortional mode was unrestricted and the tests showed that interaction of distortional buckling with other modes is weak. Furthermore, it was observed that the post-buckling capacity of distortional buckling is lower than local buckling.

RASMUSSEN and HANCOCK [19] showed the importance of different end fixity to singly symmetric columns in the post-buckling behavior local and global flexural, this study has been analytically shown that local buckling does not induce overall bending of fixed-ended, as it does of a pin-ended condition. Later, this theory was confirmed experimentally by YOUNG and RASMUSSEN [20] – consequently, the local buckling has a fundamentally different effect on the behavior of pin-ended and fixed-end singly symmetric columns.

Traditionally used for the design and profile security check cold-formed, since the 1940s, the concept of effective width involves laborious calculations and was not appropriate for cases of distortional buckling. HANCOCK *et al.* [21] suggested curves to predict resistance to profiles under distortional failure, unlike other researchers who have proposed similar treatment to that applied to local buckling, *i.e.*, application of the concept of effective width [12]. In this sense, SCHAFER [8] proposed a new methodology to estimate the resistance of cold-formed steels called Direct Strength Method (DSM) that had its roots in the original idea of HANCOCK *et al.* [21]. Due to its simplicity, the DSM was incorporated into the Brazilian standard [22], American [23] and Australian/New Zealander [24] codes as an alternative to the concept of effective width. The main advantages of the method are its facility for design engineers and its ability to accurately account for the behavior of complex shapes [25]. The DSM is predicated upon the idea that if an engineer determines all of the elastic instabilities for the column, *i.e.* local ($P_{cr.L}$), distortional ($P_{cr.D}$) and global buckling ($P_{cr.e}$), and also determines the load that causes the section to yield (P_y), then the strength can be directly determined, *i.e.*, $P_n = f(P_{cr.L}, P_{cr.D}, P_{cr.e}, P_y)$. The method is essentially an extension of the use of column curves for global buckling, but with application to local and distortional buckling instabilities and appropriate consideration of post-buckling reserve and interaction in these modes [8].

1.2 Motivation

Generally, compressive thin-walled column tests are conducted on rigid plates welded in the specimen's end cross-sections – *e.g.* [26], [27], [28] and [29]. Therefore, compression tests in end-bolted cold-formed columns to analyze distortional buckling have not been performed until now. Figure 1.1 shows a lipped channel column in a compressive test in which there are rigid plates welded at the ends. Furthermore, the existing DSM expressions were calibrated against experimental results concerning mostly fixed columns (rigid plates attached to their end sections) [30]. Although SCHAFER mentions that "they were tested in the pin-pin condition", this statement concerns the column global behavior (the rigid plates usually rest on spherical hinges, knife edges or wedges) – as far as the distortional behavior is concerned the columns are fixed [31].

Figure 1.1 – Test in an open section column with rigid plates welded at the ends [26].

Even though a considerable number of researches reported in the literature that studied cold-formed columns with fixed ends, building construction industries have used bolted connections for structural assemblies. An example of trusses assembly with bolted connections is illustrated in Figure 1.2(a) and (b), respectively.


(a) (b)

Figure 1.2 – (a) Trusses assembly and (b) bolted connections in cold-formed steel members.

In addition, a numerical investigation conducted by LANDESMANN and CAMOTIM [31] on cold-formed steel columns with simply supported[1] end sections demonstrated that the currently DSM distortional design curve is not able to predict adequately (safely and accurately) the failure loads of columns with different conditions than the fixed ends.

The absence (at least to the best of author's knowledge) of researches in end-bolted columns subject to distortional buckling, the constant use of bolted connections in cold-formed steel constructions and the results derived from the previously mentioned research of LANDESMANN and CAMOTIM [31] constitutes the motivation for the studies exposed in this thesis.

1.3 Objectives

The objective of this work is to assess the quality of the failure load predictions provided by the current DSM distortional strength curve on (i) end-bolted and (ii) end-bolted and fixed cold-formed steel columns typically employed in the Brazilian construction market considering the following characteristics:

---

[1] In a simply supported end, the membrane and bending transverse displacements of all end section nodes were prevented, while keeping the axial (warping) displacements and all the rotations free [31].

i. Lipped channel columns buckling in “pure” distortional mode, as much as possible, and also exhibiting distortional collapse.
ii. Two end conditions: (ii_1) end-bolted and (ii_2) end-bolted and fixed.
iii. Two distinct bolted load-type: (iii_1) frictional and (iii_2) bearing load.
iv. Different steel grades.

The study also deals with columns numerically and experimentally analyzed. One result of this research is intended to be a suggestion of modification in the DSM distortional strength curve for cold-formed steel columns with different conditions than the fixed ends.

1.4 Outline

This thesis is divided into seven chapters and three appendices.

Initially Chapter 2 presents the main features of the cold-formed steel followed the manufacturing methods. Next, there is a review of the major research on the theme in the literature, divided into connections in cold-formed steel, instability modes and DSM.

Chapter 3 describes the assumptions used to select the columns to be tested and analyzed numerically, followed by Chapter 4, which reports the step-by-step used for the tests and its results.

Chapter 5 deals with the description of numerical methodologies proposed in this work. Next, the numerical methodologies are validated in comparison to the experimental results. Then, with the validated numerical methodologies, numerical data were acquired in order to produce representative samples to assess the columns behavior considering the influence of combinations of various parameters.

Chapter 6 addresses the applicability of the DSM to estimate the ultimate strength of columns failing in distortional modes and exhibiting boundary conditions considered in this work.

Finally, in Chapter 7 the main conclusions and recommendations obtained through the analysis of this research, as well as suggestions for future studies are highlighted.

2 Bibliography Review

2.1 Cold-Formed Steel Member

Cold-formed sections are commonly shaped from steel sheets which thickness can vary from 0.378 mm to 6.35 mm [32]. Figure 2.1 shows some possible cold-formed sections.

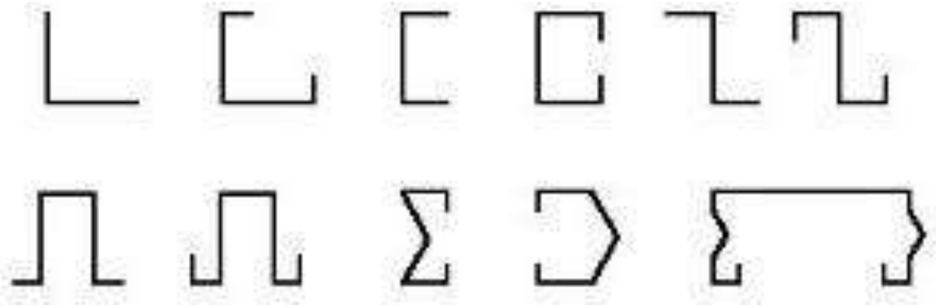

Figure 2.1 – Common cold-formed sections used in structural framing.

The cold-formed sections are produced by (i) press brake machine or (ii) roll forming equipment [32] – follows brief descriptions of these methods:

i. In press brake machine, the folding method basically consists in pressing the sheet between two tools, a punch that presses the plate against a frame with the final shape. With successive repositioning of the plate obtains the profile. Figure 2.2(a)-(b) presents a scheme of this operation at the beginning and at the end of the process respectively [33].
ii. In roll forming equipment, the process of bending is continuous and consists in passing a sheet metal strip by a series of rollers, each imposing a fold operation on the strip until the final profile. Figure 2.2(c) illustrates this process [33].

The manufacturing process of cold-formed steels imposes the same residual stresses. According to SCHAFER and PEKÖZ [34], experimental measurements through thickness of residual stress variation of a thin plate is infeasible and inclusion of residual stresses in numerical models may be complicated.

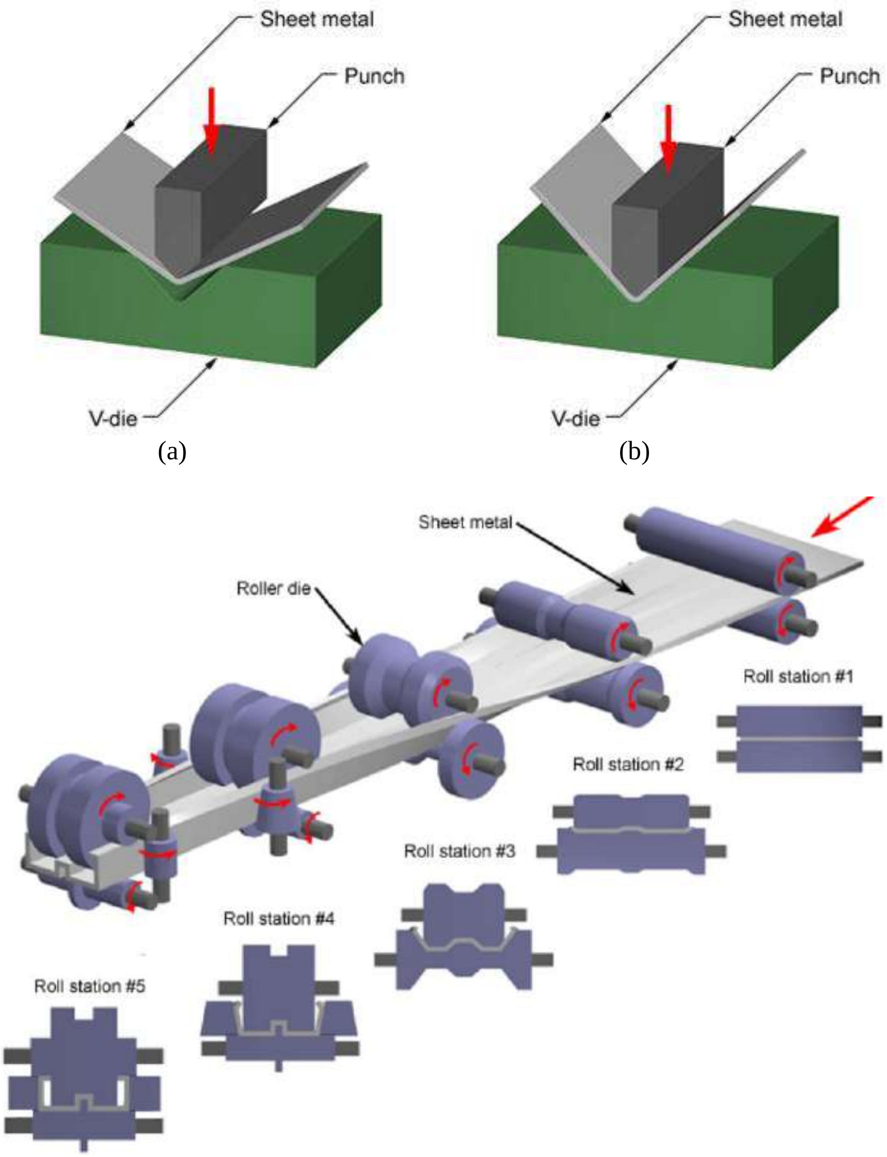

(a) (b)

(c)

Figure 2.2 – (a) Initial and (b) final process in press brake machine and (c) roll forming line [33].

Residual stresses cause direct loss of compressive strength, these residual stresses are significant in the bend regions, opposing to this effect, the yield stress (f_y) is high in these regions due to the fact that the forming work [35]. In numerical models, if residual stresses are considered in the folding regions, then the increase in yield stress in these regions must also be considered. Similarly, if the residual stresses are ignored, then the rise of the yield stress should also be ignored [34]. NARAYANAN and MAHENDRAN [36] analyzed (numerically and experimentally) the behavior of distortional buckling of a series of open section cold-formed columns and concluded that the residual stresses have little influence in regard to ultimate strength.

2.2 Connections in Cold-Formed Steel Members

Connection is defined as the physical component, which mechanically fastens the structural elements and concentrated at the location where the fastening action occurs [37]. In addition, all connections should be designed in order to transmit the maximum stress on the attached element with consideration to the eccentricity [38].

2.2.1 Welded Connection

The AISI-S100 [23] code allows, among others, welded connections such as: (i) groove welds in butt joints, (ii) fillet welds and (iii) flare groove welds. Figure 2.3 illustrates these three types of weld.

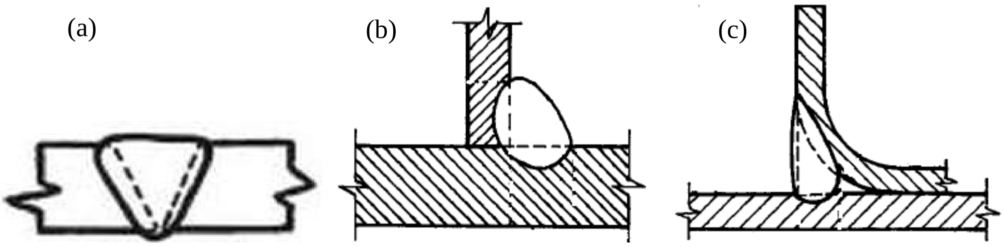

Figure 2.3 – Welded connections on cold-formed steel members: (a) groove welds in butt joints, (b) fillet welds and (c) flare groove welds [22].

2.2.2 Bolted Connection

According to LEE *et al.* [37] for ease of construction, the bolted connection is preferable in the construction sector. The reduction of skilled worker at construction site with bolted connection application is able to minimize the construction cost as compared to welded connection. MATHIESON *et. al* [39] stated that one of the disadvantages of cold-formed steel trusses is the cost of installation of connectors, given the large numbers that are required in connections carrying significant moment – industry experience with recent projects on long span portal frames show the connections can comprise up to 40% of the structural system cost.

Modern rolling lines are generally computer controlled from the design office so that not only can highly accurate complex shapes of precise lengths be produced to order but also holes, perforations and slots (*e.g.* web openings for services) can be punched in precise positions during the rolling process. A significant recent development is the automatic end forming of beams at the time of rolling, as shown in Figure 2.4 [40].

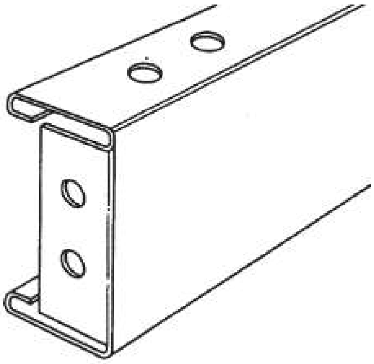

Figure 2.4 – End beam detail produced by an automated process [40].

Four failure modes can be observed in cold-formed steel bolted connections, as illustrated in Figure 2.5: (i) shear failure of sheet, (ii) bearing failure of sheet, (iii) rupture in net section and (iv) shear failure of bolt [38].

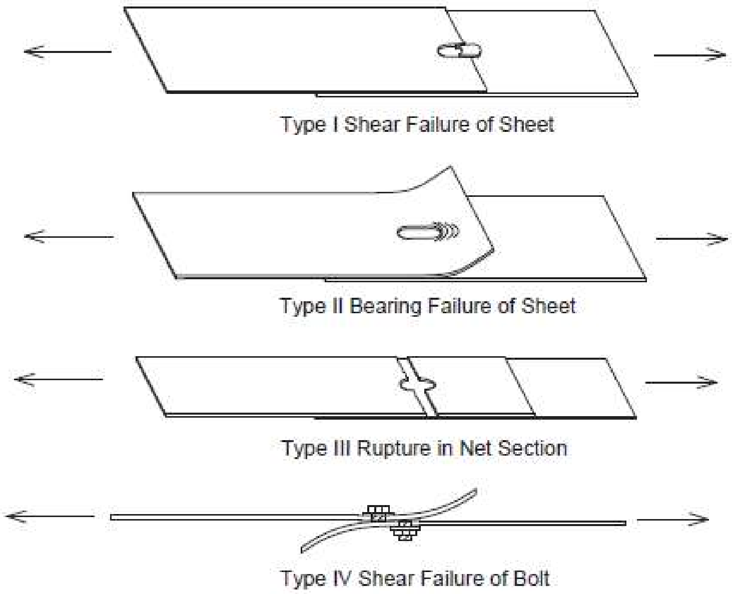

Figure 2.5 – Typical failure modes of cold-formed steel bolted connections [41].

According YU and PANYANOUVONG [41] only sheet to sheet connections were tested (see Figure 2.6(a)) – *e.g.* [42], [43], [44] and [45]. However, in many cold-formed steel assemblies such as trusses, racking systems, scaffolding systems, etc., the bolted connections have bolts going through the section with no nuts or washers installed inside the section (the gap) due to the limited space. Figure 2.6(b) shows an example where a single bolt is used in a truss joint. The chord member is restrained by the bolt nut, bolt head, and the web member. The web member on the other hand is not restrained at the bolt holes. Without having restraints on both sides of the connected sheets, the sheets may distort significantly, in return it may reduce the bearing.

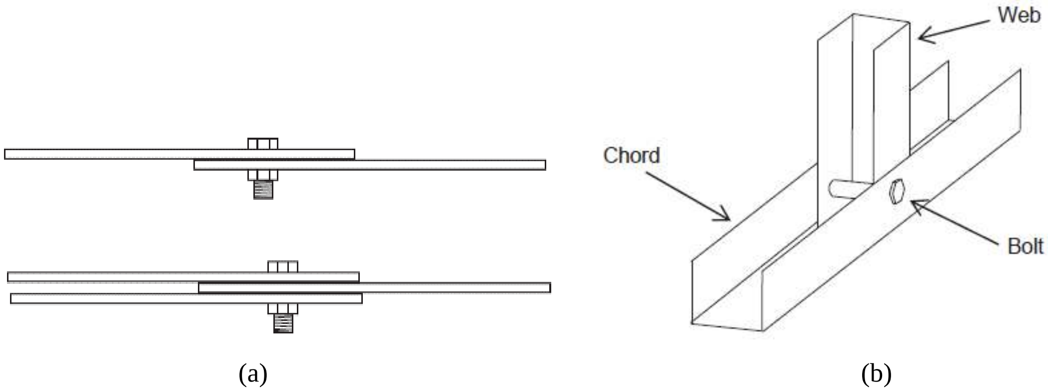

(a) (b)

Figure 2.6 – (a) Sheet to sheet connections and (b)bolted connections in assemblies [41].

According to the section 1.3, one of the objectives of this work is to analyze the distortional post-buckling behavior in end-bolted columns; thus, one bolted connection should be designed considering the principle sentenced by LEE *et. al* [37] which states: "*Buckling will occur before the formation of the yield line in cold-formed steel bolted connection*".

The ABNT NBR 14762 [22] code states that the standard hole diameter in mm should be:

$$d_f = \begin{cases} d_p + 0.8 \text{ for } d_p < 12.5 \\ d_p + 1.5 \text{ for } d_p \geq 12.5 \end{cases} \tag{2.1}$$

where d_p is the nominal bolt diameter also mm.

For bolted connection, according to ABNT NBR 14762 [22] standard and AISI-S100 [23] code, it is necessary to verify: (i) bearing strength (crushing) and (ii) bolt shear strength.

(i) Bearing strength must be calculated by:

$$F_{Rd} = \alpha_e \cdot d_p \cdot t \cdot f_u / 1.55 \tag{2.2}$$

where f_u is the ultimate stress of the steel (base metal), t is the thickness of the analyzed element and $\alpha_e = 0.183 \cdot t + 1.53$ with t in mm and less than or equal to 4.75 mm.

(ii) The bolt available shear strength is given by:

$$F_{v,Rd} = 0.23 \cdot d_p^2 \cdot f_{ub} \text{ if threads are not excluded from the shear plane} \tag{2.3}$$

$$F_{v,Rd} = 0.29 \cdot d_p^2 \cdot f_{ub} \text{ if threads are excluded from the shear plane} \tag{2.4}$$

where f_{ub} is the ultimate tensile strength of the bolt.

The AISI-S100 [23] specification does not provide design criteria for slip-critical (also called friction-type) connections because of the lack of appropriate test data and the use of numerous surface conditions. The slip-critical connection is presented here by the fact some specimens were tested considering this connection type (see chapter 4). The ABNT NBR 8800 [46] standard and AISC 360-10 [47] state that for slip-critical connections must be checked the slip resistance:

$$F_{f,Rd} = \frac{1.13 \cdot \mu \cdot C_h \cdot F_{Tb} \cdot \eta_s}{\gamma_e} \left(1 - \frac{F_{t,Sd}}{1.13 \cdot F_{Tb}} \right) \tag{2.5}$$

where F_{Tb} is the minimum fastener tension, $F_{t,Sd}$ is the required tension force, η_s is the number of slip planes, γ_e is the resistance factor, μ is the mean slip coefficient and C_h is the factor for fillers.

2.3 Instability Modes

Buckling is the phenomenon that is subject structural elements under compressive stress in with it is observed that for a small change in load occurs a large alteration in displacement [48]. Columns and plates under ideal conditions lose stability by sudden change of the deformation mode, thereby characterizing the phenomenon known as bifurcation of the equilibrium. In real conditions, *i.e.*, with initial imperfections, there is no sudden change deformation mode but a significant amplification of the deformation under small load increment value.

The appearance of large deformation characterizes the so-called post-critical phase of structural mechanical behavior of the columns or plates. If the load that the element can support after the beginning of the post-critical phase increases with the deformation, the structure has a stable post-buckling behavior, if the opposite occurs, presents a post-critical behavior unstable [49].

Factors influencing the buckling mode and the critical force in prismatic elements is the geometric relationships between cross-section components and lengths, its support conditions, its initial imperfections and the material mechanical characteristics. In addition, structures on elastic or linear regime behave differently from structures on plastic or non-linear regime, with respect to the instability.

In plastic regime, after post-buckling occurs, a complex interaction between physical and geometrical non-linearities not allowed, until now, the formulation of a general theory, as it is the case with the elastic structures. Thus, to properly explain and quantify this phenomenon is essential to use numerical methods [50].

Compressed elements may be subject to three distinct instability modes: (i) global buckling, (ii) local buckling and (iii) distortional buckling. Furthermore, there is the possibility of instability modes interact with each other modifying their behavior.

2.3.1 Global Buckling

The global buckling ($P_{cr.e}$) for compressed prismatic elements can be (i) flexural, (ii) torsional or (iii) flexural and torsional. Figure 2.7 shows these global buckling in lipped channel section.

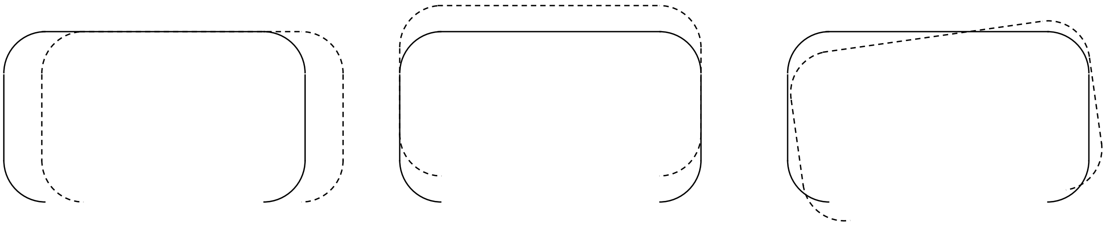
(a) (b) (c)

Figure 2.7 – Global buckling modes for lipped channel: (a) flexural about major axis, (b) flexural about minor axis and (c) flexural and torsional

Flexural buckling

The flexural buckling in columns, subjected to centered compressive force, occurs in general in long elements of double symmetrical section. The critical load in the elastic linear conditions, obtained by Euler in 1744, for ideal prismatic columns is the smallest of the forces following presented [3]:

$$P_{cr.e\_x} = \frac{\pi^2 E I_x}{\left(k_x L_x\right)^2} \text{ and } P_{cr.e\_y} = \frac{\pi^2 E I_y}{\left(k_y L_y\right)^2} \tag{2.6}$$

in which X and Y represent the principal axes of the cross-section, E is the material modulus of elasticity, I_x and I_y are the moments of inertia of the cross-section with respect to the X and Y axes, L_x and L_y are the unbraced lengths for bending about X and Y axes respectively and k_x and k_y are the effective length factors, which depend of column support conditions about X–axis and Y–axis respectively.

Torsional buckling

Torsional buckling in elements subjected to compression occurs most frequently in double symmetrical open sections, with long flanges and low torsional stiffness. In this case, the critical force in a linear elastic behavior, obtained by Wagner, in 1929, for ideal prismatic columns is [3]:

$$P_{cr.e\_z} = \frac{A}{I_o}\left(GI_T + \frac{\pi^2 EC_w}{\left(k_z L_z\right)^2} \right) \tag{2.7}$$

where Io is the polar moment of inertia of a plane area with respect to shear center, G is the material shear modulus, in other words, $G = E/2(1+\nu)$, ν is the *Poisson* coefficient, I_T is the torsional constant (*Saint Venant*) of section, C_w is its torsional warping constant, k_z is the buckling parameter by torsion of column, which depends of its supports conditions and L_z is the unbraced length about Z-axis.

Flexural and torsional buckling

Flexural and torsion buckling in elements subjected to compression occurs in open sections with low torsional rigidity, asymmetric or single symmetric in which the center of gravity does not coincide with the shear center. The critical force in linear elastic regime, obtained by Kappus in 1937, is the smallest among the solutions of the equation [3]:

$$\frac{I_o}{A}\left(P_{cr.e} - P_{cr.e\_x}\right)\left(P_{cr.e} - P_{cr.e\_y}\right)\left(P_{cr.e} - P_{cr.e\_z}\right) - P_{cr.e}^2\left[\left(P_{cr.e} - P_{cr.e\_x}\right)y_o^2 + \left(P_{cr.e} - P_{cr.e\_y}\right)x_o^2\right] = 0 \tag{2.8}$$

where x_o and y_o are the distance from centroid to shear center section in principal axes X and Y directions respectively, $P_{cr.e}$ is the flexural and torsional buckling critical force and $P_{cr.e\_x}$, $P_{cr.e\_y}$ and $P_{cr.e\_z}$ are critical forces indicated in Eqs. (2.6) and (2.7).

2.3.2 Local Buckling

The local buckling is the instability phenomenon of two-dimensional structural elements such as column components under compressive stress. Occurs generally in short columns. The components submitted to this mode of instability experiences normal translations in its average plan as shown in Figure 2.8.

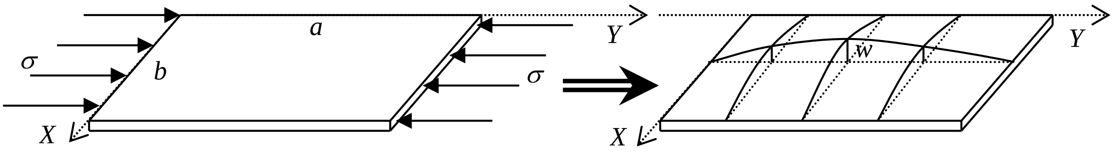

Figure 2.8 – Plate local buckling phenomenon.

The critical stress in linear elastic regime of ideal plate and its deformation mode depends of its geometry and its support conditions. The elastic critical local buckling stress to supported–supported plate, obtained by Bryan in 1891, and for supported–free, obtained by Timoshenko in 1907, [3] can be written as:

$$\sigma_{cr} = \frac{k\pi^2 E}{12\left(1-\nu^2\right)\left(b/t\right)^2} \tag{2.9}$$

where a is the length of the plate, b is the width and t its thickness, k is the plate buckling coefficient, which depends on the ratio a/b, the support conditions and the solicitation type. In this expression, ν is the *Poisson*'s ratio.

For lipped channel section, local buckling modes can be seen in Figure 2.9.

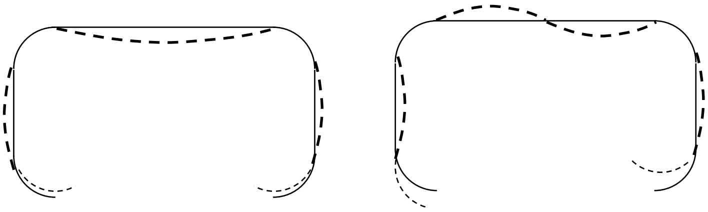

Figure 2.9 – Local instability modes in lipped channel section.

According to SCHAFER and PEKÖZ [34], local deviations are characterized by dents and regular undulations in the plate, the geometric imperfections is sorted into two categories: type 1, maximum local imperfection in a stiffened element and type 2, maximum deviation from straightness for a lip stiffened or unstiffened flange. Figure 2.10 shows the definitions of these classifications.

$$d_1 \approx 0.006b_w \tag{2.10}$$

d_1 is the amplitude of the type 1 imperfections applicable when $b_w/t < 200$.

$$d_2 \approx t \tag{2.11}$$

d_2 is the amplitude of the type 2 imperfections applicable when $b_w/t < 100$.

Moreover, in both cases, the sheet thickness must be less than 3 mm.

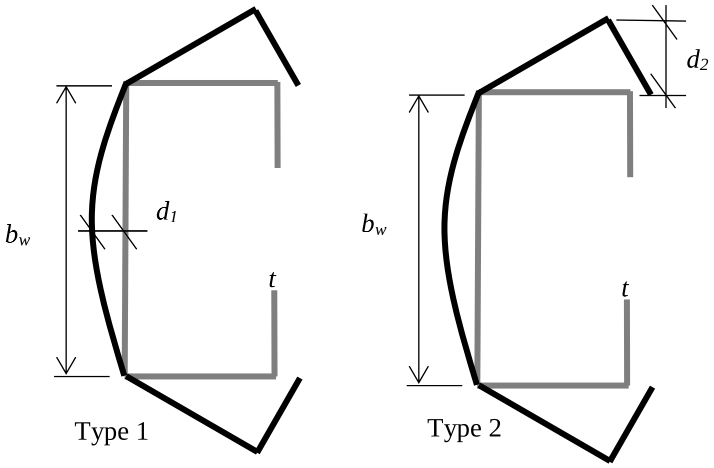

Figure 2.10 – Definition of geometric imperfections [34].

Strength of a cold-formed steel member is particularly sensitive to imperfections in the shape of its Eigen modes considering numerical models. Knowledge of the amplitude of imperfections in the lowest Eigen mode is often sufficient to characterize the influential imperfections. Maximum imperfections may be used to provide a conservative estimation of imperfection magnitude in a particular Eigen mode [34].

The usual procedure for numerical analysis of collapse is to introduce the displacements produced by critical buckling mode conveniently scaled for use as initial imperfection in further nonlinear analysis. Only a geometric imperfection with an equivalent magnitude is used to include (i) the effects of geometric imperfections and (ii) residual stresses due to the manufacturing process. Different values of the magnitude of equivalent geometric imperfection are adopted, for local and distortional mode this variation is from 0.1t up to 1.5t [51]. An usual approach to consider the maximum equivalent amplitude of geometric imperfection for local or distortional buckling is 0.1t – *e.g.* [31], [52] and [53].

2.3.3 Distortional Buckling

The buckling by distortion is an instability mode that occurs in open section thin-walled elements with stiffened edge under compressive stress and mainly with members manufactured with a high strength steel [54]. Distortional buckling is characterized by rotation of the stiffened flange at the flange/web junction [12]. Furthermore, it occurs only in sections with four or more non-aligned components [11], Figure 2.11 illustrates this instability mode in lipped channel section.

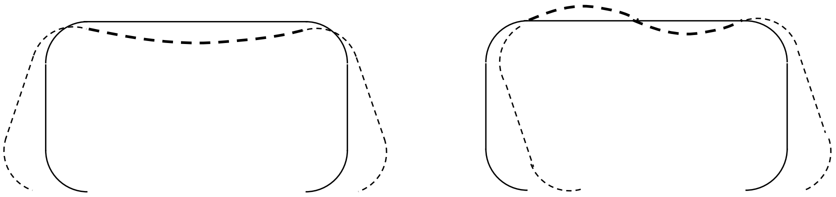

Figure 2.11 – Distortional instability modes in lipped channel section.

The geometric relationships of thin-walled open sections have an important role regarding the distortional buckling phenomenon. Relative to lipped channel sections, the geometrical relationships that favors the distortional buckling in general, are: (i) very short flanges (flanges width of less than about 1/6 of the height of the web) or very long (flanges width greater than about 3/4 of the height of the web), (ii) very short lips or with similar dimension of the flange width and (iii) deep webs [12].

For evaluate the distortional buckling stress LAU and HANCOCK [17] proposed analytical expressions applicable to opened cross-section thin-walled bars, taking into account only the set formed by the flange and its edge stiffener considering the connection effect in the web/flange by means of rotational springs. According to TENG *et. al* [55] the method presented by LAU and HANCOCK [17] appears to be the most efficient and simple closed form to design use. SCHAFER [12] proposed different distortional buckling stress equations considering the same simplified model proposed by LAU and HANCOCK [17].

With respect to the distortional deformation mechanism in thin-walled open sections, SILVESTRE and CAMOTIM [11] stated that the primary warping is a key factor in the distortional mode which should be viewed as a higher order mode of deformation due to the existence of the in-plane and out-of-plane displacements. In Figure 2.12 these displacements are shown.

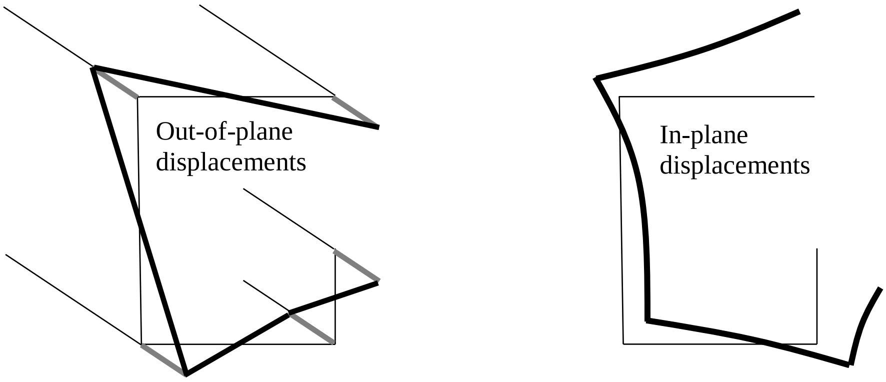

Figure 2.12 – Distortional model out- and in-plane displacements [11].

2.4 Direct Strength Method

2.4.1 Origin and Development

For columns, the beginning of the Direct Strength Method (DSM), though it was not called this at the time, can most clearly be traced to research into distortional buckling of rack post sections at the University of Sydney [17] [18]. In the work of SCHAFER and PEKÖZ [56] is that originally the DSM was so named. Later SCHAFER [57] generalized the application of this method for compressed members taking into account local buckling, distortional and global as well as the interaction between these different modes.

SCHAFER and PEKÖZ [56] proposed the DSM as an alternative to the concept of effective width method in determining the strength of cold-formed steels [8]. The concept of effective width is too laborious, especially in cases of elements consisting of several components (intermediate stiffeners provided), as well as sections under the action of bending solicitations being necessary an iterative process for determining the width effective. Furthermore, this method is not well suited to handle distortional buckling [31].

The DSM consists in using experimental adjusted resistance curves and from the axial elastic buckling load to the element as a whole, so it is possible estimate the axial strength resistant to this member. According MACDONALD *et al.* [58] the DSM requires large amounts of testing for validation, because only were tested in single sections such as angle, channel and hats and even according to these authors the DSM constitutes a step in the wrong direction. In contrast, SILVESTRE *et al.* [59] argue that the DSM is an effective alternative to traditional concept of effective width.

The North American code AISI-S100 [23], the standard of New Zealand and Australia AS/NZS 4600 [24] and Brazilian ABNT NBR 14762 [22] code incorporated the DSM.

2.4.2 Column Compressive Strength

The column ultimate strength estimative via DSM is the minimum of three nominal loads, concerning global ($P_{n.e}$), distortional ($P_{n.D}$) and interactive local/global ($P_{n.Le}$) collapses. These nominal loads are provided by the expressions (design curves):

$$P_{n.e}=\begin{cases}\left(0.658^{\bar{\lambda}_e^2}\right)P_y \text{ for } \bar{\lambda}_e \le 1.5\\ \left(0.877/\bar{\lambda}_e^2\right)P_y \text{ for } \bar{\lambda}_e > 1.5\end{cases} \tag{2.12}$$

$$P_{n.D}=\begin{cases}P_y \text{ for } \bar{\lambda}_D \le 0.561\\ P_y\left[1-0.25\left(P_{cr.D}/P_y\right)^{0.6}\right]\left(P_{cr.D}/P_y\right)^{0.6} \text{ for } \bar{\lambda}_D > 0.561\end{cases} \tag{2.13}$$

$$P_{n.Le}=\begin{cases}P_{n.e} \text{ for } \bar{\lambda}_{L.e} \le 0.776\\ P_{n.e}\left[1-0.15\left(P_{cr.L}/P_{n.e}\right)^{0.4}\right]\left(P_{cr.L}/P_{n.e}\right)^{0.4} \text{ for } \bar{\lambda}_{L.e} > 0.776\end{cases} \tag{2.14}$$

where P_y is the column squash load and $\bar{\lambda}_e=(P_y/P_{cr.e})^{0.5}$, $\bar{\lambda}_D=(P_y/P_{cr.D})^{0.5}$ and $\bar{\lambda}_{Le}=(P_{n.e}/P_{cr.L})^{0.5}$ are the global, distortional and interactive local/global slenderness, respectively [8].

2.4.3 Determination of Critical Buckling Loads

Since the accurate determination of the column buckling loads is a key aspect in the application of the DSM, it is essential for designer to be equipped with efficient computational tools to perform member elastic buckling analyses, aimed at obtaining local ($P_{cr.L}$), distortional ($P_{cr.D}$) and/or global/Euler ($P_{cr.e}$) critical buckling (bifurcation) loads (or stresses). Once these buckling loads are known, the application of the DSM is quite straightforward [60].

Nowadays, the column local, distortional and global critical buckling loads can be easily calculated by resorting to either shell finite element (SFE), constrained finite strip (cFS) or Generalized Beam Theory (GBT) [61] elastic linear buckling analyses. While the SFE analyses must generally be performed in commercial software packages (ANSYS [62] is one of the most commonly used), it is possible to carry out the remaining ones in freely available open source codes, namely CUFSM [63] and GBTUL [64]. Although the SFE analyses are more versatile, in the sense that they can be applied to columns with all types of support and loading conditions, the cFS or GBT analyses should be employed whenever possible. Indeed, due to their modal character, they make it much easier to identify the nature of the critical buckling modes (or calculate the critical buckling load associated with a specific buckling mode nature) – the SFE analyses often entail the need to consider a large number of buckling modes to determine a given elastic buckling load. In particular, it is worth mentioning that, as far as prismatic cold-formed steel members are concerned, the GBTUL capabilities match very closely those exhibited by the SFE analysis [60].

The software GBTUL is a powerful tool to perform buckling analyses. As input data in GBTUL program mechanical characteristics of the material and the dimensions of the member cross-section are required. Figure 2.13 shows the in-plane shapes of the most relevant deformation modes for lipped channel section: (i) the first 4 are the rigid-body global modes – axial extension (mode 1), major and minor axis bending (modes 2 and 3) and torsion (mode 4), (ii) modes 5 and 6 are distortional and (iii) the remaining are local-plate modes [61].

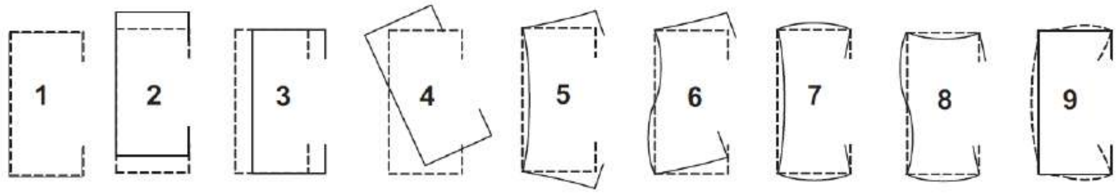

Figure 2.13 – In plane shapes of the most relevant lipped channel section deformation modes [61].

One of the result of GBTUL buckling analysis is the signature curve which relates the member length and its critical load. Figure 2.14 illustrates signature curves for lipped channel indicating the buckling mode by bands of length, in these samples were considered (i) simple supported end conditions (*S*) and (ii) one simple supported end and other constrained (*SC*) – the cross-section dimensions and material features are indicated. The signature curve of *SC* columns (Figure 2.14(b)) does not present minimum unlike *S* columns (Figure 2.14(a)).

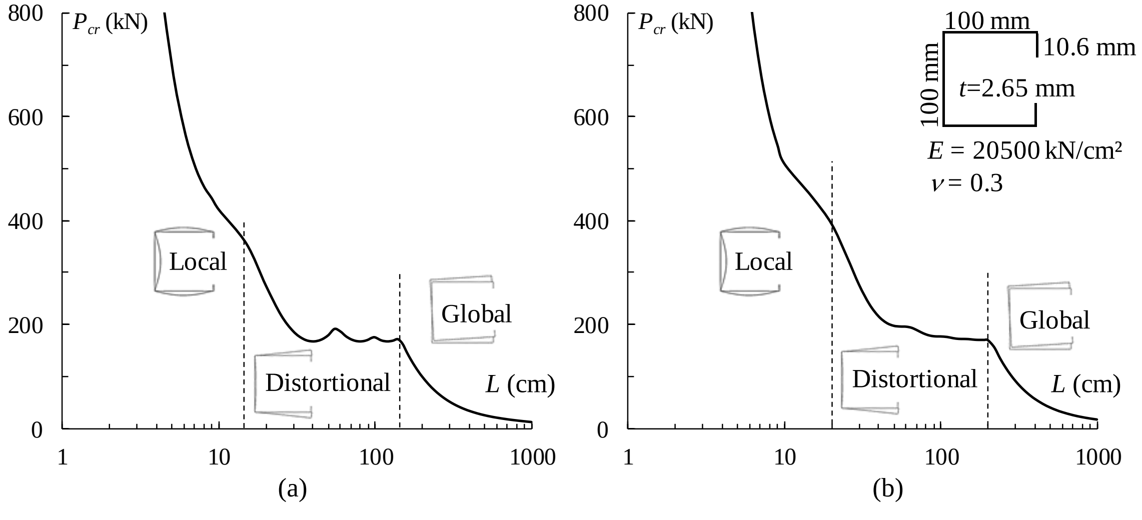

Figure 2.14 – GBTUL signature curve for lipped channel column considering (a) simply supported ends and (b) one simple supported end and other constrained.

2.4.4 Remarkable Advance

Recently, LANDESMANN and CAMOTIM [31] throughout the numerical investigation reported results on the influence of the cross-section geometry and end support conditions on the post-buckling behavior of columns buckling and failing in distortional modes. The columns analyzed presented four cross-section types: (i) lipped channels (C), hat-section (H), zed-section and rack-section (R) and (ii) four end-conditions: fixed (F), pinned-fixed (P-F), pinned (P) and fixed-free (F-F). Figure 2.15 shows, for P and P-F columns, the elastic equilibrium paths P *vs.* $|\delta|/t$, where P is the applied load and $|\delta|$ is the maximum absolute transversal displacement occurring at the flange-lip edges normalized by t the wall thickness. As one of the results, they concluded that the post-buckling strength decreases as one travels along the column end support condition sequence F, P-F, P and F-F.

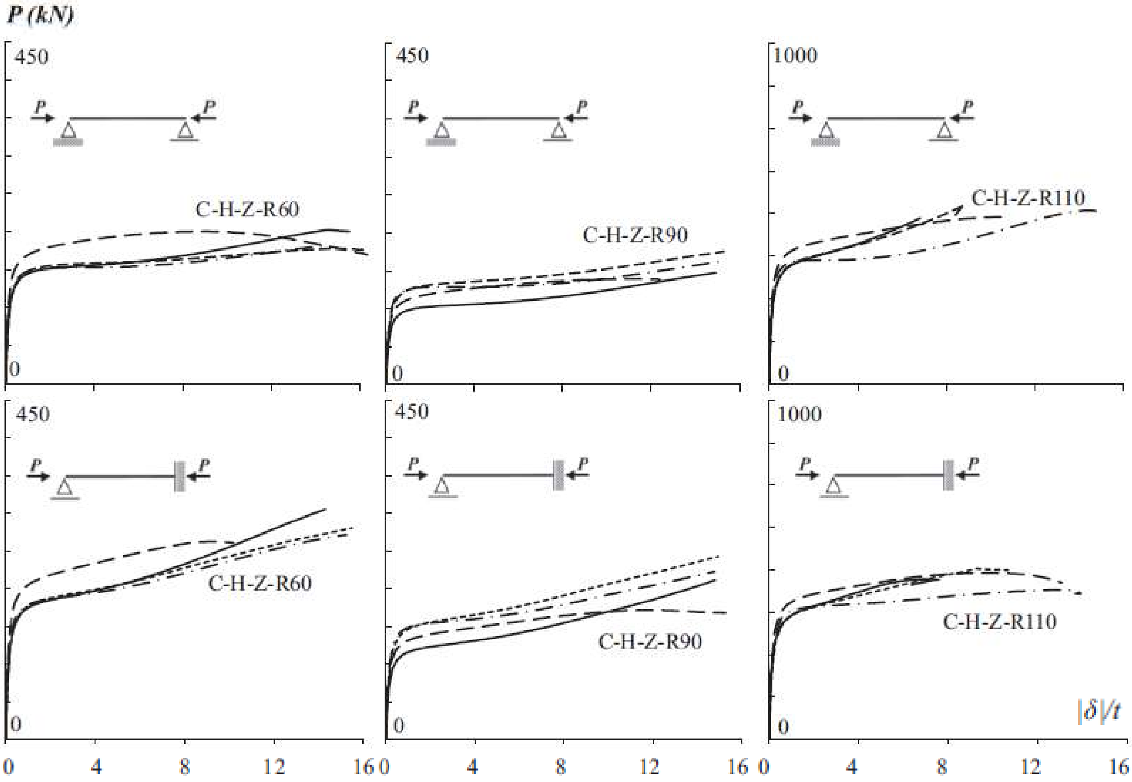

Figure 2.15 – Elastic equilibrium paths *P vs.* $|\delta|/t$ concerning the C–H–Z–R60/90/110 columns with P and P-F end support conditions [31].

Still referring to the paper of LANDESMNN and CAMOTIM [31], Figure 2.16(a) presents the elastic-plastic equilibrium path ($P/P_{cr.D}$ *vs.* $|\delta|/t$) of P and P-F C-H-Z-R90 columns, where the applied load P is normalized by the critical distortional force

$P_{cr.D}$, the ultimate load (P_u) are identified by white circles, Figure 2.16(b) depicts the column deformed configurations (distortional) occurring in the close vicinity of the limit points of each equilibrium path displayed in Figure 2.16(a).

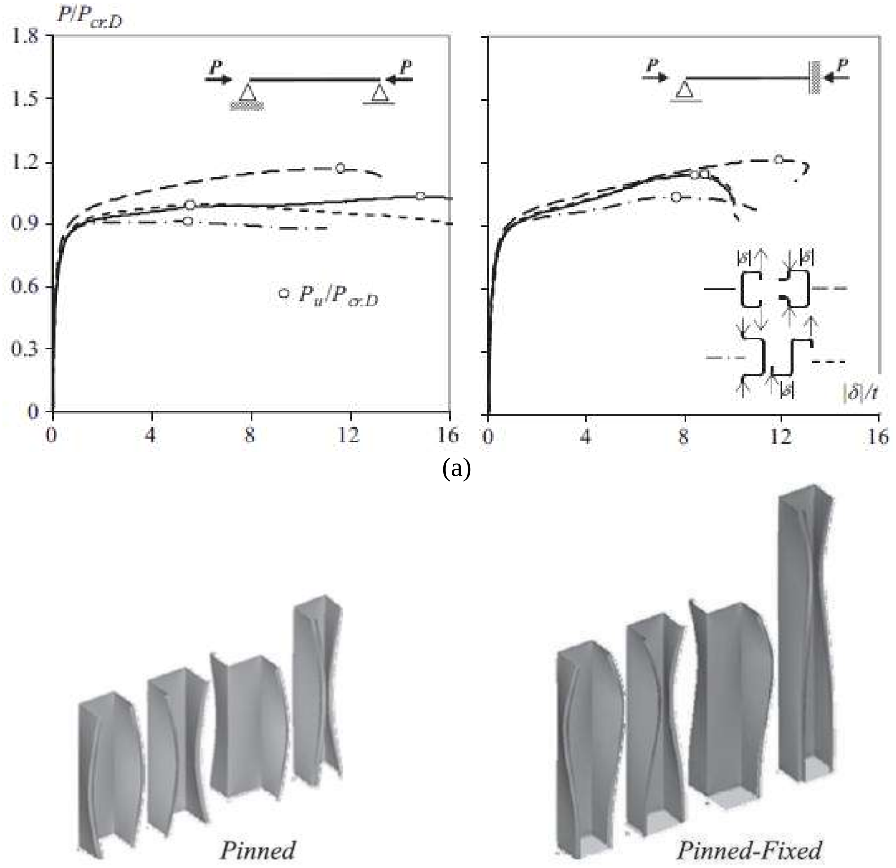

(a)

(b)

Figure 2.16 – (a) Elastic-plastic distortional equilibrium paths (P/P_{cr} *vs.* $|\delta|/t$) and (b) distortional failure modes concerning the P and P-F C–H–Z–R90 columns [31].

With the numerical data of the ultimate loads collected, LANDESMANN and CAMOTIM [31] concluded that F columns were predicted quite accurately by DSM distortional curve, differently from the P-F, P and F-F columns which were clearly over-estimated, especially in the intermediate and high slenderness ranges. As main result, they proposed modification of the DSM distortional curve defined by Eq. (2.15) recommended for use in lipped channel, hat, rack and Z sections under simply supported end conditions or with one fixed end and the other simply supported. As mentioned by the authors this preliminary result requires validation in order to prove its robustness and universality.

$$P_{n.D}^{*}=\begin{cases} P_y \text{ for } \overline{\lambda}_D \le 0.561 \\ P_y\left[1-0.25\left(P_{cr.D}/P_y\right)^{0.6}\right]\left(P_{cr.D}/P_y\right)^{0.6} \text{ for } 0.561<\overline{\lambda}_D \le 1.133 \\ P_y\left[0.65-0.2\left(P_{cr.D}/P_y\right)^{0.75}\right]\left(P_{cr.D}/P_y\right)^{0.75} \text{ for } \overline{\lambda}_D > 1.133 \end{cases} \tag{2.15}$$

Figure 2.17 summarizes the LANDESMAN and CAMOTIM [31] work and makes it possible to compare the current distortional DSM design curve (Eq. (2.13)) with the proposed design curve (Eq. (2.15)).

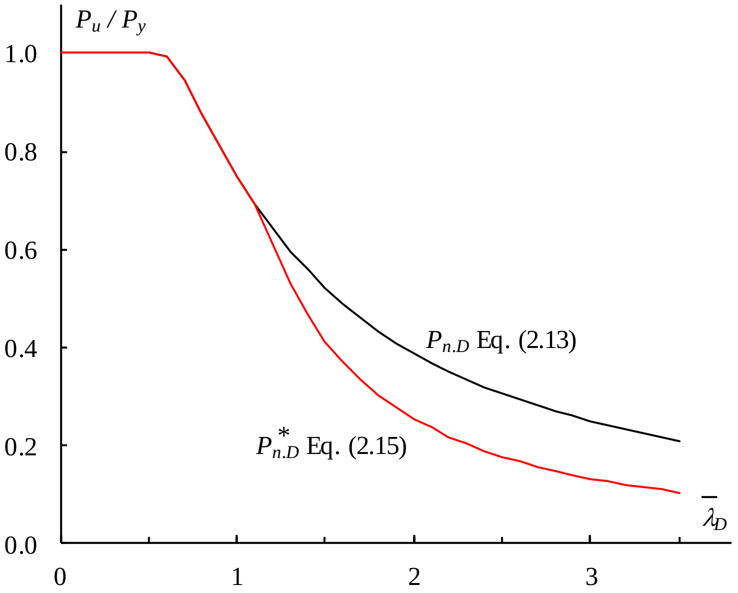

Figure 2.17 – Comparison between the current distortional DSM design curve and the modifications proposed by LANDESMANN and CAMOTIM [31].

3 Column Geometry Selection – Buckling Behavior

The first step in this work consisted of carefully selecting the cross-section dimensions and lengths of the lipped channel columns to be analyzed numerically and tested experimentally, which exhibit two different end support conditions: (i) end-bolted (both bolted ends – *P*) and (ii) end-bolted and fixed (one end bolted and another end fixed – *PF*).

It should be mentioned that the column "end-bolted" support conditions are characterized by connection of two bolts mounted in the flange's holes (see Figure 3.1(b) and (c)) whose centers are properly located on the minor main axis of the section. On the other hand, the "Fixed" end condition (see Figure 3.1(c)) refers to the attachment of a rectangular plate sufficiently rigid welded on column in order to prevent local and global displacements, including warping and the rotations in the regions near of this connection.

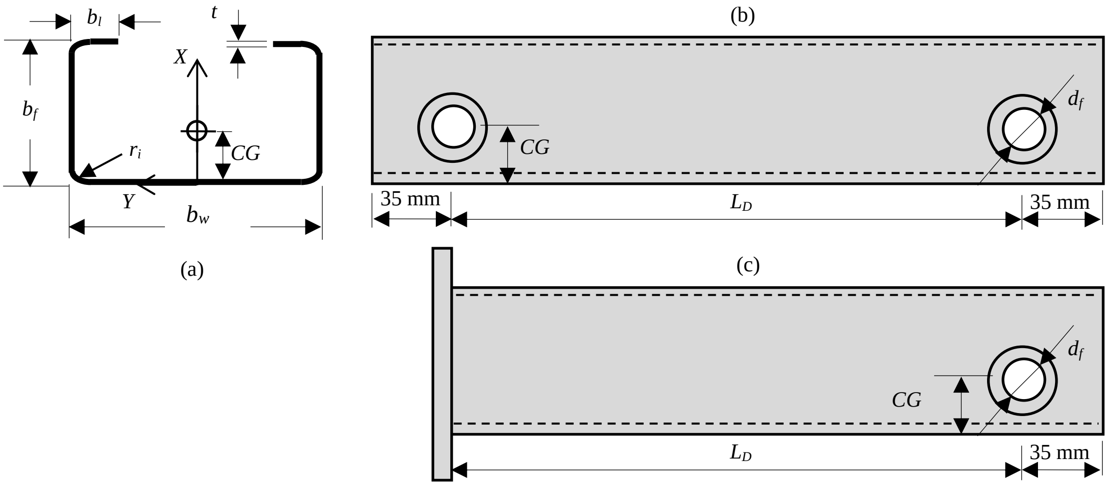

Figure 3.1 – (a) Cross-section dimensions, side view with length for (b) *P* and (c) *PF* columns.

In end-bolted connection, the column loading happens through (i) friction in washer areas (friction load-type – P_F or PF_F) or (ii) bearing contacts between the bolts and the hole circular sectors (bearing load-type – P_B or PF_B). This study set a maximum compressive force as 180 kN (this limit higher than the ultimate strength of the toughest column proposed in this study considering a steel with yield stress f_y = 35.0 kN/cm²) –

this estimate is aimed at determining the bolt and washer to be used in the models. To determine the bolt diameter, it was considered the threads are excluded from the shear plane, so the calculation shear strength is given by the Eq. (2.4). Considering the material of the bolt as ASTM A490 [65] (f_{ub} = 103.5 kN/cm²) it has for the connection of two bolts on the column edge the diameter d_p = 17.3 mm, being adopted d_p = 20 mm (M20). Found the bolt diameter has become the standard hole diameter d_f = 21.5 mm according to Eq. (2.1).

As for M20 bolt are used washers with 37 mm outer diameter and 3 mm thickness made of carbon steel according to ASTM F436 [66]. The contribution of washers in strength was seen in end-bolted models whose connection is through contact (bearing load-type), as if it were otherwise, there would be a very high tensions concentration in the loading region and possibly crushing collapse, precluding any buckling analysis (in real tests washers were welded on column holes – see Chapter 4). The bearing strength should be checked with Eq. (2.2), considering the washers contribution, this connection is resistant to crushing.

The distance from the center of the fastener to the edge took as a basis the AISI-S100 [23] code which states that for the M20 bolt has this minimum distance as 30 mm, being adopted 35 mm.

The combination of "*P*" and "*F*" end conditions, allow three different boundary conditions types for columns, namely: end-bolted (*P*), end-bolted and fixed (*PF*) and fixed (*F*). However, the *F* end condition is not considered in this study because it has previously been studied by many researchers and have been targeted (exclusively) for the creation of DSM.

The selection procedure involved "trial-and-error" Eigen buckling analysis, performed with shell finite element analysis[2] (SFEA [62]), aimed at satisfying the following requirements:

i. Columns buckling and failing in "pure" distortional mode, as much as possible. This goal is achieved by ensuring, that the critical buckling stress (i_1) is clearly distortional and (i_2) falls considerably below the lowest local and/or global bifurcation stresses.

---

[2] The numerical methodologies will be explained in chapter 5.

ii. Lipped channel column dimensions that are commonly used and involve different wall width proportions, namely web-to-flange width ratios.

Fortunately, it was possible to fulfil all the above requirements and the end results of the “trial-and-error” selection procedure are the 15 sets of cross-section dimensions given in Table 3.1. The nominal out-to-out cross-section dimensions are defined in Figure 3.1(a) – note that web-to-flange width ratio (b_w/b_f) varies between 0.70, 1.00 and 1.43. The wall thickness (t), the width of the edge stiffener (b_l) and the inner radius (r_i) were considered constant equal to 2.65 mm, 10.6 mm and 1.325 mm respectively. All angles formed by two consecutive walls were considered right angles.

For each end-bolted column, considering both types of loading (Frictional P_F and Bearing-type P_B), different length columns (L) were numerically calculated (SFEA), starting from 10 cm up to 1000 cm with 5 cm increments, in order to determine the length (L_D) which would result, in Eigen buckling analyses, distortional buckling deformation with one half-wave and a minimum in the P_{cr} *vs.* L curve where P_{cr} is the critical buckling force. Figure 3.2(a) illustrates an example of determining the distortional length L_D of a section. The same procedure was done with the *PF* columns; however, such columns does not present minimum in the curve P_{cr} *vs.* L (see example in Figure 3.2(b)), thus, in this work, the lengths L_D for these columns were considered the same as the correlated *P* columns. Also in Figure 3.2 deformations from Eigen buckling analyses are shown for the first buckling mode in bolted *P* and *PF* columns and comparisons with the curves considering a simply supported end-condition (*S*) and with one simply supported end and another end constrained (*SC*) are illustrated – these last two curves were extracted from GBTUL [64] program.

Table 3.1 also provide, for each column labeled by the web and flange widths, the corresponding (i) cross-section area (A), (ii) the distance from the centroid of the section to the outer face of the web column (CG) and (iii) the length associated with critical distortional buckling (L_D) for both load conditions.

Table 3.1 - Nominal dimensions, area and center of gravity position of cross-section and column lengths for frictional and bearing load-type.

Columns	b_w (mm)	b_f (mm)	*A* (cm²)	*CG* (mm)	*Frictional load-type*	*Bearing load-type*
					L_D (mm)	L_D (mm)
100x70	100	70	6.52	24.22	400	350
100x100	100	100	8.11	37.47	450	450
100x142.9	100	142.9	10.38	57.35	600	550
130x91	130	91	8.43	30.39	450	450
130x130	130	130	10.50	47.51	550	550
130x185.7	130	185.7	13.45	73.23	650	650
150x105	150	105	9.70	34.49	500	500
150x150	150	150	12.09	54.19	650	600
150x214.3	150	214.3	15.49	83.84	750	700
180x126	180	126	11.61	40.64	600	550
180x180	180	180	14.47	64.21	700	650
180x257.1	180	257.1	18.56	99.70	900	800
200x140	200	140	12.88	44.74	600	600
200x200	200	200	18.06	70.89	750	750
200x285.7	200	285.7	20.60	110.3	950	900

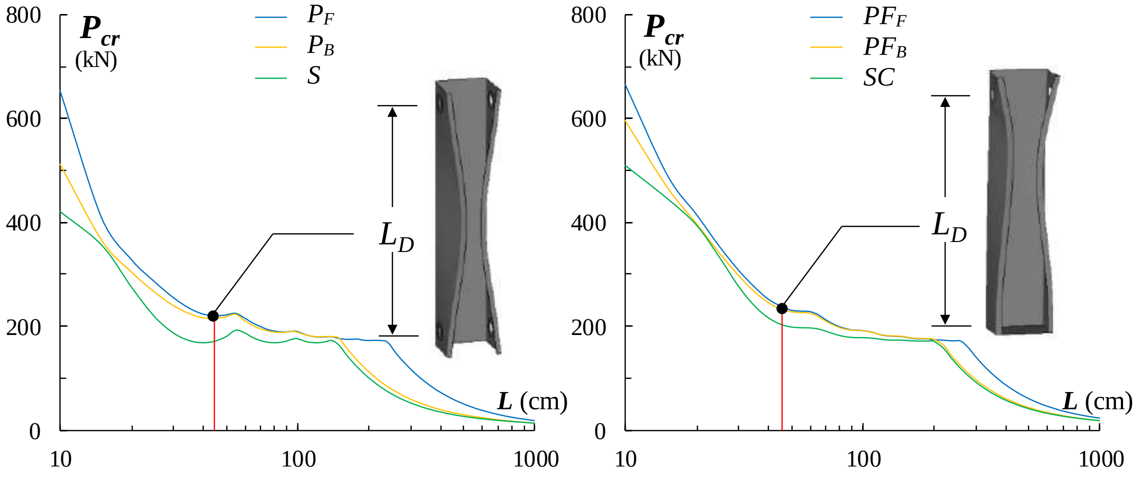

(a) (b)

Figure 3.2 – Variation of P_{cr} with L for (a) P_B, P_F and S and (b) PF_B, PF_F and SC for 100x100 columns.

Analyzing the graphs in Figure 3.2 it can be seen the considerable difference between the curves extracted from Eigen buckling SFEA [62] of the ones extracted from GBTUL [64] analysis.

Table 3.2 shows, for each column and all boundary condition considered in this work, (i) the critical (distortional) buckling force ($P_{cr.D}$) and the ratios between (ii) the lowest local bifurcation forces related to distortional buckling force ($P_{b1.L}/P_{cr.D}$) and (iii) the lowest global bifurcation forces with respect to distortional buckling force

($P_{b1.e}/P_{cr.D}$), indicating how far apart they are. The local buckling forces ($P_{b1.L}$) were extracted from numerical Eigen buckling SFEA [62] while the global buckling ($P_{b1.e}$) were calculated using GBTUL [64] program.

Table 3.2 - Column critical (distortional) buckling forces and their relations with the lowest local and global bifurcation forces for (i) end-bolted and (ii) end-bolted and fixed columns.

Columns	*(P_F)*			*(P_B)*			*(PF_F)*			*(PF_B)*		
	$P_{cr.D}$ (kN)	$\frac{P_{b1.L}}{P_{cr.D}}$	$\frac{P_{b1.e}}{P_{cr.D}}$	$P_{cr.D}$ (kN)	$\frac{P_{b1.L}}{P_{cr.D}}$	$\frac{P_{b1.e}}{P_{cr.D}}$	$P_{cr.D}$ (kN)	$\frac{P_{b1.L}}{P_{cr.D}}$	$\frac{P_{b1.e}}{P_{cr.D}}$	$P_{cr.D}$ (kN)	$\frac{P_{b1.L}}{P_{cr.D}}$	$\frac{P_{b1.e}}{P_{cr.D}}$
100x70	321	1.44	5.34	323	1.51	6.93	331	1.41	10.2	349	1.35	13.1
100x100	218	2.22	8.14	216	1.81	8.24	237	1.64	15.2	234	1.64	15.5
100x142.9	142	1.88	8.95	140	1.93	10.8	152	1.64	17.1	154	1.66	20.0
130x91	234	1.67	15.4	236	1.54	12.1	265	1.49	22.9	264	1.41	22.1
130x130	158	1.86	16.0	157	1.83	16.1	173	1.86	29.8	171	1.66	30.2
130x185.7	103	2.37	22.6	102	1.97	24.9	115	1.98	41.3	113	1.97	41.9
150x105	197	1.85	17.8	199	1.59	17.6	215	1.52	33.2	214	1.44	33.4
150x150	134	1.99	34.7	132	1.87	24.4	153	1.66	39.4	145	1.68	45.5
150x214.3	85.8	2.38	31.0	85.4	2.03	35.8	94.5	1.74	57.5	96.4	1.76	64.8
180x126	159	1.52	30.9	160	1.69	30.8	176	1.47	49.3	175	1.49	57.5
180x180	107	1.91	38.1	106	1.96	44.3	117	1.72	71.2	119	1.73	80.8
180x257.1	69.0	2.36	46.0	68.6	2.07	58.6	74.7	2.06	87.1	77.3	2.14	106
200x140	140	1.74	40.2	141	1.72	39.9	154	1.63	74.4	154	1.52	74.7
200x200	94.2	1.94	51.3	93.8	1.89	51.6	103	2.00	95.5	103	1.72	96.5
200x285.7	60.7	2.45	64.2	60.3	2.04	72.0	66.3	2.12	121	67.0	2.16	133

One observes that the first “non-distortional” bifurcation load always corresponds to local buckling and that the ratio $P_{b1.L}/P_{cr.D}$ varies between 1.44 and 2.45 and from 1.51 up to 2.04 for P_F and P_B columns respectively and from 1.41 until 2.12 and from 1.35 up to 2.16 to PF_F and PF_B columns respectively. The first global bifurcation load is invariably quite higher (often much higher) – indeed, the $P_{b1.e}/P_{cr.D}$ values range from 5.34 to 64.2 and from 6.93 to 72.0 for P_F and P_B columns respectively and from 10.2 to 121 and from 13.1 to 133 for PF_F and PF_B columns respectively.

4 Experimental Investigation

This chapter addresses the experimental investigation carried out at the Federal University of Rio de Janeiro (COPPE/UFRJ). Initially, this section provides the characterization of the column specimens, which is followed by a description of the test procedure. Then, attention is devoted to presenting and discussing the experimental results recorded and observed before and during the tests, namely the specimen initial geometric imperfections, measured displacements, equilibrium paths, failure loads and collapse mechanisms.

4.1 Column Specimens

The column specimens were manufactured by press braking from structural sheets with nominal thickness t = 2.65 mm and made of either (i) galvanized steel ASTM A653 [67] or ABNT NBR 7008-1 [68] or (ii) carbon steel EN 10149-2 [69] (identified as "G" or "C", respectively). Ten lipped channel sections given in Table 3.1, were selected to be tested experimentally exhibiting the following requirement: web-to-flange width ratio (b_w/b_f) equal to 0.70 or 1.00 (sections 100x142.9-130x185.7-150x214.3-180x257.1-200x285.7, *i.e.* displaying $b_w/b_f < 1$ were excluded from the experimental program due to fabrication difficulties).

Figure 4.1 shows the cross-section dimensions and overall view with lengths for *P* and *PF* columns. The cross-section dimensions and the angles formed by the consecutive walls (θ_n) were measured at three equally spaced locations along the specimen length L_0 (0-0.5-1·L_0). Figure 4.2 illustrates the manual measurement process performed on specimens – the values obtained were found to correlate very well with the nominal ones. Table 4.1 provides (i) the average values of the out-to-out measured specimen cross-section dimensions, (ii) the areas (A) obtained from the average values of the measured cross-section dimensions and (iii) the calculated distance from the centroid of the section to the outer face of the web column (CG) to be compared with (iv) the drilling center obtained by indirect measurement $b_a + d_f/2$ (see Figure 4.1), where b_a is the shorter distance from the hole edge to the web. Table 4.1 also gives the lengths (L_D, L_0 and L_T – see Figure 4.1). The specimen labelling is similar as adopted in Table 3.1 –

nominal web and flanges width b_w x b_f, followed by letter "G" or "C" to identify the column's steel (galvanized or carbon, respectively), the letters "*P*" or "*PF*" to define the boundary condition (end-bolted or end-bolted and fixed, respectively) and the subscripts letter "*F*" or "*B*" to determine the end-bolted load-type (frictional load-type or bearing load-type).

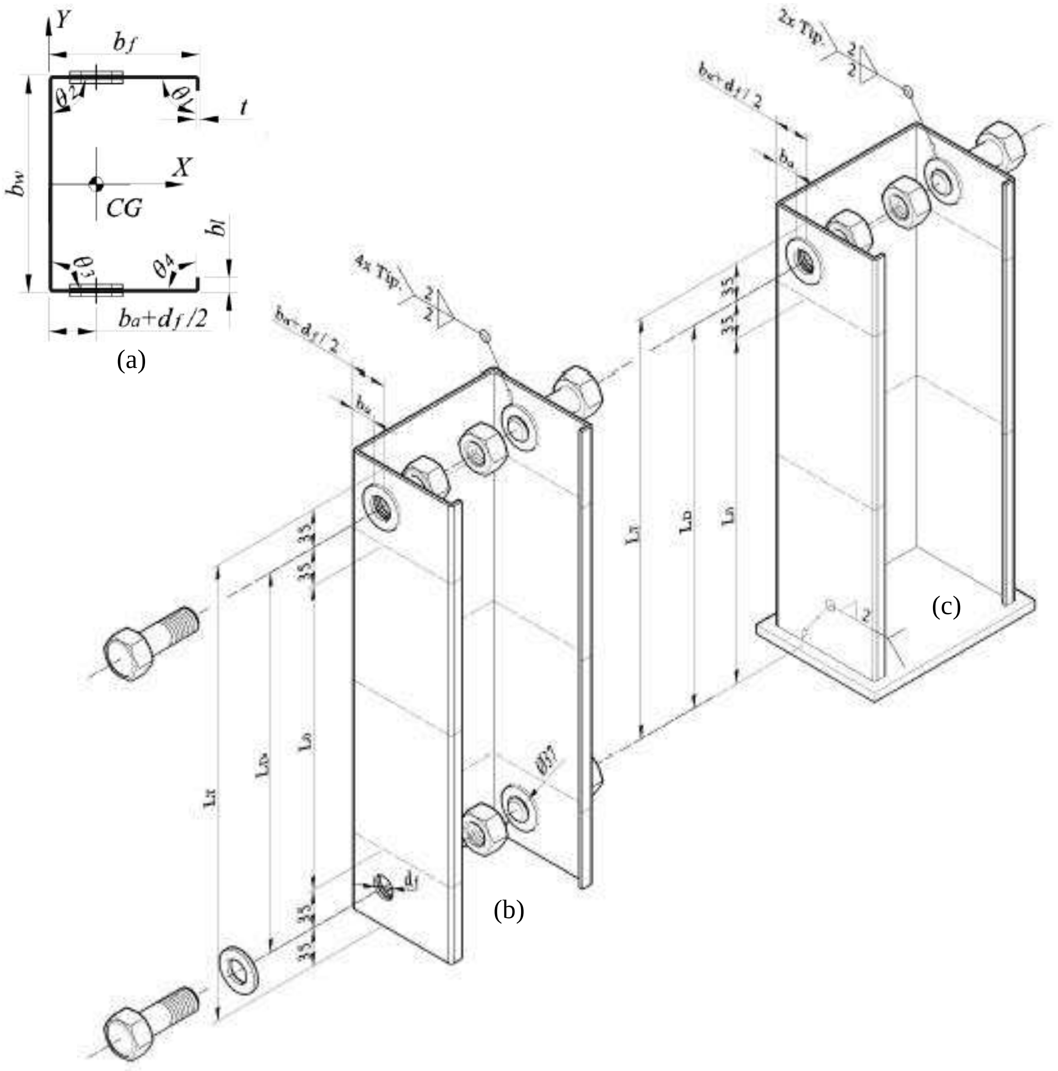

Dimensions in millimeters.

Figure 4.1 – (a) Cross-section dimensions, overall view with lengths for (b) *P* and (c) *PF* columns.

The measured thickness values ranged from 2.40 to 2.65 mm (according to the tolerance limits set out in the ABNT NBR 7013 [70] standard and ABNT NBR 11888 [71] code – Brazilian standards for G and C sheet and coils steels, respectively) and (ii) the ratios between the measured and nominal web widths, flange and lip varied from 0.99 to 1.02, from 0.99 to 1.00 and from 0.97 to 1.16, respectively. The angles formed by the two consecutive walls (θ_n) were also measured at the same three cross-sections and the average and standard deviation values obtained were 90.18° and 0.84, respectively. It was observed that a press braking manufacturing condition imposed internal bending radii approximately equal to half of the sheet nominal thickness ($r_i \approx 1.325$ mm). Finally, it was noted that the average difference of center hole localization ($b_a + d_f/2$) and the calculated centroids (CG) is 0.66 mm, knowing that the loading occurs in the holes, this ensures for all the columns one despicable eccentricity.

In end-bolted support each hole had a couple flat washers (37 mm outer diameter and 3 mm thickness) welded to the inner and outer flange surfaces, which prevents localized collapse near the hole, the centroid is marked in flanges distant 35 mm from free edge and perforated (see Figure 4.3(a)). After making sure that the flange centroids are coincident, the two washers are carefully TIG welded to each the specimen hole (see Figure 4.3(b)).

Table 4.1 - Average values of the measured column specimen cross-section dimensions, area, *CG* position, position of the drilling center and lengths.

Column	b_w (mm)	b_f (mm)	b_l (mm)	t (mm)	A (cm²)	CG (mm)	$b_a+d_f/2$ (mm)	L_D (mm)	L_0 (mm)	L_T (mm)
100x70G–P_F	100.17	69.37	10.58	2.65	6.50	23.92	23.94	400	331	471
100x70C–P_F	99.13	69.18	11.33	2.59	6.35	24.22	24.78	399	329	469
100x100C–P_F	99.47	99.80	10.57	2.45	7.50	37.45	34.68	452	380	520
130x91G–P_F	130.18	90.29	10.30	2.65	8.38	29.96	30.34	450	381	521
130x91C–P_F	131.60	90.20	11.80	2.61	8.36	30.35	30.96	398	329	469
130x130C–P_B	131.47	129.13	10.93	2.50	9.95	47.10	47.83	549	479	619
150x105G–P_F	149.68	104.14	10.52	2.60	9.46	34.13	34.53	500	430	570
150x105C–P_F	151.53	103.63	11.27	2.50	9.18	34.04	34.35	501	429	569
150x150C–P_B	150.93	148.42	12.28	2.45	11.24	54.08	54.33	550	479	619
180x126C–P_F	181.00	126.18	10.37	2.52	11.08	40.55	40.66	551	480	620
180x180C–P_B	180.60	179.33	11.15	2.44	13.38	64.09	64.41	701	630	770
200x140C–P_B	199.67	139.38	11.23	2.44	11.90	44.77	45.48	599	527	667
200x200C–P_B	199.83	198.98	10.92	2.47	14.98	70.61	71.00	752	681	821
100x70C-PF_F	100.53	69.27	10.88	2.44	6.02	23.97	24.75	400	295	435
100x100C-PF_F	102.07	98.78	10.73	2.40	7.38	36.76	37.70	450	345	485
130x91C-PF_F	130.97	90.85	11.08	2.53	8.10	30.43	31.20	366	260	400
130x130C-PF_F	132.13	128.22	11.48	2.42	9.64	46.84	47.50	549	443	583
150x105C-PF_F	150.20	104.18	11.72	2.55	9.38	34.56	35.45	499	392	532
150x150C-PF_B	151.20	149.60	11.57	2.51	11.54	54.29	55.03	550	446	586
180x126C-PF_F	181.30	125.15	11.18	2.44	10.72	40.41	40.90	550	445	585
180x180C-PF_B	180.67	179.47	11.12	2.51	13.74	64.13	62.40	699	594	734
200x140C-PF_B	200.27	138.68	11.33	2.48	12.04	44.46	45.15	602	497	637
200x200C-PF_B	199.23	199.45	11.23	2.48	15.01	71.02	71.00	749	645	785

Figure 4.2 – Specimens dimensional manual measurements.

(a) (b)

Figure 4.3 – Attachment of the washers in specimen holes: (a) positioning and (b) continuously TIG welding around the washer contour.

4.2 Material Properties

The mechanical properties of the structural G [67] and C [69] steel sheets employed to manufacture the column specimens were experimentally obtained by means of two sets of three standard tensile coupon tests. The coupons were extracted, longitudinally, from virgin steel sheet (belonging to the same batch of those used to manufacture the both specimen types) prior to the initiation of the cold-forming (press-braking) procedure. The coupon dimensions conformed to ASTM E8 [72] for the tensile testing of metals: 12.5 mm wide coupons with 50 mm gauge length ("sheet-type") – design and the coupons are shown in Figure 4.4. Figure 4.5 shows a general view of a coupon tensile test and illustrates the experimental stress-strain-curves obtained (G [67] and C [69] steel coupons). The tests were performed according to ASTM E8 [72] in a Shimadzu AGX-100kN (see Figure 4.6) displacement controlled universal testing machine (UTM) using friction grips. The longitudinal strains were measured through a

50 mm clip-on gage (see Figure 4.5 (a)). A data acquisition system was used to record the load and strain readings at a frequency of 15 Hz. Table 4.2 and Table 4.3 show de basic dimensions of tensile specimens for both steels. Furthermore, it is shown the values of f_y (yield stress), f_u (ultimate stress) and E (*Young*'s modulus) for each coupon.

(a) (b)

Figure 4.4 – (a) Dimensions of the specimens of the material characterization test and (b) specimens for testing characteristics of the material.

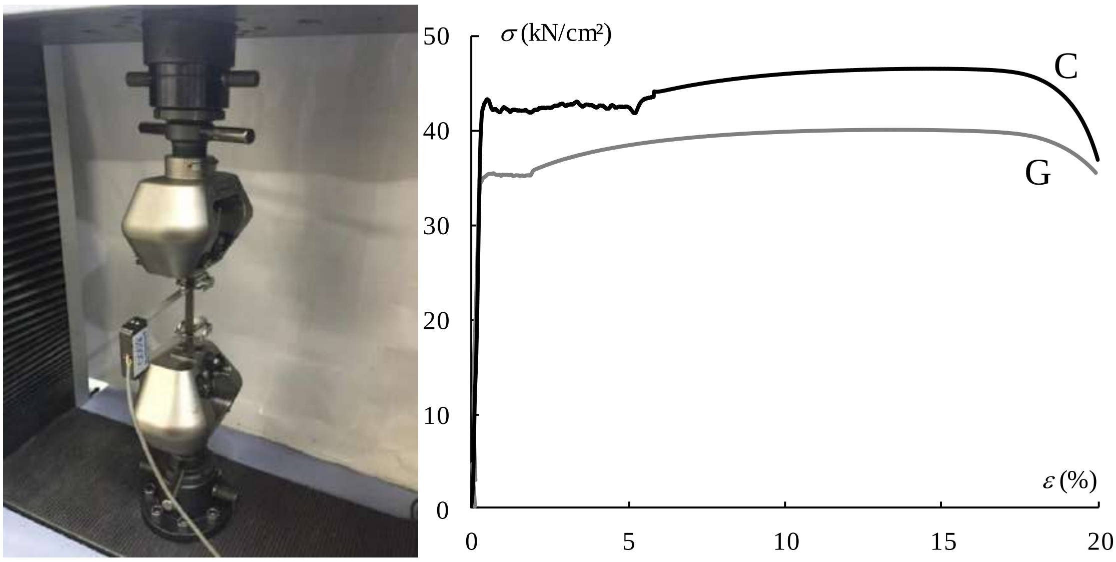

(a) (b)

Figure 4.5 – (a) General view of a coupon tensile test and (b) illustrative stress-strain curves experimentally obtained.

Table 4.2 – Basic dimensions and mechanical properties of the G [67] steel.

Identification of Specimens	t (mm)	d (mm)	f_y (kN/cm²)	f_u (kN/cm²)	E (kN/cm²)
G.1	2.74	12.75	34.98	42.42	20678.77
G.2	2.73	12.77	35.00	42.95	20459.81
G.3	2.72	12.76	35.02	42.99	20377.21
Average	2.73	12.76	35.00	42.78	20505.26

Table 4.3 – Basic dimensions and mechanical properties of the C [69] steel.

Identification of Specimens	t (mm)	d (mm)	f_y (kN/cm²)	f_u (kN/cm²)	E (kN/cm²)
C.1	2.60	12.40	42.60	47.21	21260.49
C.2	2.60	12.40	42.70	46.64	20857.35
C.3	2.60	12.50	42.50	46.54	20884.92
Average	2.60	12.43	42.60	46.80	21000.92

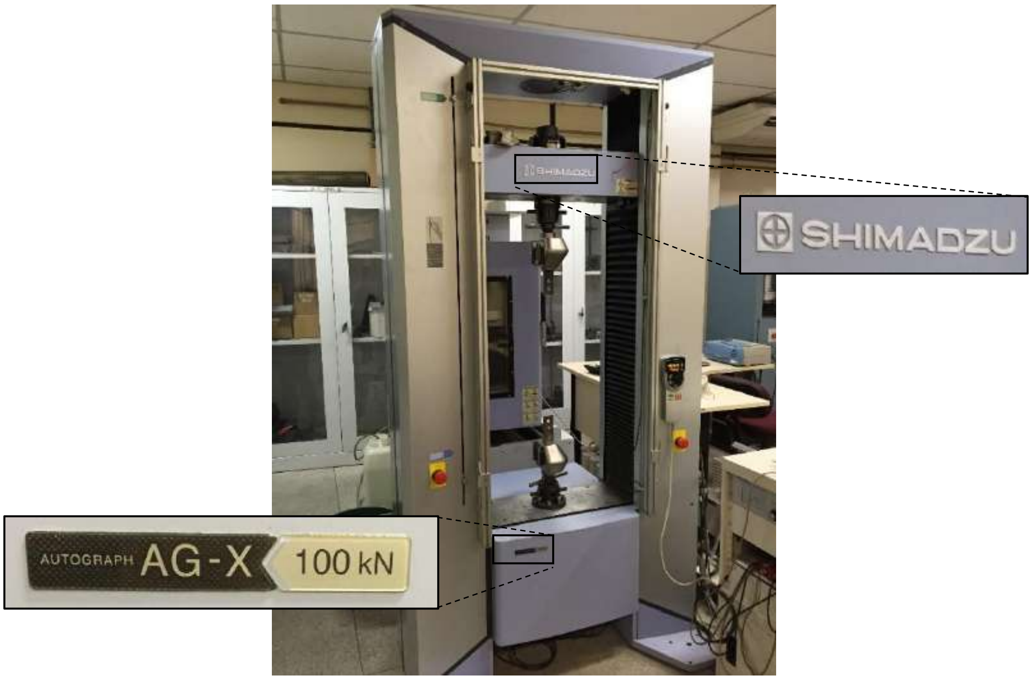

Figure 4.6 – Machine used to perform the test characterization of materials.

On the basis of the stress-strain curves determined experimentally, it was possible to obtain estimates of the steel mechanical properties – the corresponding average values for G [67] steel are f_y = 35 kN/cm² (yield stress), f_u = 43 kN/cm² (ultimate stress) and E = 20500 kN/cm² (*Young*'s modulus[3]) and the corresponding average values for C [69] steel are f_y = 42.6 kN/cm², f_u = 46.8 kN/cm² and E = 21000 kN/cm².

4.3 Initial Geometric Imperfections

Initial geometric imperfections were measured using seven displacement transducers (DT1-7 – see Figure 4.7(b)) fixed on the (rigid) arm of a milling machine. The specimen was placed on the (also rigid) table of the same machine which could move horizontally thereby allowing the DTs to move along the specimen outer faces (see Figure 4.7(a)). The positions of the seven DTs were monitored by means of an eighth DT (DT8) wire potentiometer-type displacement transducer. The DT locations were properly positioned objectifying the reading of the column local flanges initial warping, local web initial displacements and global imperfections.

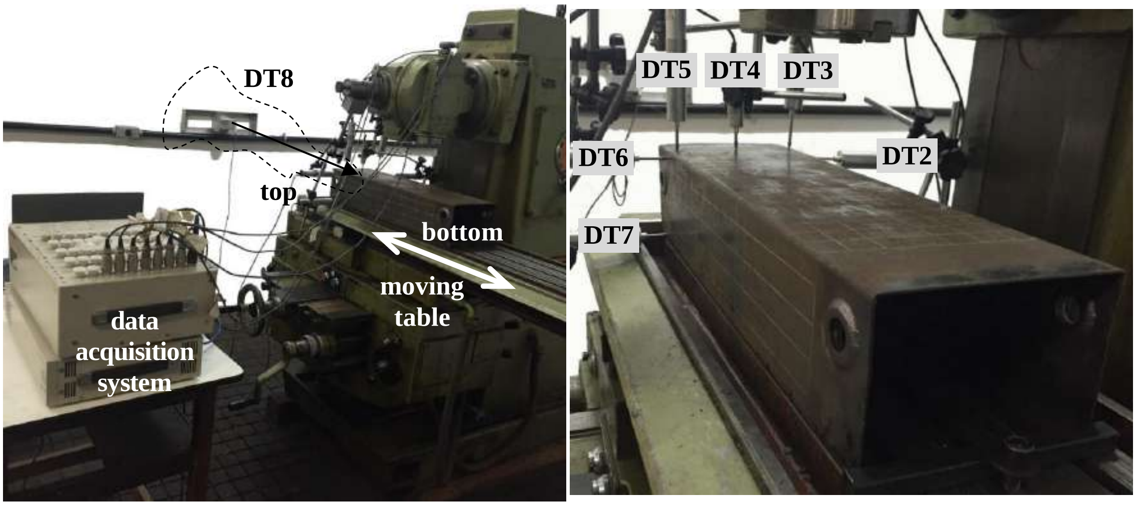

(a) (b)

Figure 4.7 – DTs involved in the initial geometric imperfections measurement (a) general view and (b) DTs identifications.

The transducer DT1-7 were positioned in relation to the specimen cross-section, as shown in Figure 4.8(a), on an undeformed cross-section of the *XY* plane and (i) DT1 and DT2 were placed normally to the "horizontal" flange at distances $x_1=(b_f–10)$ mm and x_2=10 mm from the corner, (ii) DT6 and DT7 followed the same positioning of DT1 and DT2 and (iii) DT3, DT4 and DT5 were oriented normally to the "vertical" web, at

---

[3] As stipulated in ASTM E8 [72], the yield stress corresponds to the onset of yielding and the ultimate stress is calculated by dividing the maximum load carried by the coupon during the tensile test by its original cross-section area.

distances $y_3=b_w/2$–10 mm, 0 and $y_5=b_w/2$–10 mm. Due to the fixing of DTs the "horizontal" and "vertical" projections of these DTs scanned the cross-section deformations. The signs of the displacements measured by the DTs are positive/negative for outward/inward displacements, respectively. The measured length is limited to the distance L_0 (see Figure 4.1) taking into account the interference that occurred in DT2 and DT6 with the welded-on washers in some specimens.

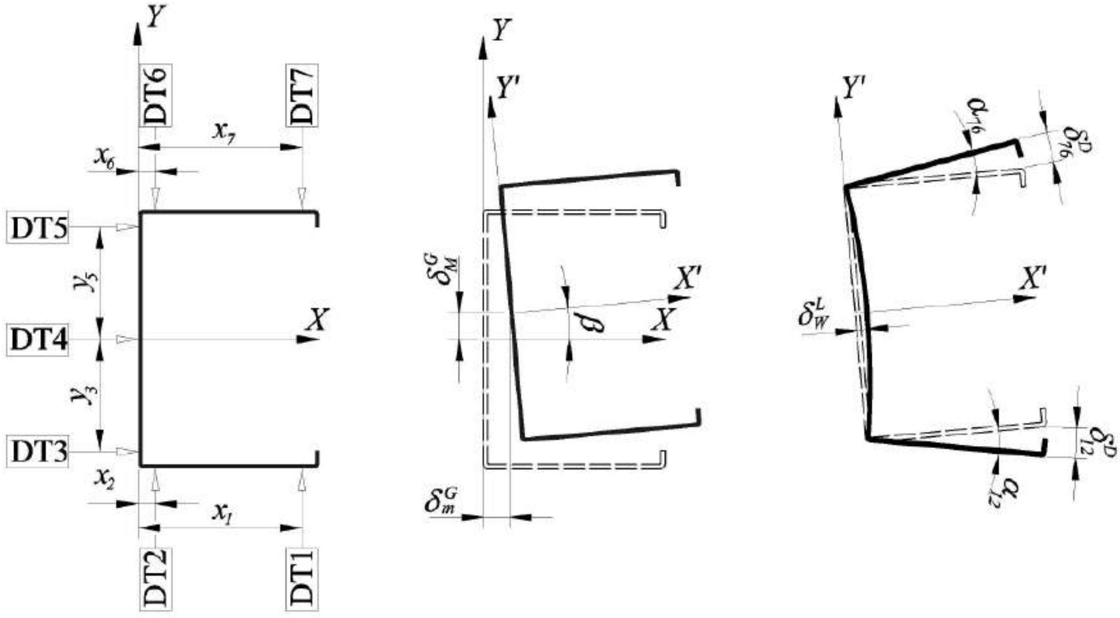

(a) (b)

Figure 4.8 – Cross-section (a) undeformed configuration and DT locations and (b) deformed configuration and definition of δs values.

Table 4.4 provides (i) the minimum and maximum values recorded, along the specimen length, by each transducer (DT1-7) and Table 4.5 presents the minimum and maximum computed values of the torsional rotation (β), flange displacements (δ_{12}^D and δ_{76}^D), local web undulations (δ_W^L) and global minor and major initial deformations (δ_m^G and δ_M^G). This computation (i) is based on the fact that the cross-sections undergo rigid-body motions and (ii) must take into account that the seven DTs remain fixed while the measured cross-sections move. In view of Figure 4.8 the first step of this procedure consists of using the seven DTs measurements to calculate these displacements as follows:

i. The cross-section torsional rotation β can be straightforwardly obtained from the expression:

$$\beta = \tan^{-1}\left(\frac{\text{DT5} - \text{DT3}}{y_5 - y_3}\right) \tag{4.1}$$

ii. The determination of δ_m^G and δ_M^G is more involved, because it must account for the continuous (as deformation evolves) change in the relative position of the seven DTs with respect to the cross-section, as illustrated in Figure 4.8(b). Each displacement measures by a DT combines two parts, one identical to a translation (δ_m^G or δ_M^G) and the other equal to the product of the torsional rotation by an "horizontal" or "vertical" distance that depends on the cross-section middle web location. Indeed, the measurements of DT3 and DT6 can be expressed in terms of δ_m^G, δ_M^G and β as (see Figure 4.8(b) – note that the values of δ_m^G, δ_M^G and β can be obtained from the measurements of only three DTs [73], being two normal to the web near the corners and another normal to the flange next to the web-flange fold line):

$$\text{DT3} = \delta_m^G + \left(y_3 - \delta_M^G\right)\tan\beta \tag{4.2}$$

$$\text{DT6} = \delta_M^G + \left(\cos\beta - 1\right)b_w/2 + \left[x_6 + \delta_m^G + \left(b_w/2\right)\sin\beta\right]\tan\beta \tag{4.3}$$

Table 4.4 – Measured minimum and maximum specimen initial displacement values.

Column	*DT1* (mm)	*DT2* (mm)	*DT3* (mm)	*DT4* (mm)	*DT5* (mm)	*DT6* (mm)	*DT7* (mm)
100x70G–P_F	0.00/087	0.00/0.31	-0.35/0.02	-0.69/0.01	-0.61/0.00	0.00/0.55	-0.42/0.18
100x70C–P_F	0.00/051	-0.12/0.00	0.00/0.22	-0.17/0.06	0.00/0.18	-0.26/0.01	-0.11/0.13
100x100C–P_F	-0.01/0.83	-0.13/0.00	0.00/0.28	0.00/0.40	0.00/0.32	-0.07/0.05	-0.38/0.01
130x91G–P_F	-0.34/0.07	-0.16/0.00	-0.17/0.38	-0.20/0.31	-0.14/0.04	0.00/0.37	-0.09/0.40
130x91C–P_F	-0.04/0.08	-0.07/0.02	0.00/0.19	-0.01/0.09	0.00/0.17	-0.08/0.02	-0.01/0.34
130x130C–P_B	-0.50/0.92	-0.09/0.58	-0.15/0.36	-0.01/0.89	0.00/0.50	-0.49/0.02	-0.72/0.49
150x105G–P_F	-0.75/0.00	-0.05/0.07	-0.22/0.03	-0.09/0.22	-0.04/0.41	-0.14/0.05	-0.03/0.21
150x105C–P_F	-0.34/0.90	-0.09/0.03	0.00/0.40	0.00/0.65	-0.01/0.41	-0.28/0.01	-0.06/0.13
150x150C–P_B	-0.07/0.62	-0.19/014	0.00/0.51	0.00/0.51	-0.10/0.34	-0.32/0.05	-0.03/0.43
180x126C–P_F	-0.02/0.49	-0.22/0.01	0.00/0.37	-0.12/0.06	0.00/0.32	-0.17/0.01	-0.06/0.54
180x180C–P_B	0.00/1.70	-0.34/0.08	-0.29/0.52	0.00/1.49	0.00/0.63	-0.13/0.03	-0.66/0.00
200x140C–P_B	-1.14/0.00	-0.31/0.01	-0.02/0.38	-1.29/0.59	0.00/0.40	-0.15/0.05	0.00/1.24
200x200C–P_B	-2.85/0.01	-0.70/0.00	0.00/0.63	-0.50/1.35	0.00/0.69	-0.27/0.03	0.00/2.28
100x70C-PF_F	-0.12/0.08	-0.20/0.02	-0.01/0.35	-0.05/0.30	-0.01/0.22	-0.05/0.21	-0.03/0.29
100x100C-PF_F	-0.07/0.09	-0.26/0.01	0.00/0.31	0.00/0.26	0.00/0.55	0.00/0.30	0.00/1.06
130x91C-PF_F	-0.22/0.12	-0.13/0.07	0.00/0.27	-0.01/0.71	0.00/0.18	-0.05/0.20	-0.02/0.34
130x130C-PF_F	-0.02/0.81	-0.06/0.08	-0.02/0.41	-0.03/0.69	-0.01/0.47	-0.15/0.10	-0.04/0.77
150x105C-PF_F	0.00/0.77	-0.05/0.07	-0.02/0.28	0.00/0.57	0.00/0.34	-0.27/0.05	-0.01/0.96
150x150C-PF_B	-0.05/0.39	0.00/0.26	-0.04/0.32	-0.01/0.91	0.00/0.58	-0.16/0.12	0.00/1.00
180x126C-PF_F	0.00/1.08	-0.02/0.15	0.00/0.48	-0.04/1.15	-0.01/0.54	-0.12/0.14	-0.23/0.99
180x180C-PF_B	-1.05/0.02	-0.34/0.22	-0.17/0.57	-0.34/1.29	-0.04/0.56	-0.17/0.21	-0.11/1.09
200x140C-PF_B	-0.79/0.02	-0.23/0.03	-0.18/0.38	-0.91/0.25	0.00/0.39	-0.14/0.16	-0.03/0.91
200x200C-PF_B	0.00/1.42	-0.13/0.12	-0.01/0.87	-0.03/1.61	0.00/0.51	-0.13/0.01	-0.89/0.00

iii. Solving the system equation formed by Eqs. (4.2) and (4.3) and taking into account Eq. (4.1), the values of δ_M^G and δ_m^G, defining the location of the cross-section outer web center disregarding local deformations, are obtained from

$$\delta_M^G = \left\{ \begin{matrix} \mathrm{DT6} + y_3 \tan^2 \beta - \left[x_3 + \mathrm{DT3} + \left(b_w/2 \right) \sin \beta \right] \tan \beta \\ + \left(b_w/2 \right)\left(1 - \cos \beta \right) \end{matrix} \right\} / \left(1 + \tan^2 \beta \right) \tag{4.4}$$

$$\delta_m^G = \mathrm{DT3} + \left(\delta_M^G - y_3 \right) \tan \beta \tag{4.5}$$

iv. The midweb wall bending displacement is defined as the distance between the *X'Y'* coordinate system origin and the maximum bending displacement considered in web center (see Figure 4.8(b)).

$$\delta_W^L = \frac{\left[\left(\mathrm{DT4} - \mathrm{DT3} \right) \delta_M^G + \left(\delta_m^G - \mathrm{DT4} \right) y_3 \right]}{\left[\left(\mathrm{DT3} - \mathrm{DT4} \right) \sin \beta - y_3 \cos \beta \right]} \tag{4.6}$$

v. The last step consists of expressing the values of δ_{12}^D and δ_{76}^D , associated with the distortional displacements. This straightforward procedure is illustrated in Figure 4.8(b) and leads to

$$\delta_{12}^D = \begin{cases} b_f \sqrt{2\left(1 - \cos \alpha_{12} \right)} & if\ \ \mathrm{DT1} \ \geq \ \mathrm{DT2} \\ -b_f \sqrt{2\left(1 - \cos \alpha_{12} \right)} & if\ \ \mathrm{DT1} \ < \ \mathrm{DT2} \end{cases} \tag{4.7}$$

$$\delta_{76}^D = \begin{cases} b_f \sqrt{2\left(1 - \cos \alpha_{76} \right)} & if\ \ \mathrm{DT7} \ \geq \ \mathrm{DT6} \\ -b_f \sqrt{2\left(1 - \cos \alpha_{76} \right)} & if\ \ \mathrm{DT7} \ < \ \mathrm{DT6} \end{cases} \tag{4.8}$$

where α_{12} and α_{76} correspond to the angles formed by the local undeformed and distortional deformed flanges 12 and 76 respectively of the cross-section in the *X'Y'* coordinate system (see Figure 4.8(b)) and are given by

$$\alpha_{12} = \tan^{-1} \left| \frac{y_1' + b_w/2}{x_1'} \right| \ \text{and} \ \alpha_{76} = \tan^{-1} \left| \frac{y_7' - b_w/2}{x_7'} \right| \tag{4.9}$$

The pair of points x_1', y_1' and x_7', y_7' in the *X'Y'* coordinate system, for the DT1 and DT7 readings respectively, are

$$(x_1', y_1') \equiv \begin{pmatrix} \cos \beta \left(x_1 - \delta_m^G \right) + \sin \beta \left(-b_w/2 - \mathrm{DT1} - \delta_M^G \right), \\ -\sin \beta \left(x_1 - \delta_m^G \right) + \cos \beta \left(-b_w/2 - \mathrm{DT1} - \delta_M^G \right) \end{pmatrix} \tag{4.10}$$

$$(x_7', y_7') \equiv \begin{pmatrix} \cos \beta \left(x_7 - \delta_m^G \right) + \sin \beta \left(b_w/2 + \mathrm{DT7} - \delta_M^G \right), \\ -\sin \beta \left(x_7 - \delta_m^G \right) + \cos \beta \left(b_w/2 + \mathrm{DT7} - \delta_M^G \right) \end{pmatrix} \tag{4.11}$$

Table 4.5 – Calculated minimum and maximum specimen initial torsional rotation and displacement values.

Column	β (°)	δ_{12}^D (mm)	δ_{76}^D (mm)	δ_W^L (mm)	δ_m^G (mm)	δ_M^G (mm)
100x70G–P_F	-0.31/0.00	-0.55/1.39	-0.71/0.05	-0.33/0.04	-0.44/0.00	0.00/0.59
100x70C–P_F	-0.09/0.08	0.00/0.41	-0.03/0.31	-0.34/0.00	0.00/0.17	-0.26/0.01
100x100C–P_F	-0.06/0.07	0.00/0.91	-0.37/0.07	-0.01/0.13	0.00/0.28	-0.07/0.06
130x91G–P_F	-0.24/0.02	-0.37/0.11	-0.13/0.49	-0.11/0.18	-0.16/0.16	0.00/0.41
130x91C–P_F	-0.04/0.02	-0.06/0.07	-0.02/0.47	-0.15/0.00	0.00/0.16	-0.08/0.02
130x130C–P_B	-0.02/0.14	-0.76/0.99	-0.61/0.74	0.00/0.50	-0.04/0.42	-0.51/0.02
150x105G–P_F	-0.02/0.27	-0.54/0.02	-0.06/0.22	-0.18/0.10	-0.02/0.14	-0.19/0.05
150x105C–P_F	-0.10/0.06	-0.58/0.75	0.00/0.35	-0.04/0.29	0.00/0.38	-0.29/0.01
150x150C–P_B	-0.16/0.09	-0.11/0.34	0.00/0.91	-0.05/0.14	0.00/0.42	-0.32/0.08
180x126C–P_F	-0.07/0.03	0.00/0.46	-0.05/0.70	-0.40/0.01	0.00/0.33	-0.17/0.01
180x180C–P_B	0.00/0.15	-0.06/1.85	-0.94/0.09	0.00/0.96	-0.12/0.57	-0.14/0.01
200x140C–P_B	-0.03/0.05	-1.35/0.00	0.00/1.46	-1.39/0.23	-0.01/0.38	-0.15/0.05
200x200C–P_B	-0.07/0.06	-3.13/0.01	0.00/2.49	-0.63/0.72	0.00/0.64	-0.28/0.04
100x70C-PF_F	-0.12/0.02	-0.09/0.20	-0.08/0.33	-0.12/0.05	0.00/0.27	-0.06/0.23
100x100C-PF_F	-0.01/0.24	-0.02/0.55	0.00/0.61	-0.20/0.02	0.00/0.42	0.00/0.29
130x91C-PF_F	-0.08/0.02	-0.26/0.30	0.00/0.38	-0.13/0.53	0.00/0.22	-0.06/0.21
130x130C-PF_F	0.00/0.05	0.00/0.98	0.00/0.82	-0.12/0.27	-0.01/0.43	-0.16/0.10
150x105C-PF_F	-0.03/0.08	-0.05/0.80	-0.02/1.03	0.00/0.33	0.00/0.29	-0.28/0.05
150x150C-PF_B	0.00/0.20	-0.59/0.00	-0.02/0.82	-0.13/0.50	-0.01/0.44	-0.19/0.10
180x126C-PF_F	0.00/0.05	0.00/1.23	-0.26/0.97	-0.08/0.68	0.00/0.50	-0.12/0.13
180x180C-PF_B	-0.03/0.09	-1.10/0.03	0.00/1.13	-0.44/0.76	-0.05/0.54	-0.18/0.21
200x140C-PF_B	-0.03/0.09	-0.84/0.06	-0.01/0.98	-0.91/0.00	-0.07/0.38	-0.15/0.17
200x200C-PF_B	-0.14/0.03	-0.01/1.20	-0.78/0.05	-0.08/0.96	0.00/0.67	-0.13/0.02

Figure 4.9 shows the initial longitudinal displacement columns acquired from the tests involving specimens 150x105G–P_F, 180x180C–P_B, 150x105C–PF_F and 180x180C–PF_B, which were obtained either (i) directly from DT1–7 readings or (ii) using Eqs. (4.1), (4.4) – (4.8) (δ_{12}^D, δ_{76}^D, δ_W^L, δ_m^G and δ_M^G). Note that the horizontal coordinates are normalized with respect to the column measured length L_0 (DT8/L_0), where L_0 is the measured length (see Figure 4.1). The observation of these results prompts the following remarks:

i. With two exceptions, the DT1-7 measurements are fairly low, as their maximum absolute value is about 1.70 mm, *i.e.*, below to the nominal wall thickness. The exceptions are the DT1 readings of 2.85 mm and DT7 readings of 2.28 mm, for specimens 200x200C.

ii. All displacement profiles provided by the DT1-7 readings exhibit (ii$_1$) some degree of asymmetry and (ii$_2$) a dominant single half-wave sinusoidal shape, combined with minor participations of two and three half-wave sinusoids.

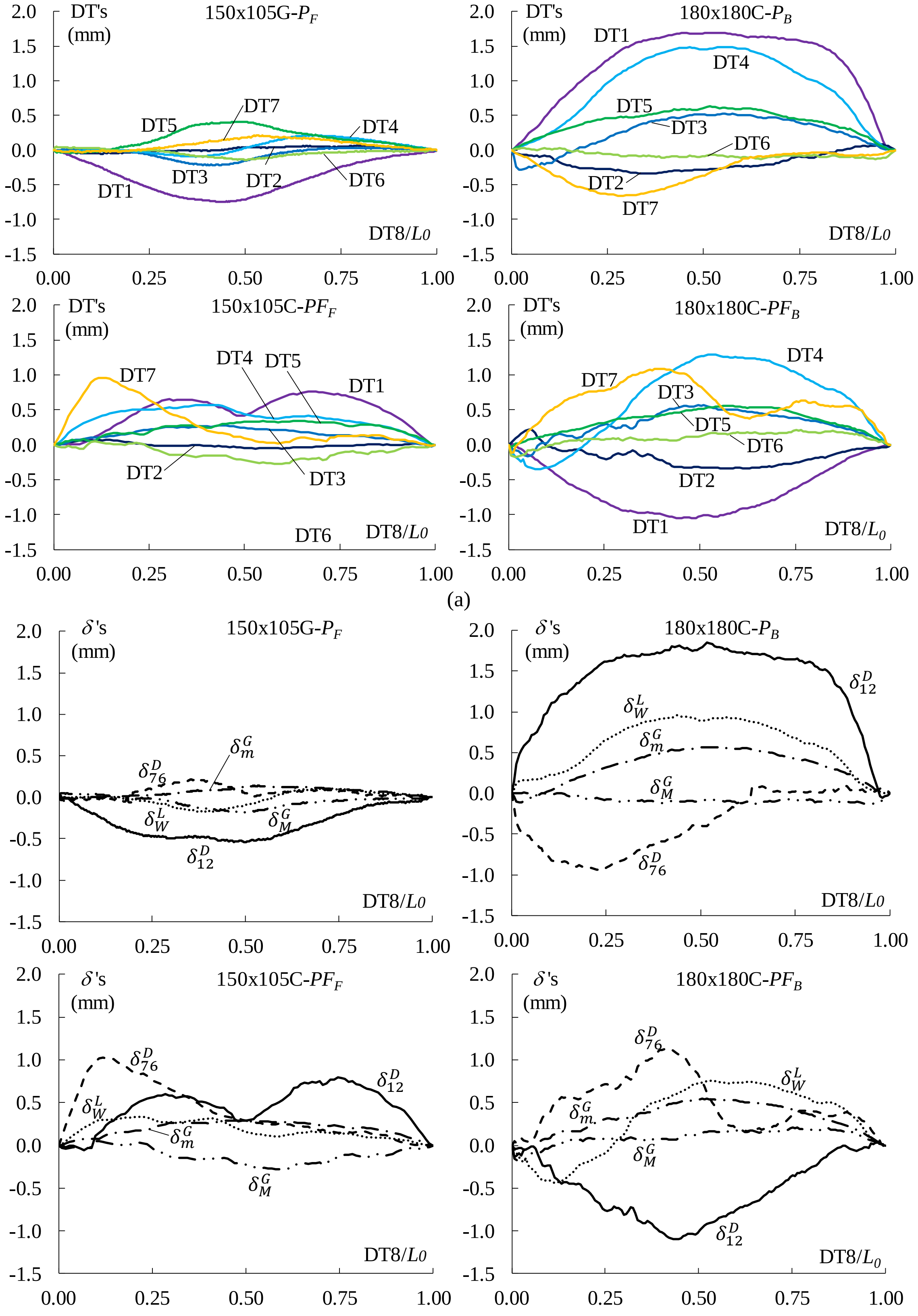

(a)

(b)

Figure 4.9 – Initial displacement longitudinal profiles concerning specimens 150x105G-P_F, 180x180C-P_B, 150x105C-PF_F and 180x180C-PF_B (a) DT1-7 readings and (b) δ values.

iii. The maximum absolute δ_{12}^{D} and δ_{76}^{D} values are also quite low: about (i) 3.13 mm and 2.49 mm, respectively for *P* columns (average about 0.23*t*) and (ii) 1.23 mm and 1.13 mm, respectively for *PF* specimens (average approximately 0.19*t*). Moreover, the δ_{12}^{D}/t and δ_{76}^{D}/t ratios vary from (i) -1.27 to 0.76, and from -0.39 to 1.01, respectively for *P* columns and (ii) -0.44 to 0.51, and from -0.31 to 0.45, respectively for *PF* specimens.

4.4 Test Set-up

All specimens were tested in a Shimadzu servo-controlled hydraulic Universal Test Machine (UTM) under displacement-control conditions. The testing machine can supply compressive loads up to 1 mN and the loads imposed during the performance of a test were measured with a 50 N accuracy and recorded in a data acquisition system. Figure 4.10 provides an overall view of the test set-up, showing a moveable lower end support that allowed tests to be conducted for specimens with various lengths. As for Figure 4.11(a)-(b), they provide a general view and schematic representations of the bottom (end-bolted) end support, formed by a pair of cylindrical hinges (i) built from machine-finished carbon steel, (ii) mounted on 12.7 mm thick steel bearing plate and (iii) to be used to fix the pair of bolted connections – the top end support in *P* columns is similar. These bolted-end supports (i) prevent transverse displacements, major-axis flexural and torsional rotations and (ii) release the secondary warping, local displacements/rotations and minor-axis flexural – the corresponding support conditions are “fixed” with respect to major-axis flexure and torsion, and “pinned” with respect to minor-axis flexure and warping. On the other hand, in *PF* columns, the fixed end support prevents all global and local displacements, rotations and warping in the region near the end-plate.

A very careful positioning procedure, aimed at achieving minute/negligible load eccentricities (lack of coincidence between the end cross-section centroids and the test frame loading axis), is performed involving the following steps:

i. The specimen ends are carefully bolted (with or without bolt shank pretension, *F* or *B* cases, respectively) to hinged-support devices (see Figure 4.11(a)-(b)), assuring that their centroids are aligned and orthogonal “as perfect as possible”.
ii. After placing the bottom hinged-support and adequately bolting it the UTM rigid base, the UTM actuator ram slowly moved until the top hinged-support (*P*

columns) or top end-plate (*PF* columns) was in full contact with the UTM “rigid” loading plate. Next, once the appropriate vertical positioning of the specimen is completed, with the help of a line laser device (self-levelling cross-line laser with plumb points, see Figure 4.10), bearing plates of top hinged-support or end-plate are tightened to UTM and whole specimen positioning procedure is finished. In view of this meticulous procedure, it seems fair to argue that the tests are performed under virtually concentric loading conditions (the load eccentricity will certainly be extremely small and, therefore, can be neglected).

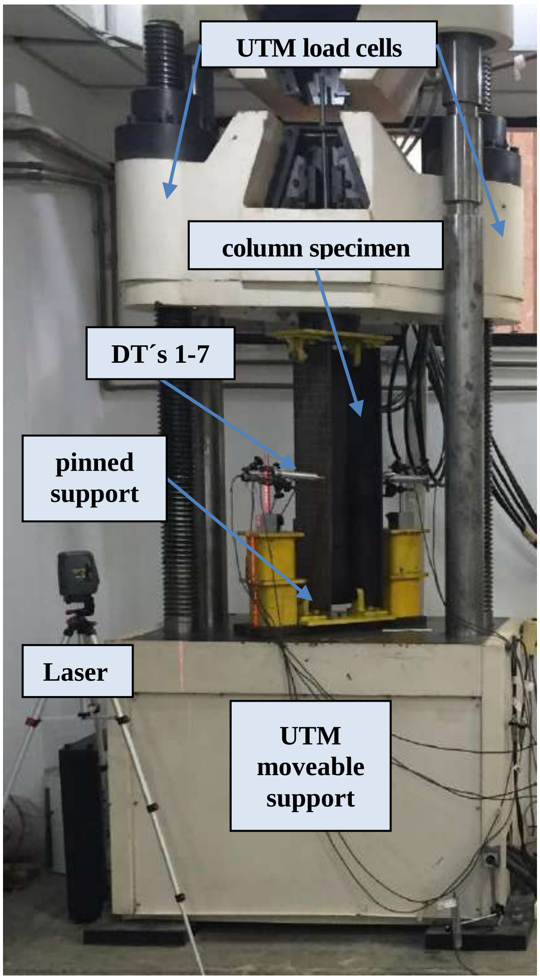

Figure 4.10 – Overall view of the experimental test set-up and servo-controlled hydraulic UTM.

iii. Properly placing the eight DTs transducers: seven at the column mid-height (see Figure 4.12(a)) and one between top and bottom bolt lines (see Figure 4.12(b)). The seven DTs (DT1-7) locations followed the same relative positions of DTs employed during the initial geometric imperfections measures (see Figure 4.7(b)).

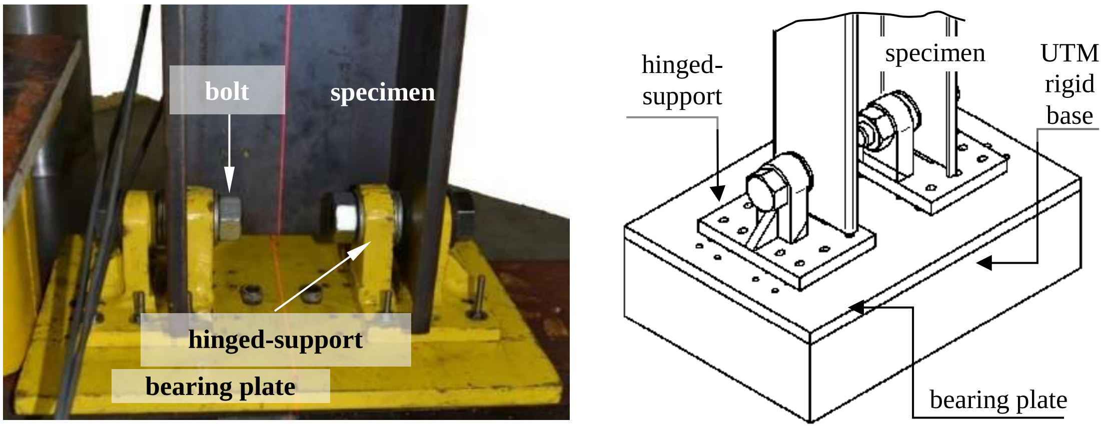

(a) (b)

Figure 4.11 – Specimens bottom end support: (a) overall view and (b) schematic 3D representation.

(a) (b)

Figure 4.12 – DT arrangements to measure mid-height displacements and axial shortening: (a) back and (b) frontal views.

iv. Slow (0.005 mm/s) application of an initial small compressive load (~1-2 kN), in order to eliminate any possible gaps between the hinged-supports or end-plate and the UTM “rigid” loading plate.

v. Application of the displacement-controlled loading, by the UTM servo-controlled hydraulic actuator, at a sufficiently low rate to preclude relevant dynamic effects.

vi. Continuous recording, by means of a high frequency (15 Hz) data acquisition system, of the mid-height DTs (see Figure 4.12(a)) outputs and the hydraulic actuator load cell readings. As the applied load approaches the anticipated column ultimate strength, the specimen deformed configurations are photographed, in order to obtain experimental evidence concerning the nature of the column failure mechanism, namely the occurrence of distortional mode.

vii. After the test, the recorded displacements and loads are post-processed to obtain experimental equilibrium paths and deformed configurations, identifying of the distortional deformations.

4.5 Test Results

The experimental results obtained from this test campaign consist of column (i) equilibrium paths, relating the applied load to relevant displacements, (ii) failure load data and (iii) deformed configurations (including the failure mode) evidencing the presence of distortional deformations. Since the 23 column specimens tested shared essentially the same structural response, only a representative sample of these various types of experimental results are individually reported and discussed in the following subsections, however, in appendix A is presented for each specimen a datasheet with main results.

4.5.1 Equilibrium paths

Figure 4.13 shows the equilibrium paths obtained from the test involving specimens 100x100C-P_F, 180x126C-P_F, 130x91C-PF_F and 150x105C-PF_F relating the applied load P, provided by the UTM hydraulic actuator load cell, to (i) axial shortening Δ (DT8 readings) and (ii) the mid-height computed displacements values δ_W^L, δ_{12}^D, δ_{12}^D, δ_m^G and δ_M^G – the values of δs are caused by the applied load (*i.e.*, do not include the initial imperfections). The observation of such equilibrium paths leads to the following comments:

i. There is an almost linear initial portion in equilibrium paths P *vs.* Δ where the slopes are quite similar to each other, thus demonstrating a relative proximity of column axial stiffness values – EA/L_0 = 4148.4 – 4847.6 – 5147.7 – 4245.7 kN/cm for the 100x100C-P_F, 180x126C-P_F, 130x91C-PF_F and 150x105C-PF_F columns.

ii. Figure 4.13 depicts the equilibrium paths P *vs.* δ_{12}^{D} and P *vs.* δ_{76}^{D}, following practically the same trend and demonstrates distortional inward flange movements.

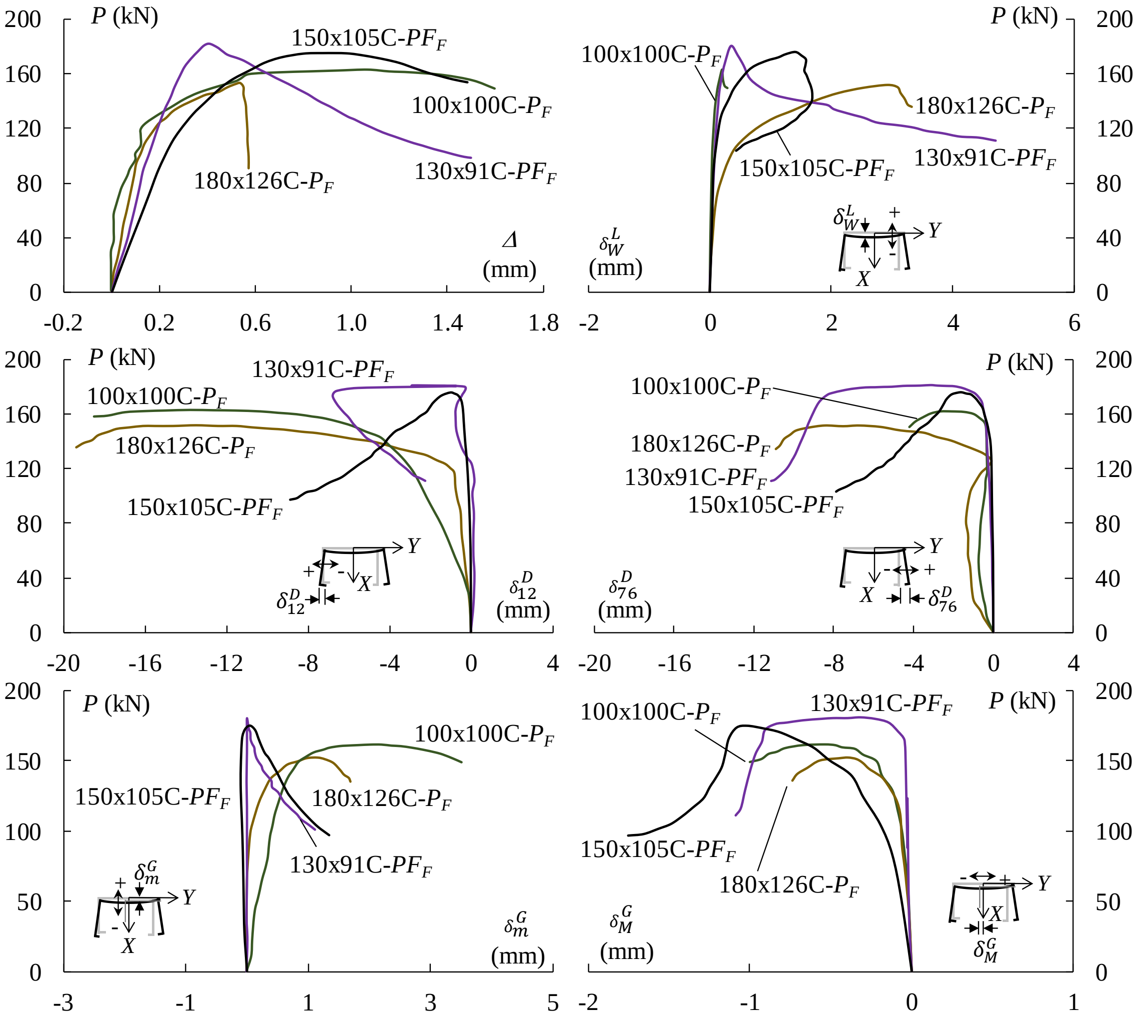

Figure 4.13 – 100x100C-P_F, 180x126C-P_F, 130x91C-PF_F and 150x105C-PF_F specimen equilibrium paths relating P to (i) axial shortening Δ and (ii) the calculated mid-height displacements δ.

iii. The equilibrium paths P *vs.* δ_{W}^{L}, presented in Figure 4.13, show the mid-web wall bending and their positives values demonstrate concordance with distortional inward flanges motion.

iv. The equilibrium paths P *vs.* δ_{m}^{G} and P *vs.* δ_{M}^{G} only branch out of the null displacement “vertical” line at quite advanced loading stages by the fact of distortional plastic hinge formation.

4.5.2 Failure Loads

Table 4.6 provides the column (i) experimental failure loads $P_{u.Exp}$, (ii) squash loads P_y, (iii) ratios $P_{u.Exp}/P_y$ and (iv) the distortional failure mode type. The values of P_y are based on (i) areas (A) obtained from the average values of the measured cross-section dimensions described in section 4.1 and (ii) the yield stress f_y=35.0 kN/cm² for G [67] or f_y=42.6 kN/cm² for C [69] steel, the average of the tensile coupon test presented in section 4.2.

The specimens failed only in pure distortional mode and most presented just one symmetric half-wave.

Concerning to the end-bolted columns most showed inward-inward (I-I) symmetrical half-wave. Only specimens 130x130C–P_B and 200x200C–P_B displayed outward-inward (O-I) failure and only 100x70G–P_F exhibited outward-outward (O-O) failure.

Relative to the end-bolted and fixed columns five showed outward-outward (O-O) symmetrical half-wave. The specimens 100x70G–PF_F, 130x91C–PF_F, 150x105C–PF_F and 200x140C–PF_B showed inward-inward (I-I) failure. Only 100x100C–PF_F column presented two half-wave symmetric distortional failure (I-I and O-O).

Table 4.6 – Experimental column failure loads, squash loads, ratio $P_{u.Exp}/P_y$ and failure modes.

Column	$P_{u.Exp}$ (kN)	P_y (kN)	$\frac{P_{u.Exp}}{P_y}$	*Distortional Failure Mode*
100x70G–P_F	162.6	227.4	0.715	O-O
100x70C–P_F	184.2	270.4	0.681	I-I
100x100C–P_F	163.0	319.8	0.510	I-I
130x91G–P_F	161.5	293.3	0.551	I-I
130x91C–P_F	192.2	356.3	0.539	I-I
130x130C–P_B	106.5	423.7	0.251	O-I
150x105G–P_F	151.4	330.9	0.457	I-I
150x105C–P_F	160.5	391.1	0.410	I-I
150x150C–P_B	101.7	478.7	0.212	I-I
180x126C–P_F	152.6	472.0	0.323	I-I
180x180C–P_B	90.8	570.0	0.159	I-I
200x140C–P_B	121.0	506.8	0.239	I-I
200x200C–P_B	86.0	638.0	0.135	O-I
100x70C-PF_F	167.0	256.6	0.651	I-I
100x100C-PF_F	144.2	314.3	0.459	I-I and O-O
130x91C-PF_F	183.0	344.9	0.531	I-I
130x130C-PF_F	134.0	410.5	0.326	O-O
150x105C-PF_F	176.7	399.6	0.442	I-I
150x150C-PF_B	116.2	491.6	0.236	O-O
180x126C-PF_F	144.0	456.5	0.315	O-O
180x180C-PF_B	119.0	585.4	0.203	O-O
200x140C-PF_B	125.7	512.9	0.245	I-I
200x200C-PF_B	99.0	639.4	0.155	O-O

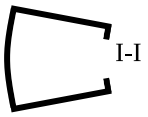

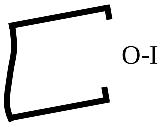

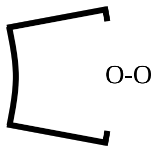

It should also be noticed that all specimens exhibit $P_{u.Exp}/P_y$ ratios varies between 0.135 and 0.715, which is in accordance with the great variation of its slenderness values.

4.5.3 Deformed configurations and failure modes

Figure 4.14 and Figure 4.15 concern specimens 180x126C-P_F and 150x105C-PF_F, respectively, provide (i) its equilibrium path P *vs.* Δ and (ii) the evolution of its deformed configuration during the test (*i.e.*, as the applied load increases) – the six deformed configuration shown in Figure 4.14(b) and Figure 4.15(b) correspond to the equilibrium states *I* to *VI* indicated by yellow circles on the equilibrium path depicted in Figure 4.14(a) and Figure 4.15(a) respectively. On the other hand, Figure 4.16 exhibit the deformed configurations, in the vicinity of the peak load ($P \approx P_{u.Exp}$), of specimens (i) 100x70C-P_F, 100x100C-P_F, 130x91C-P_F and 180x126C-P_F and (ii) 100x70C-PF_F, 130x91C-PF_F, 150x105C-PF_F and 180x126C-PF_F. Figure 4.17 shows the deformed shapes of two sets of four columns – (i) 100x70C-P_F, 100x100C-P_F, 130x91C-P_F and 180x126C-P_F and (ii) 100x70C-PF_F, 130x91C-PF_F, 150x105C-PF_F and 180x126C-PF_F – after the load removal and finally, Figure 4.18 depicts close views of the most deformed region of specimens 150x150C-P_F and 150x105C-PF_F just after collapse. The observation of these column deformed configurations makes it possible to conclude that:

i. As can be seen in Figure 4.14(b) and Figure 4.15(b), distortional inward deformations in a symmetric single half-wave emerges and develops in compliance with the corresponding critical buckling mode. In fact, until state *III* the specimen does not present visible deformations. However, beyond this point distortional inward displacements become visible. The failure occurs at state *V*. The state *VI* depicts the deformed configuration after the peak load in which the distortional displacements become more evident.
ii. In end-bolted experimental column tests, the collapse mechanism presented by all specimens are provoked by the formation of “plastic hinge” at the ¼, ½ or ¾-height cross-sections, as can be observed in Figure 4.17(a). On the other hand, in end-bolted and fixed specimens, the collapse mechanism presented were triggered by the formation of “plastic hinge” at the ¼-height cross-section near the holes (see Figure 4.17(b)).

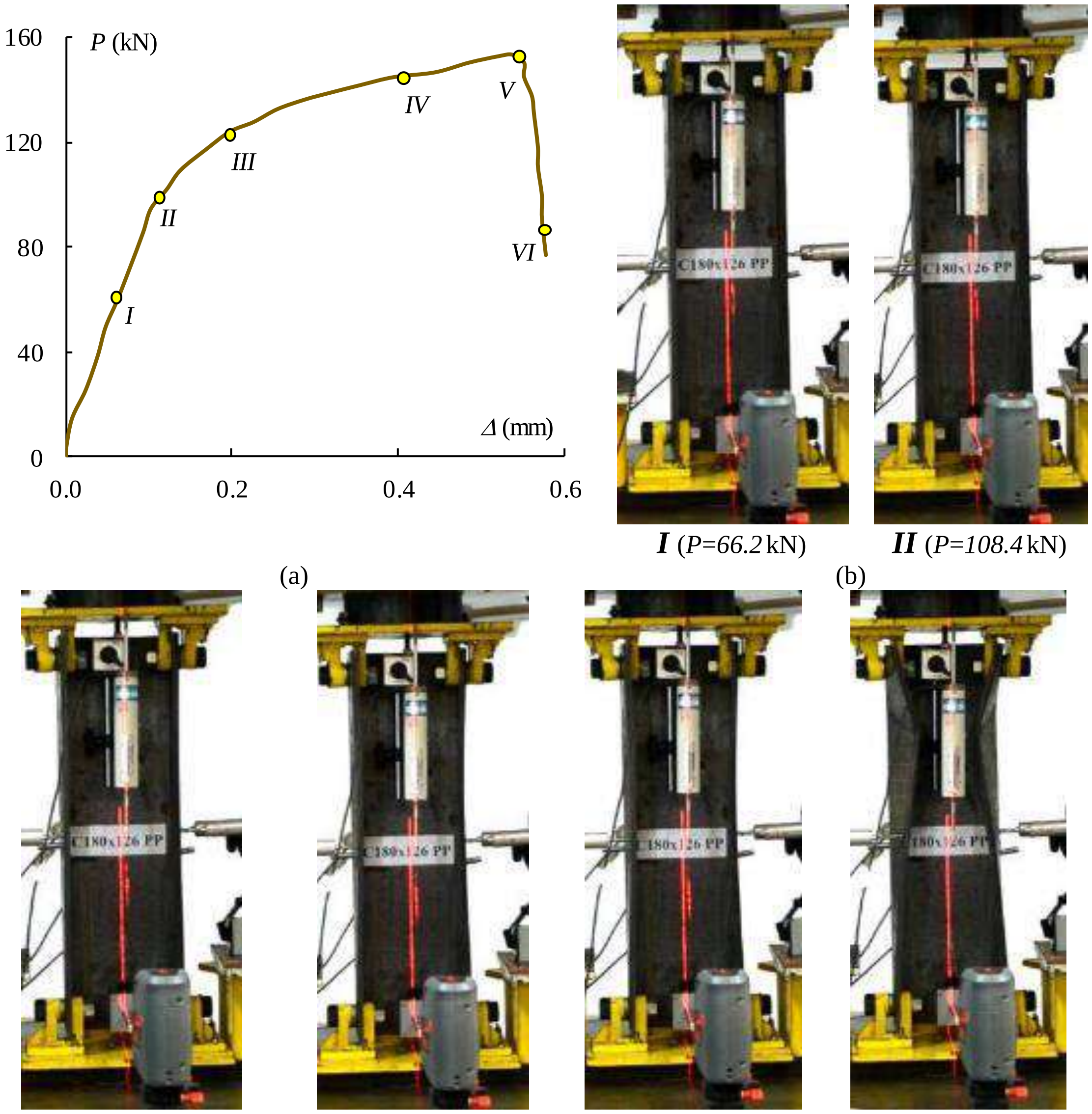

(a)

I (*P=66.2* kN) ***II*** (*P=108.4* kN)

(b)

III (*P=127.5* kN) ***IV*** (*P=147.1* kN) ***V*** (*P=152.6* kN) ***VI*** (*P=86.9* kN)

(b)

Figure 4.14 – 180x126C-P_F specimen (a) equilibrium path *P vs. Δ* and (b) deformed configuration evolution.

iii. The specimens deformed configurations depicted in Figure 4.17 make it possible to assess the amount of plastic deformation undergone by the compressed columns during the test, *e.g.*, it suffices to compare the deformed configurations displayed in Figure 4.16.

iv. The Figure 4.18(a)-(b) emphasize the deformation by distortion during the tests.

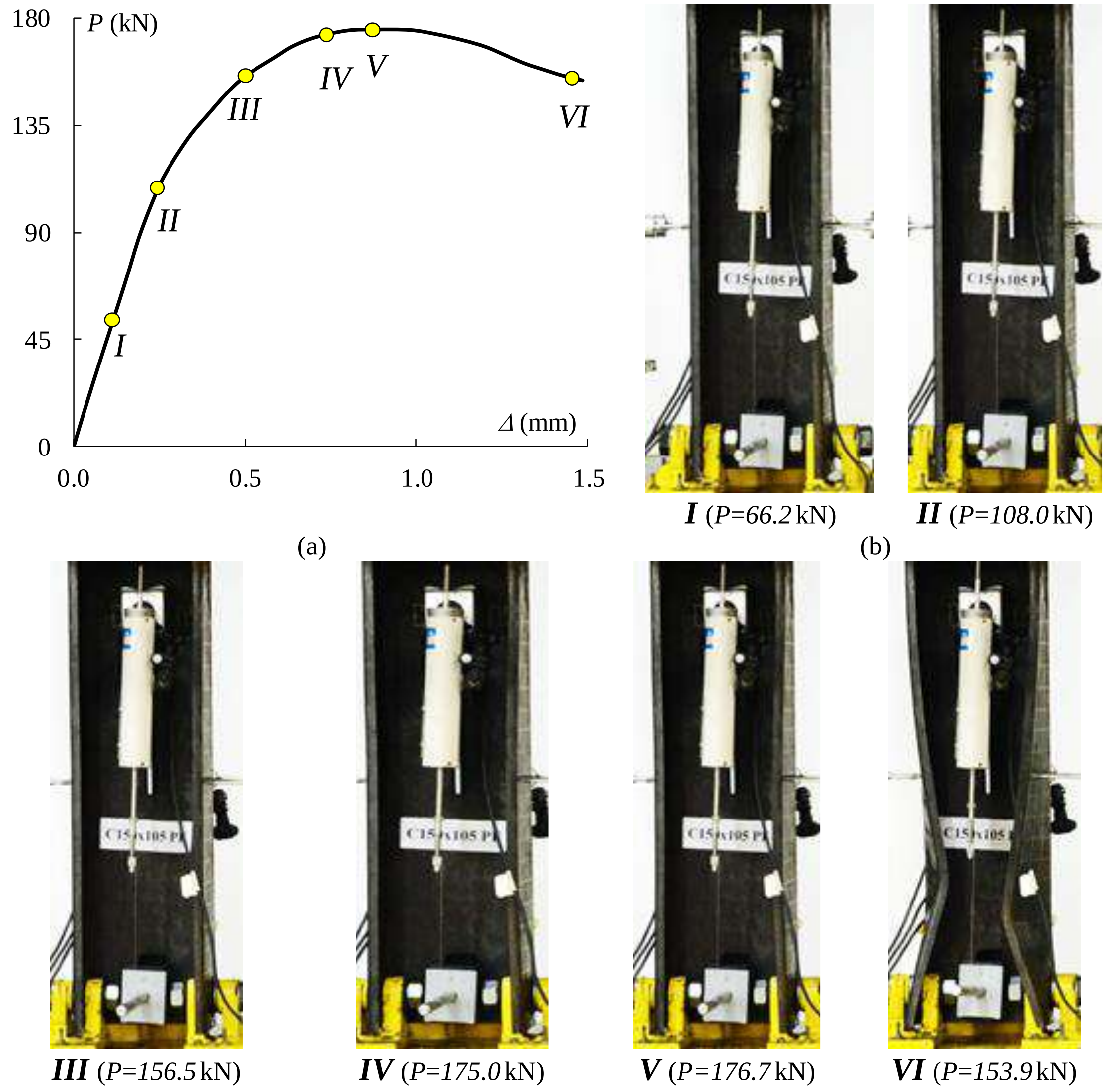

(a)

I (*P=66.2* kN) **II** (*P=108.0* kN)

(b)

III (*P=156.5* kN) **IV** (*P=175.0* kN) **V** (*P=176.7* kN) **VI** (*P=153.9* kN)

(b)

Figure 4.15 – 150x105C-*PF*$_F$ specimen (a) equilibrium path *P vs. Δ* and (b) deformed configuration evolution.

(a)

(b)

Figure 4.16 – Deformed configurations at the onset of collapse of specimens (a) 100x70C-*P_F*, 100x100C-*P_F*, 130x91C-*P_F* and 180x126C-*P_F* and (b) 100x70C-*PF_F*, 130x91C-*PF_F*, 150x105C-*PF_F* and 180x126C-*PF_F*.

(a) (b)

Figure 4.17 – Joint view of the specimens (a) 100x70C-P_F/100x100C-P_F/130x91C-P_F/180x126C-P_F and (b) 100x70C-PF_F/130x91C-PF_F/150x105C-PF_F/180x126C-P_F after the load removal.

(a) (b)

Figure 4.18 – Close view of the most deformed region of specimen (a) 150x150C-P_F and (b) 150x105C-PF_F just after collapse.

5 Numerical Investigation

This chapter presents the numerical shell finite element (SFE) methodologies for Eigen buckling, post-buckling and ultimate strength analysis as well the behavior of cold-formed steel columns under centered compression subject to distortional buckling with different boundary conditions, *i.e.*, (i) end-bolted and (ii) end-bolted and fixed.

5.1 SFE Model

The column distortional post-buckling equilibrium paths and ultimate strength values were determined through geometrically and materially non-linear SFE analysis carried out in the code ANSYS [62]. The columns were discretized into SHELL181 elements (ANSYS nomenclature – 4-nodes shear deformable thin-shell elements with six degrees of freedom per node, full integration and degeneration in triangular element).

5.1.1 Loading and End Conditions

This section describes the numerical methodology to simulate the end-bolted (P_F and P_B) and end-bolted and fixed condition (PF_F and PF_B) described in chapter 3.

For frictional loading, the compressive forces were considered nodal, dividing its magnitude by the number of existing nodes in washer area. Figure 5.1(c) shows the nodal loading in the washer area. The boundary conditions adopted were the displacement restriction in X and Y directions and the rotation around the Z-axis over the washers' areas.

For bearing loading, a pressure in contact line was considered (see Figure 5.1(d)). Studies have shown (see appendix B) that the angle of the circular sector of the contact is approximately α=97.2° (1.696 rad) and the load distribution can be considered as a gradient so that its intensity decreases from the center (greater intensity Q) to the ends (null) and that such gradient can be considered linear $q(\theta)=Q(1-2\theta/\alpha)$. Figure 5.2 shows this load distribution and the constant Q can be calculated according to integral shown in the same figure. The boundary conditions adopted were the displacement restriction in X and Y directions over the contact bolt-hole lines (see Figure 5.1(d)).

For end-bolted columns, the web center point (node) was restricted its displacement in the Z direction. On the other hand, for end-bolted and fixed columns, an end-plate (8 mm thickness) was restricted over all directions and all rotations.

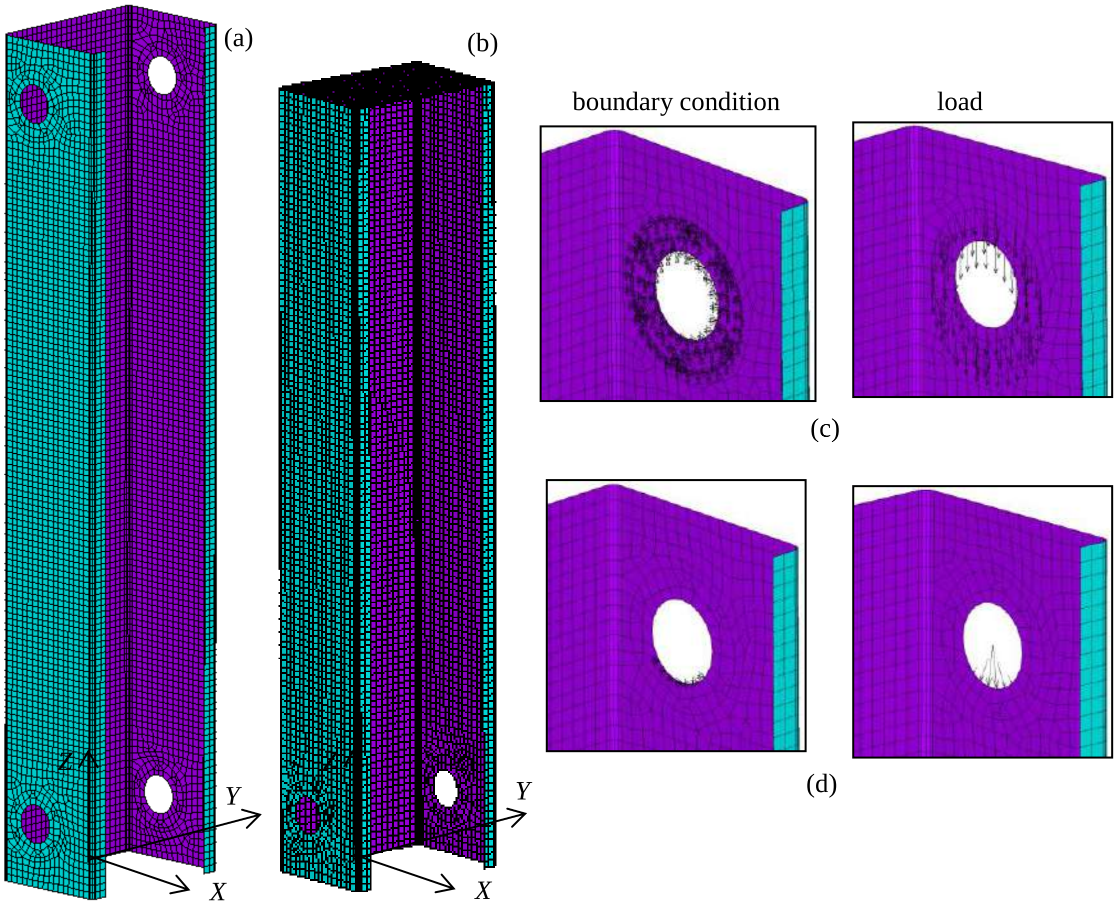

Figure 5.1 – SFE model for columns: general and mesh density for (a) end-bolted and (b) end-bolted and fixed with boundary/loading conditions for (c) frictional and (d) bearing connections.

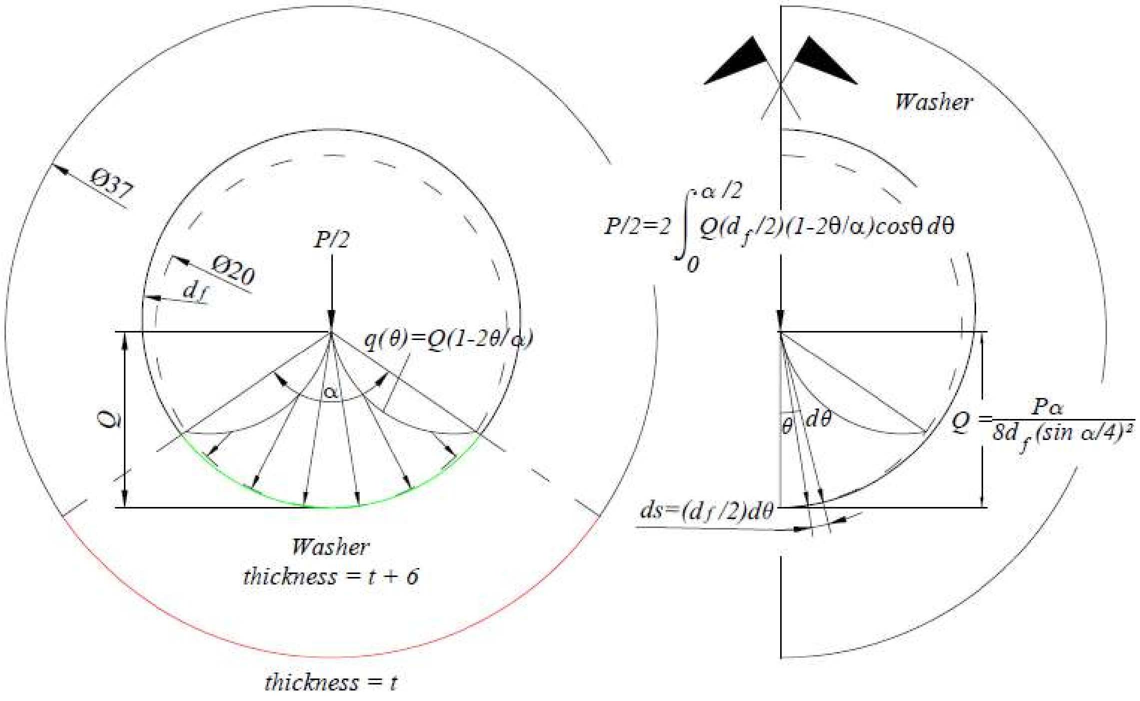

Dimensions in millimeters.

Figure 5.2 – Linear load distribution in bearing type connection.

5.1.2 Analysis

The numerical analyses were developed in two steps: (i) Eigen buckling and (ii) post-buckling analysis.

(i) Eigen Buckling Analysis

This step applies to the model the squash load (P_y), considering f_y=34.5 kN/cm² (yield stress), E=20500 kN/cm² (*Young's* modulus) and v=0.3 (*Poisson's* ratio). Then an elastic-static analysis was carried out for the creation of the stiffness matrix, followed by the eigenvalues and auto-vectors analysis, of which the main results are the qualitative deformed forms of elastic buckling and their relationship between the elastic buckling loads and the squash load, thus enabling the numerical determination of the critical buckling loads.

(ii) Post-Buckling Analysis

All post-buckling analyses were performed by means of an incremental-iterative technique combining *Newton-Raphson's* method with an *arc-length* control strategy, where axial forces are always increased in small increments, utilizing the ANSYS automatic load stepping procedure [62]. All columns exhibited an elastic-perfectly plastic material behavior (*Prandtl-Reuss's* model: *von Mises* yield criterion and associated flow rule). No strain hardening or corner effects were considered, as well as no residual stresses were included in analyses.

Two numerical methodologies of post-buckling analysis were developed in this work: (1) for validation of the experiments and (2) for parametric study, as described in the following – both considering two types of loading (frictional and bearing-type) and two types of boundary conditions ((i) end-bolted and (ii) end-bolted and fixed).

(ii$_1$) Numerical methodology for experiments validation

The materials for these analyses are characterized by E=20500 kN/cm² and yield stresses f_y=35 kN/cm² for galvanized steel G [67] or E=21000 kN/cm² and yield stresses f_y=42.6 kN/cm² for carbon steel C [69] (mechanics proprieties reported in 4.2), v=0.3 for both types of steel was assumed.

Figure 5.3 shows the localizations on the middle-line of key-points used to form the sections numbered from 1 up to 25, the coordinate system adopted and “DT's” used with its localizations also displayed in Figure 4.8. The incorporation of the initial geometric imperfection was based on the collected measurements described in item 4.3 as follows: (i) for each reading performed by the seven DTs a sixth degree polynomial was regressed which abscissa was the measured length (DT8) normalized by its measured length L_0 (see Figure 4.1), then (ii) the length L_0 was divided into 20 equal parts and in each section the key-points were positioned according to the respective undeformed position corrected by polynomials that influence the “movements” of the same. For instance, the positions of key-points from 1 up to 7 are influenced by DT1 reading in Y direction and by DT3 in X direction, the positions of key-points from 8 up to 12 are influenced by DT2 reading in Y direction and by DT3 in X direction, the position of key-point 13 is influenced only by DT4 in X direction and so on. Note that for the creation of imperfect geometry, the corrections of the positions of key-points must take into account the DTs reading sign conventions and the coordinate system that have the same sign just for DT6 and DT7.

The seven-initial approximation longitudinal functions were then used to obtain the column “initially imperfect configuration” and incorporate it in the SFE geometry.

In order to illustrate the quality of the output of this procedure, Figure 5.4 compares the measured 180x126C-P_F and 180x126C-PF_F columns (DT1 up to DT7) shown as diamond shaped markers with their approximations obtained by means of polynomial regression functions. It is clear that there is an excellent correlation.

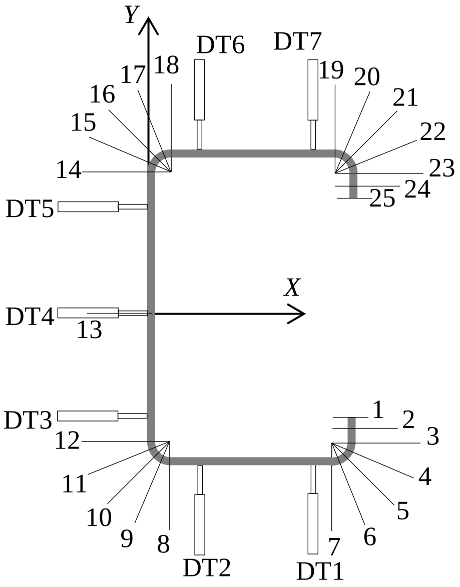

Figure 5.3 – Key-points localizations on cross-sections to form the 3D numerical model.

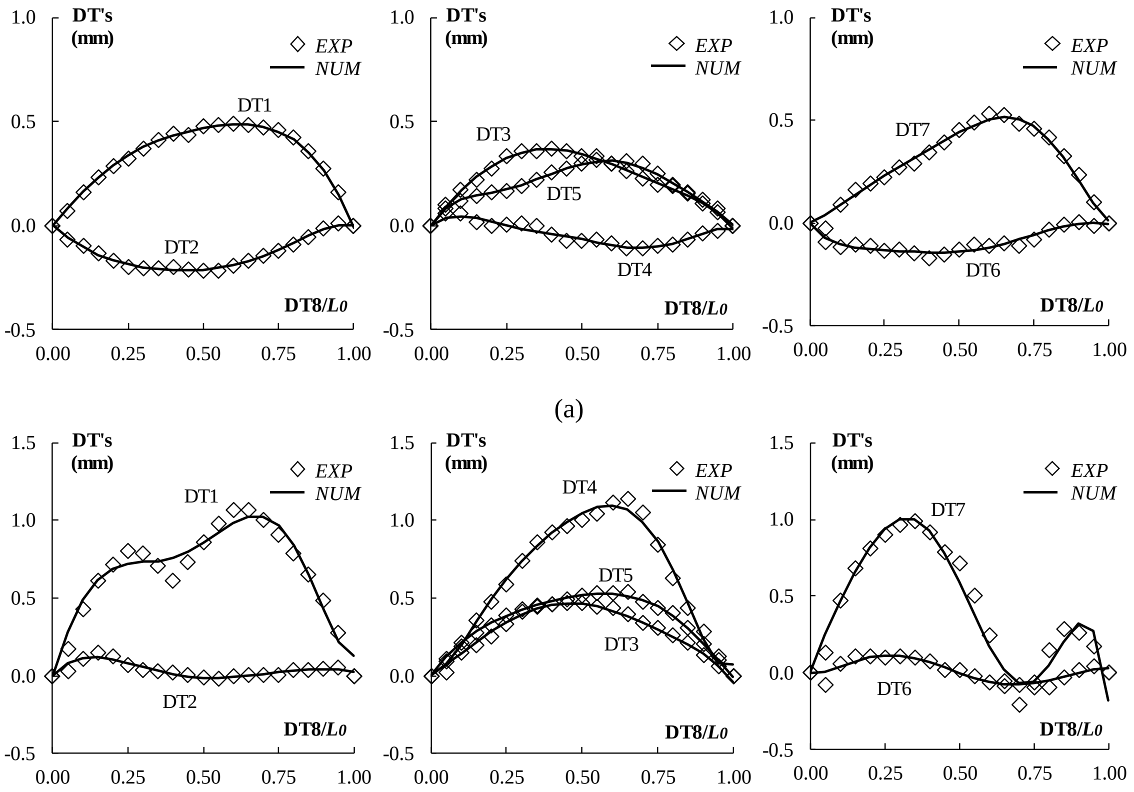

(a)

(b)

Figure 5.4 – Comparison between the measured and approximated column DTs displacement concerning to (a) 180x126C-P_F and (b) 180x126C-PF_F specimens.

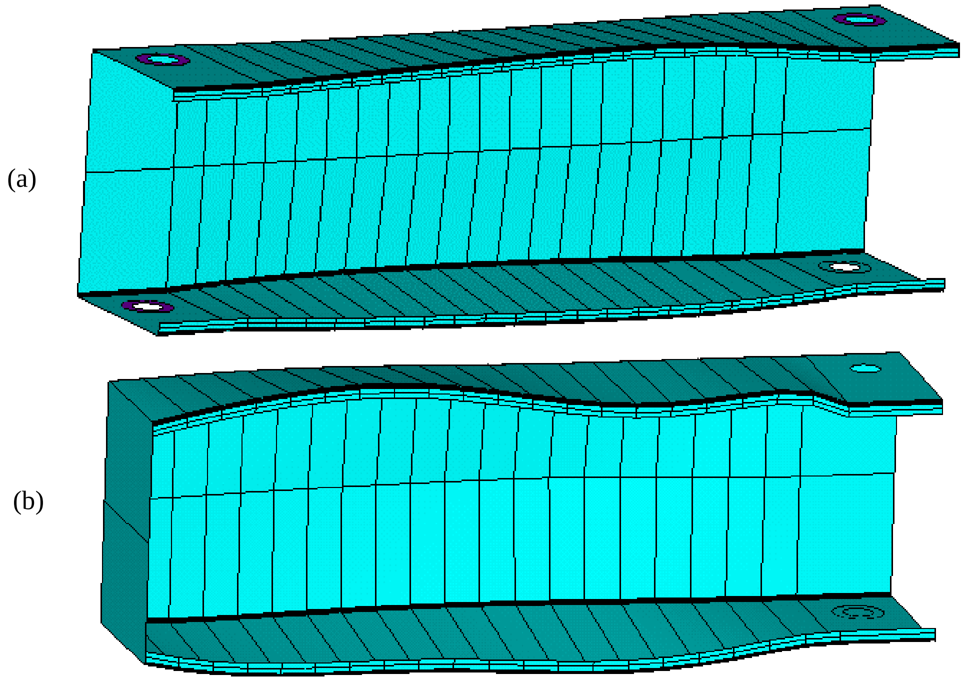

Figure 5.5 - Geometry of (a) 180x126C-P_F and (b) 180x126C-PF_F columns considering reading initial imperfections scaled by a factor of 20.

Figure 5.5 illustrate the geometry of numerical model of 180x126C-P_F and 180x126C-PF_F columns, where the DT1-7 readings were scaled by a factor of 20 to facilitate visualization of initial imperfections. In this figure is possible to see that these imperfections are in accordance to the graphic in Figure 5.4.

(ii₂) Numerical methodology for parametric post-buckling analysis

In this analysis, it was considered that E=20500 kN/cm² (*Young's* modulus) and ν=0.3 (*Poisson's* coefficient). For each column presented in Table 3.1 fourteen different steel grades (f_y) were incorporated into the numerical models considering (i) end-bolted and end-bolted and fixed end conditions and (ii) frictional and bearing-type loading.

The imposition of the critical-mode initial equivalent geometrical imperfections in the columns was made automatically by means of the following procedure: (i) determination of the critical buckling mode shape, through an ANSYS shell finite element Eigen buckling analysis, that adopted exactly the same discretization/mesh employed to carry out the subsequent post-buckling analysis, which was then (ii) scaled to exhibit maximum "vertical" displacements along the longitudinal flange stiffener edges equal to (i) $0.10 \cdot t$, (ii) $1.00 \cdot t$ (see Eq. (2.11)) and (iii) $0.19 \cdot t$ (end-bolted and fixed columns) and $0.23 \cdot t$ (end-bolted columns) – these amplitudes were selected according to LANDESMANN and CAMOTIM [31], the recommendation of SCHAFER and PEKÖZ [34] – Eq. (2.11) and average readings in the test specimens described in item 4.3, respectively. This output of the Eigen buckling analysis was then "transformed" into an input of the non-linear one.

The post-buckling analysis is subdivided into (i) elastic and (ii) elastic-plastic with the ultimate strength.

The elastic post-buckling analysis aims to determine the post-buckling behavior for elastic material, of which the main result is the elastic equilibrium path. Analyzing the elastic equilibrium trajectories for columns with (i) end-bolted and (ii) end-bolted and fixed end conditions is possible to determine the buckling mode (if distortional or not). Additionally, the equilibrium trajectory accounts for which initial geometric imperfection, if inward or outward flanges "motions", results in lower equilibrium path.

In elastic-plastic post-buckling analysis a perfect elastic-plastic material for steel is implemented to the model being used plasticizing criterion of *von Mises* [3]. Also in this step applies to model a compressive force equal to the squash load (P_y). The main outcome of the elastic-plastic post-buckling analysis, beyond the equilibrium path is the ultimate strength, which is defined as the greatest force reached in the elastic-plastic trajectory of the equilibrium.

5.1.3 Mesh

Four maximum element dimensions were tested to form the mesh. The meshes were M1 with 21.2 mm maximum element size, M2 with 10.6 mm, M3 with 5.3 mm and M4 with 2.65 mm.

In the middle lines of bending was considered a magnitude of radius equal to the wall thickness. In this region was considered four elements to compose such curvature and in straight section of the edge stiffener were considered at least two elements. In Figure 5.6 is illustrated the elements highlighting fold line and in the lip elements:

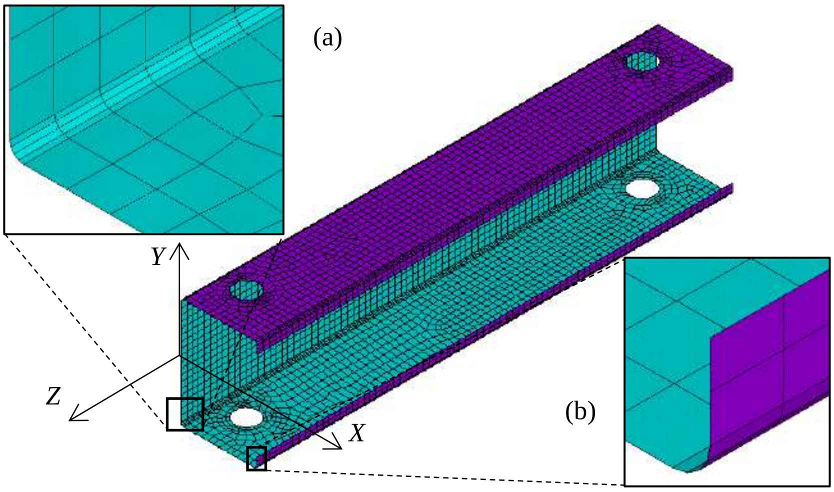

Figure 5.6 – Mesh, (a) elements in the fold line and (b) in the edge stiffener.

In the following example, the meshes (M1-4) were performed in 100x100-P_F column, in this test it was used an elastic-plastic steel whose yield stress is f_y = 34.5 kN/cm², E = 20500 kN/cm² (*Young's* modulus) and ν = 0.3 (*Poisson's* ratio). In Figure 5.7 are represented these four meshes.

Figure 5.8 illustrates the equilibrium path in tested meshes for 100x100-P_F column, in this graph the ordinate axis is given by the applied force P (kN) and in the abscises axis is given by maximum displacement δ (cm) in the middle of the span on the Y direction. Analyzing Figure 5.8 is noticed that the equilibrium trajectories for the M1 and M2 meshes are slightly above of others, since the M3 mesh equilibrium path is very close to the M4 with the exception that the equilibrium path mesh M3 “progresses” more, in other words, with less difficulty regarding numerical convergence.

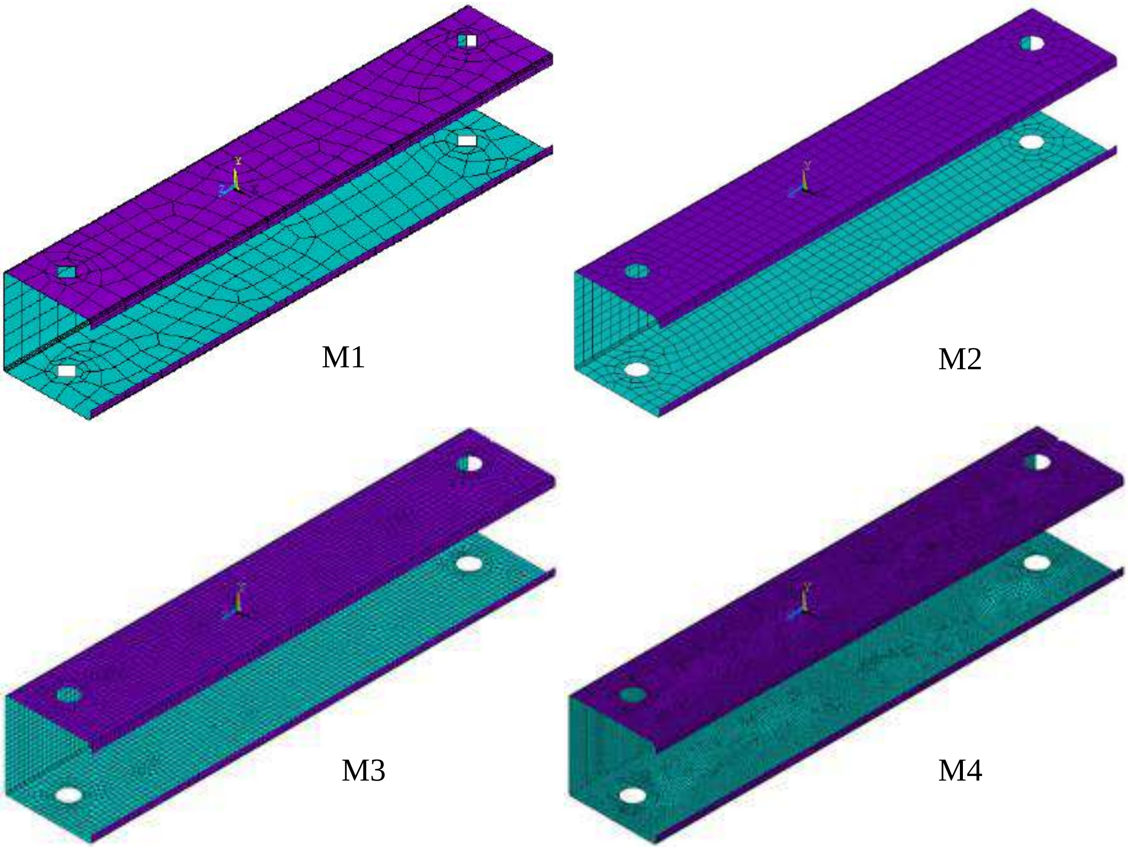

Figure 5.7 – Finite element meshes M1, M2, M3 and M4 in 100x100-P_F column.

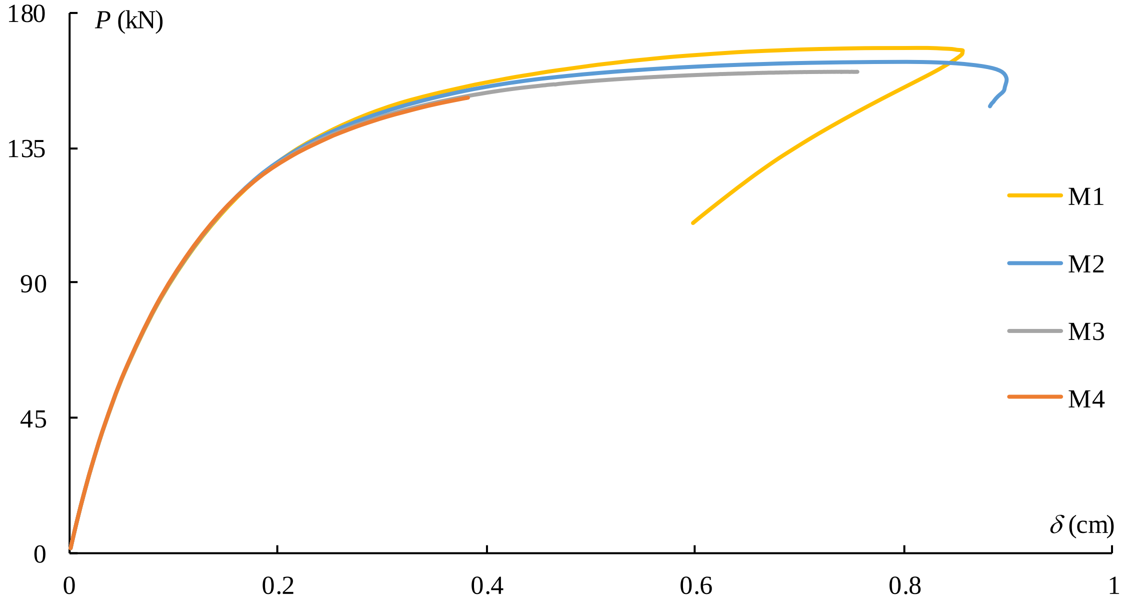

Figure 5.8 – Elastic-plastic equilibrium path P vs. δ in tested meshes for 100x100-P_F column with initial imperfections $0.1 \cdot t$ inward[4].

---

[4] The “direction” (inward or outward) of the initial imperfection will be described in item 5.3.1.

Table 5.1 shows the results of tested meshes where the critical and ultimate load were obtained from Eigen buckling and elastic-plastic post-buckling analyses.

Table 5.1 - Critical and ultimate load to tested mesh in 100x100-P_F column

Mesh	M1	M2	M3	M4
Critical load	$0.786 \cdot P_y$	$0.779 \cdot P_y$	$0.779 \cdot P_y$	$0.778 \cdot P_y$
Ultimate load	$0.602 \cdot P_y$	$0.586 \cdot P_y$	$0.573 \cdot P_y$	$0.542 \cdot P_y$

The relative difference of the critical load of buckling of M1 mesh to M4 mesh is 1.03% and the relative difference between the M2 or M3 mesh to M4 mesh is 0.13%.

The relative difference of the ultimate load of the M1 mesh to the M4 mesh is 11.7%, the relative difference of the mesh M2 to the mesh M4 is 8.12% and the relative difference of the mesh M3 to the mesh M4 is 5.72%, noting that for the M4 mesh there was numerical convergence difficulty and the solution was interrupted prematurely.

Considering the results of tested meshes, the discretization finite element chosen for the acquisition of the results was the mesh M3 with maximum elements of size of 5.3 mm agreeing with LANDESMANN and CAMOTIM [31] which maximum size considered was 5 mm.

5.2 Validation Study

In this section, the numerical ANSYS SFE validation study is presented. This study compares experimental results reported in section 4.5 with the corresponding values provided by the column geometrically and materially non-linear analyses, which procedures was described in section 5.1.

Table 5.2 provides for the specimens (i) their experimental failure loads (already presented in Table 4.6), (ii) the column numerical failure loads and (iii) its relative differences with regards to the experimental ones.

Assuming that the columns considered in this validation study had presented similar structural responses, four representative cases were selected for the presentation of individual results and subsequent discussions. Figure 5.9 and Figure 5.10 compare the numerical and experimental (i) equilibrium paths (P *vs.* Δ, δ_{12}^{D}, δ_{76}^{D} and δ_{W}^{L}) and (ii) failure modes (deformed shapes at the onset of collapse) for 130x91G-P_F, 180x180C-P_B, 130x91C-PF_F and 150x105C-PF_F columns. The following observations were made from these comparisons:

Table 5.2 - Experimentally tested columns with their (i) experimental and (ii) numerical failure loads and (iii) percentage difference between them.

Column	$P_{u.Exp}$ (kN)	$P_{u.Num}$ (kN)	$\frac{P_{u.Exp}-P_{u.Num}}{P_{u.Exp}}$
100x70G–P_F	162.6	167.8	-3.20%
100x70C–P_F	184.2	193.5	-5.05%
100x100C–P_F	163.0	174.1	-6.81%
130x91G–P_F	161.5	162.8	-0.82%
130x91C–P_F	192.2	187.4	2.49%
130x130C–P_B	106.5	106.8	-0.27%
150x105G–P_F	151.4	155.3	-2.59%
150x105C–P_F	160.5	171.5	-6.85%
150x150C–P_B	101.7	111.7	-9.87%
180x126C–P_F	152.6	159.7	-4.66%
180x180C–P_B	90.8	96.1	-5.84%
200x140C–P_B	121.0	112.5	7.04%
200x200C–P_B	86.0	85.6	0.52%
100x70C-PF_F	167.0	175.9	-5.35%
100x100C-PF_F	144.2	160.5	-11.29%
130x91C-PF_F	183.0	190.5	-4.10%
130x130C-PF_F	134.0	144.0	-7.46%
150x105C-PF_F	176.7	186.1	-5.31%
150x150C-PF_B	116.2	118.3	-1.83%
180x126C-PF_F	144.0	163.0	-13.21%
180x180C-PF_B	119.0	114.8	3.53%
200x140C-PF_B	125.7	128.1	-1.88%
200x200C-PF_B	99.0	102.2	-3.19%

i. First it is noted that the maximum absolute relative difference between the experimental and numerical peak load is 13.21% and most of these values are less than 7.5%.

ii. The numerical and experimental post-buckling equilibrium paths are close to each other and showed a similar behavior. However, it should be noted that the ductility was considerably higher in the experiments. Those differences concern mainly the equilibrium path shapes and stem, essentially, from the fact that (ii$_1$) the experimental displacement control provided by the UTM was not fine enough to enable capturing adequately the ductility prior to failure obtained in the numerical simulations, and (ii$_2$) the displacement transducer tips “slip” during a test, due to the mid-height cross-section rigid-body motion, which means that the measured displacements do not concern exactly the same points throughout a given test.

iii. With respect to the failure mechanisms, the numerical models are able to reflect accurately the distortional failure mode, in these four cases, one symmetrical inward half-wave.

iv. Based on the above facts it is possible to conclude that the SFE models can represent with good accuracy the geometrically and materially nonlinear post-buckling behavior and ultimate strength.

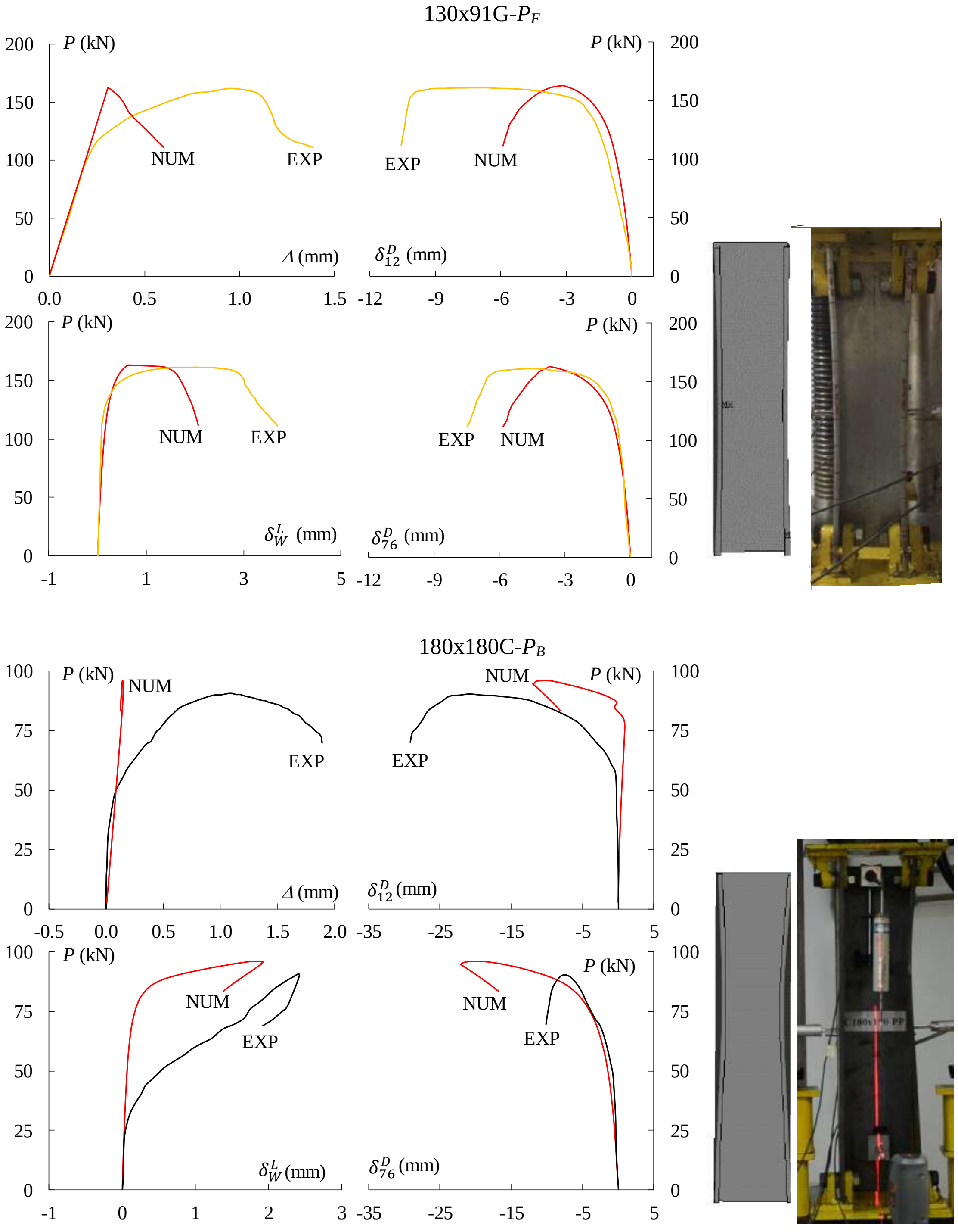

(a) (b)

Figure 5.9 – (a) Experimental and numerical equilibrium paths relating P vs. Δ and δs, and (b) numerical and experimental collapse mechanisms for 130x91G-P_F and 180x180C-P_B columns.

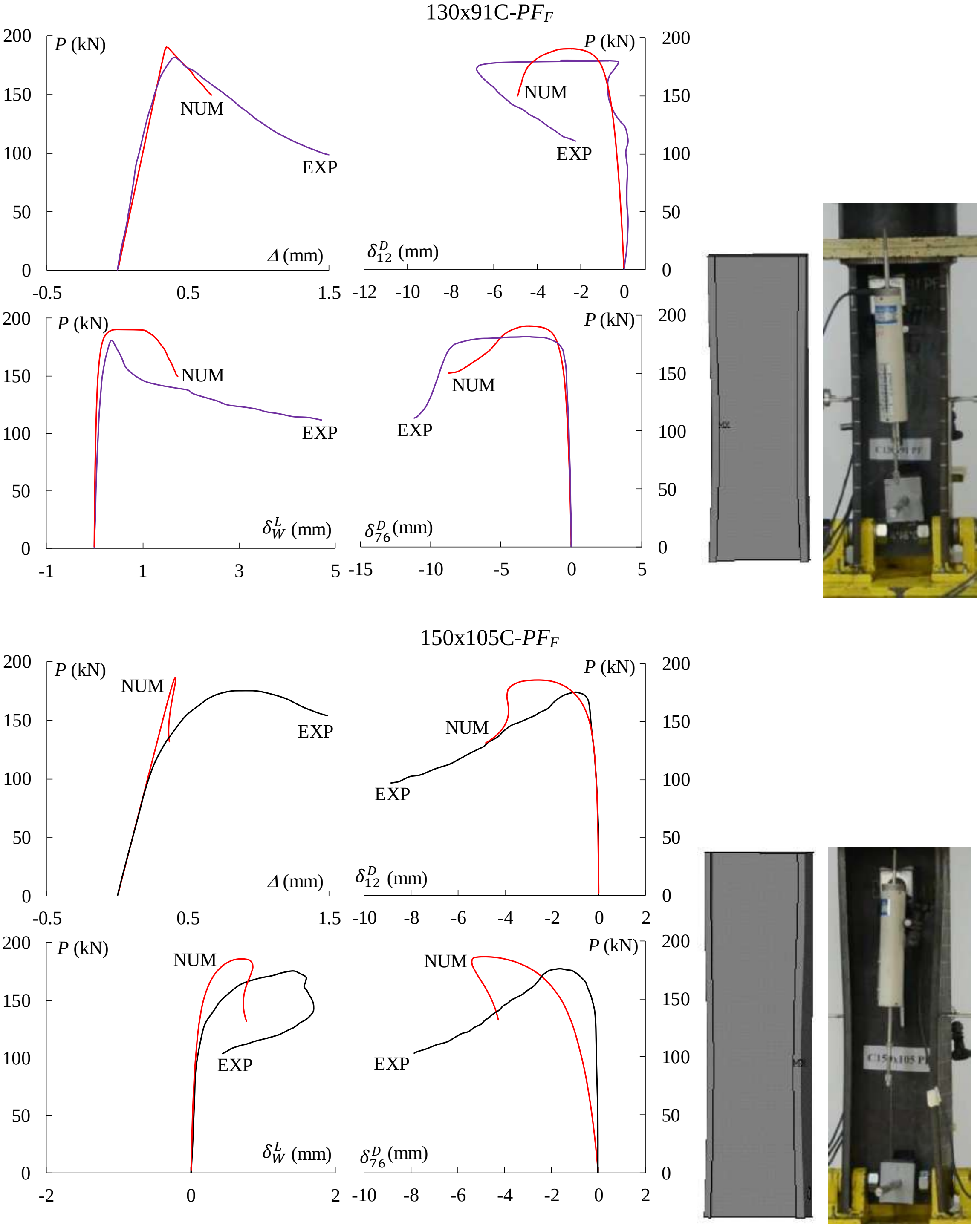

(a)

(b)

Figure 5.10 – (a) Experimental and numerical equilibrium paths relating *P vs.* *Δ* and *δ*s, and (b) numerical and experimental collapse mechanisms for 130x91C-*PF*$_F$ and 150x105C-*PF*$_F$ column.

5.3 Numerical Results

From the previously validated methodologies, the following sections describe results of the parametric study, involving the sections presented in Table 3.1. The results presented here are (i) elastic post-buckling analysis to determine the lower equilibrium path considering the “direction” to the initial deformation according to critical distortional mode (inward or outward flanges “motion”), (ii) elastic-plastic post-buckling analysis, collapse mechanism and comparison between models with (ii_1) end-bolted and (ii_2) end-bolted and fixed ends considering loading by friction and contact and finally (iii) ultimate strength data.

5.3.1 Elastic Post-Buckling Analysis

In order to illustrate the elastic post-buckling equilibrium paths obtained and address the qualitative and quantitative assessment of how the column elastic distortional post-buckling behavior is influenced by the end support conditions, Figure 5.11 shows the post-buckling equilibrium paths of the 200x200 columns exhibiting the four boundary conditions dealt with in this work. These equilibrium paths plot the applied load *P* against the maximum absolute displacement $|\delta|$ occurring along the flange–stiffener longitudinal edges. In these examples, the maximum amplitude of critical buckling form as initial geometric imperfections was considered as 0.1*t*. The observation of these four sets of two distortional elastic post-buckling equilibrium paths prompts the following remark:

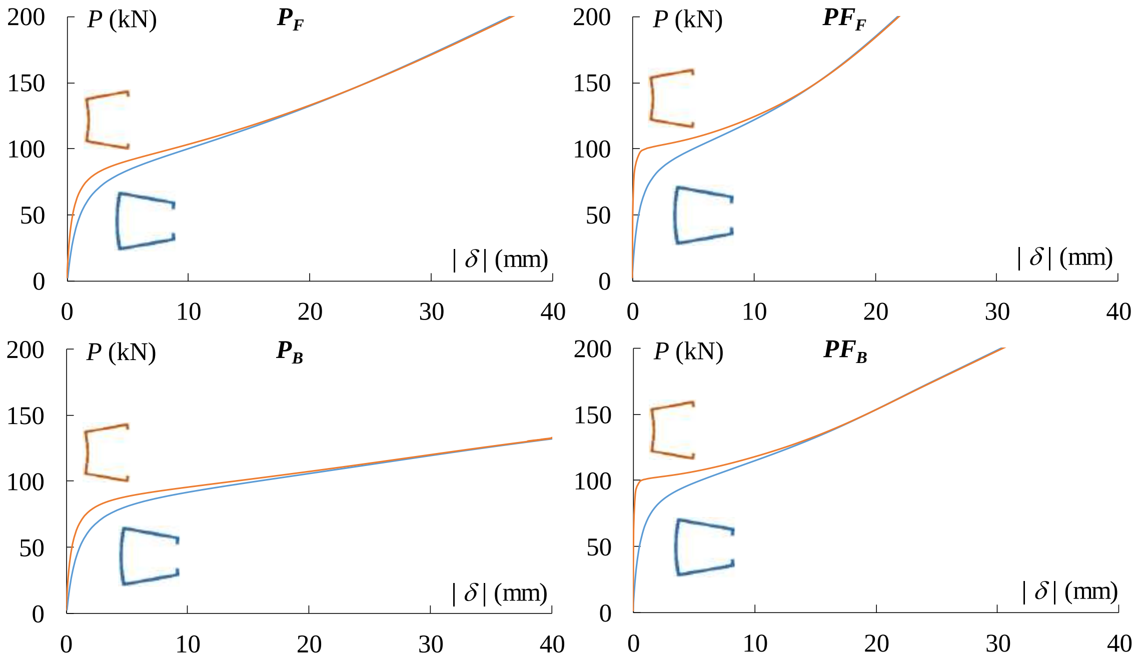

Figure 5.11 – Elastic equilibrium path *P vs.* $|\delta|$ to 200x200 columns under (i) end-bolted and (ii) end-bolted and fixed end conditions, frictional and bearing load type with initial distortional outward and inward deflections.

i. The post-buckling strength increases as one travels along the column end support condition sequence *P* to *PF* agreeing with LANDESMANN and CAMOTIM [31].

ii. The same can be said to the loading sequence bearing-type to frictional-type.

iii. The lower equilibrium path is the inward initial distortional imperfection.

5.3.2 Elastic-plastic Post-Buckling Analysis and Ultimate Strength

Attention is now devoted to the qualitative and quantitative influence of the end support and bolt load-type conditions on the column elastic-plastic distortional post-buckling and ultimate strength behavior. In this section, the columns with different geometries (dimensions and lengths) presented in Table 3.1 are discussed considering (i) the material mechanics propriety f_y=34.5 kN/cm² (yield strength), E=20500 kN/cm² (*Young's* modulus) and v=0.3 (*Poisson's* ratio) and (ii) the initial imperfection as critical distortional inward buckling with maximum amplitude of 0.1t.

Table 5.3 shows for each boundary condition (i) the critical (distortional) buckling loads $P_{cr.D}$ (already presented in Table 3.2), (ii) the distortional relative slenderness ratio and (iii) the relationship between the ultimate load P_u (obtained from ANSYS second-order elastic-plastic shell finite element analysis) with the critical buckling load (which provides an estimation of the post-critical reserve) together with the corresponding mean values and standard deviations.

Table 5.3 - Distortional critical loads, distortional slenderness and ultimate load ratios for P_F, PF_F, P_B and PF_B columns

Column	(P_F)			(PF_F)			(P_B)			(PF_B)		
	$P_{cr.D}$ (kN)	$\bar{\lambda}_D$	$\frac{P_u}{P_{cr.D}}$	$P_{cr.D}$ (kN)	$\bar{\lambda}_D$	$\frac{P_u}{P_{cr.D}}$	$P_{cr.D}$ (kN)	$\bar{\lambda}_D$	$\frac{P_u}{P_{cr.D}}$	$P_{cr.D}$ (kN)	$\bar{\lambda}_D$	$\frac{P_u}{P_{cr.D}}$
100x70	321.4	0.84	0.51	330.7	0.82	0.49	322.9	0.83	0.52	349.4	0.80	0.48
100x100	217.8	1.13	0.74	236.5	1.09	0.69	215.5	1.14	0.75	234.4	1.09	0.39
100x142.9	142.0	1.59	1.01	151.9	1.54	0.96	139.7	1.60	0.92	154.0	1.53	0.90
130x91	234.1	1.11	0.69	264.8	1.05	0.63	235.5	1.11	0.70	264.1	1.05	0.64
130x130	157.9	1.51	0.96	172.8	1.45	0.89	157.0	1.52	0.90	171.4	1.45	0.87
130x185.7	102.7	2.13	1.18	114.7	2.01	1.08	101.6	2.14	0.98	113.3	2.02	1.01
150x105	196.7	1.30	0.81	214.7	1.25	0.76	198.7	1.30	0.76	214.1	1.25	0.77
150x150	134.0	1.76	1.03	153.1	1.65	0.94	132.3	1.78	0.93	145.4	1.69	0.94
150x214.3	85.8	2.50	1.29	94.5	2.38	1.20	85.5	2.50	1.01	96.5	2.35	1.10
180x126	159.0	1.59	0.96	175.5	1.51	0.89	159.6	1.58	0.92	175.3	1.51	0.88
180x180	106.6	2.16	1.21	117.3	2.06	1.11	106.6	2.16	1.04	119.3	2.05	1.02
180x257.1	69.0	3.05	1.41	74.7	2.93	1.36	68.6	3.06	1.08	77.5	2.87	1.28
200x140	139.8	1.78	1.05	154.0	1.70	0.98	140.9	1.78	0.99	154.2	1.70	0.95
200x200	94.2	2.43	1.28	103.1	2.32	1.18	93.8	2.43	1.16	102.6	2.32	1.10
200x285.7	60.7	3.42	1.46	66.3	3.27	1.47	60.3	3.43	1.13	67.0	3.26	1.41
Mean			1.04			0.98			0.92			0.92
S. D.			0.27			0.27			0.17			0.27

Figure 5.12 displays, for each end support and bolt load-type condition, samples of non-linear (geometrically and materially) equilibrium paths determined to obtain the ultimate loads P_u (identified by white circles) – these equilibrium paths concern P_F, P_B, PF_F and PF_B for 100x70, 180x126 and 200x140 columns where the ordinate axis is given by the compressive force P normalized by the critical distortional buckling load $P_{cr.D}$, since the abscissa is given by maximum absolute displacement $|\delta|$ on the Y axis normalized by wall thickness t. Figure 5.13 depicts the column deformed configurations occurring in the close vicinity of the limit points of each equilibrium path displayed in Figure 5.12, also in this figure are shown the *von Mises* equivalent stress distribution. It is worth noting that the deformed have been amplified by a factor of 2.5.

Figure 5.14 and Figure 5.15 show the elastic-plastic equilibrium path and the evolution of its deformed configuration with the *von Mises* equivalent stress distribution (*I* at the beginning of yield, *II* and *III* in evolution and *IV* at the ultimate load) for 200x140 (i) P_F and P_B and (ii) PF_F and PF_B columns, respectively. Also in these figures, the amplitudes of the deformed have been scaled by a factor of 2.5.

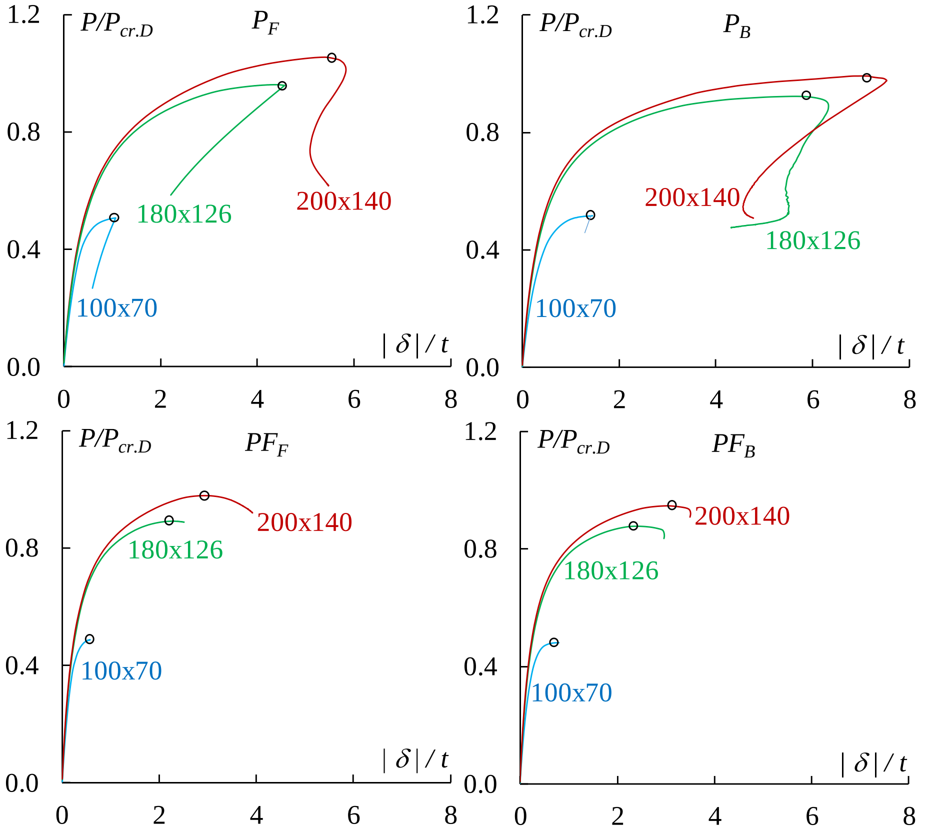

Figure 5.12 – Elastic-plastic distortional equilibrium paths (P/P_{cr} *vs.* $|\delta|/t$) concerning P_F, P_B, PF_F and PF_B for 100x70, 180x126 and 200x140 columns.

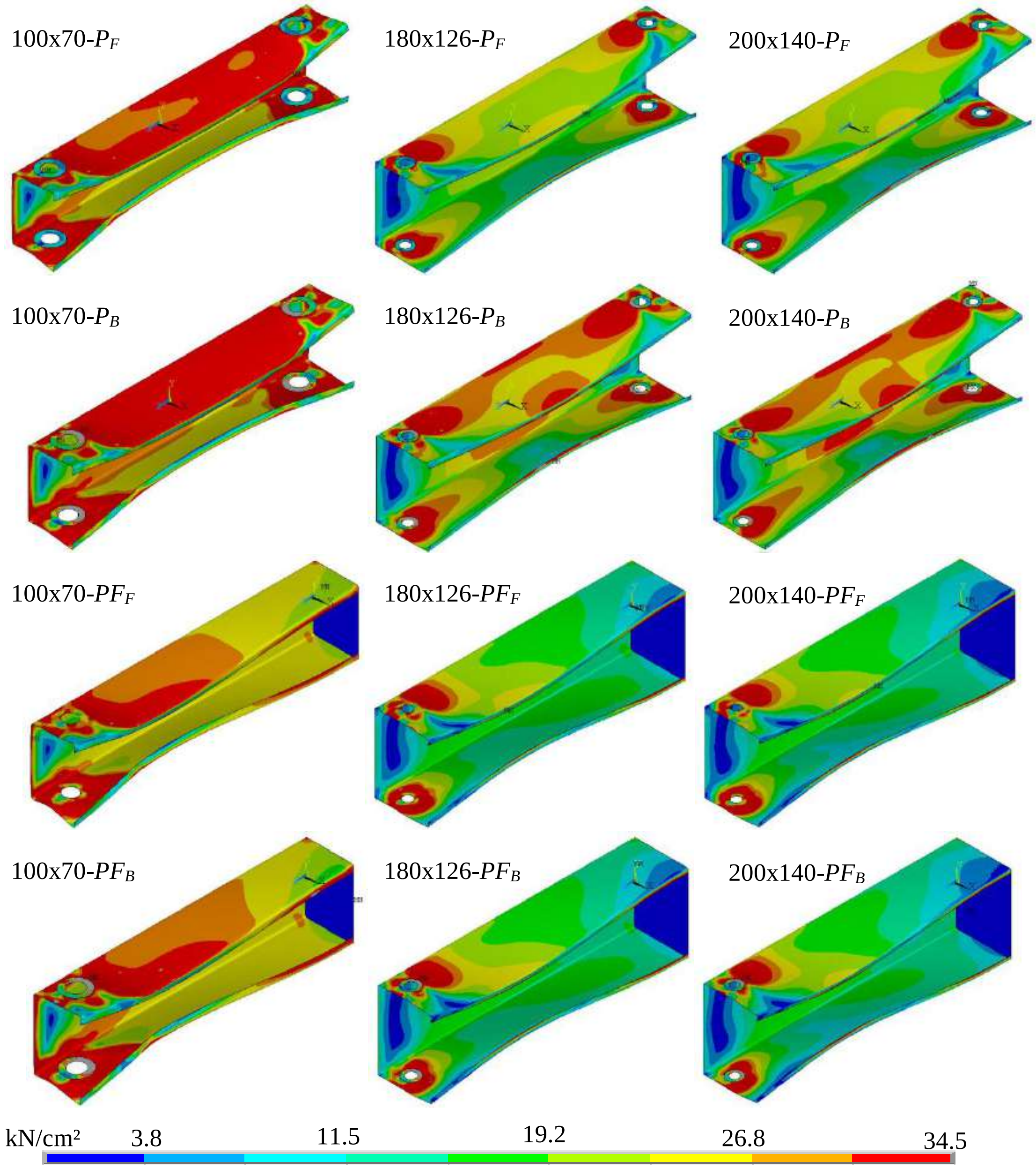

Figure 5.13 – Distortional failure modes and *von Mises* equivalent stress distribution concerning P_F, P_B, PF_F and PF_B for 100x70, 180x126 and 200x140 columns.

After observing the elastic-plastic distortional post-buckling and ultimate strength results presented in Figure 5.12 up to Figure 5.15, the following conclusions can be drawn:

i. First, it is noted that there is a slight difference between the equilibrium paths concerning the (i) P_F and P_B and (ii) PF_F and PF_B columns, respectively, which are presented in Figure 5.12 that shows that the ductility prior to failure also varies slightly between these pair of columns ((i) end-bolted and (ii) end-bolted and fixed).

ii. Figure 5.13 depicts the deformed columns settings that occurs close to the ultimate point for each equilibrium path described in Figure 5.12, these promote an accurate representation of the failure mode (distortional) displayed for 100x70/180x126/200x140-P_F, P_B, PF_F and PF_B columns. For each boundary condition, the nature of failures is exactly the same as the distortional mode shown by the Eigen buckling analysis.

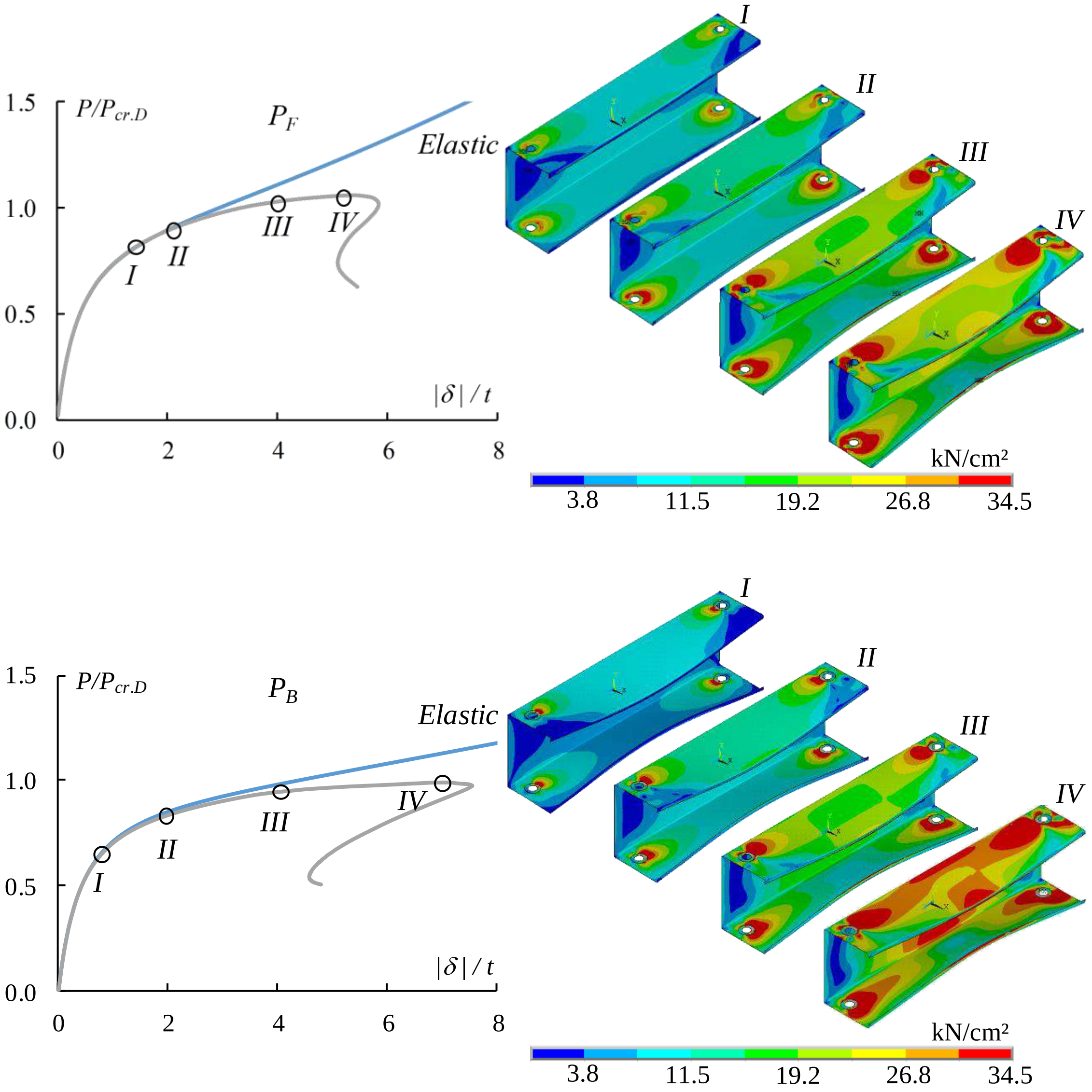

Figure 5.14 – The elastic and elastic-plastic equilibrium path with the distortional buckling collapse mechanism for 200x140 P_F and P_B columns.

iii. Figure 5.14 shows in 200x140 P_F and P_B columns the yield begins at the loading area, specifically near at holes – see stage *I*. With the loading progress, according to the columns present the distortional deformed, yield also starts at stiffeners in the center of the span – see stage *III*. Continuing charging, occurs the formation of one "distortional plastic hinge" in the middle of the column –

see stage *IV*. In addition, the 200x140 P_F column was slightly more resistant than 200x140 P_B column, however, 200x140 P_B was more ductile than 200x140 P_F.

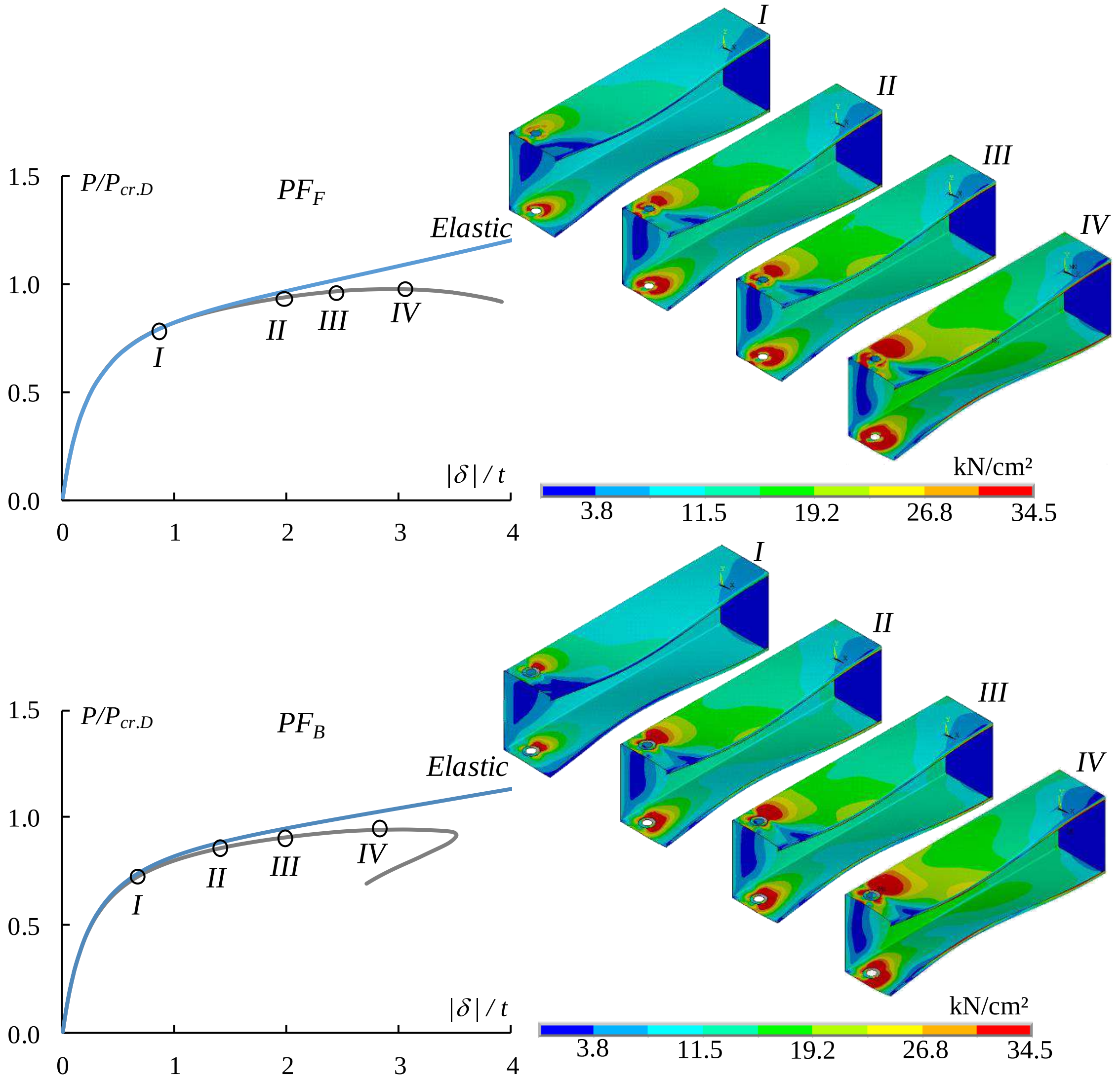

Figure 5.15 – The elastic and elastic-plastic equilibrium path with the distortional buckling collapse mechanism for 200x140 PF_F and PF_B columns.

iv. In Figure 5.15 can be seen in 200x140 PF_F and PF_B columns the yield starts at the loading region – see the stage *I*. With the progress of loading, according to the columns present the distortional deformed, also yield starts in lips about ¼-height from the region between the holes to the fixed end – see stage *III*. Continuing charging it leads to the formation of one “distortional plastic hinge” at same height as the beginning of lip yield (see stage *IV*). As well, the 200x140 PF_F column was slightly more resistant than 200x140 PF_B column.

5.3.3 Ultimate Strength Data

The aim of this section is to present and discuss the ultimate strength data gathered from the parametric study carried out. In order to achieve a more meaningful comparison, all the post-buckling results presented and discussed in this section concern columns made of a steel with their distortional slenderness $\bar{\lambda}_D=(P_y/P_{cr.D})^{0.5}$ varying from 0.4 to 3.5 – this slenderness are ensured by properly selecting "custom made" yield stresses (f_y)[5].

This parametric study, which involved a total of 2520 columns, corresponding to all possible combinations of (i) the fifteen cross-sections described in Table 3.1, (ii) four boundary conditions dealt with in this work (P_F, P_B, PF_F and PF_B), (iii) fourteen distortional slenderness and (iv) three different maximum amplitudes of distortional form as initial imperfection (see item ii$_2$ in section 5.1.2) for each column. Tables C1-20, presented in appendix C, provide the squash loads ($P_y=A{\cdot}f_y$), the associated distortional slenderness values ($\bar{\lambda}_D$) and all the numerical column ultimate loads (P_u) for each column. Those four sets of values (one for each column boundary condition-type) are also plotted in Figure 5.16 where on the vertical axis is the ultimate load P_u normalized by the squash load P_y and on the horizontal axis the relative distortional slenderness $\bar{\lambda}_D$.

Examining the type of failure of the columns plotted in Figure 5.16 it was found that in some of them, especially those that distortional slenderness is less than 1.50, occurred localized yielding in the region close to the holes (loading). In these cases, the numerical solution was interrupted by the program and the "development" of distortional buckling was not possible. The collapse of these columns was identified in the Tables C1-20 as Yield Nearby the Hole (*YNH*). In Figure 5.17 is shown the qualitatively *von Mises* equivalent stresses distribution in the 200x285.7 P_F, P_B, PF_F and PF_B columns with $\bar{\lambda}_D \approx 1.5$ in which solutions were discontinued due to localized effect for the three initial imperfections – the deformed have been amplified by a factor of 2.5.

The criterion to determine the localized failure, besides the observation of the equilibrium trajectory and the failure mode figure, was $P_u/(2A_c) \geq K{\cdot}f_y$, where A_c is contact area and K is the stress concentrator coefficient. Two contact areas were analyzed $A_{c.1}$ represented by green line in Figure 5.2 and $A_{c.2}$ represented by red line in the same figure,

---

[5] Note that some of the yield stresses considered in this work are unrealistically high, leading to E/f_y that largely exceed the current DSM limit for pre-qualified columns ($E/f_y=340$). The reason for selecting such high yield stresses was to make it possible to analyses columns with high slenderness values, thus covering a wide slenderness range [31].

thus, $A_{c.1} = d_f \cdot \alpha \cdot (t+2\cdot3.00)/2 = 21.5\cdot1.696\cdot(2.65+2\cdot3.00)/2 = 157.7$ mm² and $A_{c.2} = 37\cdot\alpha\cdot t/2 = 37\cdot1.696\cdot2.65/2 = 83.1$ mm². Considering the localized failure occurs in lower area ($A_{c.2}$) the K factor was determined approximately as 2.8.

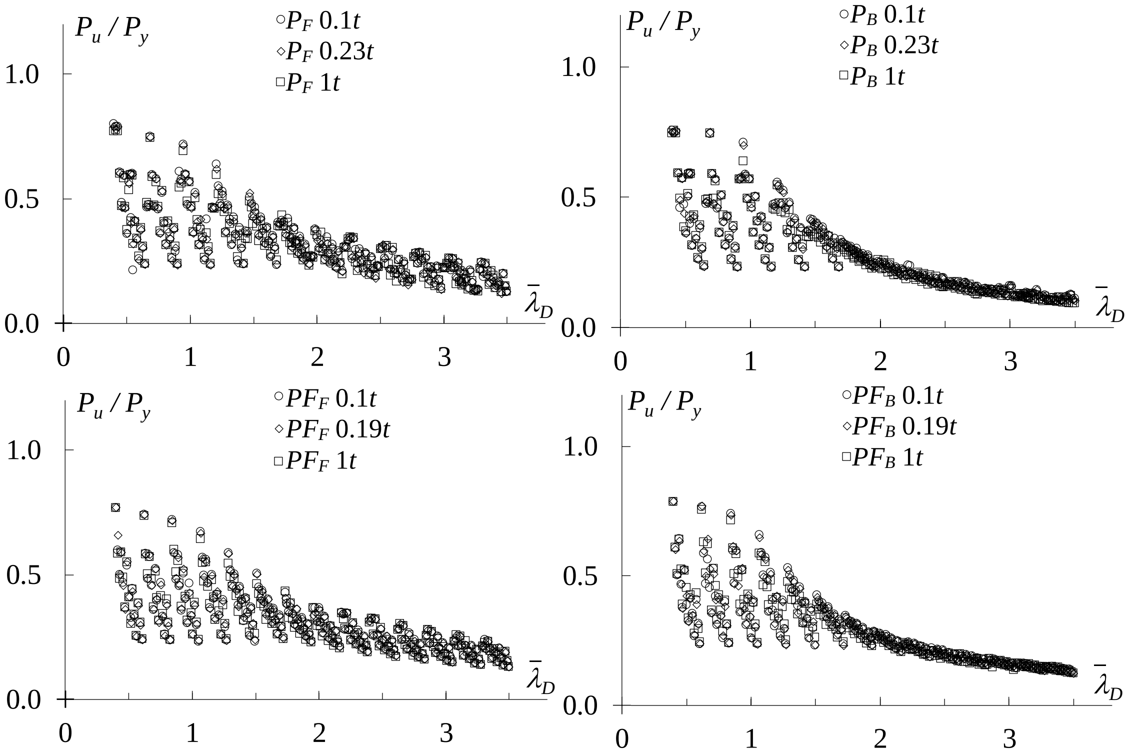

Figure 5.16 – Numerical results P_u/P_y *vs.* $\bar{\lambda}_D$ concern to P_F, P_B, PF_F and PF_B columns.

As the purpose of this work is not to evaluate the ultimate load of columns that presents localized effects such columns were excluded from the analysis. From a total of 2520 columns, 225 P_F columns, 216 P_B columns, 219 PF_F columns and others 216 PF_B columns were excluded. In sum 1644 columns were used for the numerical analysis in this research. Replacing the graphics of Figure 5.16 by Figure 5.18 disregarding the columns collapsed by localized effects, one can observe that the four P_u/P_y *vs.* $\bar{\lambda}_D$ "clouds" follow trends that can be accurately described by "*Winter*-type" design curves. Moreover, the "vertical dispersion" is smaller (acceptable) in columns with load condition is not by friction (P_B and PF_B).

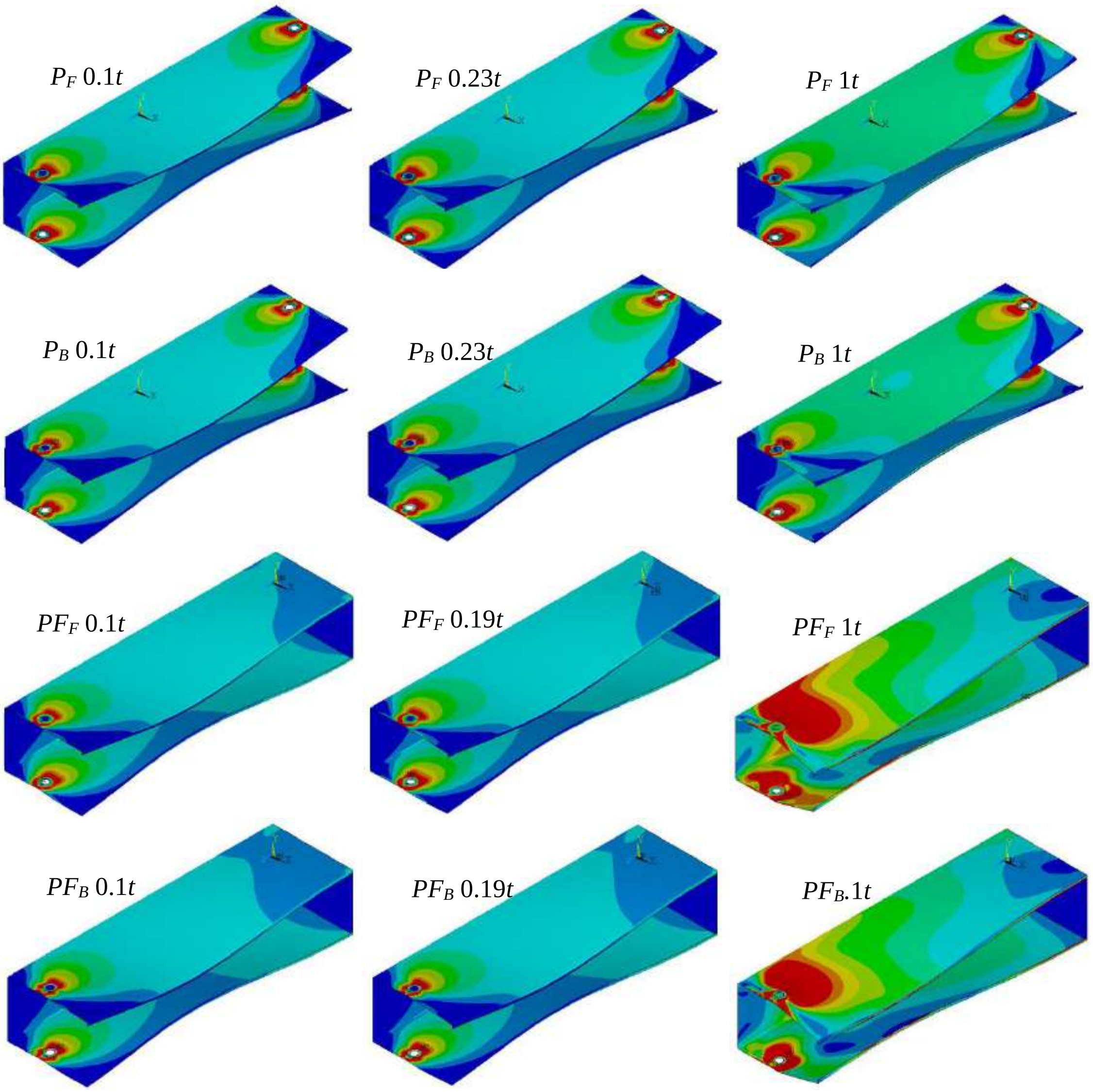

Figure 5.17 – Qualitatively distribution of equivalent *von Mises* stresses in 200x285.7 P_F, P_B, PF_F and PF_B columns with $\bar{\lambda}_D \approx 1.5$ in which solutions were discontinued.

In examining the numerical failure modes of these 1644 remaining columns were detected 267 cases of failure modes involving distortional/local interaction (108 P_F, 120 PF_F and 39 PF_B columns) – in Figure 5.18 “grey markers” identify the columns whose failure modes exhibit this interaction. Figure 5.19 shows the collapse mode and *von Mises* equivalent stress distribution in 100x70 P_F, P_B, PF_F and PF_B columns considering 0.1t inward flanges “motion” as the maximum distortional amplitude of initial imperfection. Whenever such evidence was found, the columns were identified in Tables C1–20 as exhibiting “D+L” failures. Also Figure 5.18 shows that the grey and white markers are well “blended”, which indicates that ultimate numerical loads with and without distortional/local interaction follow exactly the same trend. This interaction was considered week (agreeing with KWON and HANCOCK [18]) and these columns were included in this investigation, since they collapse in predominantly distortional modes. There was no D+L interaction in the P_B columns. The criterion to determine the D+L interaction, besides the observation of the equilibrium trajectory and the failure mode figure, was P_u reaches $P_{b1.L}$.

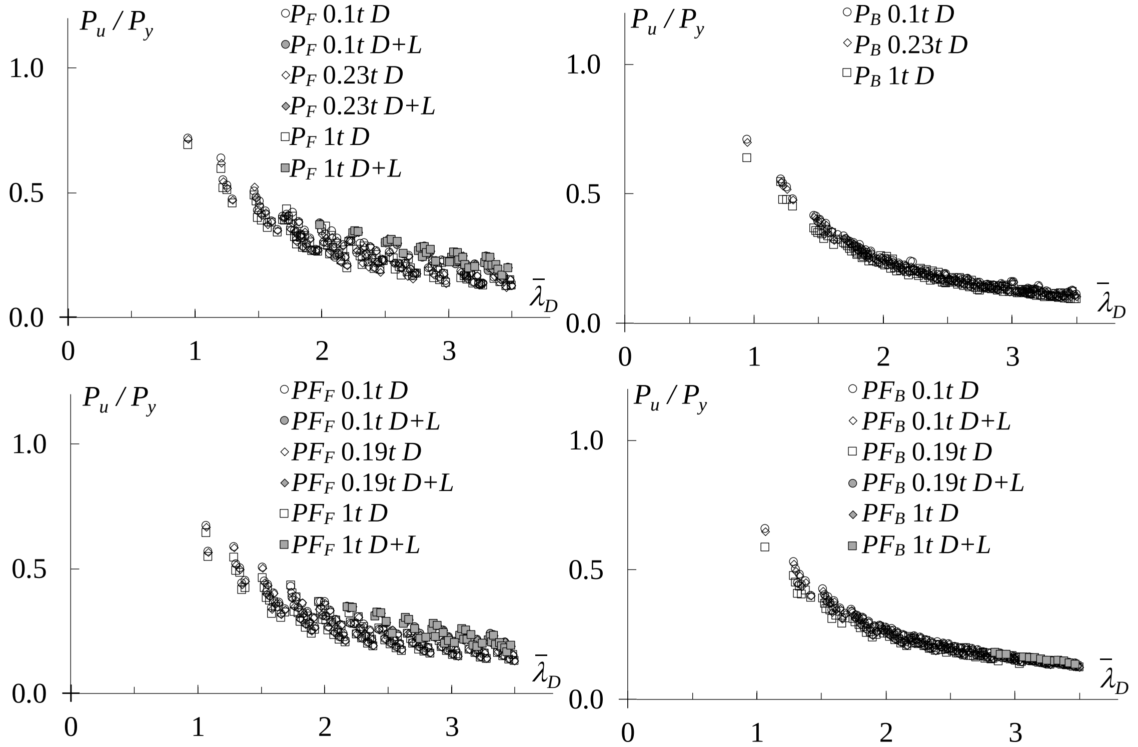

Figure 5.18 – Numerical results P_u/P_y vs. $\bar{\lambda}_D$ concern to P_F, P_B, PF_F and PF_B columns disregarding the columns collapsed by localized effects.

Analyzing the ultimate load results for each numerical solution carried out in this work (Tables C1–20) it was noted that the final strength is not very sensible to variations of the maximum amplitude of the initial imperfection (0.1t up to 1.0t) with one half-wave distortional inward shape. In fact, the maximums relative standard deviation (S. D./Mean) are 4.91%, 6.94%, 4.94% and 6.88% for P_F, P_B, PF_F and PF_B columns respectively.

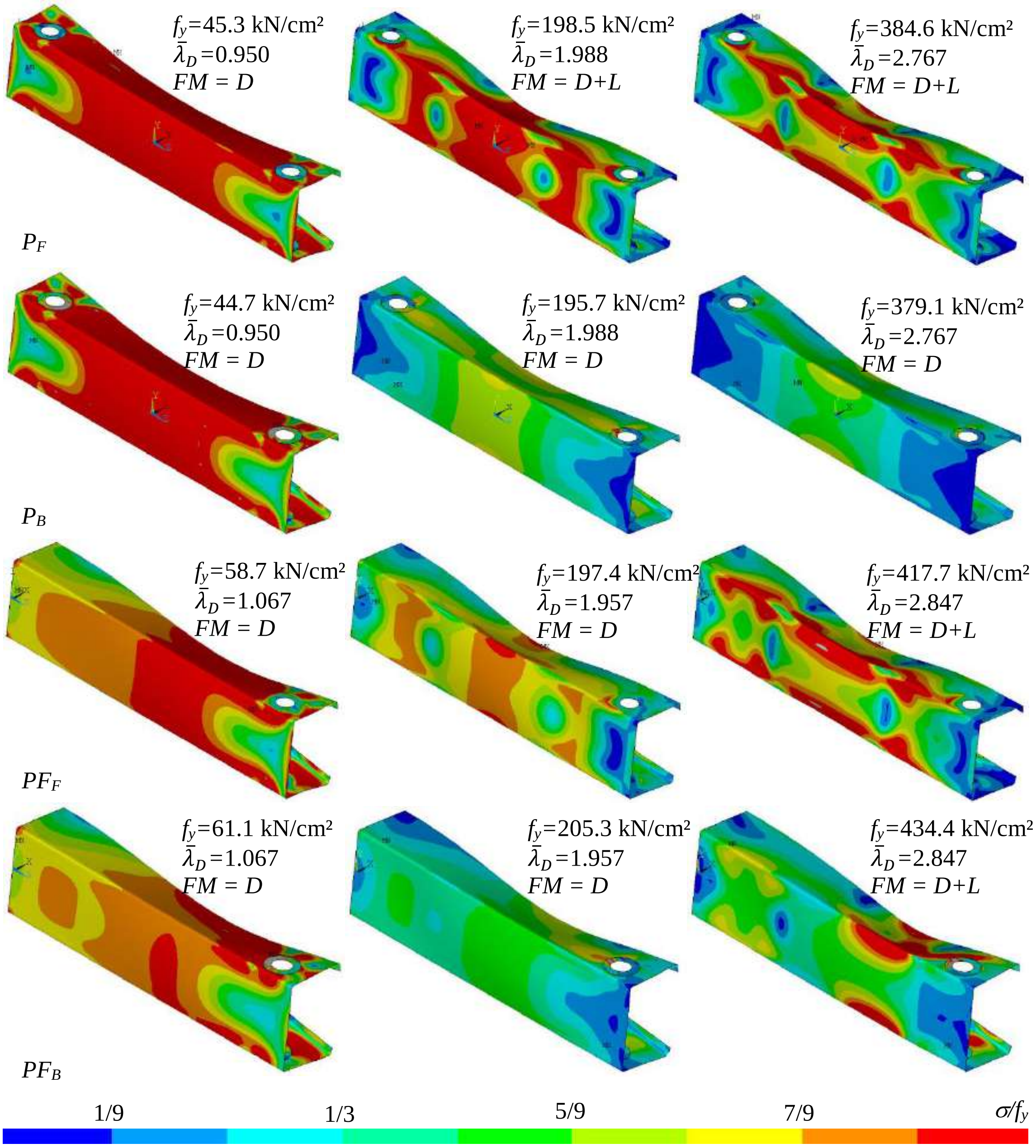

Figure 5.19 – *von Mises* equivalent stresses and collapse mode in 100x70 P_F, P_B, PF_F and PF_B columns considering maximum distortional amplitude of initial imperfection equal 0.1*t* – inward.

6 DSM Design Considerations

This section addresses the applicability of the Direct Strength Method (DSM) to estimate the ultimate strength of lipped channel columns failing in distortional modes and exhibiting four boundary conditions (P_F, P_B, PF_F and PF_B), experimentally tested and numerically analyzed in this work. The first step consists of computing $P_{n.e}$, $P_{n.D}$ and $P_{n.Le}$, according to Eqs. (2.12), (2.13) and (2.14), to 23 specimens described in chapter 4 and 2520 columns numerically analyzed in section 5.3.3, in order to assess the nature of the columns collapse predicted by DSM. The prediction failure by the DSM to the 2520 numerical columns and 23 experimental specimens was distortional, namely $P_{u,DSM}=P_{n.D}$. All the $P_{n.D}$ nominal loads, together with the corresponding slenderness values, are presented in appendix C (Tables C1-20) for numerical results and Table 6.1 for experimental values.

Table 6.1 – Experimental and DSM results concerning the columns behavior and strength.

Column	P_y (kN)	f_y (kN/cm²)	$\bar{\lambda}_D$	$P_{cr.D}$ (kN)	P_u (kN)	*FM*	$P_{n.D}$ (kN)	$P^*_{n.D}$ (kN)
100x70G-P_F	227.4	35.0	0.84	321.3	162.6	*D*	193.8	193.8
100x70C-P_F	270.4	42.6	0.90	331.7	184.2	*D*	219.3	219.3
100x100C-P_F	319.8	42.6	1.27	199.7	163.0	*D*	195.6	177.6
130x91G-P_F	293.3	35.0	1.12	231.8	161.5	*D*	199.4	199.4
130x91C-P_F	356.3	42.6	1.18	257.9	192.2	*D*	233.0	225.6
130x130C-P_B	423.7	42.6	1.72	143.1	106.5	*D*	192.1	138.6
150x105G-P_F	330.9	35.0	1.32	189.5	151.4	*D*	194.5	170.3
150x105C-P_F	391.1	42.6	1.40	199.3	160.5	*D*	217.5	181.8
150x150C-P_B	478.7	42.6	1.93	127.8	101.7	*D*	192.2	128.8
180x126C-P_F	472.0	42.6	1.83	141.5	152.6	*D*	201.3	139.8
180x180C-P_B	570.0	42.6	2.49	92.2	90.8	*D*	175.0	101.9
200x140C-P_B	506.8	42.6	2.03	122.6	121.0	*D*	193.2	125.7
200x200C-P_B	638.0	42.6	2.78	82.4	86.0	*D*	173.2	95.3
100x70C-PF_F	256.6	42.6	0.92	303.1	167.0	*D*	205.2	205.2
100x100C-PF_F	314.3	42.6	1.24	204.2	144.2	*D*	195.8	180.8
130x91C-PF_F	344.9	42.6	1.12	273.0	183.0	*D*	234.6	234.6
130x130C-PF_F	410.5	42.6	1.58	163.6	134.0	*D*	202.4	154.5
150x105C-PF_F	399.6	42.6	1.32	227.8	176.7	*D*	234.4	204.8
150x150C-PF_B	491.6	42.6	1.79	152.9	116.2	*D*	213.7	150.1
180x126C-PF_F	456.5	42.6	1.69	159.8	144.0	*D*	210.8	153.9
180x180C-PF_B	585.4	42.6	2.29	111.3	119.0	*D*	196.3	119.3
200x140C-PF_B	512.9	42.6	1.87	146.5	125.7	*D*	213.3	145.9
200x200C-PF_B	639.4	42.6	2.58	96.3	99.0	*D*	188.9	108.0

Table 6.1 summaries the experimental and DSM results obtained in the course of this work and provides the corresponding (i) squash loads (P_y), (ii) steel yield strength (f_y), (iii) distortional slenderness values ($\bar{\lambda}_D$), (iv) critical load elastic distortional buckling ($P_{cr.D}$) numerically calculated, (v) ultimate loads (P_u) experimentally obtained, (vi) the

failures mode (*FM*) observed, which were only distortional (*D*), (vii) DSM distortional ultimate strength estimates ($P_{n.D}$) and (viii) the ultimate strength estimates DSM distortional design curve suggested by LANDESMANN and CAMOTIM [31] ($P^*_{n.D}$).

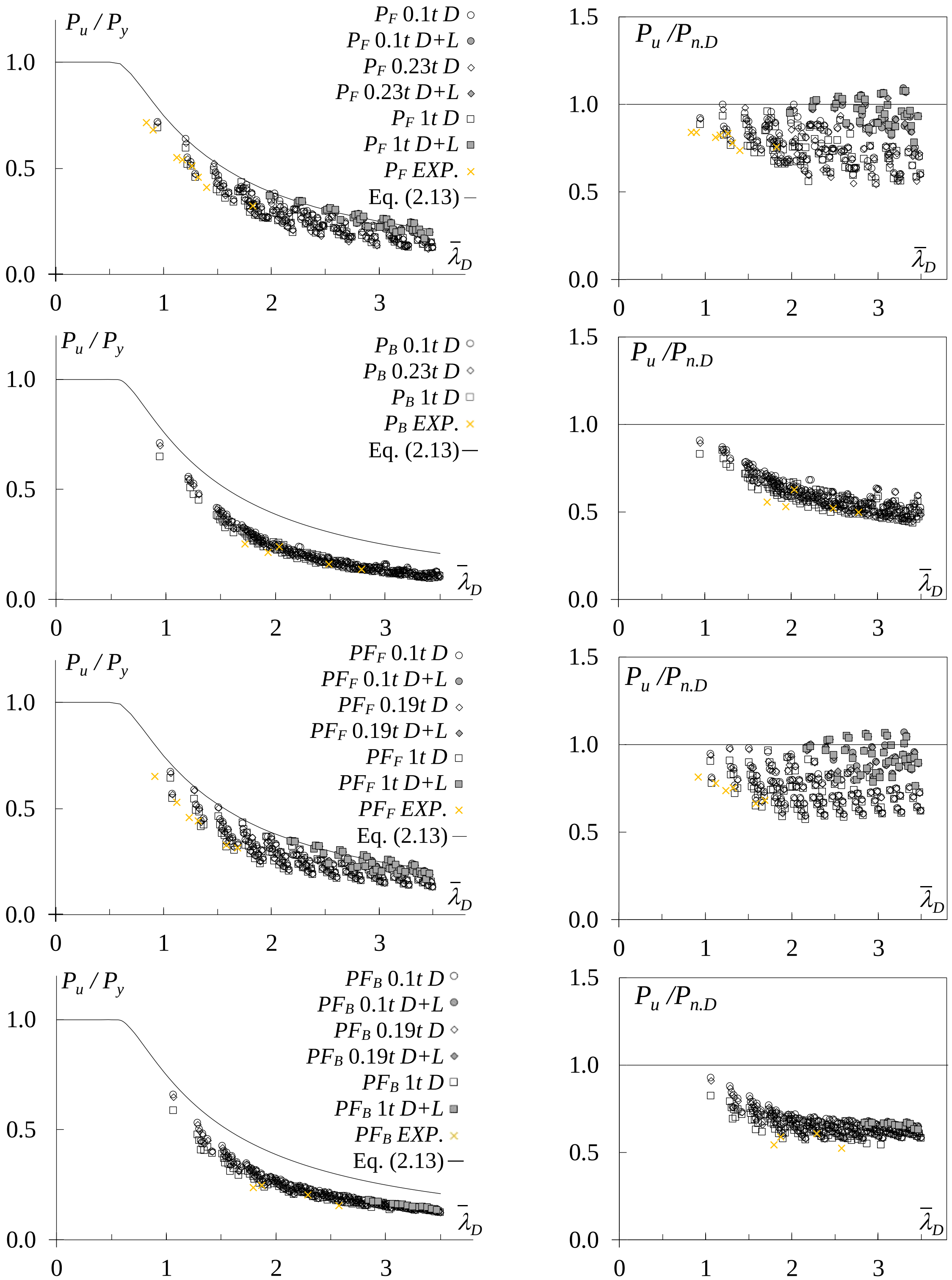

(a) (b)

Figure 6.1 – (a) Comparison between the numerical and experimental ultimate loads with current DSM distortional curve ($P_{n.D}$) and (b) $P_u/P_{n.D}$ *vs.* $\bar{\lambda}_D$ for P_F, P_B, PF_F and PF_B columns.

Figure 6.1(a) compares the current DSM distortional design curve with the numerically obtained ultimate loads that buckle in distortional modes and exhibit either distortional or interactive local–distortional collapses along with experimental data described in section 4.5.2, concerning P_F, P_B, PF_F and PF_B columns. Figure 6.1(b), on the other hand, shows the corresponding $P_u/P_{n.D}$ *vs.* $\bar{\lambda}_D$ plots (values given in Tables C1–20 and Table 6.1) thus providing pictorial representations of the accuracy and safety of the DSM ultimate strength estimates. In both figures, "grey markers" identify the columns whose failure modes exhibit distortional/local interaction. The observation of these pairs of figures prompts the following remarks:

i. It is possible to see in Figure 6.1(a) that data obtained numerically and experimentally follows the same trend and are mixed with each other. This shows a correlation between the numerical and experimental data.
ii. It is readily observed that their ultimate strengths are excessively overestimated by the DSM design curve. In Figure 6.1(b) it is noticeable the numbers of $P_u/P_{n.D}$ values closely below and/or above 0.5. This fact indicates a progressive deterioration of the (already poor to start with) quality of the DSM distortional ultimate strength estimates. This can be verified through the averages, standard deviations, maximum and minimum $P_u/P_{n.D}$ values presented in Table 6.2 for numerical and experimental *PF*, *PB*, *PFF* and *PFB* columns.

Table 6.2 – $P_u/P_{n.D}$ values for numerical and experimental P_F, P_B, PF_F and PF_B columns

$P_u/P_{n.D}$	P_F		P_B		PF_F		PF_B	
	Num	*Exp*	*Num*	*Exp*	*Num*	*Exp*	*Num*	*Exp*
Mean	0.81	0.80	0.58	0.55	0.80	0.74	0.65	0.57
S. D.	0.13	0.04	0.09	0.05	0.13	0.06	0.06	0.04
Max.	1.09	0.84	0.91	0.63	1.07	0.81	0.93	0.61
Min.	0.54	0.74	0.44	0.50	0.57	0.66	0.54	0.52

In view of the above facts, it can be stated that current distortional DSM curve is not suitable for application in P_F, P_B, PF_F and PF_B columns. Therefore, it may be necessary to consider different DSM design curve to predict efficiently the distortional failure loads of these columns.

Guided by the ultimate strength data acquired through the parametric and experimentally study carried out in this work it can be the proposal of LANDESMANN and CAMOTIM [31] described by Eq. (2.15). Figure 6.2(a) relates this proposed DSM distortional curve ($P^*_{n.D}$), comparing with results obtained in this work. Figure 6.2(b) shows the corresponding $P_u/P^*_{n.D}$ *vs.* $\bar{\lambda}_D$ plots (values given in Table C1-20 and Table 6.1).

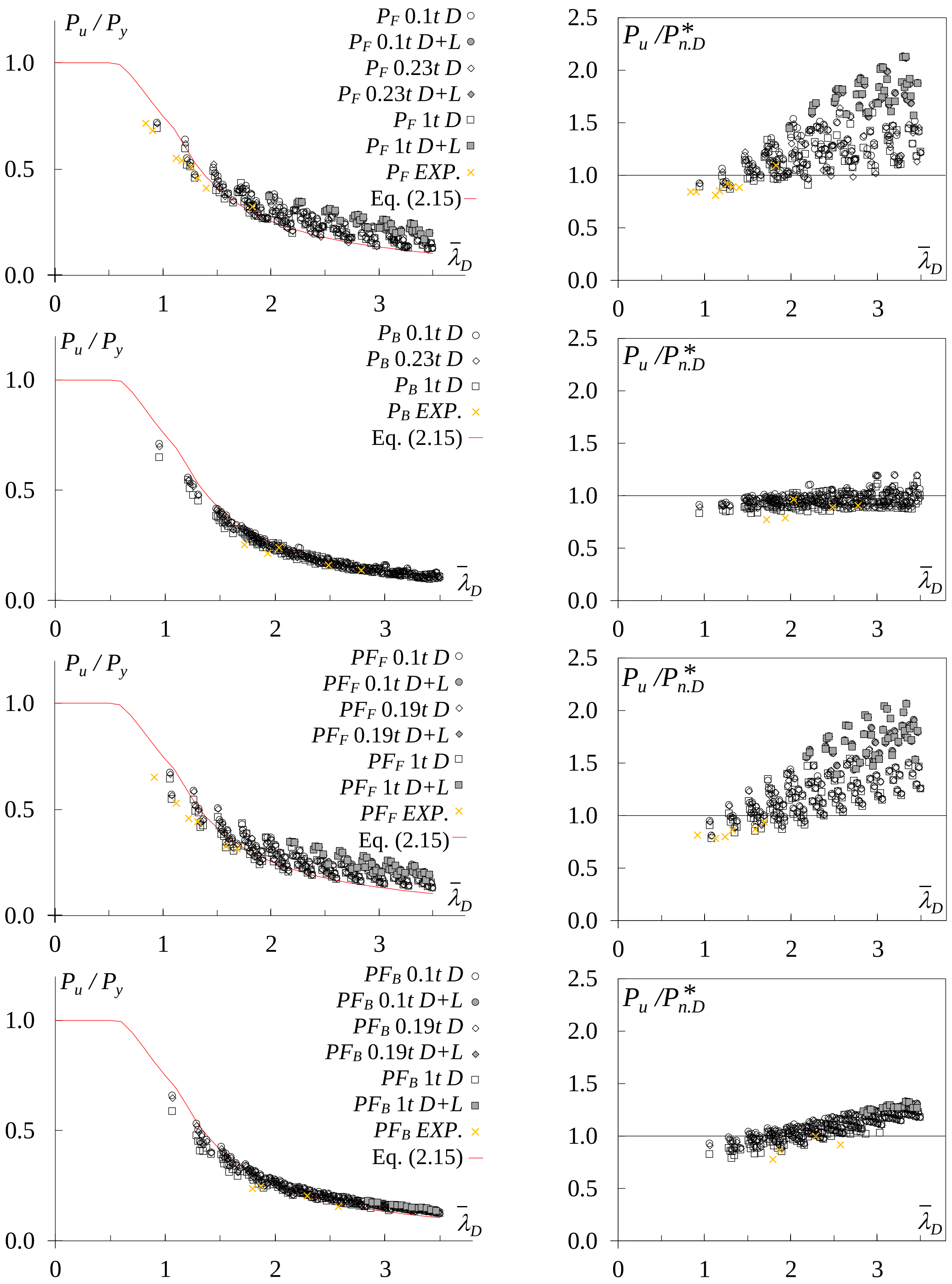

Figure 6.2 – (a) Comparison between the numerical and experimental ultimate loads with the DSM distortional curve ($P^*_{n.D}$) and (b) $P_u/P^*_{n.D}$ *vs.* $\bar{\lambda}_D$ for P_F, P_B, PF_F and PF_B columns.

For this proposal the averages, standard deviations, maximum and minimum $P_u/P^*_{n.D}$ values are given in Table 6.3 for numerical and experimental P_F, P_B, PF_F and PF_B columns.

Table 6.3 – $P_u/P^*_{n.D}$ values for numerical and experimental P_F, P_B, PF_F and PF_B columns

$P_u/P^*_{n.D}$	P_F		P_B		PF_F		PF_B	
	Num	*Exp*	*Num*	*Exp*	*Num*	*Exp*	*Num*	*Exp*
Mean	1.36	0.89	0.96	0.86	1.34	0.84	1.09	0.89
S. D.	0.30	0.09	0.07	0.08	0.31	0.06	0.12	0.09
Max.	2.13	1.09	1.19	0.96	2.06	0.94	1.32	1.00
Min.	0.86	0.81	0.83	0.77	0.78	0.78	0.79	0.77

The curve suggested by LANDESMANN and CAMOTIM [31] – (Eq. (2.15)) “fits” best to the numerical and experimental data obtained in this study. Such “agreement” occurs mainly in the columns which load condition is given by contact (P_B and PF_B) due to the smaller vertical dispersion. On the other hand, for the columns which load condition is frictional (P_F and PF_F), this proposal is also safer in relation to the current DSM distortion curve.

6.1 Load and Resistance Factor Design (LRFD)

This section addresses the evaluation of the LRFD (Load and Resistance Factor Design) resistance factor ϕ associated with the proposed DSM-based design approach. According to the North American cold-formed steel specification [23], ϕ is calculated by the formula given in section K.2.1.1 of chapter K,

$$\phi = C_\phi (M_m F_m P_m)\, e^{-\beta_0 \sqrt{V_M^2 + V_F^2 + C_P V_P^2 + V_Q^2}} \qquad \text{with} \qquad C_P = \left(1 + \frac{1}{n}\right)\frac{m}{m-2} \tag{6.1}$$

where (i) C_ϕ is a calibration coefficient (C_ϕ=1.52 for LRFD), (ii) M_m=1.10 and F_m=1.00 are the mean values of the material and fabrication factor, respectively, (iii) β_0 is the target reliability index (β_0=2.5 for structural members in LRFD), (iv) V_M=0.10, V_F=0.05 and V_Q=0.21 are the coefficients of variation of the material factor, fabrication factor and load effect, respectively , and (v) C_P is a correction factor that depends on the numbers of tests (n) and degrees of freedom (m=n-1). In order to evaluate ϕ for the proposed DSM procedure, it is necessary to calculate P_m and V_P, the average and standard deviation of the $P_u/P^*_{n.D}$ ratios – the P_u values are either experimental, numerical or experimental and numerical.

Table 6.4 shows the n, C_P, P_m, V_P and ϕ values obtained for the column failure load predictions provided by the LANDESMANN and CAMOTIM [31] DSM design approach for the experimental, numerical and combined failure loads. It is observed that:

Table 6.4 – LRFD ϕ values according to [23] concerning the prediction of the experimental, numerical and combined failure loads obtained in this work by the proposed DSM design approach.

		n	C_P	P_m	V_p	ϕ
P_F	Exp.	8	1.58	0.89	0.10	0.76
	Num.	405	1.01	1.36	0.22	1.00
	Exp. + Num.	413	1.01	1.35	0.23	0.99
P_B	Exp.	5	2.40	0.86	0.09	0.72
	Num.	414	1.01	0.96	0.07	0.86
	Exp. + Num.	419	1.01	0.95	0.07	0.86
PF_F	Exp.	6	1.94	0.84	0.07	0.74
	Num.	411	1.01	1.34	0.23	0.98
	Exp. + Num.	417	1.01	1.34	0.23	0.97
PF_B	Exp.	4	3.75	0.89	0.11	0.68
	Num.	414	1.01	1.09	0.11	0.95
	Exp. + Num.	418	1.01	1.09	0.11	0.94
Combined Columns	Exp.	23	1.15	0.87	0.09	0.77
	Num.	1644	1.00	1.18	0.24	0.85
	Exp. + Num.	1667	1.00	1.18	0.24	0.85

i. When the total (experimental and numerical) failure load data are considered, the resistance factor values associated with each proposed DSM-based procedure are (i_1) ϕ=0.76 (P_F columns), ϕ=0.72 (P_B columns), ϕ=0.74 (PF_F) and ϕ=0.68 (PF_B columns), for the experimental data, (i_2) ϕ=1.00 (P_F columns), ϕ=0.86 (P_B columns), ϕ=0.98 (PF_F columns) and ϕ=0.95 (PF_B columns), for the numerical data, and (i_3) ϕ=0.99 (P_F columns), ϕ=0.86 (P_B columns), ϕ=0.97 (PF_F columns) and ϕ=0.94 (PF_B columns), for the experimental and numerical data.

ii. There is quite solid evidence that ϕ=0.85[6] can be recommended for (i) end-bolted or (ii) end-bolted fixed lipped channel cold-formed steel columns.

---

[6] North American AISI-S100 [23] specification value recommended for cold-formed steel compression members.

7 Concluding Remarks

This work reported a numerical (ANSYS shell finite element analysis) and experimental investigation on the influence of end-bolted support conditions on the post-buckling behavior and DSM (Direct Strength Method) design of lipped channel cold-formed steel columns buckling and failing in distortional modes.

The columns analyzed exhibited (i) two end support conditions, namely (i_1) end-bolted and (i_2) end-bolted and fixed, (ii) two bolted load-types – frictional and bearing-type, (iii) fifteen geometries of lipped-channels columns (various lengths and cross-section dimensions) and (iv) several yield stresses were considered. These characteristics were carefully selected (i) to ensure, as much as possible, “pure” distortional buckling and failure modes (*i.e.*, to preclude interaction with local and/or global buckling modes) and (ii) to cover a wide (distortional) slenderness range. The experiments contributed to validate numerical methodologies which in turn increased the amount of data.

The ultimate strength data acquired during the performance of the parametric study involving 1644 columns and 23 specimens (13 end-bolted and 10 end-bolted and fixed) were tested. These data were then used to show that, regardless of the column geometry (and corresponding distortional post-buckling features), the current DSM distortional design curve is not able to predict adequately the ultimate loads of (i) end-bolted and (ii) end-bolted and fixed lipped channel columns.

Therefore, adequate ultimate strength estimates for the (i) end-bolted and (ii) end-bolted and fixed columns analyzed in this work could only be achieved by an additional DSM distortional design curve. Based on the results obtained from the experimental tests and parametric study carried out, modified distortional design curve was proposed for these columns. In fact, such a modification is the confirmation of the suggestion made by LANDESMANN and CAMOTIM [31]. The failure load predictions yielded by this proposed design curve are conservative for frictional load-type columns with $\bar{\lambda}_D$>1.5 taking into account the vertical dispersion of the numerical data. On the other hand, this proposal “fits” good for bearing-type load columns. In particular, it was confirmed (even reinforced) that the LRFD resistance factor ϕ=0.85, currently prescribed in North American cold-formed steel specification [23] for the design of compression members, can also be safely adopted for the failure load prediction of (i) end-bolted and (ii) end-bolted and fixed lipped channel columns by the proposed DSM design approach.

Finally, four important results emerge from this study: (i) the post-buckling strength increases as one travels along the column end support condition sequence *P* to *PF* agreeing with LANDESMANN and CAMOTIM [31], (ii) the same can be said to the loading sequence bearing-type to frictional-type, (iii) the distortional/local interaction was considered week agreeing with KWON and HANCOCK [18] and (iv) the ultimate strength is not sensitive to maximum amplitude variation of the inward half-wave distortional initial imperfection deals with in this research (0.1*t* up to 1.0*t*).

7.1 Suggestions for future works

In order to prove robustness and universality of the proposed method, it is suggested more compression tests.

The methodology presented here can be used in different cross-sections such hat, rack and Z-section among others. Also, it can be studied in members under action of bending moments or combined axial and bending loading.

Furthermore, the influence of the end-bolted conditions in columns with longitudinal web and/or flange stiffeners, punched columns and subjected to high temperatures could be investigated.

Also, it can be studied web end-bolted connections.

8 Bibliography

[1] G. J. HANCOCK, "Cold-formed steel structures," *Journal of Constructional Steel Research,* pp. 473-487, 17 October 2002.

[2] J. RONDAL, "Cold-formed steel members and structures - General Report," *Journal of Constructional Steel Research,* vol. 33, pp. 155-158, 2000.

[3] S. P. TIMOSHENKO and J. M. GERE, Theory of Elastic Stability, Tokyo: Tosho Printing Co.,LTD., 1961.

[4] L. SCHUMAN and G. BACK, "Strength of rectangular flat plates under edge compression," *NACA,* pp. 515-538, 1931.

[5] Y. C. FUNG and E. E. SECHLER, Thin-Shell Structures, New Jersey: Prentice-Hall, 1974.

[6] T. von KARMAN, E. E. SECHLER and L. H. DONNELL, "The Strength of Thin Plates in Compression," *Transactions of the American Society of Mechanical Engineers (ASME),* vol. 54, p. 53, 1932.

[7] G. WINTER, "Strength of thin steel compression flanges," *Transactions of ASCE, Paper No. 2305,* pp. 527-554, 1947.

[8] B. W. SCHAFER, "Review: The Direct Strength Method of cold-formed steel member design," *Journal of Constructional Steel Research,* vol. 64, p. 766–778, 18 January 2008.

[9] E. E. LUNDQUIST and E. Z. STOWELL, "Restraint provided a flat rectangular plate by a sturdy stiffener along an edge of the plate," *NACA Report 735,* pp. 123-125, 1942.

[10] G. L. GALLAHER and R. B. BOUGHAN, "A method of calculating the compressive strength of Z-stiffened panels that develop local instability," *NACA report No. 1482,* pp. 1-15, 1947.

[11] N. SILVESTRE and D. CAMOTIM, "On the mechanics of distortion in thin-walled open sections," *Journal of thin-walled structures,* pp. 469-481, 4 March 2010.

[12] B. W. SCHAFER, "Distorcional Buckling of Cold-Formed Steel Columns - Final Report," American Iron and Steel Institute (AISI), Washington, D. C., 2000.

[13] M. L. SHARP, "Longitudinal stiffeners for compression members," *Journal of the Structural Division (ASCE),* pp. 187-211, 1966.

[14] K. TAKAHASHI and D. MIZUNO, "Distortion of thin-walled open cross-section members (one degree of freedom and singly symmetrical cross-section)," *Bolletin of Journal of the Japan Society of Mechanical Engineers,* vol. 21, p. 1448–1454, Octuber 1978.

[15] S. SRIDHARAN, "A semi-analytical method for the post-local-tortional buckling analises of prismatic plate structures," *International Journal for Numerical Methods in Engineering,* vol. 18, pp. 1685-1697, 1982.

[16] S. C. W. LAU and G. J. HANCOCK, "Buckling of thin flat-walled structures by a spline finite strip method," *Thin-Walled Structures,* pp. 269-294, 1986.

[17] S. C. W. LAU and G. J. HANCOCK, ""Distortional buckling formulas for channel columns"," *Journal of Structural Engineering (ASCE),* pp. 1063-1078, 1987.

[18] Y. B. KWON and G. J. HANCOCK, "Strength test of cold-formed channel sections undergoing local and distortional buckling," *Journal Strutural Engineering (ASCE),* pp. 1786-1803, 1992.

[19] K. J. R. RASMUSSEN and G. J. HANCOCK, "The flexural behavior of thin-walled singly symmetric columns," *International Conference on Steel and Aluminium Structures,* pp. 406-417, 22 May 1991.

[20] B. YOUNG and K. J. R. RASMUSSEN, "Behaviour of cold-formed singly symmetric columns," *Thin-Walled Structures,* p. 83–102, 1999.

[21] G. J. HANCOCK, Y. B. KNOW and E. S. BERNARD, "Strength design curves for thin-walled sections undergoing distortional buckling," *Journal of Constructional Steel Research,* pp. 169-186, 5 January 1994.

[22] ABNT NBR 14762, Design cold-formed steel structures, Rio de Janeiro: Associação Brasileira de Normas Técnicas, 2014 (in Portuguese).

[23] AISI-S100, Specification for the design of cold-formed steel structural members, Washington, D. C.: American Iron and Steel Institute, 2016.

[24] AS/NZS 4600, Cold-Formed Steel Structures, North Sydney: Standards Association of Australia, 2005.

[25] S. H. PHAM, C. H. PHAM and G. J. HANCOCK, "Direct strength method of design for shear including sections with longitudinal web stiffeners," *Thin-Walled Structures,* pp. 19-28, 2013.

[26] B. YOUNG, D. CAMOTIM and N. SILVESTRE, "Ultimate strength and design of lipped channel columns experiencing local-distortional mode interaction - part I: Experimental Investigation," in *Proceedings of Sixth International Conference on Advances in Steel Structures*, Hong Kong, 2009.

[27] D. YANG and G. J. HANCOCK, Compression Tests of Cold-Reduced High Strength Steel Channel Columns failing in the Distortional Mode Research Report No R825, Sydney: Department of Civil Engineering - The University of Sydney, 2003.

[28] C. D. MOEN and B. W. SCHAFER, "Experiments on cold-formed steel columns with holes," *Thin-Walled Structures,* vol. 46, p. 1164–1182, 14 March 2008.

[29] M. CASAFONT, M. M. PASTOR, F. ROURE and T. PEKÖZ, "An experimental investigation of distortional buckling of steel storage rack columns," *Thin-Walled Structures,* vol. 49, p. 933–946, 16 April 2011.

[30] N. SILVESTRE, P. B. DINIS, D. CAMOTIM and E. M. BATISTA, "DSM design of lipped channel columns undergoing local/distortional/global mode interaction," *SDSS'Rio 2010 Stability and Ductility of Steel Structures,* pp. 1061-1068, 8 September 2010.

[31] A. LANDESMANN and D. CAMOTIM, "On the Direct Strength (DSM) design of cold-formed steel columns against distortional failure," *Thin-Walled Structures,* vol. 67, pp. 168-187, January 22 2013.

[32] W. W. YU and R. A. LABOUBE, Cold-Formed Steel Design, 3ª ed., New Jersey: John Wiley & Sons, 2010.

[33] CUSTOMPART.NET, "Sheet Metal Forming," CustomPartNet, 2009. [Online]. Available: http://www.custompartnet.com/wu/sheet-metal-forming. [Accessed 27 Octuber 2016].

[34] B. W. SCHAFER and T. PEKÖZ, "Computational modeling of cold-formed steel characterizing geometric imperfections and residual stresses," *Journal of Constructional Steel Research,* pp. 193-210, 6 January 1998.

[35] K. W. KARREN and G. WINTER, "Effects of cold-forming on light-gage steel members," *Journal of the Structural Division (ASCE),* pp. 433-469, 1967.

[36] S. NARAYANAN and M. MAHENDRAN, "Ultimate capacity of innovative cold-formed steel columns," *Journal of Constructional Steel Research,* p. 489–508, 2003.

[37] Y. H. LEE, C. S. TAN, S. MOHAMMAD, M. M. TAHIR and P. N. SHEK, "Review on Cold-Formed Steel Connections," *The Scientific World Journal,* vol. 2014, pp. 1-11, 3 February 2014.

[38] W. W. YU, Cold-formed steel strutures, New York: McGRAW-HILL, 1973.

[39] C. MATHIESON, G. C. CLIFTON and J. B. P. LIM, "Novel pin-jointed connection for cold-formed steel trusses," *Journal of Constructional Steel Research,* vol. 116, p. 173–182, January 2016.

[40] J. M. DAVIES, "Recent research advances in cold-formed steel structures," *Journal of Constructional Steel Research,* vol. 55, p. 267–288, 2000.

[41] C. YU and M. X. PANYANOUVONG, "Bearing strength of cold-formed steel bolted connections with a gap," *Thin-Walled Structures,* vol. 67, p. 110–115, 20 March 2013.

[42] C. A. ROGERS and G. J. HANCOCK, "Bolted connection design for sheet steels less than 1.0 mm thick," *Journal of Constructional Steel Research,* p. 123–146, 1 April 1999.

[43] K. F. CHUNG and K. H. IP, "Finite element modeling of double bolted connections between cold-formed steel strips under static shear loading," *Proceedings of the Second International Conference on Advances in Steel Structures Cold-formed steel structure code AS/NZ,* vol. 4600, pp. 245-252, 1996.

[44] K. F. CHUNG and K. H. IP, "Finite element modeling of bolted connections between cold-formed steel strips and hot rolled steel plates under static shear loading," *Engineering Structures,* p. 1271–1284, 2000.

[45] K. F. CHUNG and K. H. IP, "Finite element investigation on the structural behaviour of cold-formed steel bolted connections," *Engineering Structures,* p. 1115–1125, 2001.

[46] ABNT NBR 8800, Design os steel and composite structures for buildings, Rio de Janeiro: Associação Brasileira de Normas Técnicas, 2008 (in Portuguese).

[47] ANSI/AISC 360-10, Specification for Structural Steel Buildings, Chicago: American Institute of Steel Construction, 2010.

[48] T. V. GALAMBOS and A. E. SUROVEK, Structural Stability of Steel: Concepts and Applications for Structural Engineers, New Jersey: John Wiley & Sons, Inc, 2008.

[49] T. V. GALAMBOS, Guide to Stability Design for Metal Structures, 5 ed., New York: John & Sons, 1998.

[50] A. REIS and D. CAMOTIM, Stability and design of structures, Lisboa: Orion, 2012 (in Portuguese).

[51] M. M. PASTOR, M. CASAFONT, F. R. BONADA and F. ROURE, "Imperfection amplitudes for nonlinear analysis of open thin-walled steel cross-sections used in rack column uprights," *Thin-Walled Structures,* vol. 76, pp. 28-41, 2014.

[52] V. M. ZEINODDINI and B. W. SCHAFER, "Simulation of geometric imperfections in cold-formed steel members using spectral representation approach," *Thin-Walled Structures,* vol. 60, pp. 105-117, 9 August 2012.

[53] M. M. PASTOR, J. BONADA, F. ROURE and M. CASAFONT, "Residual stresses and initial imperfections in non-linear analysis," *Engineering Structures,* vol. 46, pp. 493-507, 2013.

[54] G. J. HANCOCK, "Finite Strip Buckling and Nonlinear Analyses and Distortional Buckling Analysis of Thin-Walled Structural Members," pp. 225-289, 1998.

[55] J. G. TENG, J. YAO and Y. ZHAO, "Distortional buckling of channel bem-columns," *Thin-Walled Structures,* pp. 595-617, 2003.

[56] B. W. SCHAFER and T. PEKÖZ, "Direct strength prediction of cold-formed steel members using numerical elastic buckling solutions," in *Fourteenth International Specialty Conference on Cold-Formed Steel Structures*, St. Louis, Missouri, 1998.

[57] B. W. SCHAFER, "Local, distortional, and Euler buckling of thin-walled columns," *Journal of Structural Engineering,* vol. 128, no. 3, pp. 289-299, Mar 2002.

[58] M. MACDONALD, M. A. HEIYANTUDUWA and J. RHODES, "Recent developments in the design of cold-formed steel members and structures," *Thin-Walled Structures,* p. 1047–1053, 2008.

[59] N. SILVESTRE, D. CAMOTIM and P. B. DINIS, "Direct strength prediction of lipped channel columns experiencing local-plate/distortional interaction," in *Advanced Steel Construction,* Hong Kong, 2009.

[60] D. CAMOTIM, P. B. DINIS and A. MARTINS, "Direct Strength Method (DSM) - A General Approach for the Design of Cold-Formed Steel Structures," Lisboa, 2016, pp. 69-105.

[61] D. CAMOTIM and C. BASAGLIA, "Buckling analysis of thin-walled structures using generalised beam theory (GBT): state-of-the-art report," *Steel Constroction*, vol. 6, p. 117–131, 2013.

[62] Swanson Analysis System Inc., (SAS) Ansys Reference Manual (Vrs. 12), 2009.

[63] Z. LI and B. W. SCHAFER, "Buckling analysis of cold-formed steel members with general boundary conditions using CUFSM: conventional and constrained finite strip methods," *Proceedings of the 20th Int;l. Spec. Conf. on Cold-Formed Steel Structures,* 3 & 4 November 2010.

[64] R. BEBIANO, N. SILVESTRE and D. CAMOTIM, "GBTUL- a Code for the Buckling Analysis of Cold-formed Steel Members," in *19th International Specialty Conference on Cold-Formed Steel Structures*, St. Louis, 2008.

[65] ASTM A490-14a, Standard Specification for Structural Bolts, Alloy Steel, Heat Treated, 150 ksi Minimum Tensile Strength, West Conshohocken: ASTM International, 2014.

[66] ASTM F436/F0436-16, Standard Specification for Hardened Steel Washers Inch and Metric Dimensions, West Conshohocken: ASTM International, 2016.

[67] ASTM A653 / A653M-15e1, Standard Specification for Steel Sheet, Zinc-Coated (Galvanized) or Zinc-Iron Alloy-Coated (Galvannealed) by the Hot-Dip Process, West Conshohocken: ASTM International, 2015.

[68] ABNT NBR 7008-1, Steel-coated coils and plates with zinc or zinc-iron alloy by hot-dip continuous process immersion Part 1: Requirements, Rio de Janeiro: Associação Brasileira de Normas Técnicas, 2012 (in Portuguese).

[69] EN 10149-2, Hot rolled flat products made of high yield strength steels for cold forming - Part 2: Technical delivery conditions for thermomechanically rolled steels, Brussels: CEN - European Committee for Standardization, 2013.

[70] ABNT NBR 7013, Coated carbon steel plates by hot-dip continuous process – General requirements, Rio de Janeiro: Associação Brasileira de Normas Técnicas, 2013 (in Portuguese).

[71] ABNT NBR 11888, Sheet and coils of carbon and high strength alloy steel — General requirements, Rio de Janeiro: Associação Brasileira de Normas Técnicas, 2015 (in Portuguese).

[72] ASTM E8 / E8M-15a, Standard Test Methods for Tension Testing of Metallic Materials, West Conshohocken: ASTM International, 2015.

[73] A. LANDESMANN, D. CAMOTIM, P. B. DINIS and R. CRUZ, "Short-to-intermediate slender pin-ended cold-formed steel equal-leg angle columns: Experimental investigation, numerical simulations and DSM design," *Engineering Structures,* vol. 132, pp. 471-493, 2017.

Appendix A

In this appendix are presented the specimen datasheets showing:

i. the specimens design (side, front and top view) with the displacement transducers readings (DT1-7 – see Figure 4.8) of the initial imperfections.
ii. the measured dimensions at the three cross-sections according to Figure A.1 in sections 0-0.5-1L_0 (see Figure 4.1), the average lengths (L_D, L_T and L_0), the distance of the web to the hole border (b_a), the hole diameter (d_f), the calculated area according to the measured dimensions average (A), the squash load (P_y) and ultimate loads (P_u).
iii. the experimental equilibrium paths P *vs.* Δ, δ_{12}^{D}, δ_{76}^{D} and δ_{W}^{L} with the specimens before and after the test.

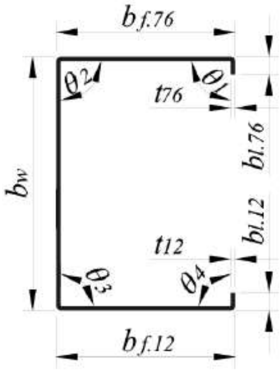

Figure A.1 - Cross-section measured dimensions in lipped channel specimens.

1. 100x70G-P_F

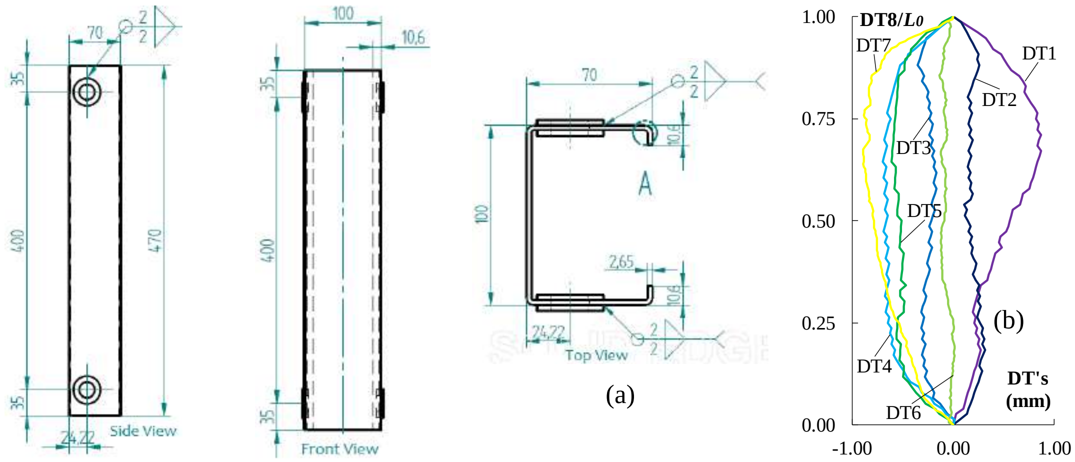

Figure A.2 - 100x70G-P_F column (a) design and (b) initial imperfection readings.

Table A.1 – Initial measures (mm), calculated area (cm²), squash and ultimate load (kN) for 100x70G-P_F column

Position	b_w	b_f		b_l		t					
	-	$b_{f.12}$	$b_{f.76}$	$b_{l.12}$	$b_{l.76}$	t_{12}	t_{76}	θ_1	θ_2	θ_3	θ_4
0	100.45	68.00	70.83	10.80	10.21	2.62	2.67	90.0	92.0	90.0	89.0
0.5L_0	100.07	68.30	70.75	10.68	10.46	2.64	2.67	90.5	92.5	91.0	88.0
L_0	99.99	68.80	69.55	10.66	10.68	2.65	2.67	88.5	90.0	90.5	90.5
Average	100.17	69.37		10.58		2.65					
	L_D	L_T	L_0	b_a	d_f	A		P_y		P_u	
Average	400	471	330	13.19	21.5	6.50		227.4		162.6	

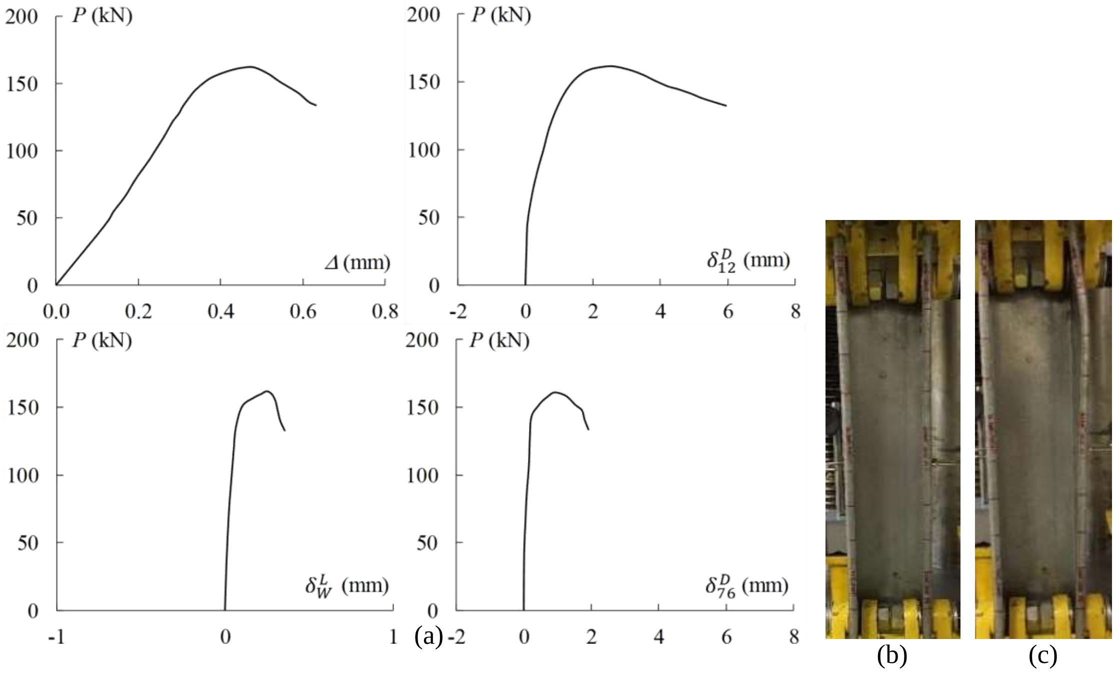

(a) (b) (c)

Figure A.3 - 100x70G-P_F column (a) experimental equilibrium paths P *vs.* Δ, δ_{12}^D, δ_{76}^D and δ_W^L, and column (b) before and (c) after the test.

2. 100x70C-P_F

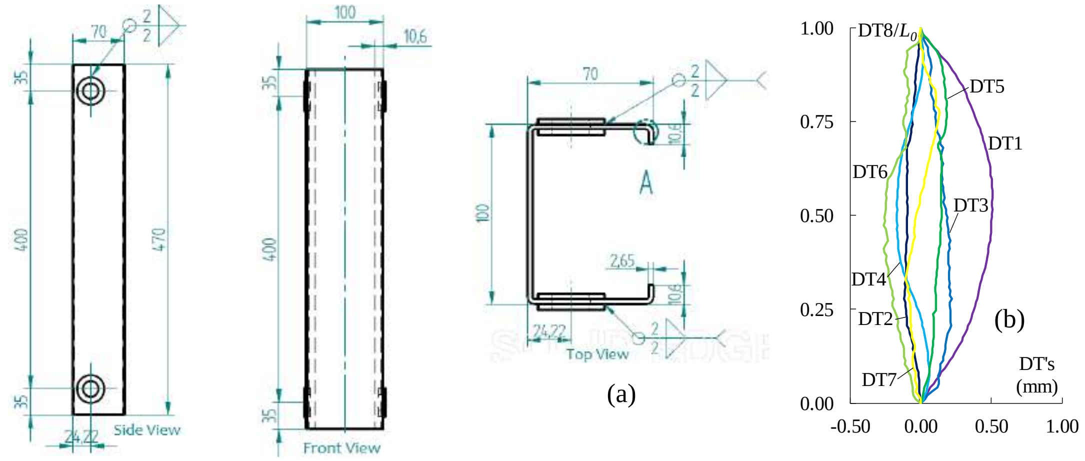

Figure A.4 - 100x70C-P_F column (a) design and (b) initial imperfection readings.

Table A.2 – Initial measures (mm), calculated area (cm²), squash and ultimate load (kN) for 100x70C-P_F column

Position	b_w	b_f		b_l		t					
	-	$b_{f.12}$	$b_{f.76}$	$b_{l.12}$	$b_{l.76}$	t_{12}	t_{76}	θ_1	θ_2	θ_3	θ_4
0	99.00	69.00	69.40	11.50	11.00	2.61	2.65	89.0	90.0	91.0	91.0
0.5L_0	99.00	69.40	69.30	11.50	11.50	2.57	2.58	89.0	89.0	90.0	91.0
L_0	99.40	69.00	69.00	11.00	11.50	2.53	2.58	90.0	88.0	90.0	91.0
Average	99.13	69.18		11.33		2.59					
	L_D	L_T	L_0	b_a	d_f	A		P_y		P_u	
Average	399	469	329	14.28	21.00	6.35		270.4		184.2	

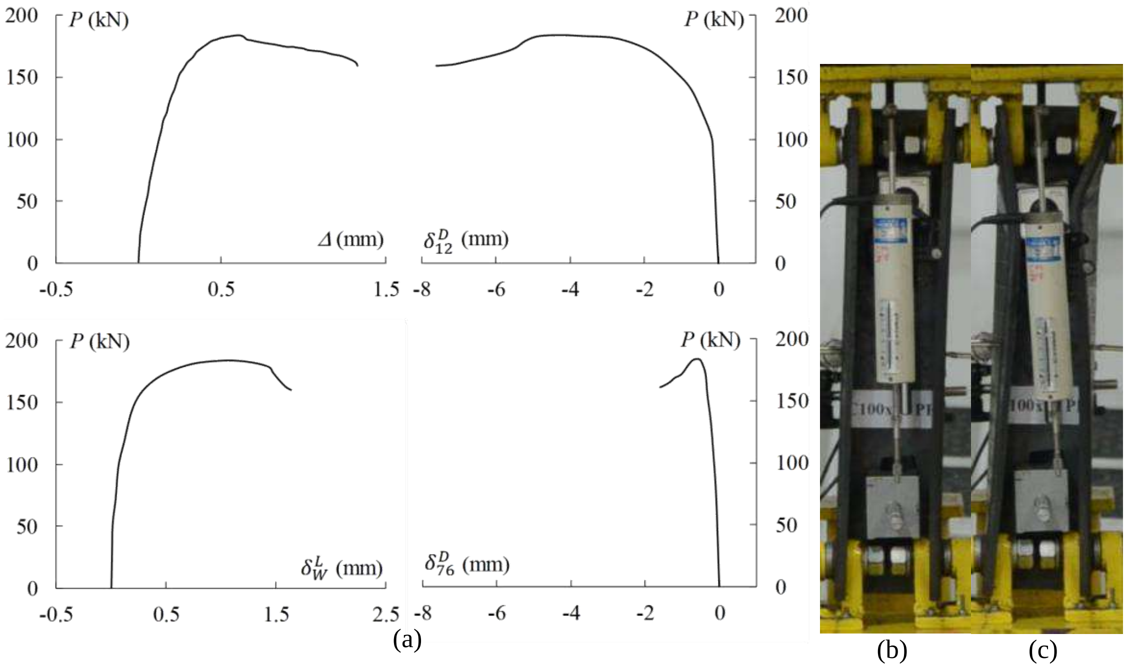

(a) (b) (c)

Figure A.5 - 100x70C-P_F column (a) experimental equilibrium paths P vs. Δ, δ_{12}^D, δ_{76}^D and δ_W^L, and column (b) before and (c) after the test.

3. 100x100C-P_F

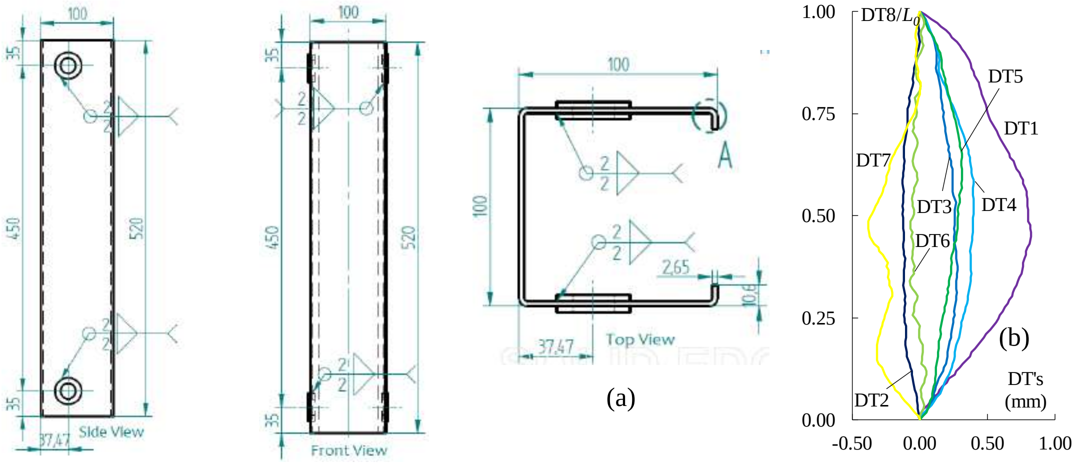

Figure A.6 - 100x100C-P_F column (a) design and (b) initial imperfection readings.

Table A.3 - Initial measures (mm), calculated area (cm²), squash and ultimate load (kN) for 100x100C-P_F column

Position	b_w	b_f		b_l		t					
	-	$b_{f.12}$	$b_{f.76}$	$b_{l.12}$	$b_{l.76}$	t_{12}	t_{76}	θ_1	θ_2	θ_3	θ_4
0	100.50	99.00	99.40	10.30	11.40	2.46	2.47	90.0	90.0	90.0	89.0
0.5L_0	99.50	100.00	100.00	10.30	11.40	2.45	2.44	90.0	90.0	91.0	89.0
L_0	98.40	100.00	100.40	9.00	11.00	2.44	2.45	90.0	90.0	91.0	88.0
Average	99.47	99.80		10.57		2.45					
	L_D	L_T	L_0	b_a	d_f	A		P_y		P_u	
Average	452	520	382	24.20	20.95	7.51		319.8		163.0	

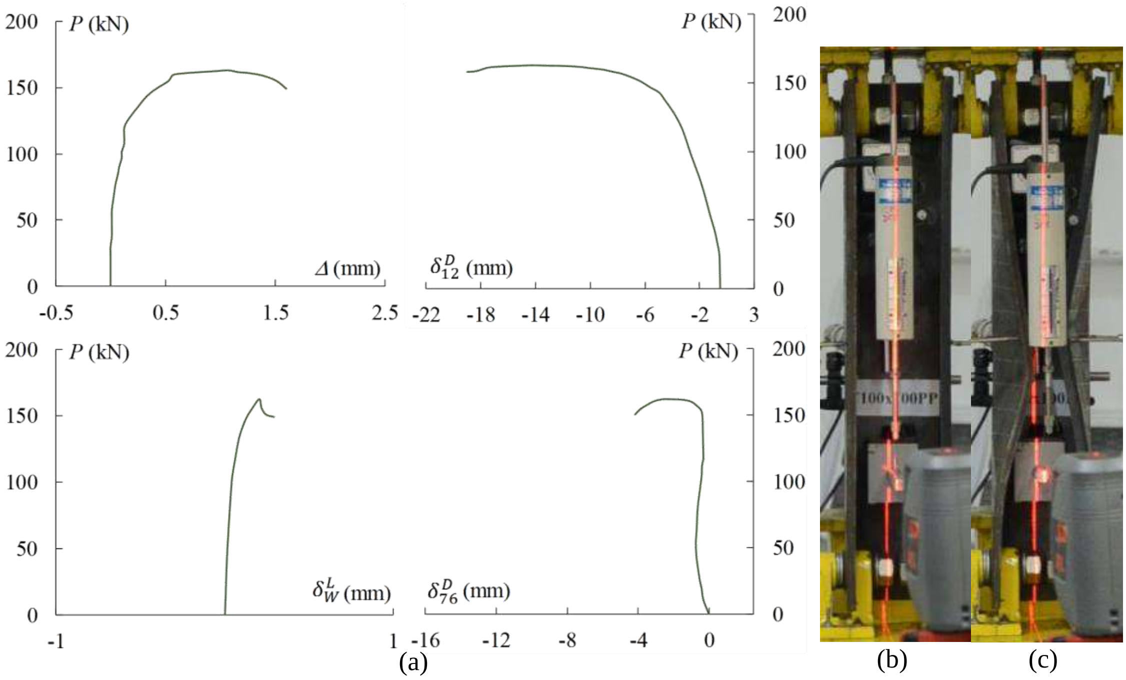

(a) (b) (c)

Figure A.7 - 100x100C-P_F column (a) experimental equilibrium paths P vs. Δ, δ_{12}^{D}, δ_{76}^{D} and δ_{W}^{L}, and column (b) before and (c) after the test.

4. 130x91G-P_F

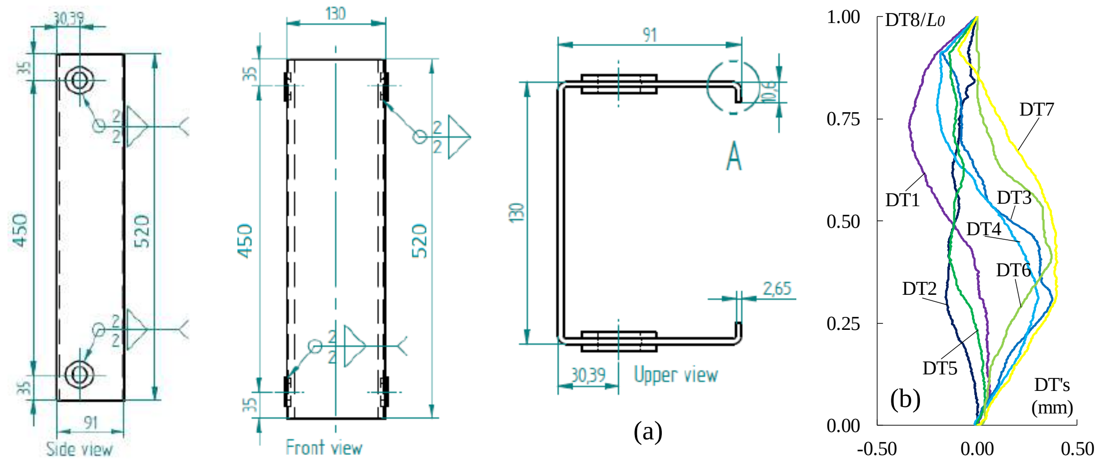

Figure A.8 - 130x91G-P_F column (a) design and (b) initial imperfection readings.

Table A.4 - Initial measures (mm), calculated area (cm²), squash and ultimate load (kN) for 130x91G-P_F column

Position	b_w	b_f		b_l		t					
	-	$b_{f.12}$	$b_{f.76}$	$b_{l.12}$	$b_{l.76}$	t_{12}	t_{76}	θ_1	θ_2	θ_3	θ_4
0	130.50	89.55	91.03	10.46	10.61	2.60	2.65	92.0	91.0	90.0	89.0
0.5L_0	130.19	89.86	90.83	9.90	10.69	2.66	2.68	92.0	90.5	90.2	89.0
L_0	129.85	90.51	89.93	9.50	10.64	2.66	2.65	90.0	90.0	89.0	93.0
Average	130.18	90.29		10.30		2.65					
	L_D	L_T	L_0	b_a	d_f	A		P_y		P_u	
Average	450	521	380	19.59	21.50	8.38		293.3		161.5	

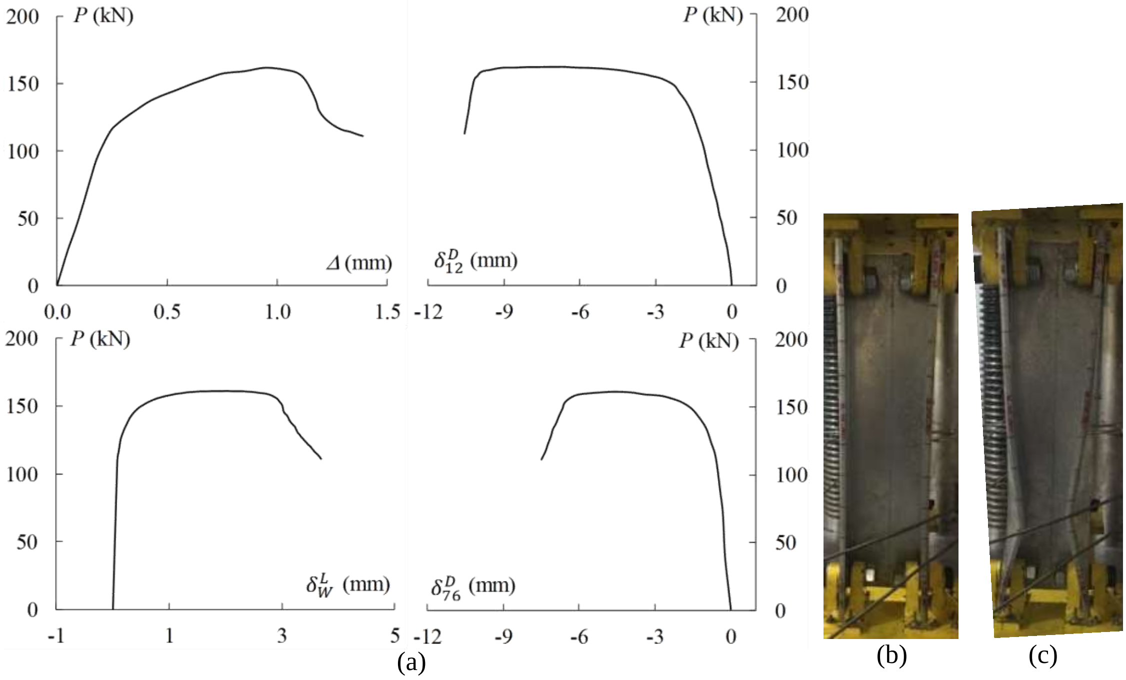

Figure A.9 - 130x91G-P_F column (a) experimental equilibrium paths P vs. Δ, δ_{12}^D, δ_{76}^D and δ_W^L, and column (b) before and (c) after the test.

5. 130x91C-P_F

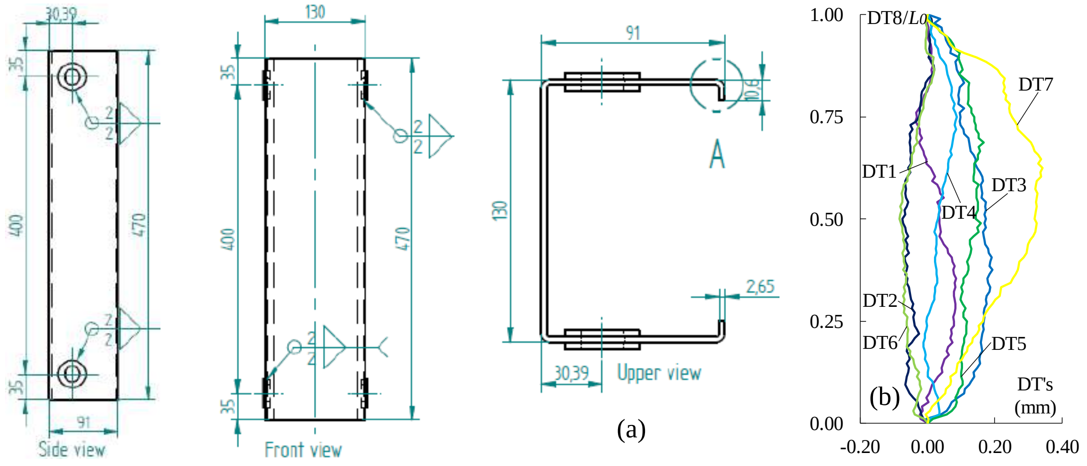

Figure A.10 - 130x91C-P_F column (a) design and (b) initial imperfection readings.

Table A.5 - Initial measures (mm), calculated area (cm²), squash and ultimate load (kN) for 130x91C-P_F column

Position	b_w	b_f		b_l		t					
	-	$b_{f.12}$	$b_{f.76}$	$b_{l.12}$	$b_{l.76}$	t_{12}	t_{76}	θ_1	θ_2	θ_3	θ_4
0	131.40	90.30	90.00	12.00	11.80	2.60	2.62	90.0	91.0	90.0	90.0
0.5L_0	131.40	90.30	90.30	12.00	11.80	2.60	2.61	90.0	90.0	90.0	90.0
L_0	132.00	90.00	90.30	11.80	11.40	2.61	2.61	90.0	90.0	90.0	90.0
Average	131.60	90.20		11.80		2.61					
	L_D	L_T	L_0	b_a	d_f	A		P_y		P_u	
Average	398	469	328	20.58	20.78	8.36		356.3		192.2	

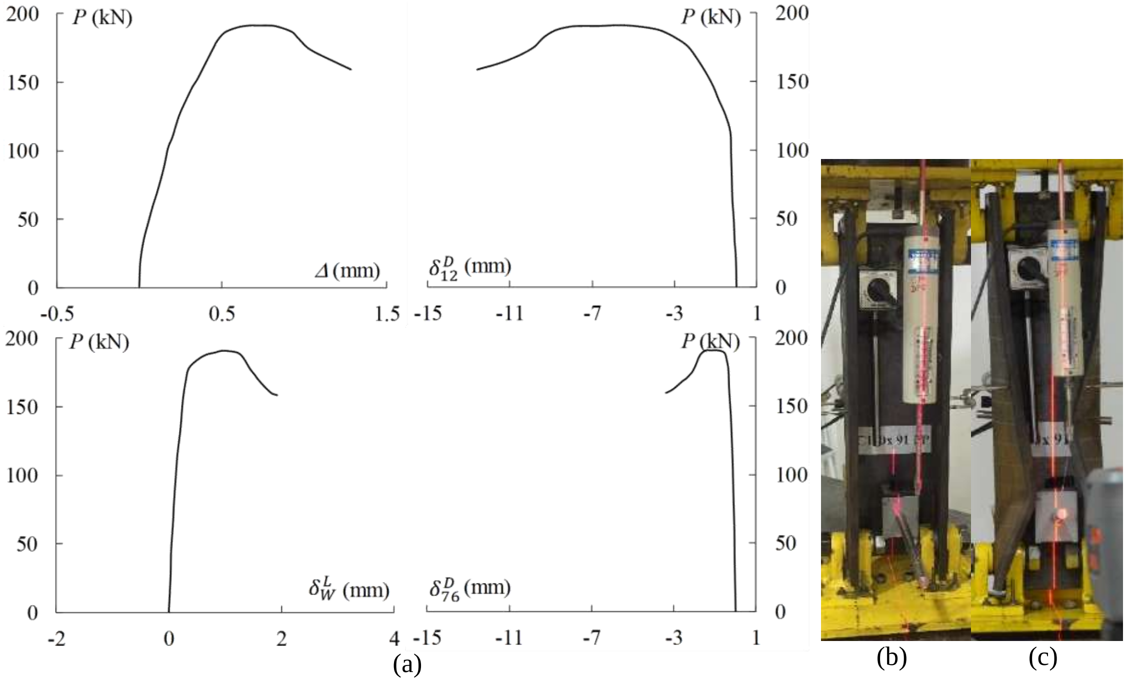

Figure A.11 - 130x91C-P_F column (a) experimental equilibrium paths P vs. Δ, δ^D_{12}, δ^D_{76} and δ^L_W, and column (b) before and (c) after the test.

6. 130x130C-P_B

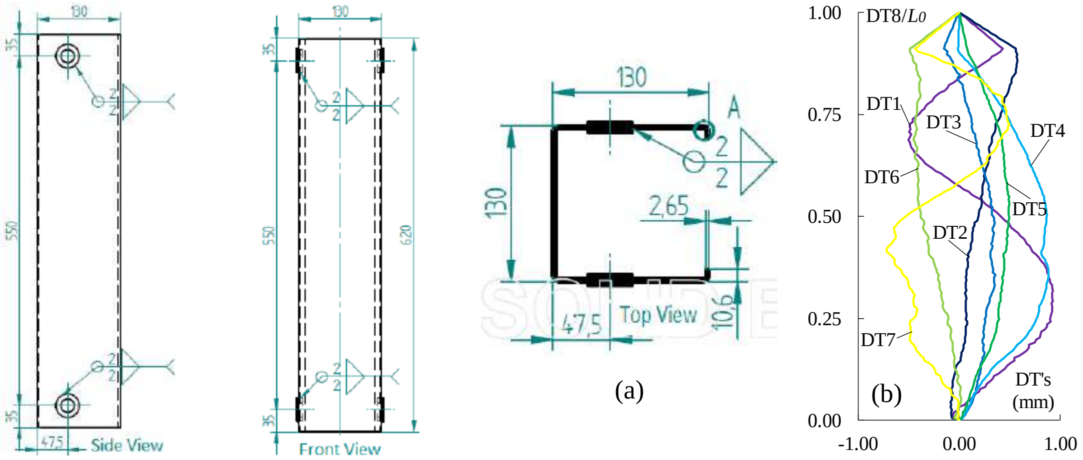

Figure A.12 - 130x130C-P_B column (a) design and (b) initial imperfection readings.

Table A.6 - Initial measures (mm), calculated area (cm²), squash and ultimate load (kN) for 130x130C-P_B column

Position	b_w	b_f		b_l		t					
	-	$b_{f.12}$	$b_{f.76}$	$b_{l.12}$	$b_{l.76}$	t_{12}	t_{76}	θ_1	θ_2	θ_3	θ_4
0	131.00	129.80	129.00	11.50	10.00	2.52	2.50	90.5	90.0	90.0	91.0
0.5L_0	131.40	129.00	129.50	12.30	10.00	2.50	2.50	90.0	90.0	90.0	90.0
L_0	132.00	127.50	130.00	12.30	9.50	2.50	2.50	91.0	90.0	90.0	90.5
Average	131.47	129.13		10.93		2.50					
	L_D	L_T	L_0	b_a	d_f	A		P_y		P_u	
Average	549	619	479	37.33	21.00	9.95		423.7		106.5	

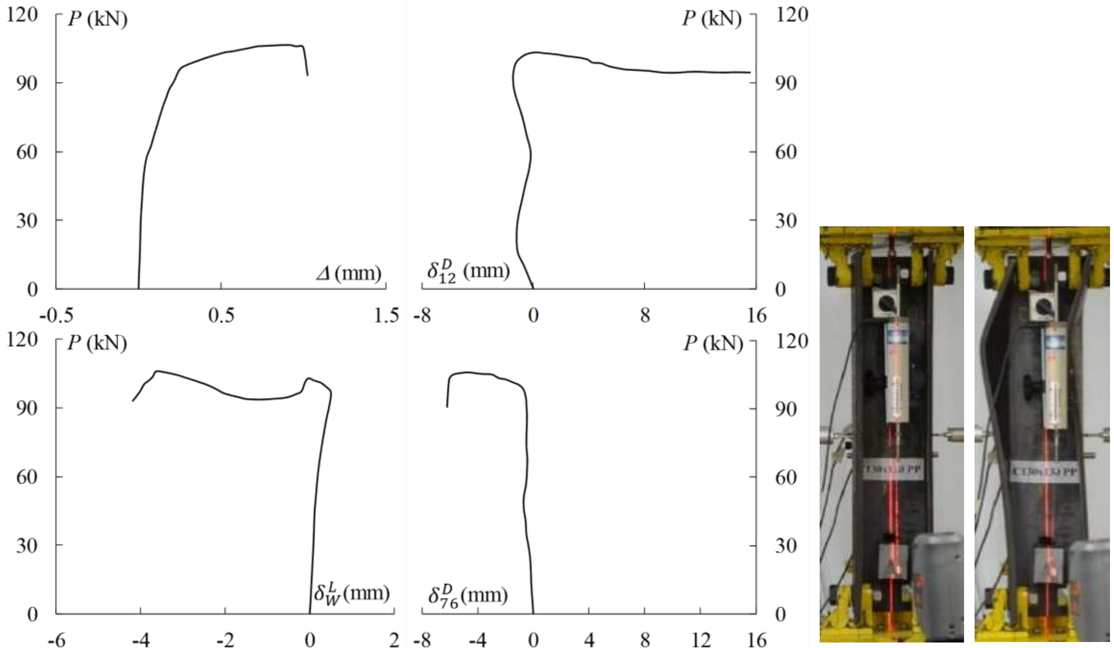

(a) (b) (c)

Figure A.13 - 130x130C-P_B column (a) experimental equilibrium paths P vs. Δ, δ_{12}^{D}, δ_{76}^{D} and δ_{W}^{L}, and column (b) before and (c) after the test.

7. 150x105G-P_F

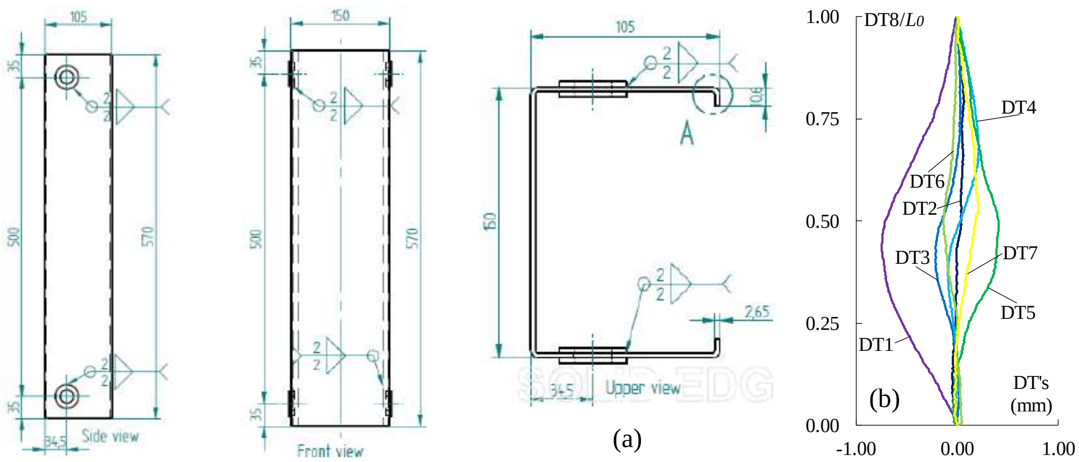

Figure A.14 - 150x105G-P_F column (a) design and (b) initial imperfection readings.

Table A.7 - Initial measures (mm), calculated area (cm²), squash and ultimate load (kN) for 150x105G-P_F column

Position	b_w	b_f		b_l		t					
	-	$b_{f.12}$	$b_{f.76}$	$b_{l.12}$	$b_{l.76}$	t_{12}	t_{76}	θ_1	θ_2	θ_3	θ_4
0	149.55	104.50	103.55	10.42	10.60	2.58	2.59	88.0	88.5	90.5	89.0
0.5L_0	149.56	105.95	103.10	10.77	10.40	2.54	2.74	89.5	88.5	91.0	88.0
L_0	149.92	104.60	103.12	10.33	10.60	2.54	2.59	91.0	89.0	92.0	89.0
Average	149.68	104.14		10.52		2.60					
	L_D	L_T	L_0	b_a	d_f	A		P_y		P_u	
Average	500	570	430	23.78	21.50	9.46		330.9		151.4	

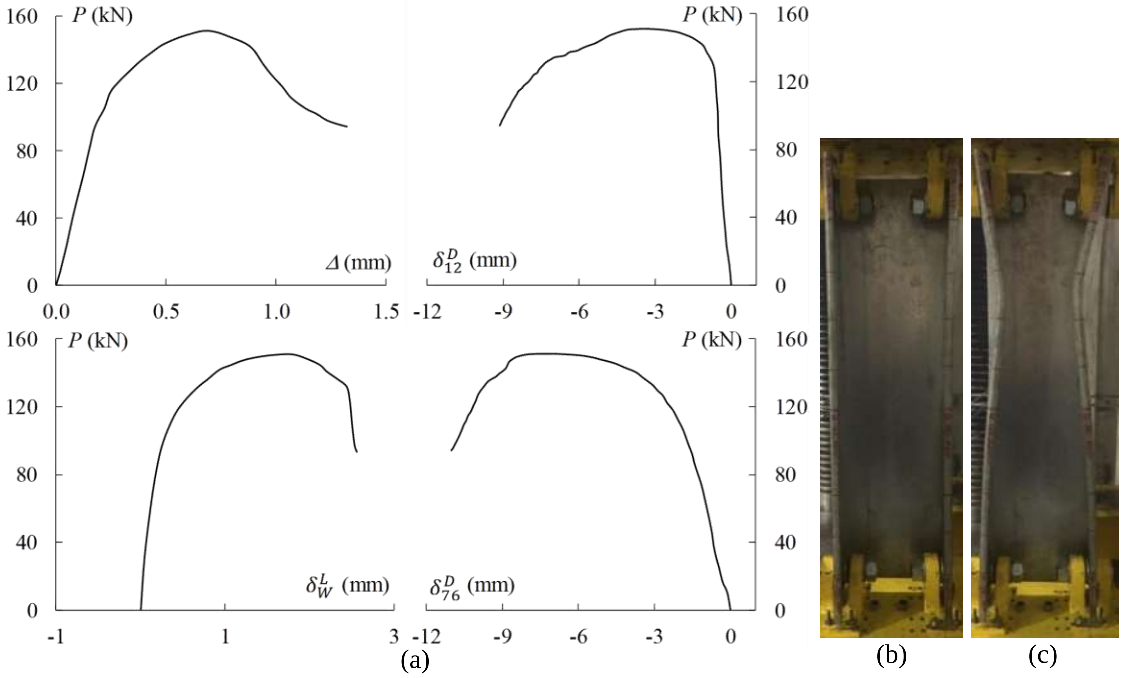

(a) (b) (c)

Figure A.15 - 150x105G-P_F column (a) experimental equilibrium paths P vs. Δ, δ_{12}^D, δ_{76}^D and δ_W^L, and column (b) before and (c) after the test.

8. 150x105C-P_F

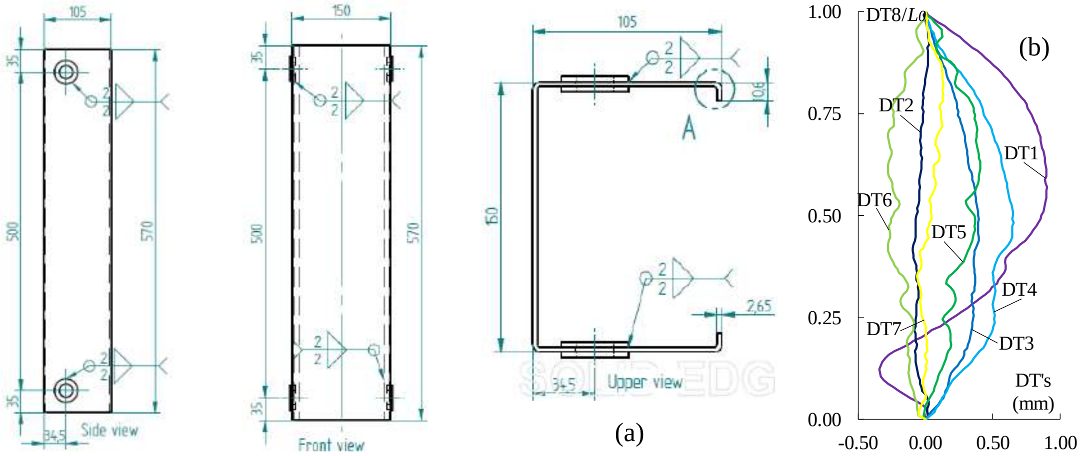

Figure A.16 - 150x105C-P_F column (a) design and (b) initial imperfection readings.

Table A.8 - Initial measures (mm), calculated area (cm²), squash and ultimate load (kN) for 150x105C-P_F column

Position	b_w	b_f		b_l		t					
	-	$b_{f.12}$	$b_{f.76}$	$b_{l.12}$	$b_{l.76}$	t_{12}	t_{76}	θ_1	θ_2	θ_3	θ_4
0	151.80	104.20	103.60	11.50	10.40	2.49	2.50	91.0	90.0	90.0	91.0
0.5L_0	151.40	104.00	104.00	11.50	11.20	2.50	2.50	90.0	89.0	90.0	91.0
L_0	151.40	103.00	103.00	11.50	11.50	2.51	2.51	90.0	90.0	90.0	91.0
Average	151.53	103.63		11.27		2.50					
	L_D	L_T	L_0	b_a	d_f	A		P_y		P_u	
Average	501	569	431	23.93	20.85	9.18		391.1		160.5	

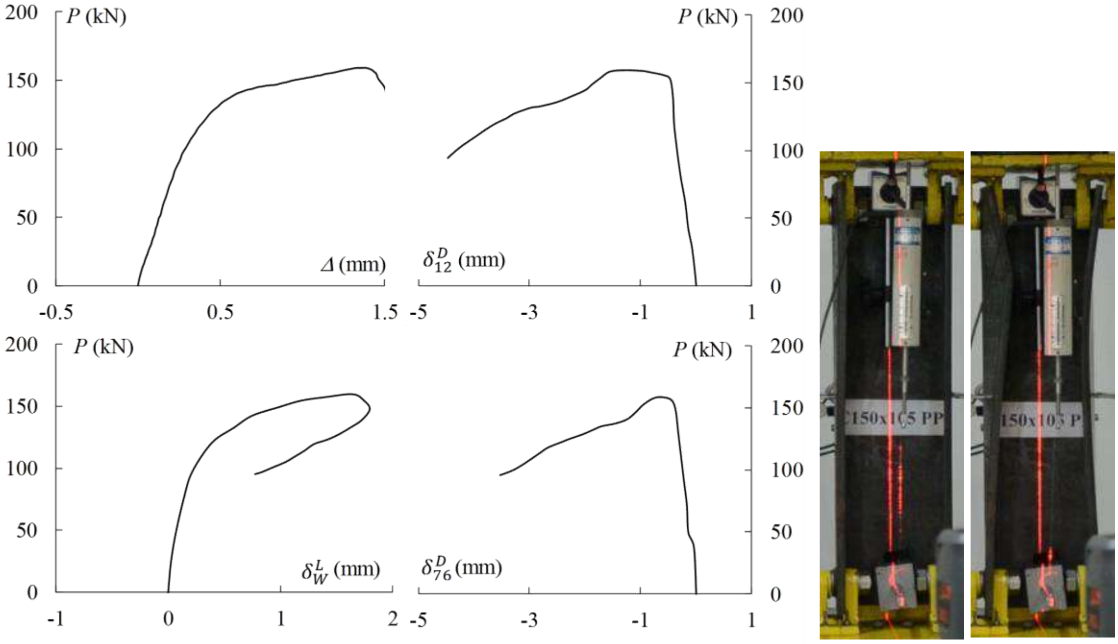

(a) (b) (c)

Figure A.17 - 150x105C-P_F column (a) experimental equilibrium paths P vs. Δ, δ_{12}^{D}, δ_{76}^{D} and δ_{W}^{L}, and column (b) before and (c) after the test.

9. 150x150C-P_B

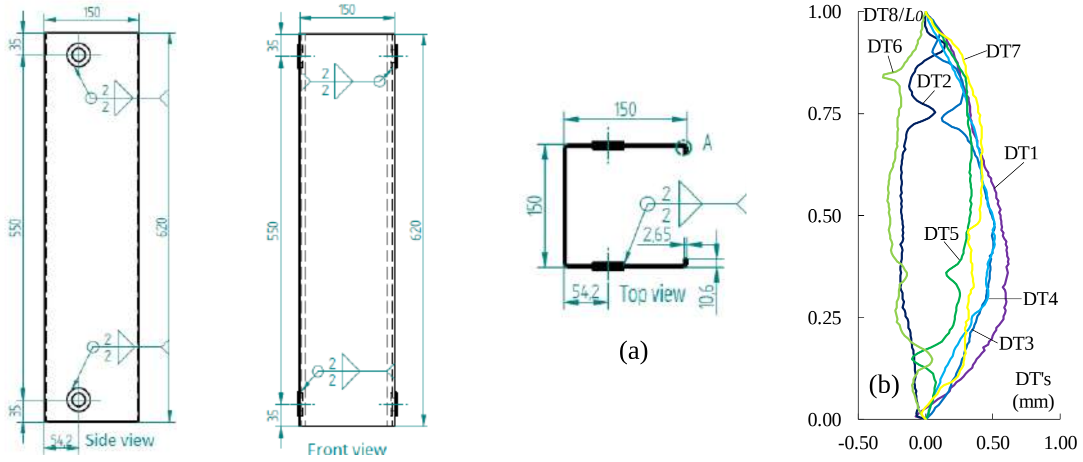

Figure A.18 - 150x150C-P_B column (a) design and (b) initial imperfection readings.

Table A.9 - Initial measures (mm), calculated area (cm²), squash and ultimate load (kN) for 150x150C-P_B column

Position	b_w	b_f		b_l		t					
	-	$b_{f.12}$	$b_{f.76}$	$b_{l.12}$	$b_{l.76}$	t_{12}	t_{76}	θ_1	θ_2	θ_3	θ_4
0	150.40	148.00	149.50	12.00	12.00	2.45	2.57	91.0	91.0	90.5	90.0
0.5L_0	150.80	148.00	149.30	12.30	12.80	2.45	2.54	91.0	90.0	90.5	90.0
L_0	151.60	147.50	148.20	12.00	12.60	2.48	2.52	91.0	90.0	90.5	90.0
Average	150.93	148.42		12.28		2.50					
	L_D	L_T	L_0	b_a	d_f	A		P_y		P_u	
Average	550	619	480	43.83	21.00	11.46		488.1		101.7	

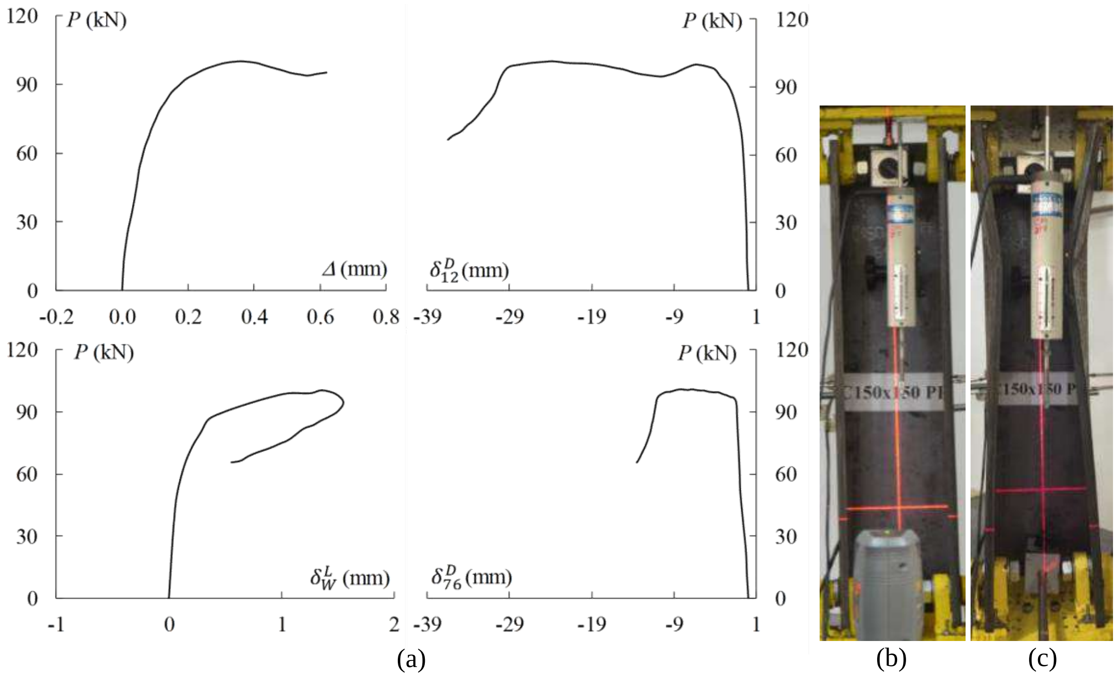

(a) (b) (c)

Figure A.19 - 150x150C-P_B column (a) experimental equilibrium paths P vs. Δ, δ_{12}^D, δ_{76}^D and δ_W^L, and column (b) before and (c) after the test.

10. 180x126C-P_F

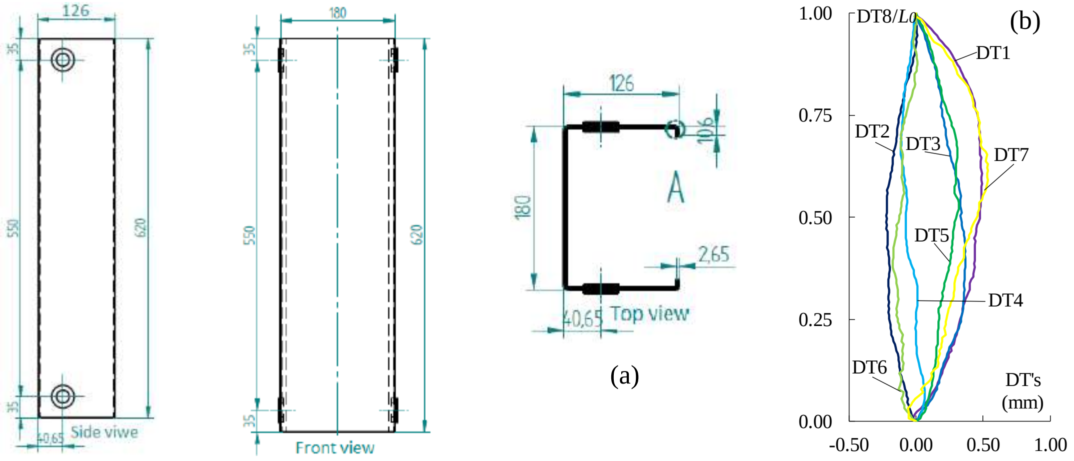

Figure A.20 - 180x126C-P_F column (a) design and (b) initial imperfection readings.

Table A.10 - Initial measures (mm), calculated area (cm²), squash and ultimate load (kN) for 180x126C-P_F column

Position	b_w	b_f		b_l		t					
	-	$b_{f.12}$	$b_{f.76}$	$b_{l.12}$	$b_{l.76}$	t_{12}	t_{76}	θ_1	θ_2	θ_3	θ_4
0	181.00	127.00	124.90	9.50	11.00	2.50	2.52	92.0	91.0	89.0	90.0
$0.5L_0$	181.00	127.00	125.80	10.00	11.20	2.51	2.53	92.0	90.5	90.0	90.0
L_0	181.00	126.60	125.80	9.30	11.20	2.52	2.54	92.0	90.5	90.0	90.0
Average	181.00	126.18		10.37		2.52					
	L_D	L_T	L_0	b_a	d_f	A		P_y		P_u	
Average	551	620	481	30.33	20.68	11.08		472.0		152.6	

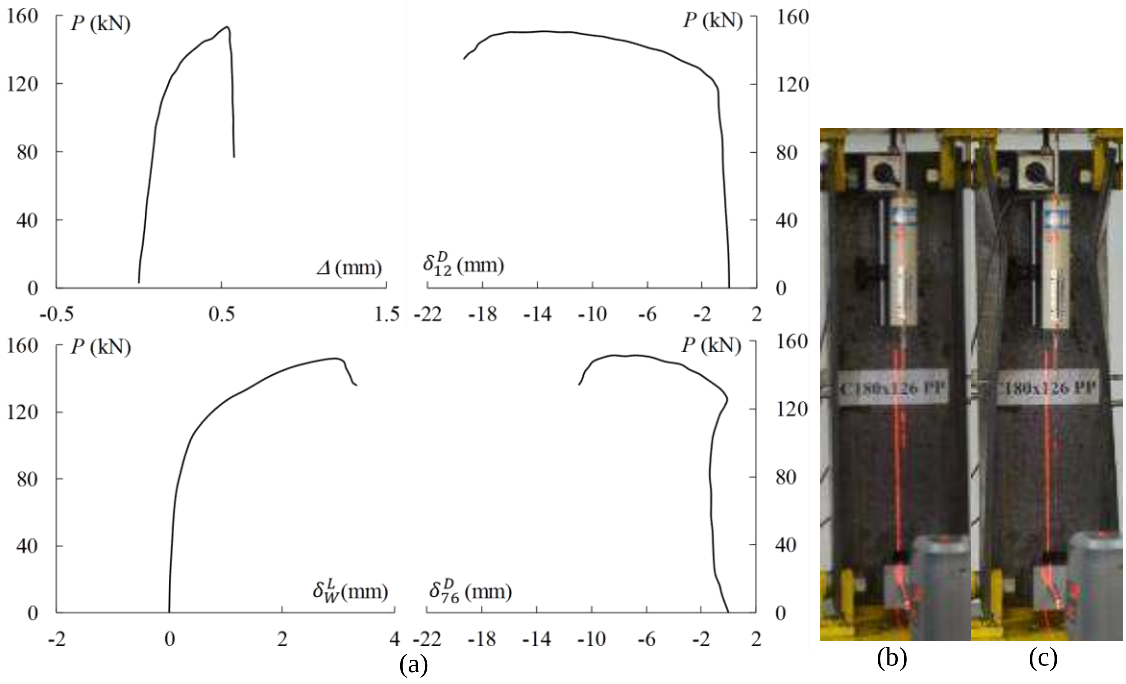

(a) (b) (c)

Figure A.21 - 180x126C-P_F column (a) experimental equilibrium paths P vs. Δ, δ_{12}^D, δ_{76}^D and δ_W^L, and column (b) before and (c) after the test.

11. 180x180C-P_B

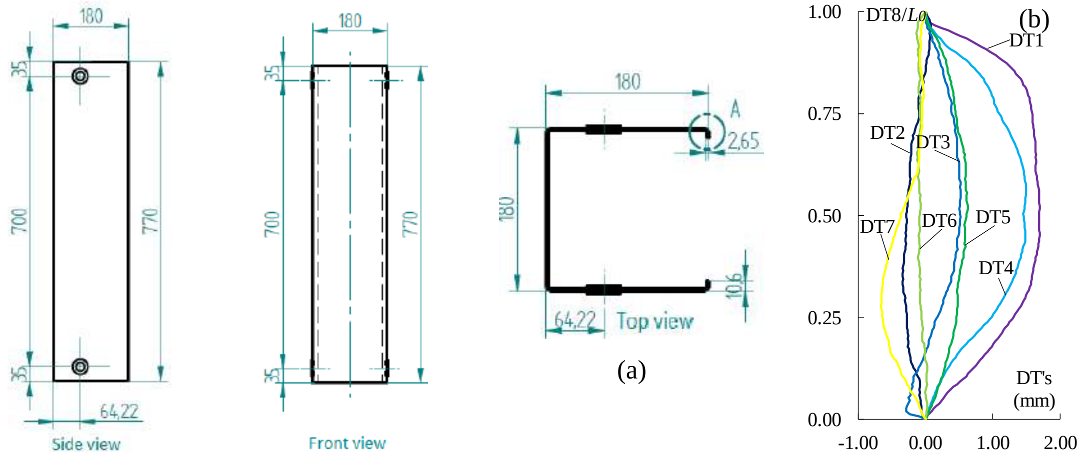

Figure A.22 - 180x180C-P_B column (a) design and (b) initial imperfection readings.

Table A.11 - Initial measures (mm), calculated area (cm²), squash and ultimate load (kN) for 180x180C-P_B column

Position	b_w	b_f		b_l		t					
	-	$b_{f.12}$	$b_{f.76}$	$b_{l.12}$	$b_{l.76}$	t_{12}	t_{76}	θ_1	θ_2	θ_3	θ_4
0	180.20	179.60	178.00	11.60	11.10	2.47	2.43	89.0	90.0	91.0	91.0
0.5L_0	180.30	180.00	179.10	12.00	10.80	2.46	2.42	92.0	90.0	89.0	92.0
L_0	181.30	179.80	179.50	11.40	10.00	2.47	2.41	90.0	90.0	89.0	92.0
Average	180.60	179.33		11.15		2.44					
	L_D	L_T	L_0	b_a	d_f	A		P_y		P_u	
Average	701	770	631	54.10	20.63	13.38		570.0		90.8	

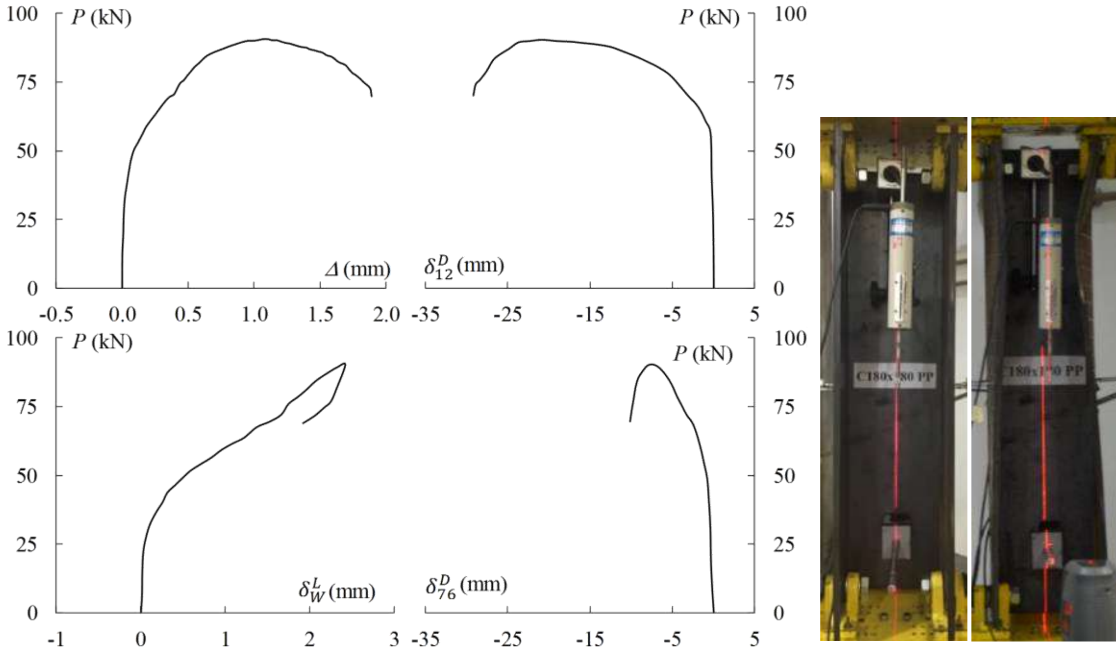

(a) (b) (c)

Figure A.23 - 180x180C-P_B column (a) experimental equilibrium paths P vs. Δ, δ_{12}^{D}, δ_{76}^{D} and δ_{W}^{L}, and column (b) before and (c) after the test.

12. 200x140C-P_B

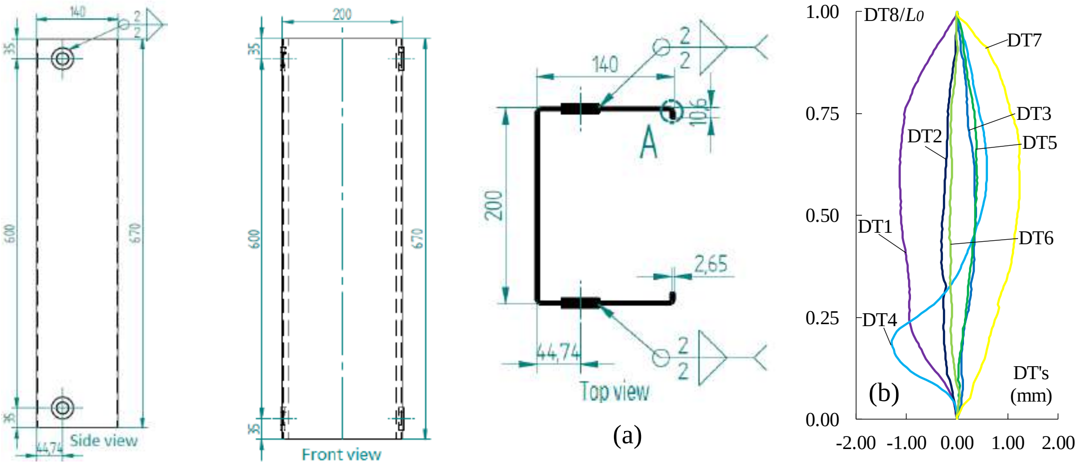

Figure A.24 - 200x140C-P_B column (a) design and (b) initial imperfection readings.

Table A.12 - Initial measures (mm), calculated area (cm²), squash and ultimate load (kN) for 200x140C-P_B column

Position	b_w	b_f		b_l		t					
	-	$b_{f.12}$	$b_{f.76}$	$b_{l.12}$	$b_{l.76}$	t_{12}	t_{76}	θ_1	θ_2	θ_3	θ_4
0	200.00	140.00	138.80	11.00	10.80	2.40	2.45	90.0	90.0	90.0	90.0
$0.5L_0$	199.80	139.70	139.40	11.50	11.40	2.45	2.44	90.0	90.0	89.0	90.0
L_0	199.20	139.00	139.40	11.80	10.90	2.43	2.49	90.0	91.0	90.5	90.0
Average	199.67	139.38		11.23		2.44					
	L_D	L_T	L_0	b_a	d_f	A		P_y		P_u	
Average	599	667	529	34.98	21.00	11.90		506.8		121.0	

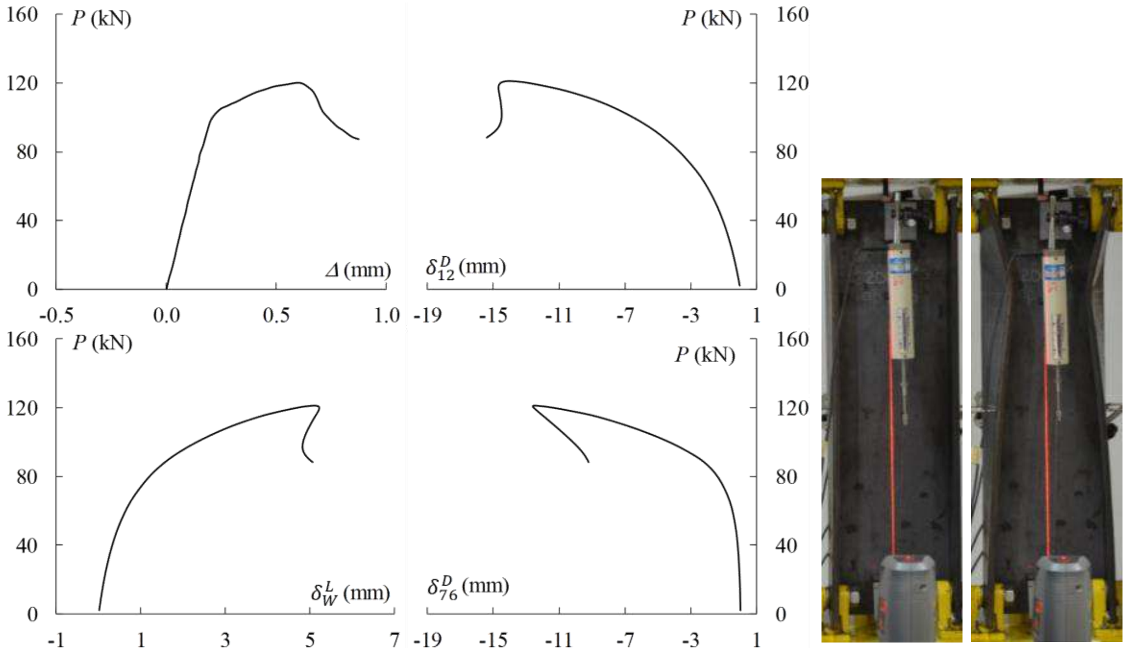

Figure A.25 - 200x140C-P_B column (a) experimental equilibrium paths P vs. $\varDelta$, δ^D_{12}, δ^D_{76} and δ^L_W, and column (b) before and (c) after the test.

13. 200x200C-P_B

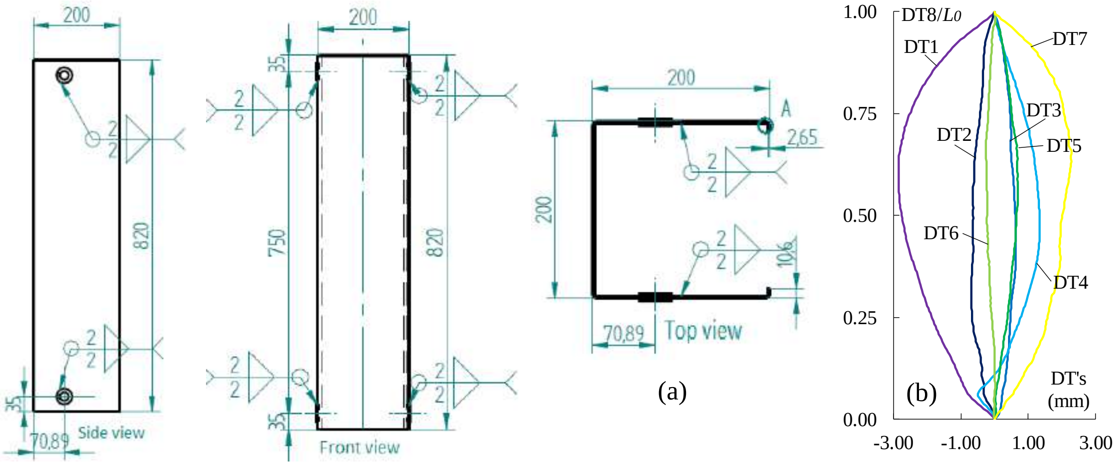

Figure A.26 - 200x200C-P_B column (a) design and (b) initial imperfection readings.

Table A.13 - Initial measures (mm), calculated area (cm²), squash and ultimate load (kN) for 200x200C-P_B column

Position	b_w	b_f		b_l		t					
	-	$b_{f.12}$	$b_{f.76}$	$b_{l.12}$	$b_{l.76}$	t_{12}	t_{76}	θ_1	θ_2	θ_3	θ_4
0	200.00	200.00	198.40	10.90	11.10	2.47	2.50	91.0	90.0	90.0	92.0
0.5L_0	199.50	199.00	199.00	11.30	11.20	2.46	2.49	92.0	90.0	92.0	92.0
L_0	200.00	198.50	199.00	10.20	10.80	2.44	2.48	92.0	89.0	91.0	92.0
Average	199.83	198.98		10.92		2.47					
	L_D	L_T	L_0	b_a	d_f	A		P_y		P_u	
Average	752	821	682	60.65	20.70	14.98		638.0		86.0	

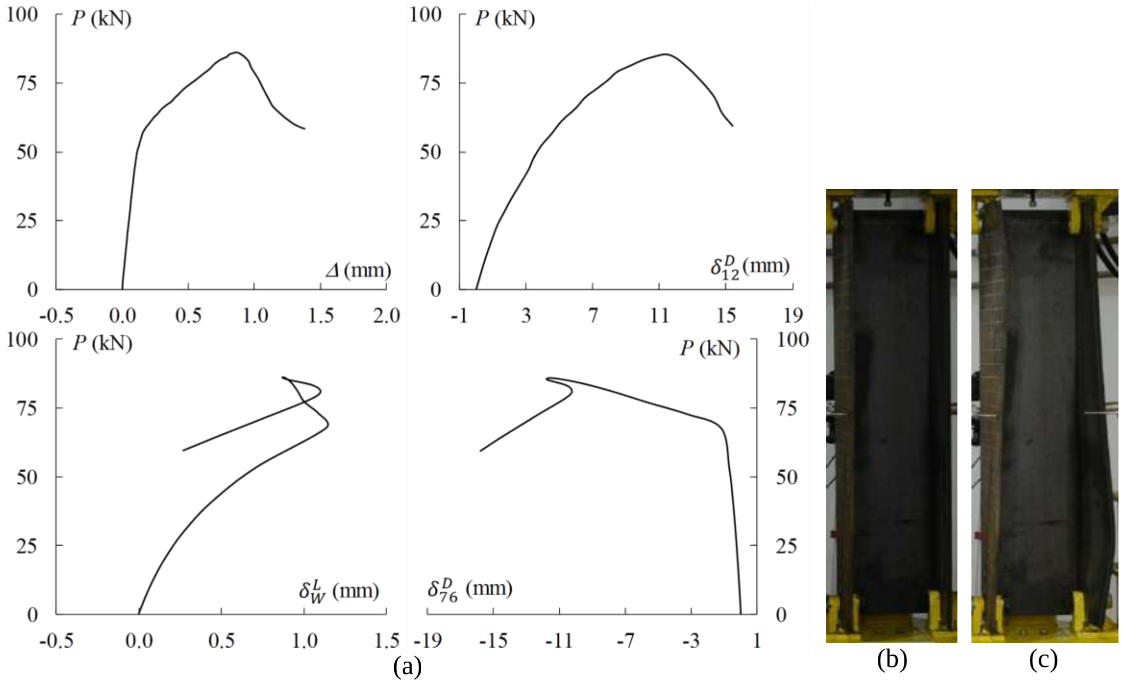

Figure A.27 - 200x200C-P_B column (a) experimental equilibrium paths P vs. Δ, δ_{12}^D, δ_{76}^D and δ_W^L, and column (b) before and (c) after the test.

14. 100x70C-PF_F

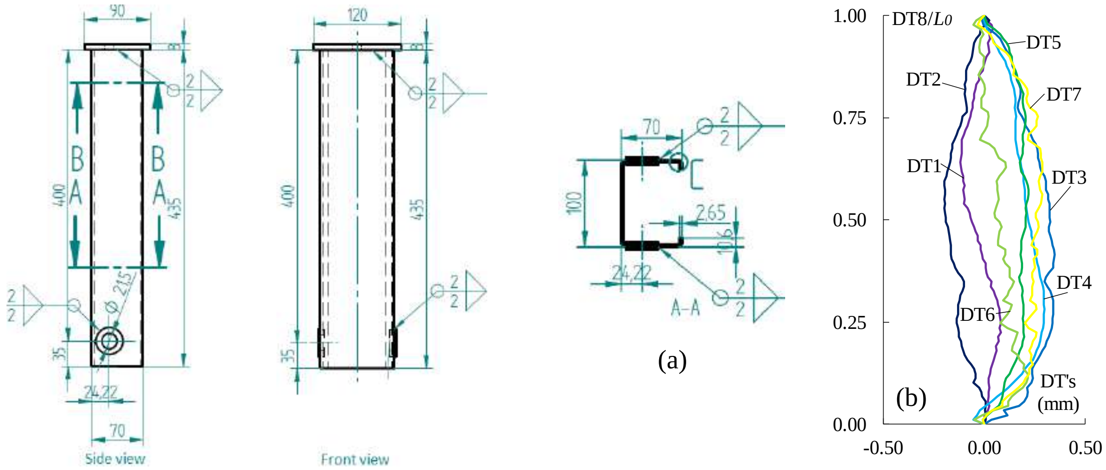

Figure A.28 - 100x70C-PF_F column (a) design and (b) initial imperfection readings.

Table A.14 - Initial measures (mm), calculated area (cm²), squash and ultimate load (kN) for 100x70C-PF_F column

Position	b_w	b_f		b_l		t					
	-	$b_{f.12}$	$b_{f.76}$	$b_{l.12}$	$b_{l.76}$	t_{12}	t_{76}	θ_1	θ_2	θ_3	θ_4
0	101.00	68.80	69.00	12.00	10.40	2.49	2.47	90.0	90.0	90.0	91.0
0.5L_0	100.40	69.50	69.00	11.00	10.90	2.42	2.37	90.0	90.0	90.0	90.0
L_0	100.20	70.30	69.00	10.00	11.00	2.47	2.42	89.0	90.0	90.0	90.0
Average	100.53	69.27		10.88		2.44					
	L_D	L_T	L_0	b_a	d_f	A		P_y		P_u	
Average	400	435	365	14.25	21.00	6.02		256.6		167.0	

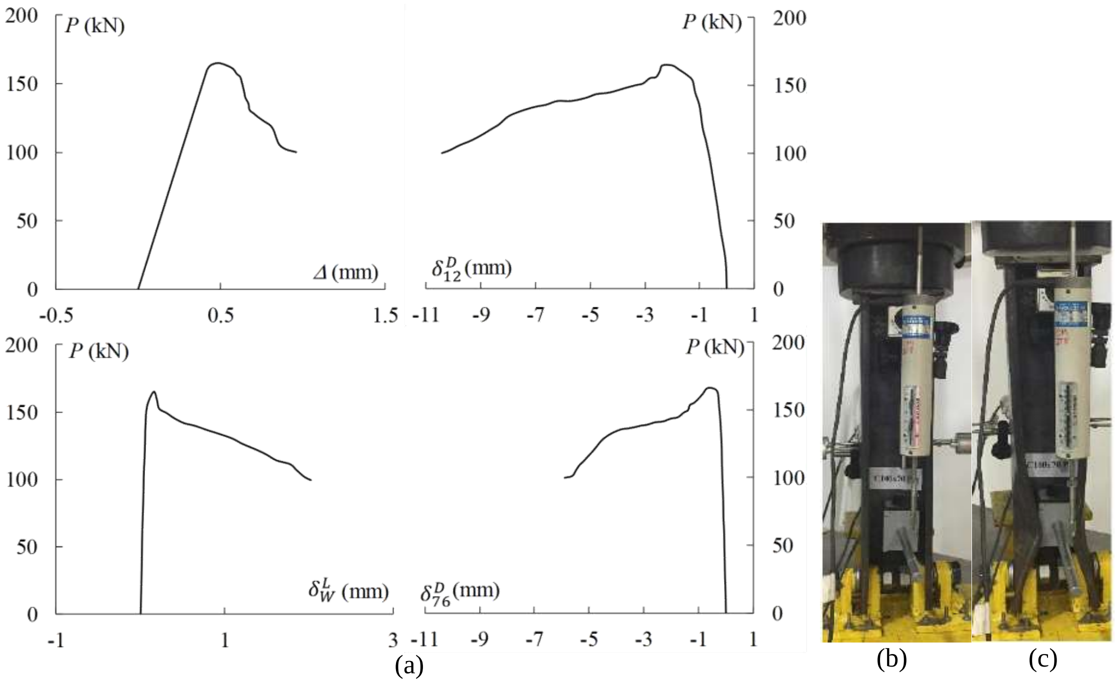

(a) (b) (c)

Figure A.29 - 100x70C-PF_F column (a) experimental equilibrium paths P *vs.* Δ, δ^D_{12}, δ^D_{76} and δ^L_W, and column (b) before and (c) after the test.

15. 100x100C-PF_F

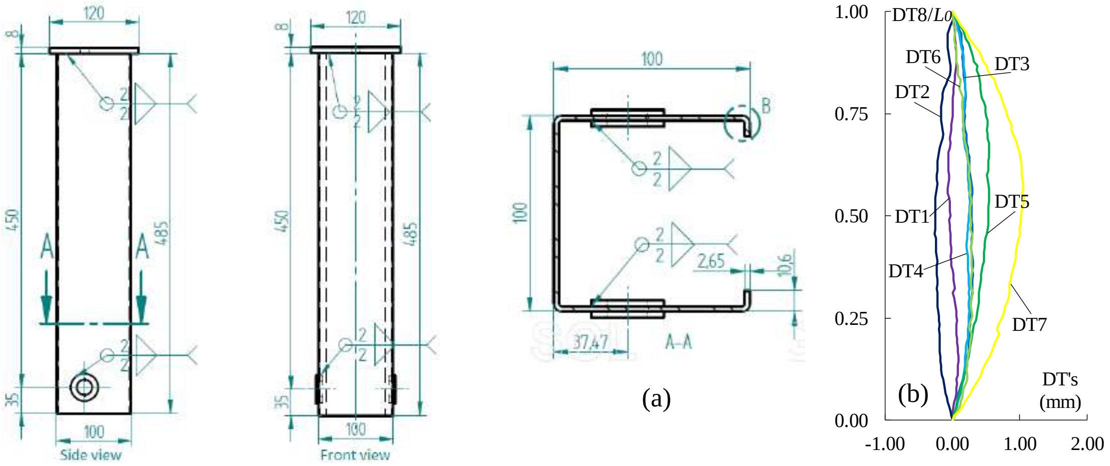

Figure A.30 - 100x100C-PF_F column (a) design and (b) initial imperfection readings.

Table A.15 - Initial measures (mm), calculated area (cm²), squash and ultimate load (kN) for 100x100C-PF_F column

Position	b_w	b_f		b_l		t					
	-	$b_{f.12}$	$b_{f.76}$	$b_{l.12}$	$b_{l.76}$	t_{12}	t_{76}	θ_1	θ_2	θ_3	θ_4
0	102.00	99.00	98.00	11.10	10.50	2.40	2.40	90.0	90.0	90.0	90.0
0.5L_0	102.00	99.00	98.80	11.00	10.50	2.40	2.40	90.0	90.0	90.0	90.0
L_0	102.20	99.00	98.90	10.60	10.70	2.40	2.40	90.0	90.0	90.0	90.0
Average	102.07	98.78		10.73		2.40					
	L_D	L_T	L_0	b_a	d_f	A		P_y		P_u	
Average	450	485	415	27.20	21.00	7.38		314.3		144.2	

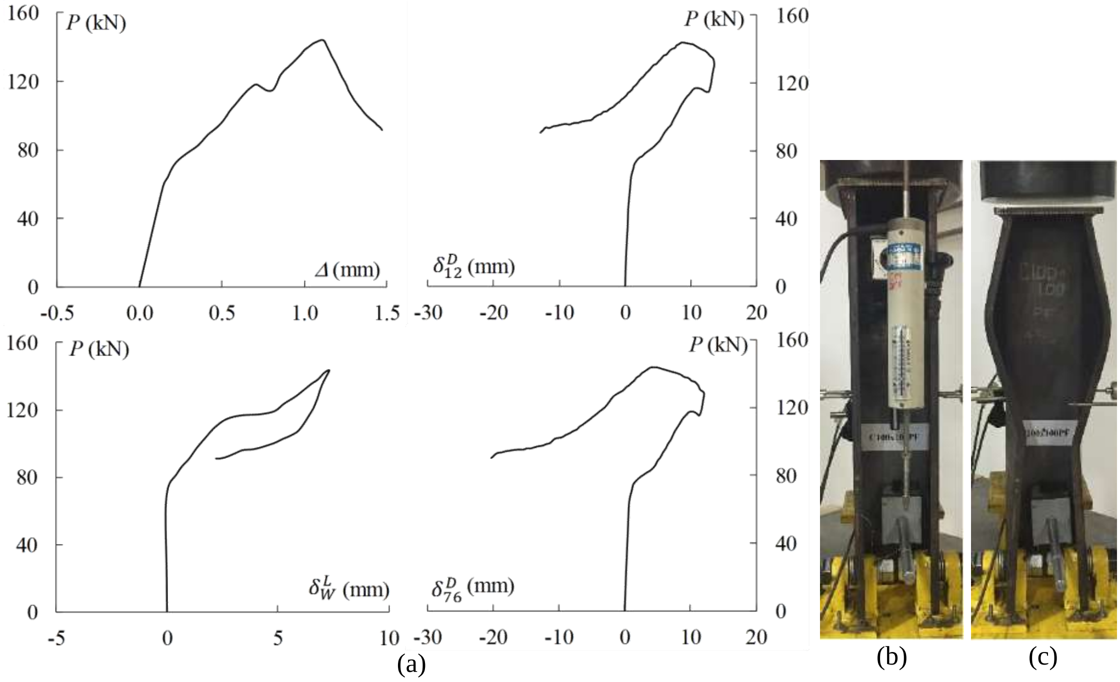

(a) (b) (c)

Figure A.31 - 100x100C-PF_F column (a) experimental equilibrium paths P vs. Δ, δ_{12}^D, δ_{76}^D and δ_W^L, and column (b) before and (c) after the test.

16. 130x91C-PF_F

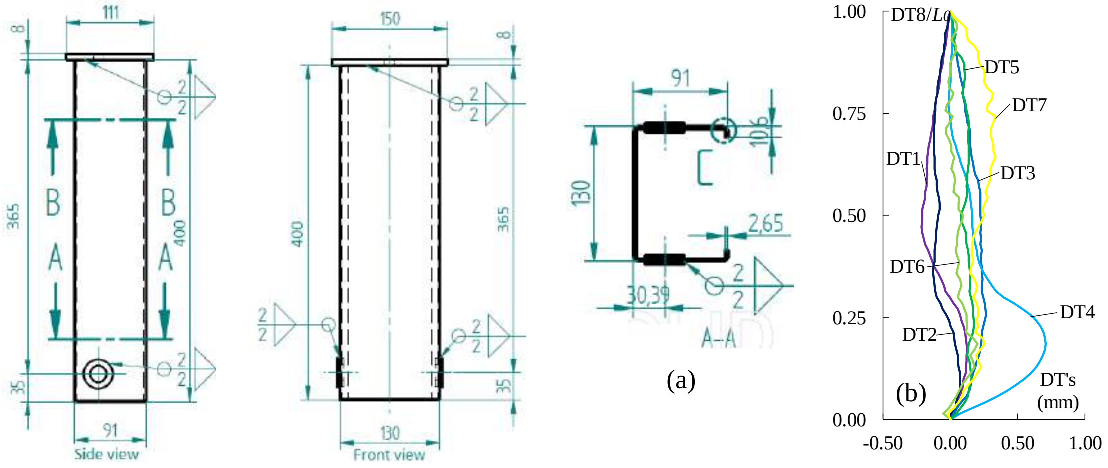

Figure A.32 - 130x91C-PF_F column (a) design and (b) initial imperfection readings.

Table A.16 - Initial measures (mm), calculated area (cm²), squash and ultimate load (kN) for 130x91C-PF_F column

Position	b_w	b_f		b_l		t					
	-	$b_{f.12}$	$b_{f.76}$	$b_{l.12}$	$b_{l.76}$	t_{12}	t_{76}	θ_1	θ_2	θ_3	θ_4
0	131.70	90.20	91.40	9.20	11.50	2.63	2.46	90.0	90.0	90.0	90.0
0.5L_0	130.80	90.80	91.60	10.20	12.50	2.58	2.45	90.0	90.0	90.0	91.0
L_0	130.40	90.70	90.40	11.80	11.30	2.52	2.52	90.0	90.0	90.0	90.0
Average	130.97	90.85		11.08		2.53					
	L_D	L_T	L_0	b_a	d_f	A		P_y		P_u	
Average	366	400	331	20.70	21.00	8.10		344.9		183.0	

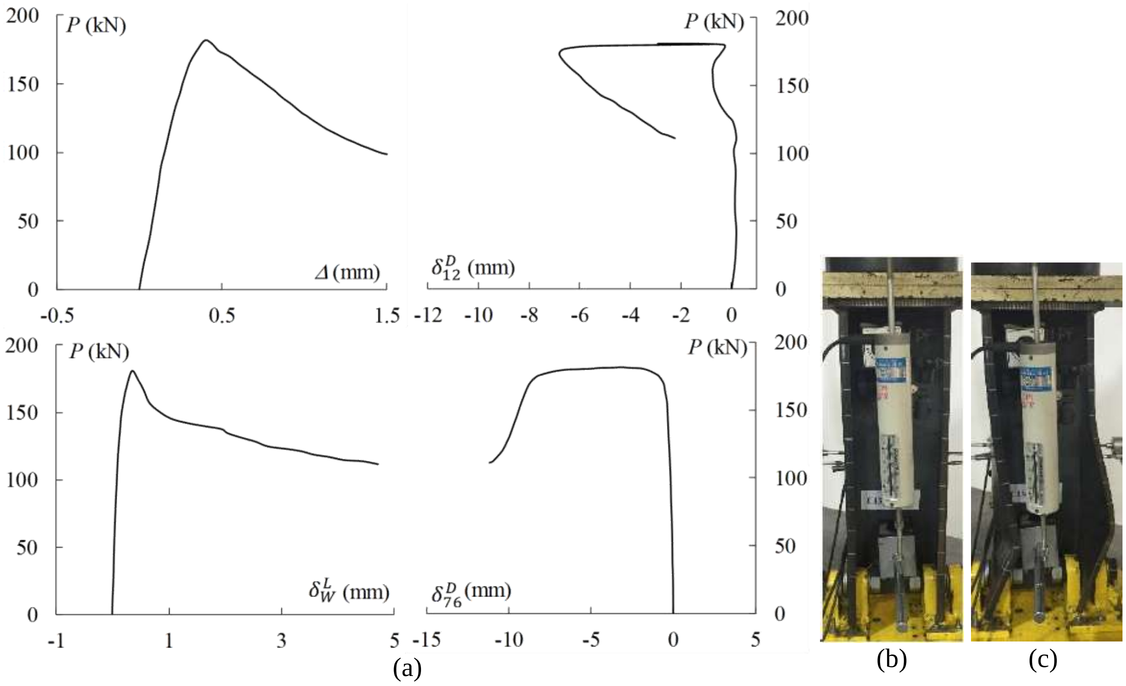

(a) (b) (c)

Figure A.33 - 130x91C-PF_F column (a) experimental equilibrium paths P *vs.* Δ, δ_{12}^D, δ_{76}^D and δ_W^L, and column (b) before and (c) after the test.

17. 130x130C-PF_F

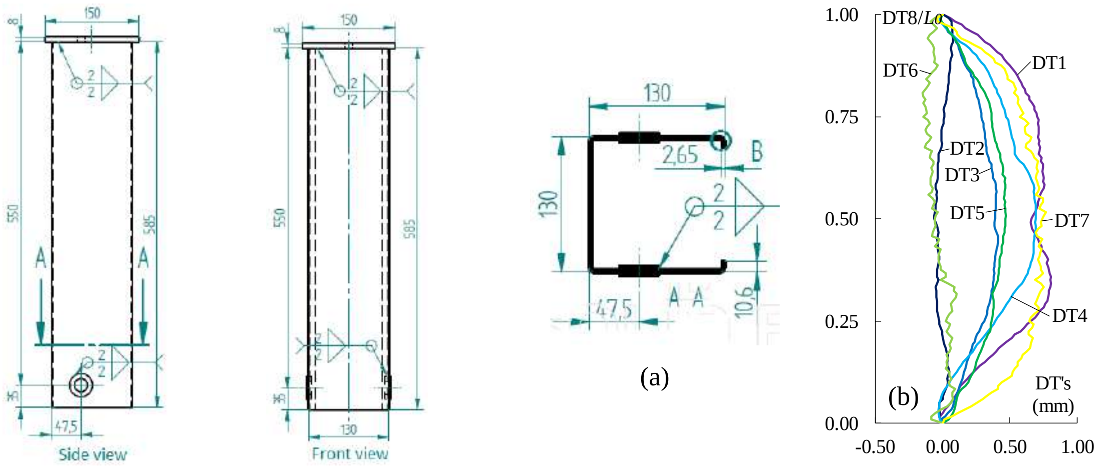

Figure A.34 - 130x130C-PF_F column (a) design and (b) initial imperfection readings.

Table A.17 - Initial measures (mm), calculated area (cm²), squash and ultimate load (kN) for 130x130C-PF_F column

Position	b_w	b_f		b_l		t					
	-	$b_{f.12}$	$b_{f.76}$	$b_{l.12}$	$b_{l.76}$	t_{12}	t_{76}	θ_1	θ_2	θ_3	θ_4
0	133.00	128.00	127.50	11.50	11.50	2.43	2.39	91.0	90.0	89.0	90.0
$0.5L_0$	132.00	128.40	128.40	11.50	12.10	2.44	2.42	90.0	91.0	90.0	90.0
L_0	131.40	128.40	128.60	10.40	11.90	2.42	2.44	90.0	90.0	90.0	90.0
Average	132.13	128.22		11.48		2.42					
	L_D	L_T	L_0	b_a	d_f	A		P_y		P_u	
Average	549	583	514	37.00	21.00	9.64		410.5		134.0	

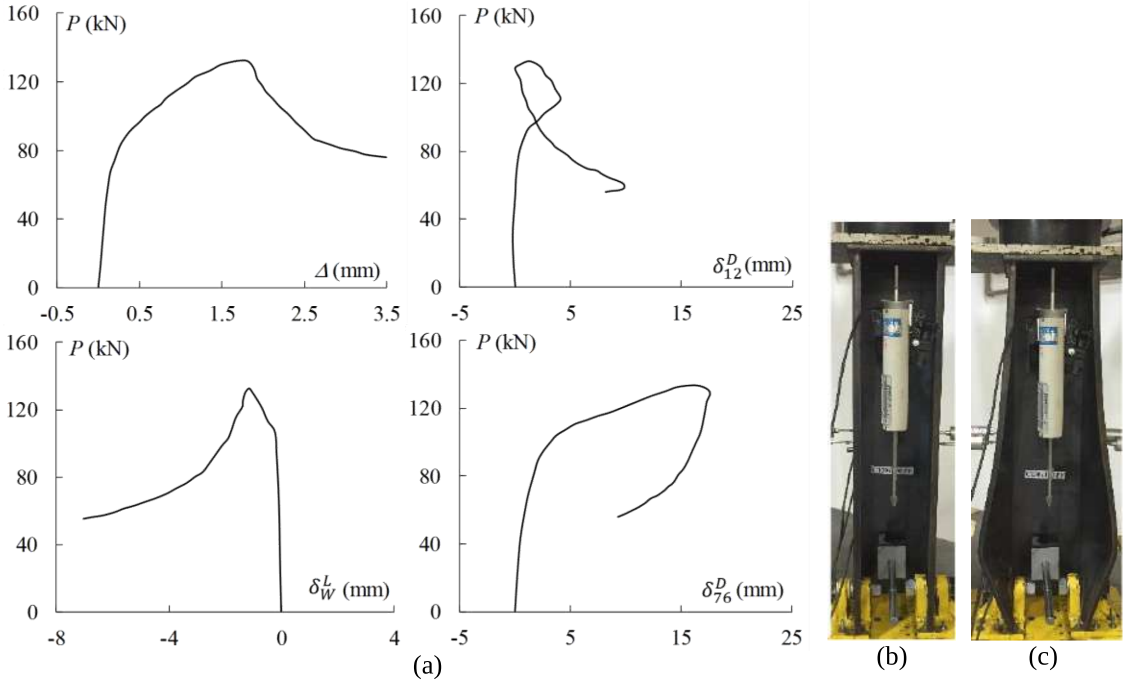

(a) (b) (c)

Figure A.35 - 130x130C-PF_F column (a) experimental equilibrium paths P *vs.* Δ, δ_{12}^D, δ_{76}^D and δ_W^L, and column (b) before and (c) after the test.

18. 150x105C-*PF*

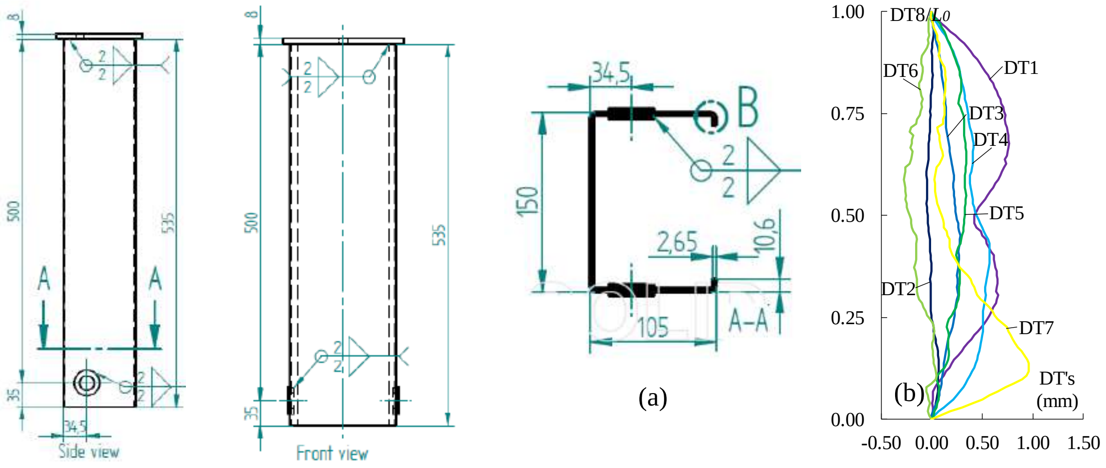

Figure A.36 - 150x105C-*PF*$_F$ column (a) design and (b) initial imperfection readings.

Table A.18 - Initial measures (mm), calculated area (cm²), squash and ultimate load (kN) for 150x105C-*PF*$_F$ column

Position	b_w	b_f		b_l		t					
	-	$b_{f.12}$	$b_{f.76}$	$b_{l.12}$	$b_{l.76}$	t_{12}	t_{76}	θ_1	θ_2	θ_3	θ_4
0	149.80	105.50	103.80	11.80	10.90	2.60	2.50	90.0	90.0	92.0	89.0
0.5L_0	150.10	104.60	104.00	12.00	11.40	2.59	2.50	90.0	90.5	90.0	90.0
L_0	150.70	103.40	103.80	12.20	12.00	2.58	2.55	89.0	90.0	89.5	91.0
Average	150.20	104.18		11.72		2.55					
	L_D	L_T	L_0	b_a	d_f	A		P_y		P_u	
Average	499	532	464	24.95	21.00	9.38		399.6		176.7	

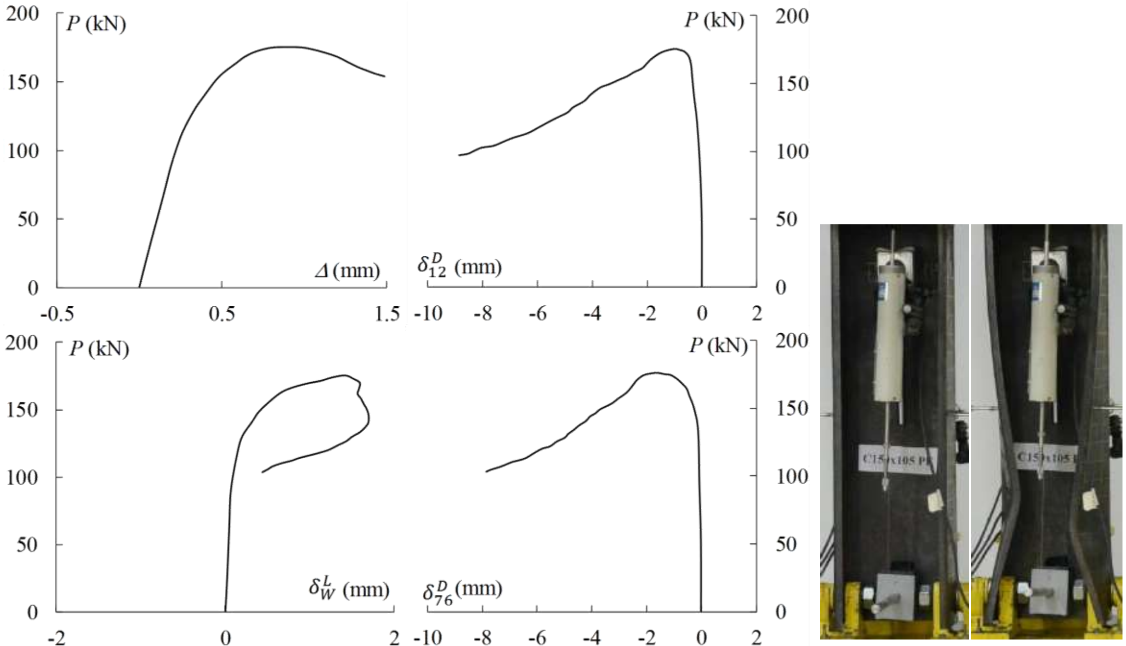

(a) (b) (c)

Figure A.37 - 150x105C-*PF*$_F$ column (a) experimental equilibrium paths *P vs.* Δ, δ^D_{12}, δ^D_{76} and δ^L_W, and column (b) before and (c) after the test.

19. 150x150C-PF_B

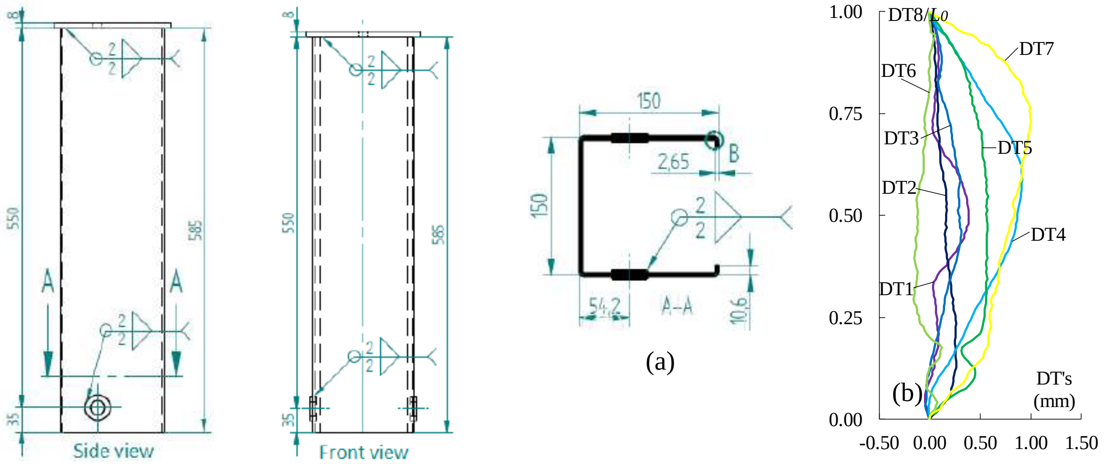

Figure A.38 - 150x150C-PF_B column (a) design and (b) initial imperfection readings.

Table A.19 - Initial measures (mm), calculated area (cm²), squash and ultimate load (kN) for 150x150C-PF_B column

Position	b_w	b_f		b_l		t					
	-	$b_{f.12}$	$b_{f.76}$	$b_{l.12}$	$b_{l.76}$	t_{12}	t_{76}	θ_1	θ_2	θ_3	θ_4
0	151.30	150.70	149.30	11.00	11.70	2.48	2.55	89.0	90.0	90.5	89.0
0.5L_0	151.30	150.30	149.40	11.70	11.80	2.50	2.54	89.5	90.0	89.5	90.0
L_0	151.00	149.20	148.70	11.60	11.60	2.47	2.54	89.5	90.0	90.5	90.0
Average	151.20	149.60		11.57		2.51					
	L_D	L_T	L_0	b_a	d_f	A		P_y		P_u	
Average	550	586	515	44.85	20.35	11.54		491.6		116.2	

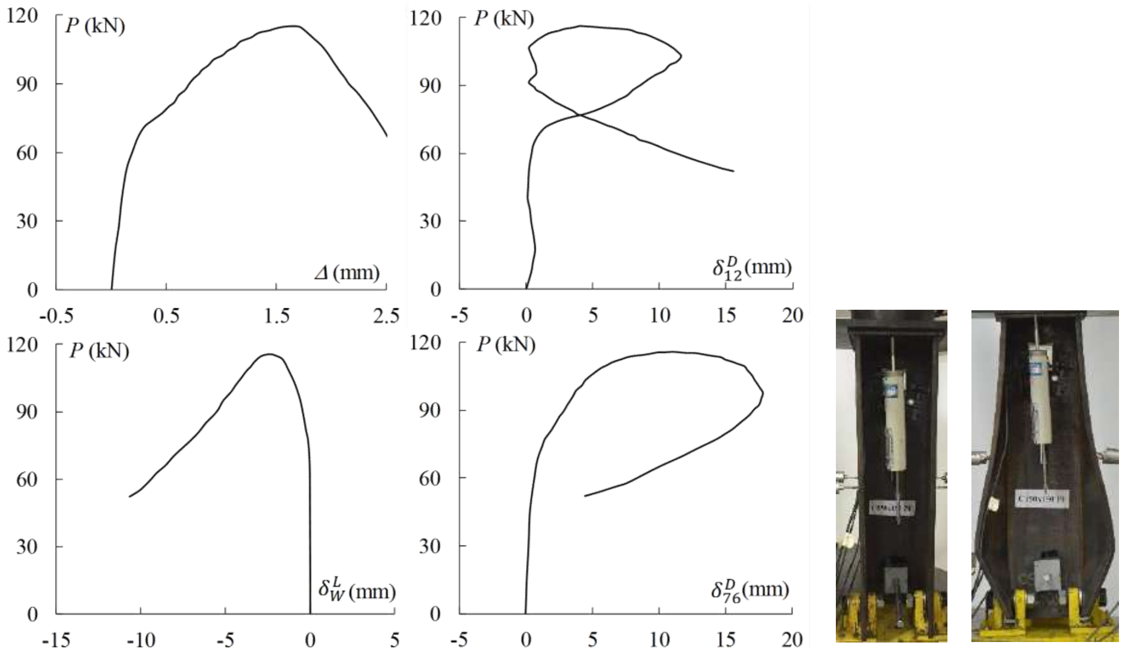

(a) (b) (c)

Figure A.39 - 150x150C-PF_B column (a) experimental equilibrium paths P vs. Δ, δ_{12}^{D}, δ_{76}^{D} and δ_{W}^{L}, and column (b) before and (c) after the test.

20. 180x126C-PF_F

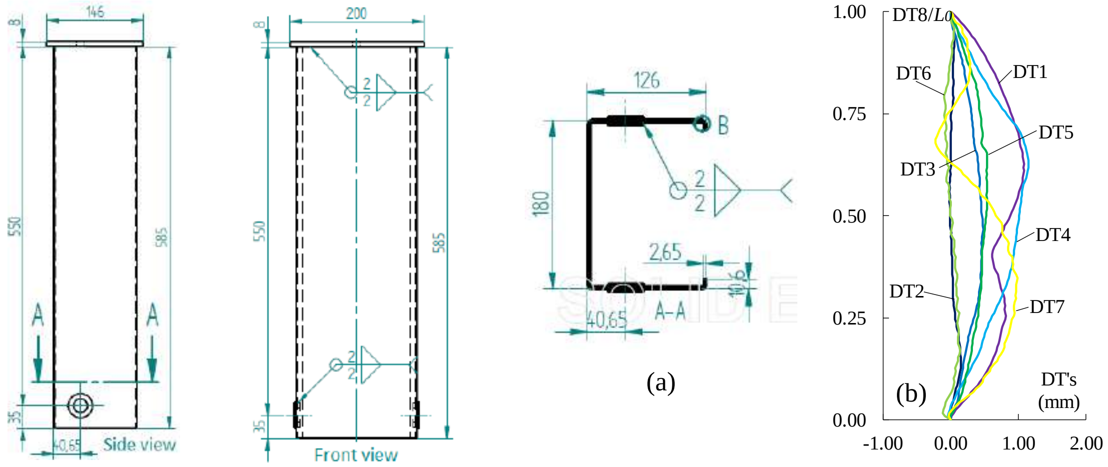

Figure A.40 - 180x126C-PF_F column (a) design and (b) initial imperfection readings.

Table A.20 - Initial measures (mm), calculated area (cm²), squash and ultimate load (kN) for 180x126C-PF_F column

Position	b_w	b_f		b_l		t					
	-	$b_{f.12}$	$b_{f.76}$	$b_{l.12}$	$b_{l.76}$	t_{12}	t_{76}	θ_1	θ_2	θ_3	θ_4
0	181.20	125.60	125.20	11.00	10.50	2.44	2.45	90.0	90.0	90.0	90.0
$0.5L_0$	181.80	125.20	125.30	11.50	11.20	2.42	2.44	90.0	89.5	90.0	90.0
L_0	180.90	124.70	124.90	11.50	11.40	2.44	2.42	90.0	90.0	90.0	90.0
Average	181.30	125.15		11.18		2.44					
	L_D	L_T	L_0	b_a	d_f	A		P_y		P_u	
Average	550	585	515	30.40	21.00	10.72		456.5		144.0	

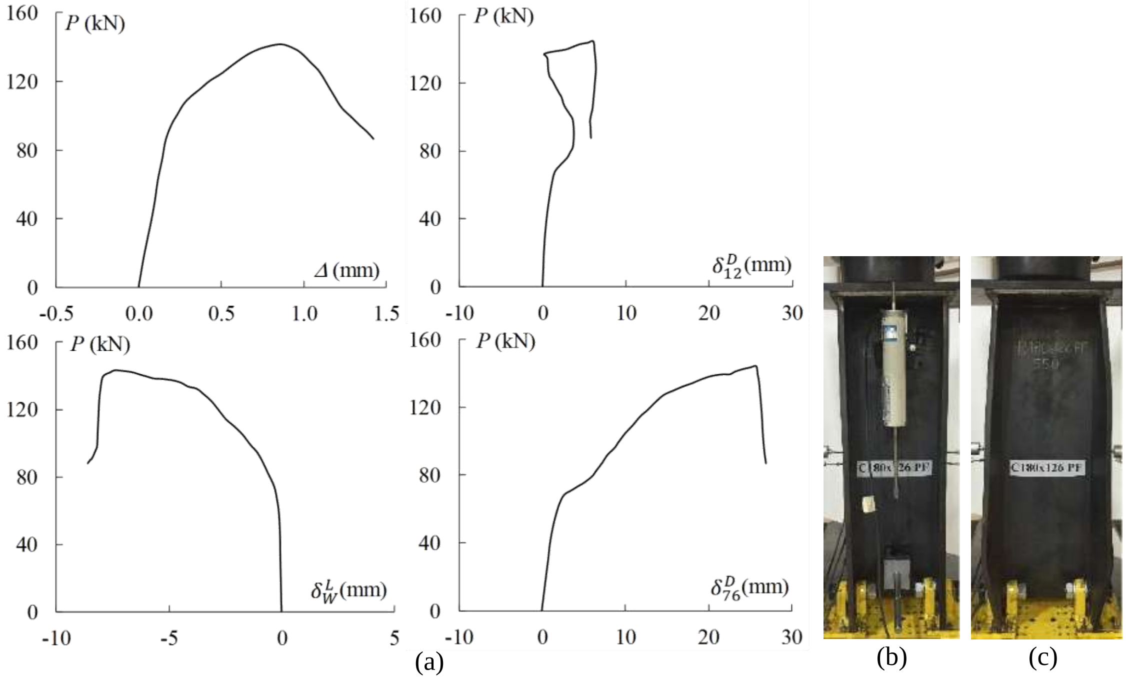

Figure A.41 - 180x126C-PF_F column (a) experimental equilibrium paths P vs. Δ, δ^D_{12}, δ^D_{76} and δ^L_W, and column (b) before and (c) after the test.

21. 180x180C-PF_B

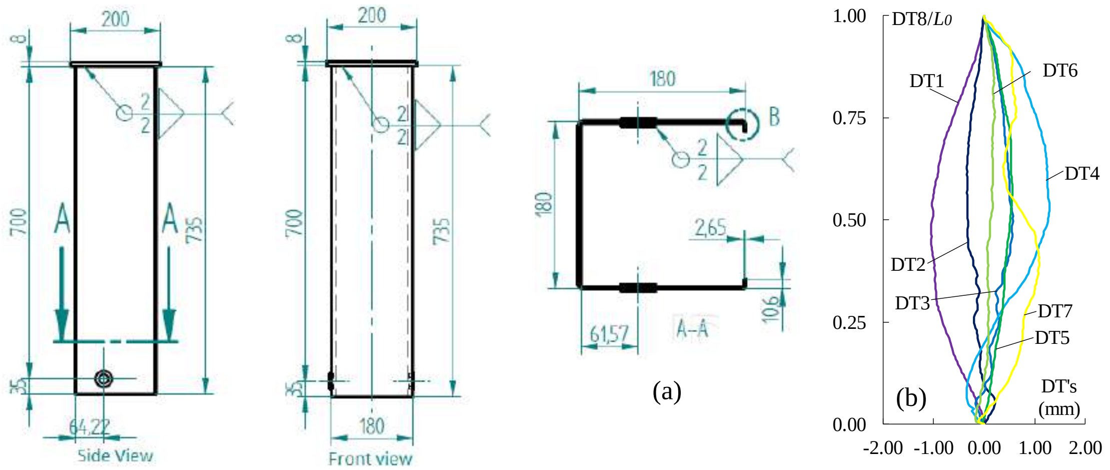

Figure A.42 - 180x180C-PF_B column (a) design and (b) initial imperfection readings.

Table A.21 - Initial measures (mm), calculated area (cm²), squash and ultimate load (kN) for 180x180C-PF_B column

Position	b_w	b_f		b_l		t					
	-	$b_{f.12}$	$b_{f.76}$	$b_{l.12}$	$b_{l.76}$	t_{12}	t_{76}	θ_1	θ_2	θ_3	θ_4
0	181.30	179.00	179.80	10.30	11.00	2.51	2.50	92.0	89.0	90.0	92.0
$0.5L_0$	180.30	179.60	180.00	11.40	11.40	2.48	2.52	92.0	89.5	91.0	92.0
L_0	180.40	178.80	179.60	11.80	10.80	2.51	2.54	92.0	89.5	89.0	92.0
Average	180.67	179.47		11.12		2.51					
	L_D	L_T	L_0	b_a	d_f	A		P_y		P_u	
Average	699	734	664	51.90	21.00	13.74		585.4		119.0	

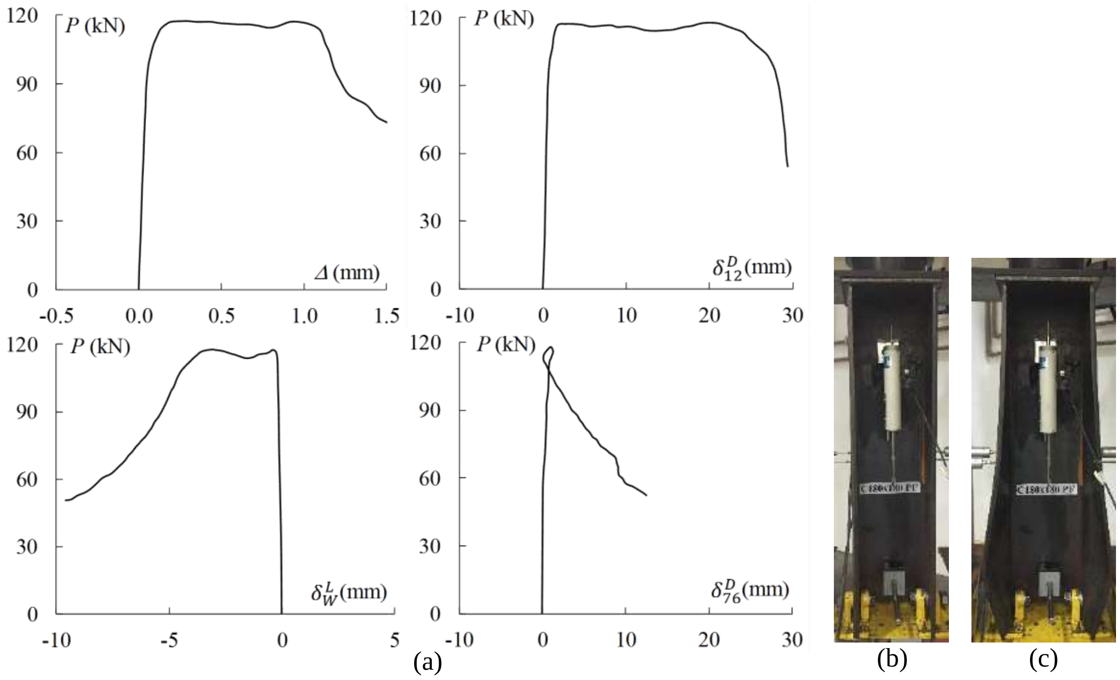

(a) (b) (c)

Figure A.43 - 180x180C-PF_B column (a) experimental equilibrium paths P *vs.* Δ, δ_{12}^D, δ_{76}^D and δ_W^L, and column (b) before and (c) after the test.

22. 200x140C-PF_B

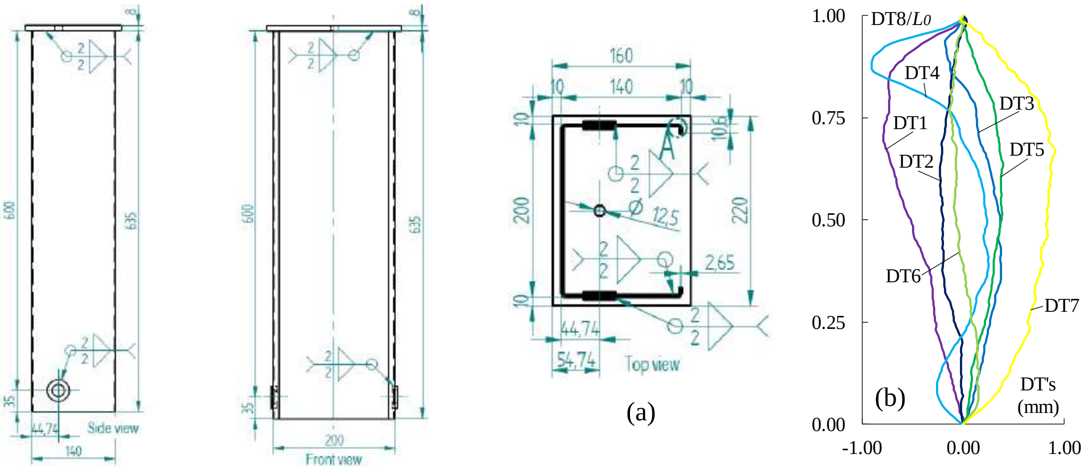

Figure A.44 - 200x140C-PF_B column (a) design and (b) initial imperfection readings.

Table A.22 - Initial measures (mm), calculated area (cm²), squash and ultimate load (kN) for 200x140C-PF_B column

Position	b_w	b_f		b_l		t					
	-	$b_{f.12}$	$b_{f.76}$	$b_{l.12}$	$b_{l.76}$	t_{12}	t_{76}	θ_1	θ_2	θ_3	θ_4
0	201.00	139.00	139.00	10.90	11.30	2.47	2.50	90.0	90.0	90.0	90.0
0.5L_0	199.80	138.50	139.10	11.30	11.50	2.45	2.48	90.0	90.0	90.0	90.0
L_0	200.00	137.50	139.00	11.50	11.50	2.45	2.51	90.0	90.0	90.0	90.0
Average	200.27	138.68		11.33		2.48					
	L_D	L_T	L_0	b_a	d_f	A		P_y		P_u	
Average	602	637	567	34.65	21.00	12.04		512.9		125.7	

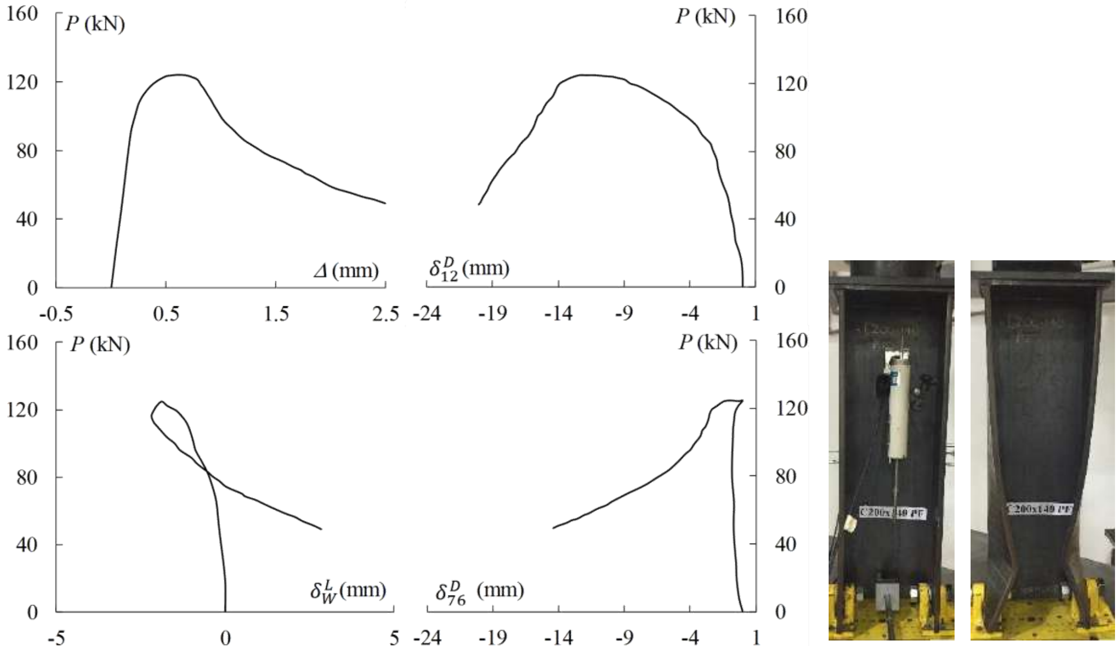

(a)

(b)

(c)

Figure A.45 - 200x140C-PF_B column (a) experimental equilibrium paths P *vs.* Δ, δ_{12}^D, δ_{76}^D and δ_W^L, and column (b) before and (c) after the test.

23. 200x200C-PF_B

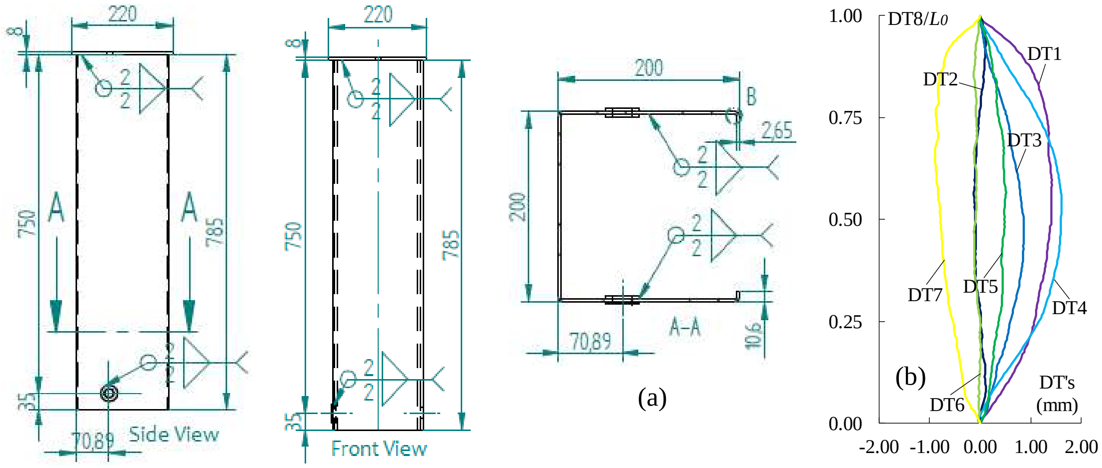

Figure A.46 - 200x200C-PF_B column (a) design and (b) initial imperfection readings.

Table A.23 - Initial measures (mm), calculated area (cm²), squash and ultimate load (kN) for 200x200C-PF_B column.

Position	b_w	b_f		b_l		t					
	-	$b_{f.12}$	$b_{f.76}$	$b_{l.12}$	$b_{l.76}$	t_{12}	t_{76}	θ_1	θ_2	θ_3	θ_4
0	198.80	199.40	199.00	10.60	11.80	2.49	2.44	90.0	91.0	90.0	90.0
$0.5L_0$	199.00	199.10	200.10	11.40	11.80	2.50	2.46	90.0	90.0	92.0	90.0
L_0	199.90	198.90	200.20	10.40	11.40	2.50	2.46	90.0	90.5	90.0	90.0
Average	199.23	199.45		11.23		2.48					
	L_D	L_T	L_0	b_a	d_f	A		P_y		P_u	
Average	749	785	714	60.5	21.0	15.01		639.4		99.0	

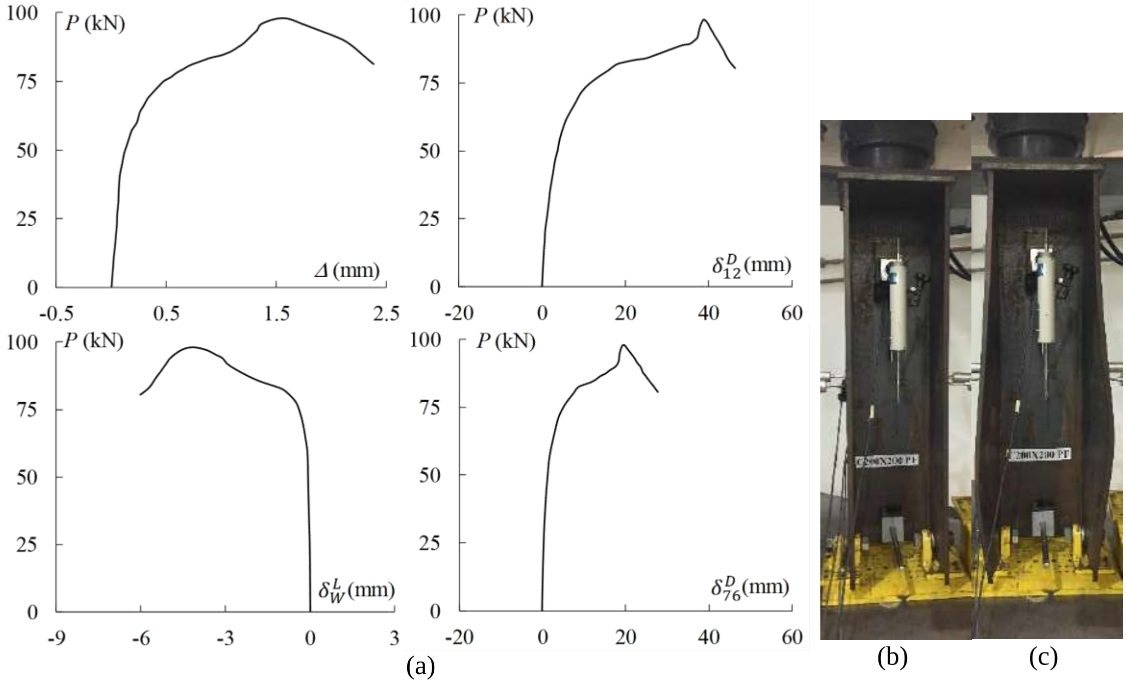

Figure A.47 - 200x200C-PF_B column (a) experimental equilibrium paths P vs. Δ, δ_{12}^{D}, δ_{76}^{D} and δ_{W}^{L}, and column (b) before and (c) after the test.

Appendix B

This annex presents comparisons between numerical methodologies for bearing load in end-bolted columns (P_B) considering (i) contact finite element and (ii) the methodology presented in 5.1.1.

For bearing loading using contact elements, bolts were modeled as circular areas of 20 mm diameter that the contact takes place initially by a point as shown in Figure B.1(b).

The SHELL181 [62] element was adopted to model the column as described in item 5.1. Contact was modeled with CONTA178 [62] element capable of simulating the contact and sliding between two nodes of any element. This element has two nodes with three degrees of freedom per node – translational *X*, *Y* and *Z*. The element is able to support compression perpendicular to the contact and friction in the tangential direction.

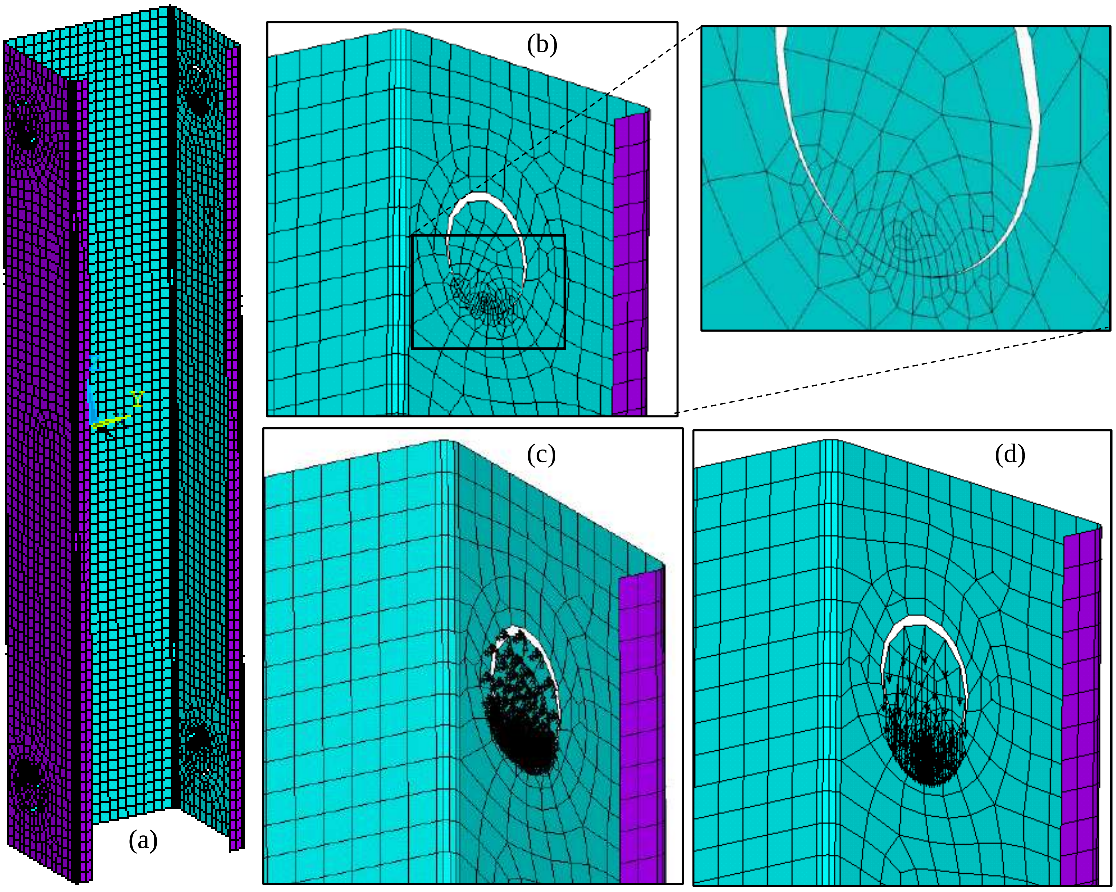

Figure B.1 - SFE model for columns: (a) general and mesh density for end-bolted bearing load using (b) contact element - (c) boundary and (d) loading conditions.

It adopted as the boundary conditions the displacement restriction in X and Y axes as well as all rotations in bolt areas and restrictions in X and Y axes in circular sector in washer contact lines. Moreover, restricted to the displacement in Z direction in web center point. Figure B.1(c) shows the boundary conditions for P_B columns with contact element. The loading was nodal – after defining the finite element mesh, was applied at each node of the bolt cross section an equal share of the load applied to the bolt (see Figure B.1(d)).

The Eigen buckling and post-buckling analysis are described in section 5.1 (E=20500 kN/cm², f_y=35 kN/cm² and ν=0.3).

Following are presented two comparative examples of the methodology that considered the contact element (between the bolt and the washers) and the methodology that considers gradient load described in item 5.1.1 for P_B columns.

Eigen buckling and Elastic-plastic post-buckling analyses

For the first comparison, the initial imperfection was considered critical Eigen buckling with the maximum amplitude along the longitudinal flange stiffener edges equal to $0.10 \cdot t$.

Figure B.2 shows the first elastic buckling mode for the 100x142.9 and 200x140 P_B columns considering (i) contact elements and (ii) gradient load which are half-wave distortional forms.

The critical buckling loads are presented in Table B.1 for 100x142.9 and 200x140 columns taking into account contact elements and gradient load respectively, and the relative difference between these values are 0.31% and 0.44% respectively.

Table B.1 - Critical buckling loads and ultimate strength for 100x142.9 and 200x140 P_B columns considering contact elements and gradient load.

	Critical buckling loads			Ultimate strengths		
Column	contact elements	gradient load	Relative difference	contact elements	gradient load	Relative difference
100x142.9	$0.389P_y$	$0.390P_y$	0.31%	$0.359P_y$	$0.358P_y$	0.40%
200x140	$0.316P_y$	$0.317P_y$	0.44%	$0.314P_y$	$0.314P_y$	0.13%

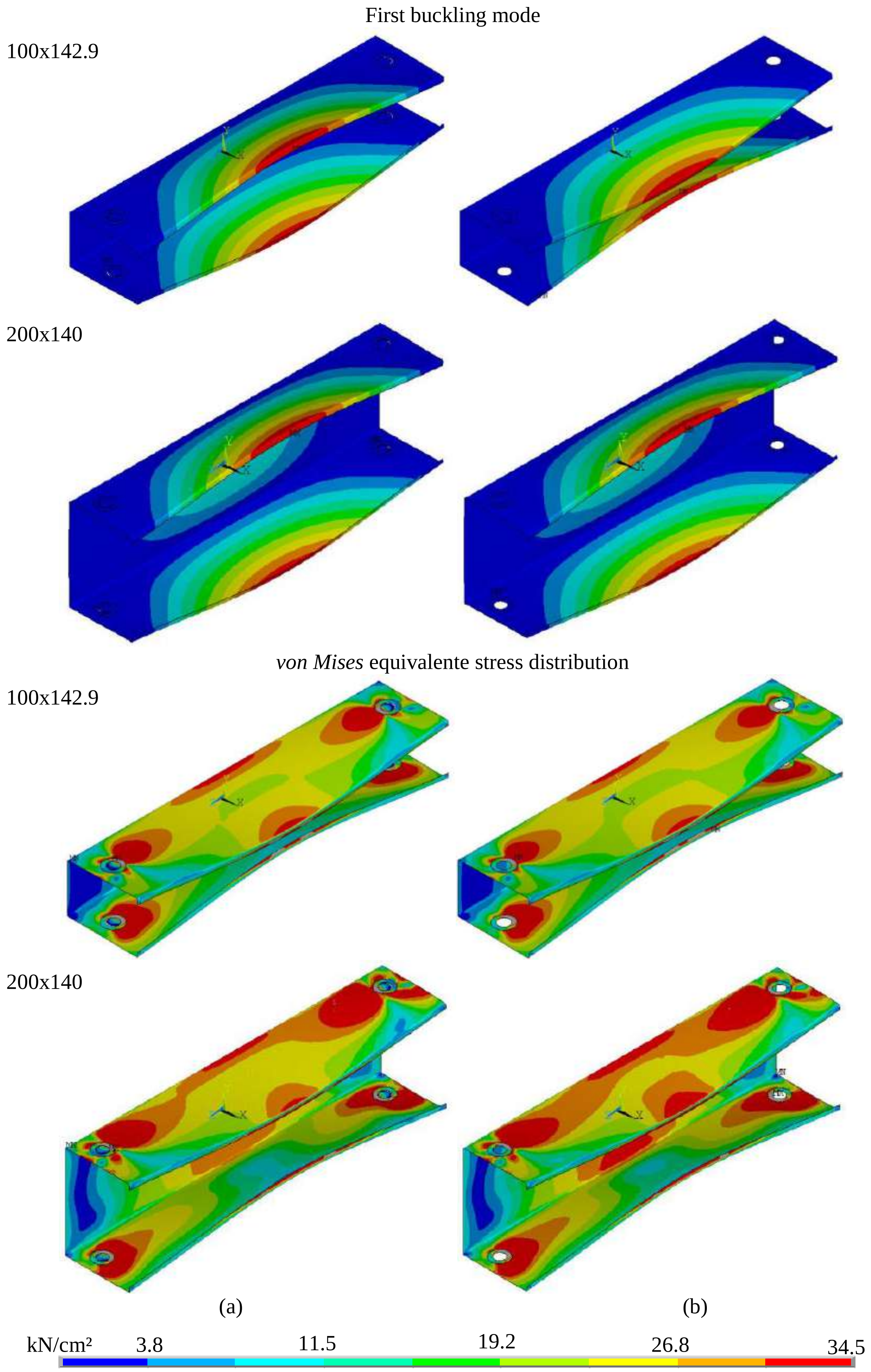

Figure B.2 - First buckling mode and *von Mises* equivalent stress distribution at the peak point for 100x142.9 and 200x140 P_B columns considering (a) contact elements and (b) gradient load.

Figure B.2 also shows the *von Mises* equivalent stress distribution at the peak point for the 100x142.9 and 200x140 P_B columns considering (i) contact elements and (ii) gradient load (deformed have been amplified by a factor of 2.5). In these cases, the collapses are in half-wave distortional forms too and the *von Mises* equivalent stress distribution are similar with each other between the same columns.

The ultimate strengths are presented in Table B.1 for 100x142.9 and 200x140 columns taking into account contact elements and gradient load respectively, and the relative difference between these values are 0.40% and 0.13% respectively.

Figure B.3 presents the equilibrium paths for the 100x142.9 and 200x140 P_B columns considering (i) contact elements and (ii) gradient load, in the ordinate axis is given by the compressive force P and the abscissa is given by maximum flange transversal displacement δ. In these cases, also the equilibrium paths are similar with each other between the same columns.

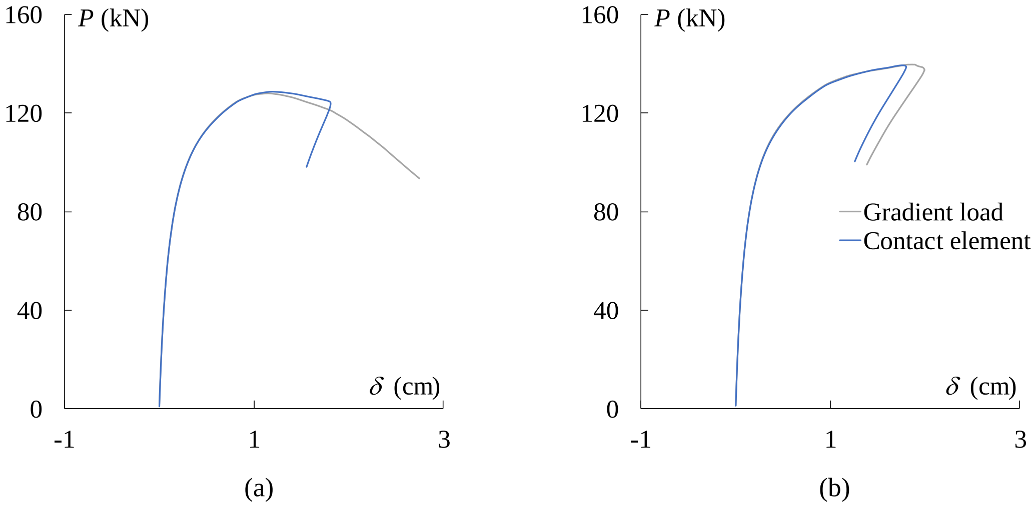

Figure B.3 - Equilibrium paths for (a) 100x142.9 and (b) 200x140 P_B columns considering contact elements and gradient load.

Figure B.4 shows the contact bolt-washers where could be estimated the "contact angle" in these numerical examples.

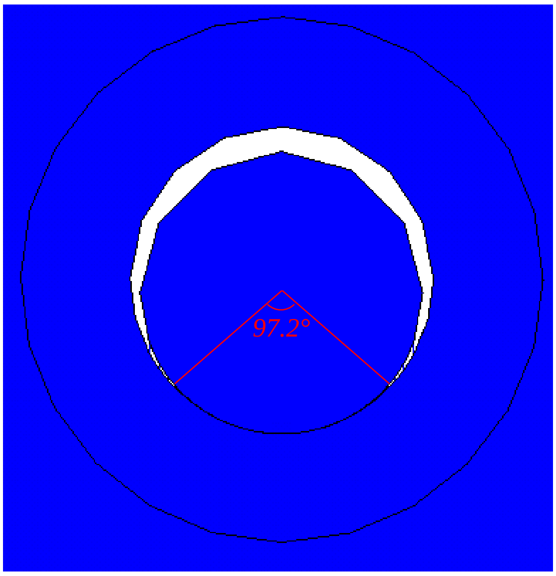

Figure B.4 – Measured "contact angle" in SFEA using contact elements.

Two more examples are given below comparing again the methodology that considered the contact element (between the bolt and the washers) and the methodology that considers gradient load described in item 5.1.1, but now for 180x180C-P_B and 200x140C-P_B tested columns.

The material and initial imperfection was considered as described in item 5.3.2 – numerical methodology for experiments validation.

Figure B.5 shows the first elastic buckling mode for the 180x180C-P_B and 200x140C-P_B columns considering (i) contact elements and (ii) gradient load. In these cases, the deformed are half-wave distortional forms.

The critical buckling loads considering contact elements and gradient load are presented in Table B.2 for 180x180C-P_B and 200x140C-P_B columns. The relative difference between these values are 1.56% and 0.37% respectively.

Table B.2 - Critical buckling loads and ultimate strength for 180x180C-P_B and 200x140C-P_B columns considering contact elements and gradient load.

	Critical buckling loads			Ultimate strengths		
Column	contact elements	gradient load	Relative difference	contact elements	gradient load	Relative difference
180x180C-P_B	0.164P_y	0.162P_y	1.56%	0.159P_y	0.1692P_y	5.59%
200x140C-P_B	0.243P_y	0.242P_y	0.37%	0.169P_y	0.222P_y	23.85%

First buckling mode

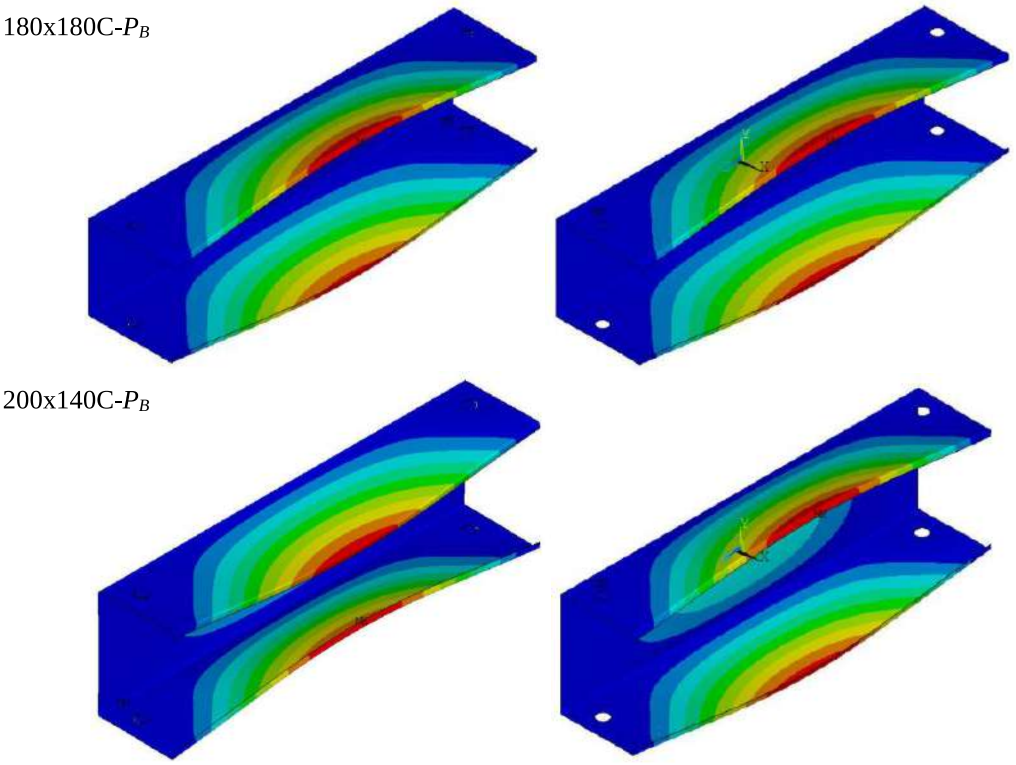

von Mises equivalente stress distribution

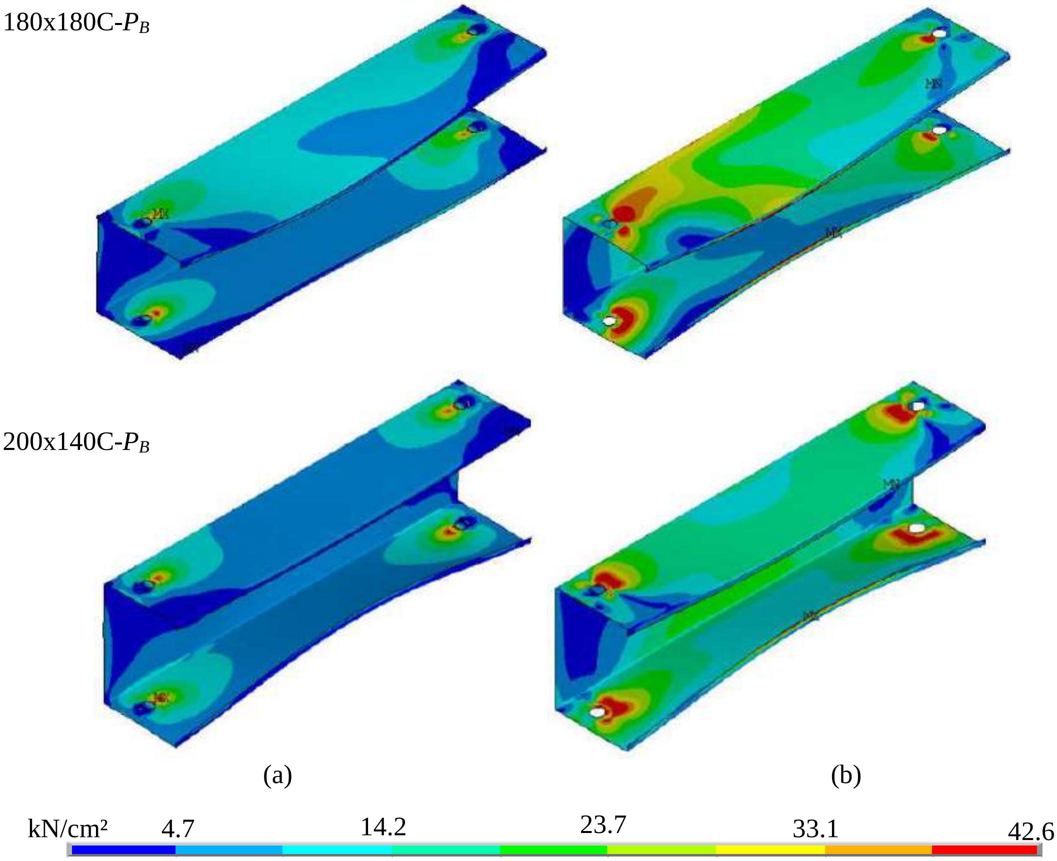

Figure B.5 - First buckling mode and *von Mises* equivalent stress distribution at the peak point for 180x180C-P_B and 200x140C-P_B columns considering (a) contact elements and (b) gradient load.

Figure B.5 also illustrates the *von Mises* equivalent stress distribution at the limit point for the 180x180C-P_B column considering (i) contact elements and (ii) gradient load (deformed also have been amplified by a factor of 2.5). For the contact element cases the solutions were interrupted by the program, due to numerical difficulty, and it was not possible the total "development" of the distortional mechanism.

The ultimate strengths are presented in Table B.2 for 180x180C-P_B and 200x140C-P_B columns considering contact elements and gradient load respectively, and the relative difference between these values are 5.59% and 23.85%.

Figure B.6 presents the equilibrium paths for the 180x180C-P_B and 200x140C-P_B column considering (i) contact elements and (ii) gradient load. In these cases, also the equilibrium paths are similar with each other, but in the contact element cases the solutions were suddenly interrupted.

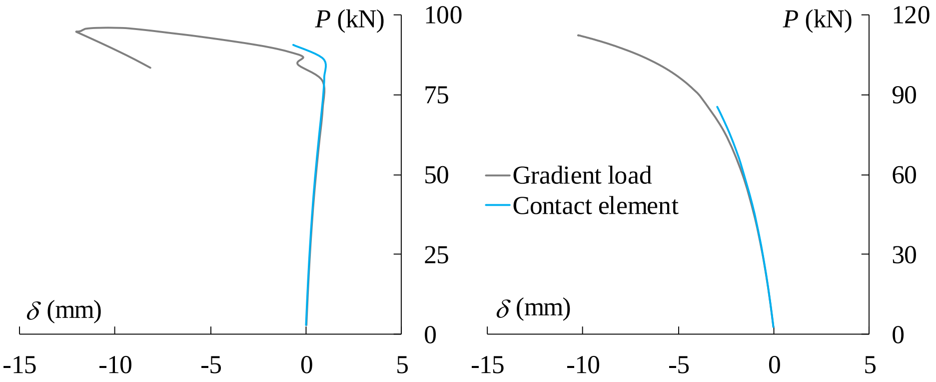

(a) (b)

Figure B.6 - Equilibrium paths considering contact elements and gradient load for (a) 180x180C-P_B and 200x140C-P_B columns.

Figure B.7 depicts the contact bolt-washers where could be estimated the "contact chord" in these columns, in this measurement was estimated 16.1 mm.

(a) (b)

Figure B.7 – (a) Undeformed and (b) deformed washer and measured contact chord.

Considering the standard hole diameter as 21.5 mm and the measured chord the “contact angle” can be estimated as 97.2°.

Conclusion

This annex presented the comparisons between numerical methodologies for bearing load in end-bolted columns (P_B) considering (i) contact finite element and (ii) the methodology considering gradient loading presented in item 5.1.1. Both methodologies present similar results.

When making use of contact elements the processing time to calculation is considerably greater than when not using this type of elements. Moreover, in some cases, the numerical solution presents difficulties being interrupted suddenly by the program. Therefore, to evaluate the development of distortional buckling phenomenon, the methodology that do not use contact elements is preferable.

Appendix C

Tables C.1-5 (P_F columns), C.6-10 (P_B columns), C.11-15 (PF_F columns) and C.16-20 (PF_B columns) summaries the numerical (ANSYS shell finite element analysis) and DSM results obtained in the course of this research. Each of them concerns a specific column family (same web width and boundary condition) and provides the corresponding (i) squash loads (P_y), (ii) steel yield strength (f_y), (iii) distortional slenderness values ($\bar{\lambda}_D$), (iv) critical load elastic distortional buckling ($P_{cr.D}$), (v) ultimate loads (P_u) numerically obtained considering three different maximum amplitudes for distortional inward buckling form, (vi) the failures mode (*FM*), which may be either distortional (*D*), interactive distortional/local (*D*+*L*) or failure by Yield Near the Hole (*YNH*), (vii) DSM distortional ultimate strength estimates ($P_{n.D}$) and (viii) the ultimate strength estimates DSM distortional design curve suggested by LANDESMANN and CAMOTIM [31] ($P^*_{n.D}$).

Table C.1: Numerical and DSM results concerning the behavior and strength of b_w=100 mm P_F columns

Column	P_y (kN)	f_y (kN/cm²)	$\bar{\lambda}_D$	$P_{cr.D}$ (kN)	$P_{u,0.1t}$ (kN)	$P_{u,0.23t}$ (kN)	$P_{u,1t}$ (kN)	*FM*	$P_{n.D}$ (kN)	$P^*_{n.D}$ (kN)
100x70	52.4	8.0	0.400	327.5	41.9	41.3	40.4	*YNH*	52.4	52.4
	56.5	8.7	0.415		44.5	43.9	43.8	*YNH*	56.5	56.5
	60.7	9.3	0.431		47.9	47.9	46.7	*YNH*	60.7	60.7
	156.0	23.9	0.690		116.7	116.5	116.2	*YNH*	148.5	148.5
	295.4	45.3	0.950		212.0	211.3	204.1	*D*	230.7	230.7
	479.0	73.5	1.209		304.9	296.5	285.2	*D*	305.4	288.3
	706.7	108.4	1.469		355.8	368.6	344.7	*D*	375.3	302.6
	978.5	150.1	1.729		402.6	397.3	423.5	*D*	441.6	317.8
	1294.5	198.5	1.988		487.2	487.8	478.8	*D+L*	505.3	333.1
	1654.7	253.8	2.248		549.7	550.3	558.7	*D+L*	566.9	348.3
	2059.0	315.8	2.507		611.7	611.3	614.0	*D+L*	626.6	363.2
	2507.4	384.6	2.767		667.5	668.1	666.8	*D+L*	684.8	377.8
	3000.0	460.1	3.027		718.9	719.8	717.6	*D+L*	741.7	392.0
	3536.7	542.4	3.286		763.3	763.3	763.8	*D+L*	797.5	405.8
100x100	43.8	5.4	0.446	220.1	26.5	26.4	26.3	*YNH*	43.8	43.8
	61.8	7.6	0.530		37.0	37.0	36.7	*YNH*	61.8	61.8
	65.4	8.1	0.545		39.3	39.1	38.8	*YNH*	65.4	65.4
	109.5	13.5	0.705		65.2	65.1	64.4	*YNH*	103.2	103.2
	205.0	25.3	0.965		122.5	123.1	121.1	*YNH*	158.1	158.1
	330.1	40.7	1.225		181.0	179.6	171.3	*D*	208.1	194.3
	484.9	59.8	1.484		232.8	232.1	225.3	*D*	254.9	204.0
	669.4	82.5	1.744		271.3	258.8	261.3	*D*	299.4	214.2
	883.6	108.9	2.003		304.1	292.3	311.4	*D*	342.1	224.5
	1127.4	139.0	2.263		385.4	386.8	389.9	*D+L*	383.4	234.7
	1400.9	172.7	2.523		426.4	441.8	424.0	*D+L*	423.5	244.7
	1704.0	210.1	2.782		479.4	480.7	476.1	*D+L*	462.6	254.5
	2036.8	251.1	3.042		528.3	534.3	530.0	*D+L*	500.8	264.0
	2399.3	295.8	3.301		586.3	581.4	578.7	*D+L*	538.2	273.3
100x142.9	30.3	2.9	0.461	142.6	14.6	14.1	14.2	*YNH*	30.3	30.3
	62.0	6.0	0.660		28.9	28.9	29.9	*YNH*	60.1	60.1
	64.9	6.3	0.675		30.8	30.3	30.6	*YNH*	62.4	62.4
	74.0	7.1	0.721		34.6	34.5	35.0	*YNH*	69.1	69.1
	137.0	13.2	0.980		65.1	65.5	66.8	*YNH*	104.4	104.4
	219.2	21.1	1.240		104.9	104.4	102.2	*YNH*	136.6	126.2
	320.5	30.9	1.500		137.2	136.0	127.2	*D*	166.8	132.5
	441.1	42.5	1.759		157.4	155.7	152.0	*D*	195.6	139.1
	580.9	55.9	2.019		174.4	174.0	168.5	*D*	223.2	145.8
	740.0	71.3	2.278		189.8	198.2	200.1	*D*	249.8	152.4
	918.2	88.4	2.538		238.4	237.9	218.4	*D*	275.8	158.9
	1115.6	107.4	2.798		267.2	273.9	270.5	*D+L*	301.0	165.2
	1332.3	128.3	3.057		281.1	295.9	298.3	*D+L*	325.7	171.3
	1568.2	151.0	3.317		306.4	311.6	325.2	*D+L*	349.9	177.4

Table C.2: Numerical and DSM results concerning the behavior and strength of b_w=130 mm P_F columns

Column	P_y (kN)	f_y (kN/cm²)	$\bar{\lambda}_D$	$P_{cr.D}$ (kN)	$P_{u,0.1t}$ (kN)	$P_{u,0.23t}$ (kN)	$P_{u,1t}$ (kN)	*FM*	$P_{n.D}$ (kN)	$P^*_{n.D}$ (kN)
130x91	53.4	6.3	0.476	235.4	31.6	31.6	31.1	*YNH*	53.4	53.4
	127.5	15.1	0.736		73.8	73.6	72.2	*YNH*	117.7	117.7
	198.9	23.6	0.919		115.1	113.6	108.2	*YNH*	159.2	159.2
	205.6	24.4	0.935		118.2	116.8	115.2	*YNH*	162.5	162.5
	233.3	27.7	0.996		132.5	132.3	131.9	*YNH*	175.6	175.6
	370.9	44.0	1.255		195.7	192.4	189.3	*D*	228.6	208.9
	540.2	64.1	1.515		250.8	242.2	235.8	*D*	278.3	219.4
	741.2	87.9	1.774		311.0	298.3	299.2	*D*	325.6	230.4
	973.9	115.6	2.034		369.4	359.4	352.7	*D*	371.1	241.4
	1238.3	146.9	2.294		421.4	422.0	424.5	*D+L*	415.1	252.2
	1534.5	182.1	2.553		474.7	465.3	477.0	*D+L*	457.8	262.9
	1862.4	221.0	2.813		526.0	526.3	522.1	*D+L*	499.5	273.3
	2222.1	263.6	3.072		574.3	574.5	572.7	*D+L*	540.3	283.5
	2613.4	310.1	3.332		618.9	619.2	623.7	*D+L*	580.2	293.4
130x130	38.4	3.7	0.492	159.1	17.7	17.7	18.0	*YNH*	38.4	38.4
	89.8	8.6	0.751		41.0	41.4	42.0	*YNH*	81.9	81.9
	162.5	15.5	1.011		75.9	75.0	75.7	*YNH*	120.8	120.8
	221.0	21.1	1.179		102.6	102.0	102.1	*YNH*	144.2	139.2
	226.8	21.6	1.194		103.8	105.2	104.3	*YNH*	146.3	139.6
	256.7	24.5	1.270		118.3	117.7	114.7	*YNH*	156.5	141.6
	372.3	35.5	1.530		153.8	152.6	144.3	*D*	190.0	148.7
	509.4	48.5	1.790		177.0	175.1	163.3	*D*	221.8	156.1
	667.9	63.6	2.049		197.6	203.2	191.7	*D*	252.5	163.5
	847.8	80.8	2.309		249.6	248.3	247.7	*D*	282.2	170.9
	1049.2	100.0	2.568		283.3	291.4	281.5	*D*	311.0	178.1
	1272.0	121.2	2.828		317.0	326.4	326.9	*D+L*	339.1	185.1
	1516.2	144.5	3.088		332.7	337.3	345.2	*D+L*	366.6	192.0
	1781.9	169.8	3.347		344.1	340.5	370.1	*D+L*	393.6	198.6
130x185.7	26.5	2.0	0.507	103.1	9.5	9.6	9.9	*YNH*	26.5	26.5
	60.6	4.5	0.767		21.9	21.8	22.3	*YNH*	54.7	54.7
	108.5	8.1	1.026		39.5	39.3	39.6	*YNH*	79.7	79.7
	170.4	12.7	1.286		62.4	62.4	61.3	*YNH*	102.7	92.0
	213.3	15.9	1.438		78.7	77.1	72.5	*YNH*	115.6	94.7
	217.8	16.2	1.454		80.0	78.5	73.2	*YNH*	116.9	95.0
	246.2	18.3	1.545		87.1	86.3	81.1	*YNH*	124.4	96.6
	335.8	25.0	1.805		103.0	101.1	97.5	*D*	145.0	101.4
	439.4	32.7	2.065		111.7	118.1	110.7	*D*	164.8	106.3
	556.8	41.4	2.324		133.2	132.7	131.9	*D*	184.0	111.0
	688.1	51.2	2.584		147.2	149.2	149.8	*D*	202.6	115.7
	833.3	62.0	2.843		163.6	165.2	151.4	*D*	220.8	120.2
	992.5	73.8	3.103		181.2	181.1	179.0	*D*	238.6	124.7
	1165.5	86.7	3.363		186.0	191.5	185.4	*D*	256.1	129.0

Table C.3: Numerical and DSM results concerning the behavior and strength of b_w=150 mm P_F columns

Column	P_y (kN)	f_y (kN/cm²)	$\bar{\lambda}_D$	$P_{cr.D}$ (kN)	$P_{u,0.1t}$ (kN)	$P_{u,0.23t}$ (kN)	$P_{u,1t}$ (kN)	*FM*	$P_{n.D}$ (kN)	$P^*_{n.D}$ (kN)
150x105	54.3	5.6	0.522	199.2	30.6	30.4	29.0	*YNH*	54.3	54.3
	121.8	12.6	0.782		63.7	64.7	64.6	*YNH*	108.7	108.7
	216.1	22.3	1.041		113.2	111.9	108.4	*YNH*	156.8	156.8
	337.2	34.8	1.301		159.4	158.2	153.7	*D*	201.1	178.3
	485.2	50.0	1.561		205.7	203.9	198.4	*D*	242.8	187.3
	574.4	59.2	1.698		231.1	229.0	224.1	*D*	264.0	192.2
	584.8	60.3	1.713		234.1	232.7	226.6	*D*	266.3	192.8
	660.1	68.0	1.820		252.7	252.2	246.5	*D*	282.5	196.6
	861.8	88.8	2.080		297.3	277.1	281.9	*D*	320.8	205.9
	1090.4	112.4	2.339		323.7	306.5	310.5	*D*	357.8	215.1
	1345.8	138.7	2.599		390.7	399.3	405.3	*D+L*	393.8	224.1
	1628.1	167.8	2.859		424.1	431.9	440.2	*D+L*	428.9	232.9
	1937.2	199.7	3.118		459.9	479.3	460.2	*D+L*	463.3	241.5
	2273.2	234.3	3.378		460.8	465.7	478.3	*D+L*	497.0	249.8
150x150	38.7	3.2	0.537	134.1	16.3	15.6	15.8	*YNH*	38.7	38.7
	85.2	7.1	0.797		34.0	34.3	34.6	*YNH*	75.2	75.2
	149.8	12.4	1.057		57.4	61.1	62.1	*YNH*	107.4	107.4
	232.4	19.2	1.316		96.6	94.6	92.4	*YNH*	137.1	120.4
	333.1	27.6	1.576		126.3	123.8	119.2	*D*	165.0	126.5
	436.0	36.1	1.803		148.2	144.9	141.3	*D*	188.4	132.0
	451.9	37.4	1.835		147.8	146.5	143.4	*D*	191.7	132.7
	455.7	37.7	1.843		151.7	151.0	145.2	*D*	192.5	132.9
	588.7	48.7	2.095		163.6	164.5	164.1	*D*	217.4	139.0
	743.7	61.5	2.355		187.3	180.6	183.4	*D*	242.3	145.2
	916.7	75.9	2.614		195.6	196.4	184.0	*D*	266.5	151.2
	1107.8	91.7	2.874		249.9	251.8	248.7	*D*	290.1	157.1
	1317.0	109.0	3.133		266.2	271.2	276.2	*D+L*	313.2	162.9
	1544.3	127.8	3.393		282.7	283.2	294.2	*D+L*	335.9	168.5
150x214.3	26.3	1.7	0.553	86.1	8.4	8.4	8.4	*YNH*	26.3	26.3
	56.8	3.7	0.812		18.1	17.8	17.8	*YNH*	49.5	49.5
	98.9	6.4	1.072		31.1	31.1	31.1	*YNH*	70.1	70.1
	152.7	9.9	1.332		47.9	48.3	51.5	*YNH*	89.1	77.5
	218.0	14.1	1.591		70.2	69.5	67.4	*YNH*	107.0	81.4
	294.9	19.0	1.851		84.1	82.6	81.8	*D*	124.1	85.4
	330.0	21.3	1.958		89.3	87.6	87.4	*D*	130.9	87.1
	335.1	21.6	1.973		90.0	89.6	88.2	*D*	131.9	87.3
	383.5	24.8	2.110		91.4	95.9	94.5	*D*	140.5	89.5
	483.6	31.2	2.370		106.4	97.9	106.5	*D*	156.5	93.4
	595.4	38.4	2.630		116.3	117.3	109.9	*D*	172.0	97.3
	718.7	46.4	2.889		126.0	121.0	120.0	*D*	187.1	101.1
	853.7	55.1	3.149		135.9	132.1	128.2	*D*	201.9	104.8
	1000.2	64.6	3.408		140.6	152.0	140.1	*D*	216.5	108.4

Table C.4: Numerical and DSM results concerning the behavior and strength of b_w=180 mm P_F columns

Column	P_y (kN)	f_y (kN/cm²)	$\bar{\lambda}_D$	$P_{cr.D}$ (kN)	$P_{u,0.1t}$ (kN)	$P_{u,0.23t}$ (kN)	$P_{u,1t}$ (kN)	*FM*	$P_{n.D}$ (kN)	$P^*_{n.D}$ (kN)
180x126	51.5	4.4	0.568	159.7	20.9	21.4	21.0	*YNH*	51.5	51.5
	109.4	9.4	0.828		43.9	42.2	44.6	*YNH*	94.2	94.2
	188.8	16.3	1.087		72.0	71.8	70.8	*YNH*	132.1	132.1
	289.7	25.0	1.347		122.9	118.4	120.0	*YNH*	167.2	144.2
	412.2	35.5	1.606		158.4	157.0	156.1	*D*	200.3	151.5
	556.1	47.9	1.866		192.8	190.6	181.8	*D*	232.0	158.9
	721.6	62.2	2.126		228.0	219.6	212.6	*D*	262.4	166.4
	785.1	67.6	2.217		240.8	240.0	236.7	*D*	272.9	169.0
	796.0	68.6	2.233		242.6	241.8	241.1	*D*	274.7	169.4
	908.6	78.3	2.385		256.4	256.7	248.4	*D*	292.0	173.7
	1117.2	96.2	2.645		282.7	286.3	285.1	*D+L*	320.7	180.9
	1347.3	116.1	2.904		302.2	291.4	299.4	*D+L*	348.7	187.9
	1598.9	137.7	3.164		308.0	329.3	311.6	*D+L*	376.2	194.8
	1872.0	161.3	3.424		299.4	290.3	314.4	*D+L*	403.1	201.4
180x180	36.4	2.5	0.583	107.1	12.3	12.3	12.3	*YNH*	36.3	36.3
	76.1	5.3	0.843		25.5	25.7	26.3	*YNH*	64.7	64.7
	130.1	9.0	1.103		44.2	43.8	44.9	*YNH*	90.0	90.0
	198.6	13.7	1.362		70.6	70.5	69.2	*YNH*	113.4	96.9
	281.5	19.5	1.622		92.9	92.4	89.8	*YNH*	135.5	101.8
	378.9	26.2	1.881		111.1	108.8	104.6	*D*	156.7	106.8
	490.7	33.9	2.141		124.1	123.9	124.3	*D*	177.1	111.8
	616.9	42.6	2.401		145.8	145.9	144.1	*D*	196.8	116.7
	656.7	45.4	2.477		150.7	151.0	148.3	*D*	202.5	118.2
	664.8	45.9	2.492		151.7	151.8	149.0	*D*	203.7	118.4
	757.5	52.4	2.660		162.3	162.8	160.3	*D*	216.1	121.5
	912.6	63.1	2.920		177.8	178.7	179.0	*D*	234.8	126.2
	1082.1	74.8	3.179		191.5	192.9	191.1	*D*	253.2	130.8
	1266.0	87.5	3.439		204.0	196.8	192.2	*D*	271.2	135.3
180x257.1	24.7	1.3	0.599	69.0	6.3	6.2	6.6	*YNH*	24.6	24.6
	50.8	2.7	0.858		13.2	12.8	13.3	*YNH*	42.7	42.7
	86.2	4.6	1.118		21.8	22.5	22.7	*YNH*	59.0	59.0
	131.0	7.1	1.377		33.1	31.7	34.6	*YNH*	74.0	62.7
	185.0	10.0	1.637		49.3	50.0	51.0	*YNH*	88.2	65.8
	248.3	13.4	1.897		64.3	63.8	62.8	*YNH*	101.8	69.1
	320.9	17.3	2.156		71.1	70.7	72.9	*D*	115.0	72.3
	402.9	21.7	2.416		80.6	79.7	78.3	*D*	127.7	75.5
	494.1	26.6	2.675		88.9	88.8	88.4	*D*	140.1	78.6
	517.0	27.9	2.737		90.8	91.3	89.9	*D*	142.9	79.3
	522.7	28.2	2.752		91.2	91.7	91.5	*D*	143.6	79.5
	594.7	32.0	2.935		96.2	91.4	88.8	*D*	152.1	81.6
	704.5	38.0	3.195		99.6	98.7	94.4	*D*	164.0	84.5
	823.7	44.4	3.454		102.6	98.8	102.7	*D*	175.6	87.4

Table C.5: Numerical and DSM results concerning the behavior and strength of b_w=200 mm P_F columns

Column	P_y (kN)	f_y (kN/cm²)	$\bar{\lambda}_D$	$P_{cr.D}$ (kN)	$P_{u,0.1t}$ (kN)	$P_{u,0.23t}$ (kN)	$P_{u,1t}$ (kN)	*FM*	$P_{n.D}$ (kN)	$P^*_{n.D}$ (kN)
200x140	53.0	4.1	0.614	140.6	19.9	19.8	20.3	*YNH*	52.4	52.4
	107.2	8.3	0.873		40.7	40.5	41.1	*YNH*	89.1	89.1
	180.5	14.0	1.133		75.0	74.7	72.1	*YNH*	121.9	121.9
	272.6	21.2	1.393		104.2	98.4	101.4	*YNH*	152.4	128.0
	383.7	29.8	1.652		134.6	133.7	130.8	*D*	181.3	134.5
	513.8	39.9	1.912		162.1	161.4	154.6	*D*	209.0	141.0
	662.8	51.5	2.171		191.1	190.4	176.9	*D*	235.6	147.6
	830.8	64.5	2.431		219.6	220.2	207.8	*D*	261.5	154.0
	1017.7	79.0	2.691		249.6	249.3	238.0	*D*	286.7	160.3
	1223.5	95.0	2.950		277.4	277.3	264.6	*D*	311.2	166.5
	1261.9	98.0	2.996		282.4	282.2	282.0	*D+L*	315.5	167.6
	1274.8	99.0	3.011		283.8	284.3	281.7	*D+L*	317.0	167.9
	1448.3	112.5	3.210		306.2	306.5	292.6	*D+L*	335.3	172.5
	1692.1	131.4	3.469		334.7	334.7	333.8	*D+L*	358.9	178.3
200x200	37.4	2.3	0.629	94.4	11.4	11.3	11.5	*YNH*	36.8	36.8
	74.6	4.6	0.889		21.4	22.6	22.9	*YNH*	61.2	61.2
	124.5	7.8	1.148		35.8	35.6	38.0	*YNH*	83.1	82.2
	187.2	11.7	1.408		56.1	56.8	59.7	*YNH*	103.6	86.2
	262.5	16.3	1.668		79.9	79.2	77.0	*YNH*	122.9	90.6
	350.6	21.8	1.927		94.2	93.7	92.9	*D*	141.4	95.0
	451.5	28.1	2.187		108.9	108.4	108.9	*D*	159.3	99.4
	565.0	35.2	2.446		123.3	123.5	122.1	*D*	176.6	103.7
	691.3	43.0	2.706		132.2	132.8	134.7	*D*	193.5	107.9
	830.3	51.7	2.966		145.8	143.3	143.8	*D*	210.0	112.0
	922.5	57.4	3.126		157.2	158.0	152.2	*D*	220.0	114.5
	931.5	58.0	3.141		155.4	158.8	152.8	*D*	221.0	114.8
	982.0	61.1	3.225		159.5	162.7	165.4	*D*	226.1	116.1
	1146.5	71.4	3.485		168.7	173.9	170.3	*D*	242.0	120.0
200x285.7	25.2	1.2	0.644	60.8	5.9	5.9	6.0	*YNH*	24.6	24.6
	49.6	2.4	0.904		11.7	11.6	11.8	*YNH*	40.2	40.2
	82.3	4.0	1.164		19.3	19.3	19.6	*YNH*	54.3	53.0
	123.1	6.0	1.423		29.0	29.2	29.5	*YNH*	67.4	55.7
	172.0	8.4	1.683		40.0	40.4	43.2	*YNH*	79.8	58.5
	229.2	11.1	1.942		54.6	54.0	52.8	*YNH*	91.7	61.3
	294.6	14.3	2.202		61.9	61.1	57.7	*D*	103.2	64.1
	368.1	17.9	2.462		68.9	66.6	69.9	*D*	114.3	66.9
	449.9	21.8	2.721		74.8	68.5	74.4	*D*	125.2	69.6
	539.8	26.2	2.981		78.4	73.4	74.6	*D*	135.8	72.3
	638.0	31.0	3.240		84.1	81.8	82.0	*D*	146.1	74.8
	644.0	31.3	3.256		87.5	85.0	85.8	*D*	146.7	75.0
	650.1	31.6	3.271		88.5	89.1	82.9	*D*	147.3	75.1
	744.3	36.1	3.500		93.3	93.8	94.4	*D*	156.3	77.4

Table C.6: Numerical and DSM results concerning the behavior and strength of b_w=100 mm P_B columns

Column	P_y (kN)	f_y (kN/cm²)	$\bar{\lambda}_D$	$P_{cr.D}$ (kN)	$P_{u,0.1t}$ (kN)	$P_{u,0.23t}$ (kN)	$P_{u,1t}$ (kN)	*FM*	$P_{n.D}$ (kN)	$P^*_{n.D}$ (kN)
100x70	51.7	7.9	0.400	322.9	38.9	38.7	38.4	*YNH*	51.7	51.7
	55.7	8.5	0.415		41.4	41.6	42.0	*YNH*	55.7	55.7
	59.8	9.2	0.431		44.8	45.1	44.5	*YNH*	59.8	59.8
	153.8	23.6	0.690		114.1	115.3	114.3	*YNH*	146.3	146.3
	291.2	44.7	0.950		206.2	203.3	188.2	*D*	227.4	227.4
	472.2	72.4	1.209		261.5	256.5	256.6	*D*	301.1	284.2
	696.7	106.8	1.469		288.4	284.8	264.6	*D*	370.0	298.3
	964.7	147.9	1.729		305.2	299.8	285.2	*D*	435.4	313.3
	1276.2	195.7	1.988		320.3	319.8	329.9	*D*	498.2	328.4
	1631.2	250.2	2.248		330.9	326.1	323.7	*D*	558.8	343.4
	2029.8	311.3	2.507		342.9	337.7	324.5	*D*	617.7	358.1
	2471.8	379.1	2.767		352.3	348.3	341.6	*D*	675.1	372.4
	2957.4	453.6	3.027		360.8	363.8	352.9	*D*	731.2	386.4
	3486.5	534.7	3.286		367.9	366.0	361.4	*D*	786.2	400.1
100x100	42.8	5.3	0.446	215.6	25.3	25.4	25.3	*YNH*	42.8	42.8
	60.5	7.5	0.530		35.7	35.8	35.4	*YNH*	60.5	60.5
	64.0	7.9	0.545		37.8	37.7	37.7	*YNH*	64.0	64.0
	107.3	13.2	0.705		63.2	63.3	63.0	*YNH*	101.1	101.1
	200.7	24.8	0.965		117.6	117.5	115.3	*YNH*	154.8	154.8
	323.3	39.9	1.225		173.9	170.8	163.4	*D*	203.8	190.2
	474.8	58.5	1.484		195.2	190.9	178.6	*D*	249.6	199.7
	655.5	80.8	1.744		205.4	201.5	187.4	*D*	293.2	209.7
	865.2	106.7	2.003		213.8	210.2	196.0	*D*	335.0	219.8
	1103.9	136.1	2.263		218.9	217.5	207.8	*D*	375.4	229.8
	1371.7	169.1	2.523		225.8	224.0	219.5	*D*	414.7	239.6
	1668.5	205.7	2.782		230.7	229.0	224.9	*D*	452.9	249.2
	1994.4	245.9	3.042		235.8	235.1	228.7	*D*	490.3	258.5
	2349.4	289.7	3.301		241.2	240.7	236.3	*D*	527.0	267.6
100x142.9	29.7	2.9	0.461	139.7	13.6	14.5	14.6	*YNH*	29.7	29.7
	60.8	5.9	0.660		28.7	29.2	29.6	*YNH*	58.9	58.9
	63.6	6.1	0.675		30.5	30.3	31.2	*YNH*	61.1	61.1
	72.6	7.0	0.721		34.1	34.5	35.8	*YNH*	67.7	67.7
	134.2	12.9	0.980		65.8	66.3	66.3	*YNH*	102.3	102.3
	214.7	20.7	1.240		101.7	100.7	94.8	*YNH*	133.9	123.6
	314.1	30.2	1.500		122.5	120.9	113.1	*D*	163.5	129.8
	432.2	41.6	1.759		131.3	128.6	120.6	*D*	191.6	136.3
	569.2	54.8	2.019		136.7	133.9	126.1	*D*	218.6	142.8
	725.0	69.8	2.278		141.6	139.7	131.9	*D*	244.8	149.3
	899.7	86.6	2.538		145.4	145.0	138.4	*D*	270.2	155.6
	1093.2	105.3	2.798		149.5	148.2	143.5	*D*	295.0	161.9
	1305.4	125.7	3.057		156.0	152.4	147.3	*D*	319.2	167.9
	1536.6	148.0	3.317		160.2	156.4	152.0	*D*	342.9	173.8

Table C.7: Numerical and DSM results concerning the behavior and strength of b_w=130 mm P_B columns

Column	P_y (kN)	f_y (kN/cm^2)	$\bar{\lambda}_D$	$P_{cr.D}$ (kN)	$P_{u,0.1t}$ (kN)	$P_{u,0.23t}$ (kN)	$P_{u,1t}$ (kN)	*FM*	$P_{n.D}$ (kN)	$P^*_{n.D}$ (kN)
130x91	53.4	6.3	0.476	235.5	30.4	30.4	30.6	*YNH*	53.4	53.4
	127.5	15.1	0.736		72.3	72.3	71.2	*YNH*	117.7	117.7
	198.9	23.6	0.919		112.8	113.0	112.7	*YNH*	159.2	159.2
	205.6	24.4	0.935		117.5	117.6	116.8	*YNH*	162.6	162.6
	233.4	27.7	0.996		132.2	132.7	132.1	*YNH*	175.7	175.7
	371.0	44.0	1.255		194.2	191.5	175.9	*D*	228.7	209.0
	540.3	64.1	1.515		215.6	215.8	198.0	*D*	278.4	219.4
	741.3	88.0	1.774		229.4	227.2	215.5	*D*	325.7	230.4
	974.1	115.6	2.034		241.0	239.6	247.1	*D*	371.2	241.4
	1238.6	147.0	2.294		252.0	250.7	259.1	*D*	415.2	252.3
	1534.8	182.1	2.553		263.0	263.1	266.8	*D*	457.9	263.0
	1862.8	221.0	2.813		274.0	273.1	268.6	*D*	499.6	273.4
	2222.5	263.7	3.072		284.4	284.5	281.7	*D*	540.4	283.6
	2614.0	310.1	3.332		293.9	294.4	292.1	*D*	580.3	293.5
130x130	37.9	3.6	0.492	157.0	16.8	16.6	15.5	*YNH*	37.9	37.9
	88.6	8.4	0.751		40.3	40.8	41.6	*YNH*	80.9	80.9
	160.4	15.3	1.011		75.7	73.4	73.6	*YNH*	119.2	119.2
	218.1	20.8	1.179		102.7	101.5	99.0	*YNH*	142.3	137.4
	223.8	21.3	1.194		105.5	103.7	100.6	*YNH*	144.3	137.8
	253.3	24.1	1.270		115.2	115.9	110.9	*YNH*	154.4	139.7
	367.4	35.0	1.530		142.0	138.2	128.4	*D*	187.5	146.7
	502.7	47.9	1.790		149.1	147.8	138.7	*D*	218.9	154.0
	659.1	62.8	2.049		156.2	154.0	147.7	*D*	249.2	161.4
	836.7	79.7	2.309		161.6	160.5	157.7	*D*	278.5	168.6
	1035.4	98.7	2.568		167.4	166.1	165.4	*D*	306.9	175.7
	1255.3	119.6	2.828		172.7	171.8	176.5	*D*	334.7	182.7
	1496.4	142.6	3.088		177.9	177.7	176.8	*D*	361.8	189.4
	1758.6	167.6	3.347		184.3	183.9	179.6	*D*	388.4	196.0
130x185.7	26.1	1.9	0.507	101.6	9.4	9.4	9.6	*YNH*	26.1	26.1
	59.7	4.4	0.767		21.5	21.7	21.7	*YNH*	53.9	53.9
	106.9	8.0	1.026		38.6	38.9	38.7	*YNH*	78.5	78.5
	167.9	12.5	1.286		60.5	61.4	62.8	*YNH*	101.2	90.6
	210.1	15.6	1.438		75.9	77.5	73.1	*YNH*	113.9	93.3
	214.6	16.0	1.454		79.7	77.6	74.0	*YNH*	115.1	93.6
	242.5	18.0	1.545		84.7	82.8	78.7	*D*	122.5	95.2
	330.8	24.6	1.805		94.0	92.0	88.6	*D*	142.8	99.9
	432.8	32.2	2.065		98.4	96.3	90.9	*D*	162.4	104.7
	548.5	40.8	2.324		101.8	100.4	94.7	*D*	181.3	109.4
	677.9	50.4	2.584		105.3	104.2	100.3	*D*	199.6	114.0
	821.0	61.1	2.843		108.6	107.5	105.6	*D*	217.6	118.4
	977.7	72.7	3.103		111.6	111.3	110.5	*D*	235.1	122.8
	1148.2	85.4	3.363		114.6	114.2	110.9	*D*	252.3	127.1

Table C.8: Numerical and DSM results concerning the behavior and strength of b_w=150 mm P_B columns

Column	P_y (kN)	f_y (kN/cm^2)	$\bar{\lambda}_D$	$P_{cr.D}$ (kN)	$P_{u,0.1t}$ (kN)	$P_{u,0.23t}$ (kN)	$P_{u,1t}$ (kN)	*FM*	$P_{n.D}$ (kN)	$P^*_{n.D}$ (kN)
150x105	54.2	5.6	0.522	198.6	27.1	27.2	27.6	*YNH*	54.2	54.2
	121.4	12.5	0.782		61.0	61.7	61.4	*YNH*	108.3	108.3
	215.4	22.2	1.041		107.8	108.2	107.3	*YNH*	156.3	156.3
	336.2	34.7	1.301		160.7	159.6	151.2	*D*	200.5	177.8
	483.8	49.9	1.561		185.6	182.6	173.6	*D*	242.0	186.8
	572.7	59.0	1.698		192.1	185.0	176.7	*D*	263.2	191.6
	583.1	60.1	1.713		189.1	190.7	177.0	*D*	265.5	192.2
	658.1	67.8	1.820		197.7	193.1	185.5	*D*	281.7	196.0
	859.3	88.6	2.080		205.5	204.0	210.1	*D*	319.8	205.3
	1087.1	112.1	2.339		216.4	216.9	221.6	*D*	356.7	214.5
	1341.8	138.3	2.599		226.9	225.3	231.0	*D*	392.6	223.4
	1623.2	167.3	2.859		237.0	237.1	232.0	*D*	427.6	232.2
	1931.4	199.1	3.118		247.0	248.7	246.4	*D*	461.9	240.7
	2266.4	233.6	3.378		258.9	259.2	257.4	*D*	495.5	249.1
150x150	38.2	3.2	0.537	132.4	15.1	15.8	16.2	*YNH*	38.2	38.2
	84.1	7.0	0.797		33.8	33.9	36.1	*YNH*	74.2	74.2
	147.8	12.2	1.057		60.1	60.0	59.8	*YNH*	105.9	105.9
	229.3	19.0	1.316		91.7	91.4	84.7	*YNH*	135.2	118.8
	328.7	27.2	1.576		118.2	113.8	110.0	*D*	162.8	124.8
	430.1	35.6	1.803		126.2	121.2	113.2	*D*	185.9	130.2
	445.9	36.9	1.835		126.2	123.4	117.2	*D*	189.2	131.0
	449.6	37.2	1.843		125.1	122.3	112.6	*D*	189.9	131.2
	580.9	48.1	2.095		131.4	129.7	122.2	*D*	214.5	137.2
	733.8	60.7	2.355		136.5	134.9	132.8	*D*	239.1	143.3
	904.5	74.8	2.614		141.2	140.2	140.6	*D*	263.0	149.2
	1093.1	90.4	2.874		146.0	145.7	147.7	*D*	286.3	155.1
	1299.5	107.5	3.133		150.8	150.3	148.3	*D*	309.1	160.7
	1523.7	126.1	3.393		156.6	155.9	153.2	*D*	331.4	166.3
150x214.3	26.1	1.7	0.553	85.4	8.1	8.2	8.2	*YNH*	26.1	26.1
	56.4	3.6	0.812		17.6	17.6	17.8	*YNH*	49.1	49.1
	98.2	6.3	1.072		30.5	30.7	30.8	*YNH*	69.5	69.5
	151.5	9.8	1.332		46.4	46.3	46.1	*YNH*	88.4	76.9
	216.3	14.0	1.591		66.9	66.2	63.8	*YNH*	106.1	80.8
	292.6	18.9	1.851		77.9	76.4	74.6	*D*	123.1	84.8
	330.0	21.3	1.958		80.6	78.6	77.1	*D*	130.9	87.1
	335.1	21.6	1.973		80.8	77.9	77.4	*D*	131.9	87.3
	380.5	24.6	2.110		81.9	80.4	75.7	*D*	139.4	88.8
	479.8	31.0	2.370		85.2	83.7	78.6	*D*	155.2	92.7
	590.7	38.1	2.630		87.9	86.9	83.8	*D*	170.6	96.5
	713.1	46.0	2.889		90.5	89.7	88.4	*D*	185.7	100.3
	847.0	54.7	3.149		93.2	92.6	91.8	*D*	200.4	104.0
	992.4	64.1	3.408		102.7	95.8	93.5	*D*	214.8	107.5

Table C.9: Numerical and DSM results concerning the behavior and strength of b_w=180 mm P_B columns

Column	P_y (kN)	f_y (kN/cm²)	$\bar{\lambda}_D$	$P_{cr.D}$ (kN)	$P_{u,0.1t}$ (kN)	$P_{u,0.23t}$ (kN)	$P_{u,1t}$ (kN)	*FM*	$P_{n.D}$ (kN)	$P^*_{n.D}$ (kN)
180x126	51.5	4.4	0.568	159.6	21.3	21.9	22.1	*YNH*	51.5	51.5
	109.3	9.4	0.828		46.3	46.5	46.3	*YNH*	94.1	94.1
	188.7	16.3	1.087		79.8	79.7	78.8	*YNH*	132.1	132.1
	289.5	24.9	1.347		120.3	119.9	114.4	*YNH*	167.1	144.1
	411.9	35.5	1.606		144.0	146.4	142.6	*D*	200.2	151.4
	555.7	47.9	1.866		156.3	153.7	149.9	*D*	231.8	158.8
	721.1	62.1	2.126		164.6	163.3	160.3	*D*	262.3	166.3
	784.6	67.6	2.217		185.5	170.0	162.0	*D*	272.8	168.9
	795.5	68.5	2.233		186.2	170.2	165.2	*D*	274.5	169.3
	908.0	78.2	2.385		173.2	171.7	179.7	*D*	291.8	173.6
	1116.4	96.2	2.645		181.9	181.7	187.2	*D*	320.5	180.8
	1346.4	116.0	2.904		190.6	192.1	189.1	*D*	348.5	187.8
	1597.8	137.6	3.164		201.6	202.5	189.4	*D*	375.9	194.6
	1870.8	161.2	3.424		212.6	212.6	219.7	*D*	402.8	201.3
180x180	36.2	2.5	0.583	106.4	12.2	12.4	12.6	*YNH*	36.1	36.1
	75.6	5.2	0.843		25.6	25.6	26.5	*YNH*	64.3	64.3
	129.4	8.9	1.103		43.3	44.1	43.7	*YNH*	89.5	89.5
	197.5	13.6	1.362		65.9	67.0	66.4	*YNH*	112.8	96.4
	279.9	19.3	1.622		90.1	89.3	84.3	*D*	134.8	101.2
	376.7	26.0	1.881		99.2	97.4	98.6	*D*	155.8	106.2
	487.8	33.7	2.141		104.0	102.9	98.6	*D*	176.1	111.2
	613.3	42.4	2.401		108.3	107.0	104.8	*D*	195.7	116.1
	652.9	45.1	2.477		123.5	123.5	111.5	*D*	201.4	117.5
	661.0	45.7	2.492		124.0	123.6	117.6	*D*	202.5	117.8
	753.1	52.0	2.660		129.1	128.8	122.1	*D*	214.8	120.8
	907.3	62.7	2.920		136.0	135.1	126.8	*D*	233.5	125.5
	1075.8	74.3	3.179		139.9	141.5	128.1	*D*	251.7	130.0
	1258.7	87.0	3.439		146.8	146.0	131.6	*D*	269.7	134.5
180x257.1	24.6	1.3	0.599	68.6	6.4	6.4	6.5	*YNH*	24.4	24.4
	50.5	2.7	0.858		13.2	13.0	13.1	*YNH*	42.4	42.4
	85.6	4.6	1.118		21.8	22.1	22.2	*YNH*	58.5	58.5
	130.1	7.0	1.377		33.3	33.4	33.6	*YNH*	73.5	62.3
	183.7	9.9	1.637		48.1	47.6	48.5	*YNH*	87.6	65.4
	246.6	13.3	1.897		61.4	60.8	58.2	*D*	101.1	68.6
	318.7	17.2	2.156		65.3	64.0	66.4	*D*	114.2	71.8
	400.1	21.6	2.416		67.9	66.9	66.4	*D*	126.8	74.9
	490.7	26.4	2.675		70.2	69.1	67.7	*D*	139.1	78.0
	513.4	27.7	2.737		79.9	80.1	71.9	*D*	141.9	78.7
	519.1	28.0	2.752		80.2	77.8	73.0	*D*	142.6	78.9
	590.5	31.8	2.935		83.4	80.2	75.0	*D*	151.1	81.0
	699.6	37.7	3.195		87.9	80.2	77.7	*D*	162.8	83.9
	818.0	44.1	3.454		88.6	81.9	79.5	*D*	174.4	86.8

Table C.10: Numerical and DSM results concerning the behavior and strength of b_w=200 mm P_B columns

Column	P_y (kN)	f_y (kN/cm^2)	$\bar{\lambda}_D$	$P_{cr.D}$ (kN)	$P_{u,0.1t}$ (kN)	$P_{u,0.23t}$ (kN)	$P_{u,1t}$ (kN)	*FM*	$P_{n.D}$ (kN)	$P^*_{n.D}$ (kN)
200x140	53.1	4.1	0.614	140.9	20.1	20.6	20.8	*YNH*	52.5	52.5
	107.5	8.3	0.873		41.4	40.5	41.7	*YNH*	89.2	89.2
	180.8	14.0	1.133		68.6	69.4	69.6	*YNH*	122.2	122.2
	273.2	21.2	1.393		104.1	103.6	99.5	*YNH*	152.7	128.3
	384.5	29.9	1.652		130.5	123.5	124.1	*D*	181.7	134.7
	514.8	40.0	1.912		141.6	141.1	134.2	*D*	209.4	141.3
	664.2	51.6	2.171		146.7	147.7	142.6	*D*	236.1	147.9
	832.5	64.6	2.431		154.4	153.6	160.5	*D*	262.0	154.3
	1019.7	79.2	2.691		161.9	163.3	165.6	*D*	287.2	160.7
	1226.0	95.2	2.950		169.4	180.4	166.9	*D*	311.9	166.8
	1264.4	98.2	2.996		199.3	199.3	181.6	*D*	316.2	167.9
	1277.3	99.2	3.011		199.8	199.7	185.8	*D*	317.6	168.2
	1451.3	112.7	3.210		206.0	206.1	187.8	*D*	336.0	172.8
	1695.5	131.6	3.469		212.1	213.2	200.8	*D*	359.6	178.7
200x200	37.1	2.3	0.629	93.8	11.1	11.3	11.4	*YNH*	36.5	36.5
	74.1	4.6	0.889		22.9	22.4	22.3	*YNH*	60.8	60.8
	123.7	7.7	1.148		37.1	38.3	37.5	*YNH*	82.6	81.6
	185.9	11.6	1.408		56.8	55.3	58.7	*YNH*	102.8	85.6
	260.7	16.2	1.668		79.6	78.4	74.2	*YNH*	122.1	90.0
	348.3	21.7	1.927		87.6	87.2	83.8	*D*	140.5	94.3
	448.4	27.9	2.187		93.1	91.6	87.8	*D*	158.2	98.7
	561.2	34.9	2.446		96.8	95.6	94.6	*D*	175.4	103.0
	686.6	42.8	2.706		100.3	99.6	101.0	*D*	192.2	107.2
	824.7	51.3	2.966		103.8	103.9	104.1	*D*	208.6	111.3
	916.3	57.1	3.126		120.1	117.0	106.8	*D*	218.5	113.8
	925.2	57.6	3.141		119.7	120.7	108.8	*D*	219.5	114.0
	975.4	60.7	3.225		118.3	119.1	110.6	*D*	224.6	115.3
	1138.7	70.9	3.485		121.4	119.6	112.7	*D*	240.3	119.2
200x285.7	25.0	1.2	0.644	60.3	5.8	5.8	6.0	*YNH*	24.5	24.5
	49.3	2.4	0.904		11.4	11.4	11.4	*YNH*	39.9	39.9
	81.7	4.0	1.164		18.5	19.0	18.8	*YNH*	53.9	52.7
	122.2	5.9	1.423		28.0	28.1	28.2	*YNH*	66.9	55.3
	170.8	8.3	1.683		39.1	39.2	39.8	*YNH*	79.2	58.0
	227.6	11.0	1.942		53.9	51.9	50.8	*YNH*	91.1	60.9
	292.5	14.2	2.202		58.8	56.6	53.7	*D*	102.5	63.7
	365.6	17.7	2.462		60.2	59.1	56.3	*D*	113.5	66.4
	446.7	21.7	2.721		63.5	61.3	60.4	*D*	124.3	69.1
	536.1	26.0	2.981		64.1	63.4	63.3	*D*	134.8	71.8
	633.5	30.7	3.240		71.9	67.8	65.2	*D*	145.1	74.3
	639.5	31.0	3.256		74.2	73.7	66.5	*D*	145.7	74.5
	645.5	31.3	3.271		78.0	75.5	75.1	*D*	146.3	74.6
	739.1	35.9	3.500		81.1	74.9	76.6	*D*	155.2	76.8

Table C.11: Numerical and DSM results concerning the behavior and strength of b_w=100 mm PF_F columns

Column	P_y (kN)	f_y (kN/cm²)	$\bar{\lambda}_D$	$P_{cr.D}$ (kN)	$P_{u,0.1t}$ (kN)	$P_{u,0.19t}$ (kN)	$P_{u,1t}$ (kN)	*FM*	$P_{n.D}$ (kN)	$P^*_{n.D}$ (kN)
100x70	54.7	8.2	0.400	342.1	42.1	42.1	42.0	*YNH*	54.7	54.7
	132.6	20.0	0.622		98.3	98.4	97.6	*YNH*	130.7	130.7
	244.3	36.8	0.845		175.5	175.1	172.3	*YNH*	207.5	207.5
	389.8	58.7	1.067		261.6	260.3	250.3	*D*	277.1	277.1
	569.3	85.7	1.290		334.0	333.1	310.5	*D*	342.1	305.6
	782.6	117.8	1.512		394.6	392.0	361.6	*D*	403.8	318.7
	1029.7	155.1	1.735		441.2	418.6	445.9	*D*	463.0	332.3
	1310.8	197.4	1.957		479.1	442.9	481.3	*D*	520.1	346.1
	1625.7	244.8	2.180		565.7	555.8	560.9	*D+L*	575.5	359.7
	1974.5	297.3	2.402		616.4	618.3	606.5	*D+L*	629.5	373.2
	2357.1	354.9	2.625		661.0	663.2	658.6	*D+L*	682.2	386.3
	2773.6	417.7	2.847		706.9	707.1	704.8	*D+L*	733.9	399.3
	3224.0	485.5	3.070		748.8	748.5	745.2	*D+L*	784.6	411.9
	3708.3	558.4	3.292		786.5	786.7	783.1	*D+L*	834.4	424.3
100x100	40.9	5.0	0.415	237.9	24.5	25.9	24.9	*YNH*	40.9	40.9
	96.6	11.7	0.637		56.5	56.3	56.3	*YNH*	94.7	94.7
	175.9	21.4	0.860		103.2	103.2	105.4	*YNH*	147.7	147.7
	278.7	33.9	1.082		158.2	157.6	152.2	*D*	195.9	195.9
	405.1	49.2	1.305		209.9	208.5	198.6	*D*	240.9	213.1
	555.0	67.4	1.527		248.7	245.8	234.2	*D*	283.7	222.3
	728.5	88.5	1.750		278.5	276.7	291.4	*D*	324.7	231.8
	925.6	112.5	1.972		338.8	321.9	307.7	*D*	364.4	241.3
	1146.2	139.3	2.195		390.7	391.1	367.3	*D*	402.8	250.8
	1390.4	168.9	2.417		448.3	448.4	449.6	*D+L*	440.3	260.2
	1658.1	201.5	2.640		466.6	499.5	499.7	*D+L*	477.0	269.3
	1949.4	236.8	2.862		543.3	543.2	543.0	*D+L*	512.8	278.3
	2264.2	275.1	3.085		544.5	584.6	584.1	*D+L*	548.0	287.1
	2602.6	316.2	3.307		622.2	584.6	584.1	*D+L*	582.7	295.7
100x142.9	28.1	2.7	0.430	152.0	14.0	14.1	13.5	*YNH*	28.1	28.1
	64.7	6.2	0.652		31.3	31.2	32.4	*YNH*	62.9	62.9
	116.3	11.1	0.875		55.8	56.4	59.1	*YNH*	96.5	96.5
	183.0	17.4	1.097		90.9	90.0	86.4	*YNH*	127.1	127.1
	264.7	25.2	1.320		120.9	119.8	119.7	*YNH*	155.8	136.6
	361.5	34.4	1.542		145.5	144.3	138.5	*D*	183.0	142.4
	473.4	45.1	1.765		165.3	164.7	154.6	*D*	209.2	148.5
	600.3	57.1	1.987		186.2	186.4	177.2	*D*	234.5	154.6
	742.2	70.7	2.210		207.5	208.8	210.5	*D*	259.0	160.7
	899.2	85.6	2.432		229.4	232.3	233.2	*D*	282.9	166.6
	1071.3	102.0	2.655		254.3	256.8	255.7	*D*	306.3	172.5
	1258.4	119.8	2.877		281.8	279.3	283.0	*D+L*	329.2	178.2
	1460.5	139.0	3.100		309.4	309.7	313.3	*D+L*	351.6	183.8
	1677.8	159.7	3.322		337.9	333.0	340.9	*D+L*	373.7	189.3

Table C.12: Numerical and DSM results concerning the behavior and strength of b_w=130 mm PF_F columns

Column	P_y (kN)	f_y (kN/cm^2)	$\bar{\lambda}_D$	$P_{cr.D}$ (kN)	$P_{u,0.1t}$ (kN)	$P_{u,0.19t}$ (kN)	$P_{u,1t}$ (kN)	*FM*	$P_{n.D}$ (kN)	$P^*_{n.D}$ (kN)
130x91	50.3	5.9	0.444	254.5	29.7	29.6	29.6	*YNH*	50.3	50.3
	113.2	13.2	0.667		64.7	65.9	64.6	*YNH*	109.2	109.2
	201.3	23.5	0.889		116.7	114.4	112.0	*YNH*	165.0	165.0
	314.6	36.8	1.112		175.8	173.9	173.1	*YNH*	216.0	216.0
	453.1	53.0	1.334		227.6	225.4	218.5	*D*	263.8	229.2
	616.8	72.2	1.557		268.5	267.3	253.2	*D*	309.3	239.1
	805.7	94.3	1.779		310.1	299.4	310.0	*D*	353.0	249.2
	1019.8	119.3	2.002		372.4	368.5	358.2	*D*	395.2	259.4
	1259.1	147.3	2.224		434.9	438.1	430.4	*D+L*	436.2	269.6
	1523.6	178.2	2.447		488.5	489.5	487.7	*D+L*	476.2	279.5
	1813.2	212.1	2.669		534.7	534.6	534.1	*D+L*	515.2	289.3
	2128.1	248.9	2.892		577.3	577.7	576.3	*D+L*	553.5	298.9
	2468.2	288.7	3.114		618.1	619.5	619.1	*D+L*	591.1	308.2
	2833.4	331.4	3.337		657.6	655.2	654.1	*D+L*	628.0	317.4
130x130	36.6	3.5	0.459	173.6	17.1	16.8	17.9	*YNH*	36.6	36.6
	80.7	7.6	0.682		36.8	36.8	39.0	*YNH*	77.2	77.2
	142.0	13.4	0.904		64.6	65.2	65.8	*YNH*	115.0	115.0
	220.4	20.8	1.127		102.7	103.2	99.6	*YNH*	149.6	149.6
	316.1	29.8	1.349		139.0	137.9	130.7	*D*	182.1	156.8
	428.9	40.4	1.572		167.6	166.2	158.9	*D*	213.1	163.6
	559.0	52.7	1.794		191.3	190.9	180.1	*D*	242.8	170.5
	706.2	66.5	2.017		216.4	217.0	206.1	*D*	271.5	177.5
	870.6	82.0	2.239		241.0	244.7	242.3	*D*	299.5	184.4
	1052.2	99.1	2.462		270.4	273.4	264.4	*D*	326.7	191.2
	1251.0	117.8	2.684		298.0	303.1	304.3	*D*	353.3	197.8
	1466.9	138.2	2.907		329.7	333.9	307.4	*D*	379.4	204.4
	1700.1	160.2	3.129		365.0	366.5	364.1	*D+L*	405.0	210.7
	1950.5	183.7	3.352		398.9	395.5	376.2	*D+L*	430.2	217.0
130x185.7	25.8	1.9	0.474	115.0	9.5	9.3	9.5	*YNH*	25.8	25.8
	55.8	4.1	0.697		19.9	20.1	20.6	*YNH*	52.9	52.9
	97.1	7.2	0.919		34.6	35.4	36.1	*YNH*	77.7	77.7
	149.8	11.0	1.142		54.7	54.6	57.2	*YNH*	100.6	100.0
	213.9	15.8	1.364		80.4	79.3	75.0	*YNH*	122.0	104.1
	289.4	21.3	1.587		98.7	97.5	92.1	*D*	142.4	108.6
	376.3	27.7	1.809		113.1	112.1	108.0	*D*	162.1	113.2
	474.5	35.0	2.032		125.6	125.2	119.0	*D*	181.0	117.8
	584.1	43.1	2.254		138.9	138.8	138.1	*D*	199.5	122.4
	705.1	52.0	2.477		152.9	152.9	149.9	*D*	217.5	126.9
	837.5	61.7	2.699		167.6	167.8	165.7	*D*	235.1	131.3
	981.3	72.3	2.922		182.9	183.1	181.2	*D*	252.3	135.6
	1136.4	83.8	3.144		198.9	199.1	197.5	*D*	269.3	139.8
	1303.0	96.0	3.367		215.4	215.8	212.0	*D*	285.9	143.9

Table C.13: Numerical and DSM results concerning the behavior and strength of b_w=150 mm PF_F columns

Column	P_y (kN)	f_y (kN/cm²)	$\bar{\lambda}_D$	$P_{cr.D}$ (kN)	$P_{u,0.1t}$ (kN)	$P_{u,0.19t}$ (kN)	$P_{u,1t}$ (kN)	*FM*	$P_{n.D}$ (kN)	$P^*_{n.D}$ (kN)
150x105	51.5	5.2	0.489	215.4	27.6	28.5	28.3	*YNH*	51.5	51.5
	109.0	11.1	0.711		57.0	57.0	55.8	*YNH*	102.3	102.3
	187.9	19.1	0.934		94.6	98.3	96.1	*YNH*	148.6	148.6
	288.1	29.3	1.156		143.8	142.8	137.8	*YNH*	191.1	187.8
	409.6	41.7	1.379		185.2	184.0	173.3	*D*	231.2	195.6
	552.4	56.2	1.601		220.6	221.5	211.5	*D*	269.3	204.1
	716.5	73.0	1.824		256.8	259.8	240.0	*D*	306.0	212.7
	902.0	91.8	2.046		298.4	298.6	289.3	*D*	341.5	221.3
	1108.8	112.9	2.269		338.3	337.4	338.6	*D*	376.0	229.9
	1336.9	136.1	2.491		372.0	379.4	384.2	*D+L*	409.7	238.3
	1586.3	161.5	2.714		421.3	412.8	406.2	*D+L*	442.6	246.5
	1857.1	189.1	2.936		466.7	467.0	449.2	*D+L*	474.9	254.6
	2149.2	218.8	3.159		460.2	467.0	503.3	*D+L*	506.6	262.5
	2462.6	250.8	3.381		461.2	502.3	492.7	*D+L*	537.7	270.2
150x150	36.3	3.0	0.504	143.0	14.9	14.9	14.8	*YNH*	36.3	36.3
	75.4	6.2	0.726		29.8	30.5	30.7	*YNH*	70.1	70.1
	128.8	10.5	0.949		51.8	52.1	52.9	*YNH*	100.6	100.6
	196.2	16.1	1.171		79.1	79.5	80.2	*YNH*	128.7	125.0
	277.8	22.8	1.394		110.4	109.6	107.4	*YNH*	155.2	130.3
	373.6	30.6	1.616		134.7	133.6	128.8	*D*	180.5	135.9
	483.6	39.6	1.839		154.4	153.4	144.9	*D*	204.8	141.6
	607.7	49.8	2.061		172.8	172.8	172.0	*D*	228.3	147.4
	746.0	61.1	2.284		192.5	192.7	192.0	*D*	251.2	153.0
	898.4	73.6	2.506		212.9	213.2	210.5	*D*	273.5	158.6
	1065.0	87.3	2.729		234.6	235.0	218.0	*D*	295.4	164.1
	1245.7	102.1	2.951		257.2	257.6	248.2	*D+L*	316.8	169.4
	1440.6	118.0	3.174		280.9	281.2	273.9	*D+L*	337.8	174.6
	1649.7	135.2	3.396		305.8	306.1	308.5	*D+L*	358.5	179.8
150x214.3	25.5	1.6	0.519	94.8	8.3	7.9	7.7	*YNH*	25.5	25.5
	52.1	3.3	0.741		16.4	16.0	16.5	*YNH*	47.9	47.9
	88.1	5.6	0.964		26.9	27.0	27.9	*YNH*	68.0	68.0
	133.4	8.5	1.186		43.7	42.7	42.6	*YNH*	86.6	83.1
	188.2	12.1	1.409		58.8	62.0	59.3	*YNH*	104.1	86.6
	252.3	16.2	1.631		78.1	77.2	76.6	*YNH*	120.8	90.3
	325.8	20.9	1.854		90.7	89.6	85.5	*D*	136.8	94.2
	408.7	26.2	2.076		100.7	100.0	95.8	*D*	152.4	97.9
	501.0	32.1	2.299		110.5	110.4	109.9	*D*	167.5	101.7
	602.7	38.6	2.521		121.0	121.0	117.8	*D*	182.3	105.4
	713.8	45.7	2.744		131.8	132.0	125.6	*D*	196.8	109.0
	834.2	53.4	2.966		143.0	143.2	141.1	*D*	210.9	112.5
	964.1	61.7	3.189		154.6	154.8	154.6	*D*	224.9	116.0
	1103.3	70.7	3.411		166.7	166.8	164.4	*D*	238.6	119.4

Table C.14: Numerical and DSM results concerning the behavior and strength of b_w=180 mm PF_F columns

Column	P_y (kN)	f_y (kN/cm²)	$\bar{\lambda}_D$	$P_{cr.D}$ (kN)	$P_{u,0.1t}$ (kN)	$P_{u,0.19t}$ (kN)	$P_{u,1t}$ (kN)	*FM*	$P_{n.D}$ (kN)	$P^*_{n.D}$ (kN)
180x126	48.8	4.2	0.533	171.5	21.7	21.1	21.5	*YNH*	48.8	48.8
	98.0	8.4	0.756		45.7	45.0	44.7	*YNH*	89.1	89.1
	164.2	14.0	0.978		76.4	70.1	75.7	*YNH*	125.3	125.3
	247.3	21.1	1.201		103.9	107.0	103.3	*YNH*	158.7	150.7
	347.4	29.6	1.423		140.9	139.9	139.5	*YNH*	190.2	157.1
	464.5	39.6	1.646		169.0	167.9	160.3	*D*	220.3	163.8
	598.6	51.0	1.868		195.3	194.5	184.2	*D*	249.3	170.7
	749.7	63.9	2.091		220.9	221.1	218.2	*D*	277.4	177.6
	917.7	78.2	2.313		252.9	246.8	242.8	*D*	304.8	184.3
	1102.7	94.0	2.536		274.7	281.5	264.4	*D+L*	331.5	191.0
	1304.7	111.2	2.758		312.6	303.8	284.6	*D+L*	357.6	197.5
	1523.6	129.9	2.981		344.4	344.7	320.2	*D+L*	383.1	203.9
	1759.6	150.0	3.203		378.0	378.2	365.7	*D+L*	408.3	210.2
	2012.5	171.6	3.426		412.9	413.3	400.0	*D+L*	433.0	216.3
180x180	35.1	2.4	0.548	116.9	11.9	11.7	11.9	*YNH*	35.1	35.1
	69.4	4.8	0.771		23.1	23.1	23.8	*YNH*	62.5	62.5
	115.3	7.9	0.993		38.7	38.8	39.8	*YNH*	86.9	86.9
	172.8	11.8	1.216		58.0	58.2	60.8	*YNH*	109.6	103.0
	241.8	16.6	1.438		83.9	82.8	79.1	*YNH*	131.0	107.4
	322.4	22.1	1.661		102.6	101.6	97.2	*D*	151.5	112.0
	414.5	28.4	1.883		118.1	117.5	114.0	*D*	171.3	116.7
	518.3	35.5	2.106		131.8	131.7	124.5	*D*	190.4	121.3
	633.6	43.4	2.328		145.9	145.9	142.0	*D*	209.0	126.0
	760.4	52.1	2.551		160.6	160.7	159.5	*D*	227.1	130.5
	898.9	61.6	2.773		176.1	176.3	175.2	*D*	244.9	134.9
	1048.9	71.9	2.996		192.0	192.3	190.0	*D*	262.3	139.3
	1210.5	83.0	3.218		208.7	208.9	207.6	*D*	279.4	143.6
	1383.7	94.8	3.441		225.9	226.1	225.4	*D+L*	296.3	147.7
180x257.1	23.7	1.3	0.563	74.6	5.9	5.9	6.0	*YNH*	23.7	23.7
	46.0	2.5	0.786		11.9	11.8	11.8	*YNH*	41.0	41.0
	75.8	4.1	1.008		19.7	19.7	19.7	*YNH*	56.5	56.5
	112.9	6.0	1.231		29.2	29.3	29.4	*YNH*	70.9	65.9
	157.5	8.4	1.453		40.1	40.1	42.0	*YNH*	84.5	68.7
	209.4	11.2	1.676		55.2	54.9	54.6	*YNH*	97.5	71.6
	268.7	14.4	1.898		67.3	66.7	64.4	*D*	110.1	74.6
	335.4	18.0	2.121		75.9	75.4	72.0	*D*	122.3	77.6
	409.4	21.9	2.343		83.4	83.1	81.4	*D*	134.1	80.6
	490.9	26.3	2.566		90.6	90.5	88.0	*D*	145.7	83.5
	579.7	31.0	2.788		98.1	98.1	96.7	*D*	157.0	86.3
	675.9	36.2	3.011		105.8	106.0	104.6	*D*	168.1	89.1
	779.5	41.7	3.233		113.8	113.9	112.1	*D*	179.0	91.8
	890.5	47.7	3.456		122.2	122.5	121.0	*D*	189.7	94.4

Table C.15: Numerical and DSM results concerning the behavior and strength of b_w=200 mm PF_F columns

Column	P_y (kN)	f_y (kN/cm²)	$\bar{\lambda}_D$	$P_{cr.D}$ (kN)	$P_{u,0.1t}$ (kN)	$P_{u,0.19t}$ (kN)	$P_{u,1t}$ (kN)	*FM*	$P_{n.D}$ (kN)	$P^*_{n.D}$ (kN)
200x140	51.7	4.0	0.578	154.9	20.0	19.5	19.9	*YNH*	51.7	51.7
	99.2	7.6	0.800		37.9	37.4	39.8	*YNH*	87.3	87.3
	162.1	12.5	1.023		61.2	60.9	62.9	*YNH*	119.4	119.4
	240.3	18.5	1.245		95.5	94.1	90.5	*YNH*	149.1	137.2
	333.8	25.7	1.468		123.4	122.3	120.6	*YNH*	177.3	143.1
	442.6	34.0	1.690		148.9	148.1	143.7	*D*	204.3	149.2
	566.8	43.6	1.913		171.2	170.8	168.6	*D*	230.4	155.4
	706.3	54.3	2.135		193.7	192.9	191.4	*D*	255.6	161.6
	861.1	66.2	2.358		217.5	217.2	204.1	*D*	280.2	167.7
	1031.3	79.3	2.580		242.0	242.1	232.1	*D*	304.1	173.7
	1216.8	93.6	2.803		267.8	267.9	269.5	*D+L*	327.6	179.6
	1417.6	109.0	3.025		294.7	294.8	283.8	*D+L*	350.6	185.3
	1633.8	125.7	3.248		322.5	322.7	324.5	*D+L*	373.3	191.0
	1865.3	143.5	3.470		351.6	351.8	353.5	*D+L*	395.5	196.5
200x200	36.4	2.2	0.593	103.6	11.1	10.8	11.2	*YNH*	36.3	36.3
	68.9	4.3	0.815		20.9	20.2	21.2	*YNH*	59.9	59.9
	111.6	6.9	1.038		33.0	33.6	34.3	*YNH*	81.2	81.2
	164.6	10.2	1.260		47.6	49.8	49.9	*YNH*	101.1	92.0
	227.8	14.1	1.483		67.9	69.5	67.0	*YNH*	119.9	96.0
	301.3	18.6	1.705		88.2	87.4	87.2	*YNH*	137.9	100.1
	385.0	23.8	1.928		102.2	101.3	98.3	*D*	155.2	104.3
	479.0	29.6	2.150		114.0	113.6	108.1	*D*	172.1	108.4
	583.3	36.0	2.373		125.6	125.5	125.2	*D*	188.5	112.5
	697.8	43.1	2.595		137.7	137.9	135.8	*D*	204.5	116.5
	822.6	50.8	2.818		150.5	150.7	147.5	*D*	220.2	120.4
	957.6	59.2	3.040		163.7	163.9	150.2	*D*	235.6	124.2
	1102.9	68.2	3.263		177.3	177.4	176.1	*D*	250.7	128.0
	1258.5	77.8	3.485		191.4	191.7	192.4	*D*	265.6	131.7
200x285.7	24.4	1.2	0.608	66.1	5.8	5.8	5.9	*YNH*	24.2	24.2
	45.6	2.2	0.830		10.8	10.8	10.9	*YNH*	39.2	39.2
	73.3	3.5	1.053		16.9	17.3	17.6	*YNH*	52.7	52.7
	107.5	5.2	1.275		25.3	25.4	25.8	*YNH*	65.3	58.9
	148.3	7.2	1.498		34.3	35.2	37.0	*YNH*	77.3	61.4
	195.7	9.4	1.720		48.7	47.5	47.4	*YNH*	88.8	64.1
	249.6	12.0	1.943		58.1	57.5	56.8	*YNH*	99.8	66.7
	310.0	15.0	2.165		65.7	65.2	62.9	*D*	110.6	69.4
	377.0	18.2	2.388		72.3	72.1	71.4	*D*	121.0	72.0
	450.6	21.7	2.610		78.7	78.6	76.7	*D*	131.2	74.5
	530.6	25.6	2.833		85.1	85.1	83.7	*D*	141.2	77.0
	617.3	29.8	3.055		91.8	91.9	91.0	*D*	151.0	79.5
	710.5	34.3	3.278		98.6	98.9	97.2	*D*	160.7	81.9
	810.2	39.1	3.500		105.5	105.9	105.5	*D*	170.2	84.2

Table C.16: Numerical and DSM results concerning the behavior and strength of b_w=100 mm PF_B columns

Column	P_y (kN)	f_y (kN/cm^2)	$\bar{\lambda}_D$	$P_{cr.D}$ (kN)	$P_{u,0.1t}$ (kN)	$P_{u,0.19t}$ (kN)	$P_{u,1t}$ (kN)	*FM*	$P_{n.D}$ (kN)	$P^*_{n.D}$ (kN)
100x70	55.9	8.6	0.400	349.3	43.9	44.0	43.8	*YNH*	55.9	55.9
	135.4	20.8	0.622		103.4	104.1	102.0	*YNH*	133.5	133.5
	249.4	38.3	0.845		184.2	183.1	177.7	*YNH*	211.9	211.9
	398.1	61.1	1.067		261.9	257.7	233.0	*D*	283.0	283.0
	581.3	89.2	1.290		306.7	303.0	275.7	*D*	349.4	312.1
	799.2	122.6	1.512		337.9	333.3	310.0	*D*	412.4	325.5
	1051.6	161.3	1.735		363.4	358.8	350.4	*D*	472.8	339.4
	1338.6	205.3	1.957		379.1	381.6	372.2	*D*	531.1	353.4
	1660.2	254.6	2.180		382.3	385.4	399.5	*D*	587.7	367.3
	2016.4	309.3	2.402		443.2	425.0	413.3	*D*	642.9	381.1
	2407.2	369.2	2.625		472.1	471.3	471.8	*D*	696.7	394.5
	2832.6	434.4	2.847		501.7	500.5	501.3	*D+L*	749.5	407.7
	3292.5	505.0	3.070		529.9	529.0	531.3	*D+L*	801.2	420.7
	3787.1	580.8	3.292		555.1	555.9	551.6	*D+L*	852.1	433.3
100x100	40.3	5.0	0.415	234.4	24.4	24.2	24.5	*YNH*	40.3	40.3
	95.2	11.7	0.637		55.6	56.7	59.7	*YNH*	93.3	93.3
	173.3	21.4	0.860		103.1	106.0	105.0	*YNH*	145.4	145.4
	274.5	33.9	1.082		161.7	160.2	157.8	*YNH*	192.9	192.9
	399.0	49.2	1.305		199.7	196.3	179.1	*D*	237.3	209.9
	546.7	67.4	1.527		219.7	217.9	201.6	*D*	279.4	219.0
	717.6	88.5	1.750		235.5	231.9	220.6	*D*	319.9	228.3
	911.7	112.4	1.972		247.8	248.2	242.1	*D*	358.9	237.7
	1129.0	139.2	2.195		266.0	265.9	265.3	*D*	396.8	247.1
	1369.5	168.9	2.417		284.4	284.5	284.6	*D*	433.7	256.3
	1633.3	201.4	2.640		304.2	303.7	305.4	*D*	469.8	265.3
	1920.2	236.8	2.862		324.1	324.7	326.3	*D*	505.2	274.1
	2230.3	275.0	3.085		342.8	345.9	346.9	*D*	539.8	282.8
	2563.6	316.1	3.307		366.5	366.3	366.0	*D*	573.9	291.2
100x142.9	28.4	2.7	0.430	154.1	14.2	14.3	14.4	*YNH*	28.4	28.4
	65.5	6.3	0.652		30.7	32.6	33.3	*YNH*	63.8	63.8
	117.9	11.4	0.875		55.3	55.2	59.6	*YNH*	97.8	97.8
	185.5	17.9	1.097		93.0	91.7	85.7	*YNH*	128.8	128.8
	268.3	25.8	1.320		119.8	119.5	108.8	*D*	157.9	138.4
	366.4	35.3	1.542		139.6	137.1	126.7	*D*	185.5	144.4
	479.8	46.2	1.765		150.2	148.7	141.6	*D*	212.0	150.5
	608.4	58.6	1.987		159.1	158.1	153.4	*D*	237.6	156.7
	752.3	72.4	2.210		169.0	168.8	161.2	*D*	262.5	162.8
	911.4	87.8	2.432		180.8	180.8	171.1	*D*	286.7	168.9
	1085.8	104.6	2.655		193.2	193.2	179.2	*D*	310.4	174.8
	1275.4	122.8	2.877		205.6	206.2	183.1	*D*	333.6	180.6
	1480.3	142.6	3.100		219.1	219.0	218.6	*D*	356.4	186.3
	1700.4	163.8	3.322		231.8	231.8	231.6	*D*	378.8	191.8

Table C.17: Numerical and DSM results concerning the behavior and strength of b_w=130 mm PF_B columns

Column	P_y (kN)	f_y (kN/cm²)	$\bar{\lambda}_D$	$P_{cr.D}$ (kN)	$P_{u,0.1t}$ (kN)	$P_{u,0.19t}$ (kN)	$P_{u,1t}$ (kN)	*FM*	$P_{n.D}$ (kN)	$P^*_{n.D}$ (kN)
130x91	52.2	6.2	0.444	264.1	33.5	33.1	33.3	*YNH*	52.2	52.2
	117.5	13.9	0.667		66.1	75.5	72.9	*YNH*	113.4	113.4
	208.9	24.8	0.889		124.3	124.4	121.7	*YNH*	171.3	171.3
	326.5	38.7	1.112		185.8	183.7	180.0	*YNH*	224.2	224.2
	470.3	55.8	1.334		226.2	223.2	203.8	*D*	273.8	237.9
	640.1	76.0	1.557		252.2	247.0	235.6	*D*	321.0	248.1
	836.2	99.2	1.779		269.4	267.9	262.6	*D*	366.3	258.7
	1058.3	125.6	2.002		292.5	292.4	281.0	*D*	410.1	269.2
	1306.6	155.0	2.224		315.4	315.1	302.8	*D*	452.6	279.7
	1581.1	187.6	2.447		338.7	338.8	317.7	*D*	494.1	290.1
	1881.7	223.3	2.669		363.3	363.5	348.0	*D*	534.7	300.2
	2208.5	262.0	2.892		388.2	388.5	376.7	*D+L*	574.4	310.2
	2561.4	303.9	3.114		412.7	412.8	405.6	*D+L*	613.4	319.9
	2940.4	348.9	3.337		436.1	436.4	435.0	*D+L*	651.7	329.4
130x130	36.2	3.4	0.459	171.4	16.8	16.9	18.9	*YNH*	36.2	36.2
	79.7	7.6	0.682		38.0	38.9	38.7	*YNH*	76.2	76.2
	140.2	13.4	0.904		72.5	64.4	69.3	*YNH*	113.5	113.5
	217.6	20.7	1.127		106.0	104.7	98.7	*YNH*	147.7	147.7
	312.0	29.7	1.349		137.6	135.8	125.7	*D*	179.8	154.8
	423.4	40.3	1.572		158.3	156.7	144.5	*D*	210.3	161.5
	551.8	52.6	1.794		170.2	168.6	158.0	*D*	239.7	168.3
	697.1	66.4	2.017		182.2	181.3	176.0	*D*	268.0	175.2
	859.4	81.9	2.239		194.5	194.7	185.7	*D*	295.6	182.0
	1038.7	99.0	2.462		208.6	208.6	198.3	*D*	322.5	188.7
	1234.9	117.7	2.684		223.1	223.1	205.3	*D*	348.7	195.3
	1448.1	138.0	2.907		238.6	238.6	238.8	*D*	374.5	201.7
	1678.3	159.9	3.129		253.2	253.2	254.1	*D*	399.8	208.0
	1925.4	183.5	3.352		267.7	268.0	268.4	*D*	424.6	214.2
130x185.7	25.5	1.9	0.474	113.3	9.6	9.5	9.9	*YNH*	25.5	25.5
	55.0	4.1	0.697		19.5	19.5	20.0	*YNH*	52.1	52.1
	95.8	7.1	0.919		34.3	34.4	37.2	*YNH*	76.6	76.6
	147.7	11.0	1.142		53.3	53.5	56.9	*YNH*	99.1	98.6
	210.9	15.7	1.364		81.0	74.6	73.7	*YNH*	120.3	102.7
	285.3	21.2	1.587		97.3	95.6	88.3	*D*	140.4	107.1
	371.0	27.6	1.809		107.8	106.1	100.9	*D*	159.8	111.6
	467.8	34.8	2.032		115.1	114.1	111.9	*D*	178.5	116.2
	575.9	42.8	2.254		123.0	123.0	122.2	*D*	196.7	120.7
	695.2	51.7	2.477		132.3	132.4	124.3	*D*	214.4	125.1
	825.7	61.4	2.699		141.7	141.9	131.7	*D*	231.8	129.4
	967.4	71.9	2.922		151.4	151.5	151.3	*D*	248.8	133.7
	1120.4	83.3	3.144		160.9	161.0	161.1	*D*	265.5	137.8
	1284.6	95.5	3.367		170.4	170.5	170.5	*D*	281.9	141.9

Table C.18: Numerical and DSM results concerning the behavior and strength of b_w=150 mm PF_B columns

Column	P_y (kN)	f_y (kN/cm²)	$\bar{\lambda}_D$	$P_{cr.D}$ (kN)	$P_{u,0.1t}$ (kN)	$P_{u,0.19t}$ (kN)	$P_{u,1t}$ (kN)	*FM*	$P_{n.D}$ (kN)	$P^*_{n.D}$ (kN)
150x105	51.2	5.3	0.489	214.1	26.6	26.6	26.6	*YNH*	51.2	51.2
	108.4	11.2	0.711		57.0	54.9	56.9	*YNH*	101.7	101.7
	186.7	19.3	0.934		96.7	98.6	97.2	*YNH*	147.7	147.7
	286.3	29.5	1.156		146.3	144.9	137.6	*YNH*	190.0	186.7
	407.1	42.0	1.379		185.0	182.5	170.8	*D*	229.8	194.4
	549.0	56.6	1.601		207.9	205.8	195.8	*D*	267.7	202.8
	712.1	73.4	1.824		224.1	222.9	218.8	*D*	304.1	211.4
	896.5	92.4	2.046		243.0	237.1	234.6	*D*	339.4	220.0
	1102.0	113.6	2.269		261.3	261.1	252.0	*D*	373.7	228.5
	1328.7	137.0	2.491		279.3	279.4	261.0	*D*	407.2	236.8
	1576.6	162.5	2.714		297.4	297.7	263.6	*D*	439.9	245.0
	1845.8	190.3	2.936		316.1	316.7	315.0	*D+L*	472.0	253.0
	2136.1	220.2	3.159		333.6	335.6	335.8	*D+L*	503.5	260.9
	2447.6	252.3	3.381		351.6	354.7	353.5	*D+L*	534.5	268.5
150x150	36.9	3.1	0.504	145.4	15.2	15.5	15.7	*YNH*	36.9	36.9
	76.7	6.3	0.726		32.2	31.1	35.2	*YNH*	71.3	71.3
	130.9	10.8	0.949		49.9	48.5	53.2	*YNH*	102.3	102.3
	199.4	16.5	1.171		73.0	81.7	80.8	*YNH*	130.9	127.1
	282.4	23.4	1.394		112.7	111.2	103.3	*YNH*	157.8	132.4
	379.8	31.4	1.616		132.1	130.4	121.8	*D*	183.5	138.1
	491.5	40.7	1.839		143.8	141.6	136.9	*D*	208.2	143.9
	617.7	51.1	2.061		153.5	153.2	151.1	*D*	232.1	149.8
	758.2	62.7	2.284		165.0	165.0	164.7	*D*	255.3	155.5
	913.1	75.6	2.506		177.0	177.3	177.2	*D*	278.0	161.2
	1082.5	89.6	2.729		189.7	189.7	190.3	*D*	300.2	166.8
	1266.2	104.8	2.951		202.5	202.6	203.4	*D*	322.0	172.2
	1464.3	121.2	3.174		215.0	215.1	215.8	*D*	343.3	177.5
	1676.8	138.8	3.396		227.2	227.3	227.6	*D*	364.3	182.7
150x214.3	25.9	1.7	0.519	96.4	8.4	8.3	8.7	*YNH*	25.9	25.9
	53.0	3.4	0.741		16.4	16.6	17.4	*YNH*	48.7	48.7
	89.5	5.8	0.964		27.7	28.0	30.7	*YNH*	69.1	69.1
	135.7	8.8	1.186		41.2	42.6	46.4	*YNH*	88.0	84.5
	191.3	12.4	1.409		60.2	60.3	60.4	*YNH*	105.8	88.1
	256.6	16.6	1.631		79.2	77.9	77.0	*YNH*	122.8	91.9
	331.3	21.4	1.854		89.3	88.0	84.1	*D*	139.2	95.7
	415.6	26.8	2.076		96.4	95.6	94.0	*D*	155.0	99.6
	509.5	32.9	2.299		103.9	103.8	103.4	*D*	170.4	103.4
	612.9	39.6	2.521		112.2	112.3	112.2	*D*	185.4	107.2
	725.8	46.8	2.744		120.9	120.9	120.5	*D*	200.1	110.9
	848.3	54.8	2.966		129.2	129.2	129.0	*D*	214.5	114.5
	980.4	63.3	3.189		137.3	137.3	137.4	*D*	228.7	118.0
	1122.0	72.4	3.411		145.2	145.3	145.1	*D*	242.6	121.4

Table C.19: Numerical and DSM results concerning the behavior and strength of b_w=180 mm PF_B columns

Column	P_y (kN)	f_y (kN/cm²)	$\bar{\lambda}_D$	$P_{cr.D}$ (kN)	$P_{u,0.1t}$ (kN)	$P_{u,0.19t}$ (kN)	$P_{u,1t}$ (kN)	*FM*	$P_{n.D}$ (kN)	$P^*_{n.D}$ (kN)
180x126	49.9	4.3	0.533	175.2	20.6	20.5	21.1	*YNH*	49.9	49.9
	100.1	8.6	0.756		41.4	41.0	42.3	*YNH*	91.1	91.1
	167.7	14.4	0.978		68.4	70.9	71.6	*YNH*	128.0	128.0
	252.6	21.8	1.201		104.5	106.2	104.2	*YNH*	162.1	153.9
	354.9	30.6	1.423		141.7	141.6	139.0	*D*	194.3	160.4
	474.5	40.9	1.646		166.3	164.4	160.3	*D*	225.1	167.4
	611.5	52.7	1.868		182.2	181.2	177.4	*D*	254.7	174.4
	765.8	66.0	2.091		196.9	196.4	192.1	*D*	283.4	181.4
	937.4	80.8	2.313		211.9	211.8	209.0	*D*	311.3	188.3
	1126.4	97.0	2.536		227.1	227.0	222.4	*D*	338.6	195.1
	1332.7	114.8	2.758		242.3	242.3	238.3	*D*	365.2	201.8
	1556.4	134.1	2.981		258.2	258.2	255.8	*D*	391.4	208.3
	1797.4	154.8	3.203		273.6	273.7	272.8	*D+L*	417.1	214.7
	2055.8	177.1	3.426		286.3	286.9	279.6	*D+L*	442.3	221.0
180x180	35.9	2.5	0.548	119.4	12.6	12.5	12.2	*YNH*	35.9	35.9
	71.0	4.9	0.771		24.5	24.5	25.8	*YNH*	63.8	63.8
	117.8	8.1	0.993		39.8	40.2	44.2	*YNH*	88.8	88.8
	176.5	12.2	1.216		59.0	58.9	62.1	*YNH*	112.0	105.2
	247.1	17.1	1.438		81.8	82.9	79.5	*YNH*	133.9	109.7
	329.4	22.8	1.661		103.7	102.1	95.4	*D*	154.8	114.4
	423.6	29.3	1.883		115.2	113.8	109.2	*D*	175.0	119.2
	529.6	36.6	2.106		123.9	123.3	121.0	*D*	194.5	124.0
	647.4	44.7	2.328		133.6	133.5	133.0	*D*	213.5	128.7
	777.1	53.7	2.551		144.0	144.2	137.2	*D*	232.1	133.4
	918.6	63.5	2.773		154.5	154.8	143.5	*D*	250.2	137.9
	1071.8	74.1	2.996		164.6	165.0	165.6	*D*	268.0	142.3
	1237.0	85.5	3.218		176.1	176.0	176.4	*D*	285.5	146.7
	1413.9	97.7	3.441		185.9	185.9	185.8	*D*	302.7	150.9
180x257.1	24.5	1.3	0.563	77.3	6.5	6.6	6.8	*YNH*	24.5	24.5
	47.7	2.6	0.786		12.3	12.8	13.5	*YNH*	42.5	42.5
	78.6	4.2	1.008		20.2	20.3	21.8	*YNH*	58.6	58.6
	117.1	6.3	1.231		31.0	30.1	32.4	*YNH*	73.5	68.3
	163.3	8.8	1.453		42.2	41.8	46.2	*YNH*	87.7	71.3
	217.2	11.7	1.676		58.0	59.2	56.4	*YNH*	101.2	74.3
	278.7	15.0	1.898		69.1	68.2	65.7	*D*	114.2	77.4
	347.8	18.7	2.121		75.9	75.2	74.2	*D*	126.8	80.5
	424.7	22.9	2.343		81.6	82.3	82.1	*D*	139.1	83.6
	509.1	27.4	2.566		89.3	89.4	89.3	*D*	151.1	86.6
	601.3	32.4	2.788		95.9	96.4	96.3	*D*	162.8	89.5
	701.1	37.8	3.011		103.2	102.5	103.3	*D*	174.4	92.4
	808.5	43.6	3.233		109.8	109.8	110.1	*D*	185.7	95.2
	923.6	49.8	3.456		116.1	115.1	115.8	*D*	196.8	97.9

Table C.20: Numerical and DSM results concerning the behavior and strength of b_w=200 mm PF_B columns

Column	P_y (kN)	f_y (kN/cm²)	$\bar{\lambda}_D$	$P_{cr.D}$ (kN)	$P_{u,0.1t}$ (kN)	$P_{u,0.19t}$ (kN)	$P_{u,1t}$ (kN)	*FM*	$P_{n.D}$ (kN)	$P^*_{n.D}$ (kN)
200x140	51.5	4.0	0.578	154.2	21.0	20.0	22.3	*YNH*	51.4	51.4
	98.8	7.7	0.800		39.4	37.5	39.8	*YNH*	86.9	86.9
	161.3	12.5	1.023		63.3	65.5	64.0	*YNH*	118.8	118.8
	239.1	18.6	1.245		96.3	95.2	90.5	*YNH*	148.5	136.6
	332.2	25.8	1.468		123.7	122.4	119.7	*YNH*	176.5	142.4
	440.5	34.2	1.690		145.4	144.1	137.5	*D*	203.4	148.5
	564.1	43.8	1.913		158.8	159.8	154.0	*D*	229.3	154.7
	703.0	54.6	2.135		173.8	173.7	170.2	*D*	254.4	160.9
	857.1	66.5	2.358		187.1	187.5	181.7	*D*	278.9	167.0
	1026.5	79.7	2.580		200.7	201.0	199.8	*D*	302.7	172.9
	1211.2	94.0	2.803		213.9	214.4	211.3	*D*	326.1	178.8
	1411.1	109.6	3.025		227.4	227.9	224.6	*D*	349.0	184.5
	1626.3	126.3	3.248		241.4	241.9	241.6	*D+L*	371.6	190.1
	1856.7	144.2	3.470		254.6	255.2	247.3	*D+L*	393.7	195.6
200x200	36.0	2.2	0.593	102.5	11.3	11.3	10.5	*YNH*	35.9	35.9
	68.2	4.2	0.815		21.2	20.9	21.3	*YNH*	59.3	59.3
	110.4	6.9	1.038		33.0	33.4	34.4	*YNH*	80.4	80.4
	162.9	10.1	1.260		47.6	48.2	50.8	*YNH*	100.0	91.1
	225.4	14.0	1.483		66.7	72.3	68.0	*YNH*	118.6	95.0
	298.2	18.6	1.705		87.7	86.5	86.2	*YNH*	136.4	99.1
	381.0	23.7	1.928		98.6	97.7	93.8	*D*	153.6	103.2
	474.1	29.5	2.150		106.8	106.2	104.2	*D*	170.3	107.3
	577.3	35.9	2.373		114.9	114.8	113.8	*D*	186.5	111.3
	690.6	43.0	2.595		123.8	123.8	118.6	*D*	202.4	115.3
	814.1	50.7	2.818		133.0	133.0	123.8	*D*	217.9	119.2
	947.7	59.0	3.040		142.1	142.0	126.4	*D*	233.1	123.0
	1091.5	68.0	3.263		150.7	150.9	151.3	*D*	248.1	126.7
	1245.4	77.5	3.485		159.3	159.3	159.5	*D*	262.8	130.3
200x285.7	24.7	1.2	0.608	67.0	5.8	5.9	6.0	*YNH*	24.5	24.5
	46.2	2.2	0.830		11.0	11.0	11.0	*YNH*	39.7	39.7
	74.3	3.6	1.053		17.5	17.5	17.8	*YNH*	53.4	53.4
	109.0	5.3	1.275		25.5	25.2	27.3	*YNH*	66.2	59.7
	150.3	7.3	1.498		34.4	34.7	35.0	*YNH*	78.3	62.3
	198.3	9.6	1.720		46.6	45.6	48.2	*YNH*	89.9	64.9
	252.9	12.3	1.943		58.8	58.1	57.3	*YNH*	101.2	67.6
	314.2	15.3	2.165		65.2	64.6	63.9	*D*	112.0	70.3
	382.1	18.5	2.388		70.8	70.8	70.6	*D*	122.6	72.9
	456.6	22.2	2.610		77.1	77.0	77.2	*D*	133.0	75.5
	537.8	26.1	2.833		83.1	83.0	83.2	*D*	143.1	78.1
	625.6	30.4	3.055		89.1	88.7	89.3	*D*	153.1	80.5
	720.0	34.9	3.278		94.8	94.8	95.0	*D*	162.8	83.0
	821.1	39.9	3.500		100.4	100.4	100.3	*D*	172.4	85.3